DANIELA WOLTER FERREIRA

Topics in design and analysis of transcutaneous energy transfer to ventricular assist devices

São Paulo
2013

DANIELA WOLTER FERREIRA

Topics in design and analysis of transcutaneous energy transfer to ventricular assist devices

Document submitted in partial fulfillment of the requirements for the degree of Doctor of Science in Electrical Engineering in the Polytechnic School of the University of São Paulo.

Concentration area: Power Systems

Advisor:
Professor Luiz Lebensztajn

São Paulo
2013

Este exemplar foi revisado e corrigido em relação à versão original, sob responsabilidade única do autor e com a anuência de seu orientador.

São Paulo,   de outubro de 2013.

Assinatura do autor ____________________________

Assinatura do orientador _______________________

FICHA CATALOGRÁFICA

Ferreira, Daniela Wolter
Topics in design and analysis of transcutaneous energy transfer to ventricular assist devices / D.W. Ferreira. -- versão corr. -- São Paulo, 2013.
236 p.

Tese (Doutorado) - Escola Politécnica da Universidade de São Paulo. Departamento de Engenharia de Energia e Automação Elétricas.

1.Energia elétrica (Trtansferência) 2.Ventrículo cardíaco (Assistência) 3.Dispositivos e instrumentos médicos I.Universidade de São Paulo. Escola Politécnica. Departamento de Engenharia de Energia e Automação Elétricas II.t.

ACKNOWLEDGMENTS

The outcome of this thesis would not have been possible without the guidance and support of so many people in so many ways. I owe them all a very important debt and it is now the moment that I would like to express my deepest gratitude to the many talented individuals whom I have had the pleasure of working with and learning from. They, more than I, are the most important producers of this thesis.

I begin with my advisor, Professor Luiz Lebensztajn, who always contributed with the right words to the building of my knowledge and personality along with my academic evolution since my early years of graduation. Supporting me and criticizing me at the right moments, he encouraged me to do my best. I can never forget his words “A PhD thesis is not a patent!” when I was discouraged by a procedure that did not work well. Or “You must focus better on your research!” when I was too confident of what I was doing. I cannot thank him enough for all his tolerance and patience and the time he spent guiding me.

This research is also a product of several fortuities and encounters with the right people who have changed the path of my research. Had I not have visited the École Centrale de Lyon (ECL) in between two conference trips, I would not have spent six months in France as part of my academic research. This changed completely the course of my research which afterwards followed a path of more focus and quality. It was thanks to Dr. Laurent Krahenbühl and his wife that my stay in France was very smooth. I am very grateful to all their kindness and support. More than that, Dr. Krahenbühl made enormous contributions to my research and without them I would not have finished my thesis at the same level that I have achieved.

It was Dr. Krahenbühl who also introduced me to Dr. Ruth Sabariego, who helped me greatly with her extensive knowledge in homogenization methods in Gmsh and GetDP. In addition to her academic knowledge, she provided special friendship that I will always cherish. I have no words to express my greatest appreciation and admiration for her.

I would like to express my sincere gratitude towards Dr. Florent Morel and Dr. Christian Vollaire, who deeply interacted with my research, pointing out important considerations to facilitate its development. Without their guidance and persistent help, much of what I have done would not have been possible. Specially Florent; besides his direct contribution to my work, he always revised all my reports and papers with constructive remarks. I have no doubt that my abilities as an engineer have improved by an order of magnitude having researched with him.

Turning to my lab mates, I have greatly benefited from Lucas Blattner Martinho, who has been a good friend and copartner that I respect and admire. I cannot forget all the support he gave me, mainly with my posters in the conferences. In general, his meticulous comments were an enormous help to me in a way that I saw myself always trying to overcome my limitations. I certainly expect to continue working with him in my academic life. Another lab mate who challenged me a lot when in France was Moises Ferber. I want to thank him for all his patience and support. I shall not forget to thank Renan B. Muller, who incited me several ideas with his many questions about the subject of my research.

Apart from my fellow PhD students, I would like to thank all the professors and researchers who directly or indirectly enlightened me with several ideas to develop my research, especially Professor Lourenço Matakas Junior who, despite the lack of time, had interacted in my research before my trip to France. I hope we continue

working together in the near future. I have also gratitude to Professor Ivan Eduardo Chabu, who provided me the data of the artificial organ.

I would also like to express my gratitude to the financial support from CNPq, through process number 140907/2010-6 and FAPESP, through processes numbers 2011/18341-3 and 2012/06254-1. I also appreciate the financial support received from the international associated laboratory (LIA-Maxwell) and the ECL who supported me when I had no further financing to participate in conferences like MOMAG, EMF and COMPUMAG. Moreover, ECL provided me with lab instruments to make the physical measurements.

In the same way, the Institute of Technological Research (IPT) facilitated me to make some measurements while in Brazil. Hence, I would like to thanks IPT and its members Ramon Martin and Diego Nazarre for their help and support in some of my final measurements.

I cannot conclude without expressing my sincerest appreciation to all the members of my family for all their support and patience with my worries and absences in many family events because I was deep in my studies or travelling to conferences or academic meetings.

Last but not least, I come to the most personal and deepest appreciation to Roger Touma for all his help and support along the long journey of my research. Even with miles apart, he inspired me with his affection and patience to always do better and never surrender my project. He has been my enduring source of strength and has helped with the research in innumerable ways. I really appreciate what he sacrificed for me to complete this research and I am confident that the end of this thesis marks the beginning of a new life with him.

“I never did anything by accident, nor did any of my inventions come by accident; they came by work.”

Thomas A. Edison

ABSTRACT

This research studies a Transcutaneous Energy Transfer (TET) system which uses electromagnetic fields to transfer power from outside the body to an artificial organ (AO) in the body. It works like a high frequency transformer whereas the skin is part of the magnetic coupling between the primary (external) and secondary (internal) coils. Thus, the external coil (transmitter), which is excited by an oscillator circuit that transforms the continuous (DC) voltage to high-frequency alternating (AC) voltage, transfers energy to an internal system (receiver) containing a coil associated with a rectifier-regulator circuit to supply power to the AO and an internal rechargeable battery. Due to the diversity of research areas in TET systems, this thesis focused mainly on the TET coils, exploring few aspects of the electronic circuits which directly affect the proper design of the coils. Simulations of different configurations of coils (with different magnetic material types and different core geometrical dimensions) and different electrical parameters were performed via Finite Element Method (FEM) applications. Analyses of the results of these simulations with and without serial resonant capacitors (SRCs) observed the behavior of the coils considering the efficiency, regulation, specific absorption rate (SAR) and current density induced in the skin. These results also facilitated an optimization procedure using Kriging method without the need for new simulations via FEM. In parallel with the optimization procedure, different physical prototypes were created and tested to validate the simulations and explore the behavior of the coils. The temperature increase of the coils and the threshold limits of the electronic circuits were observed, suggesting new optimization strategies. Since the computation of the temperature is too complicated, the temperature rise was indirectly considered in this research by the use of a factor called “thermo factor”, which represents the relationship between the dissipated power and the area of the coil. Moreover, since the AO requires a constant power, the load of the TET system was modeled as a variable resistance. This thesis proposed an algorithm to compute this value of the variable resistance directly in the FEM simulations. Thus, another optimization procedure was proposed with the new mentioned strategy by directly interacting with the FEM application. In this second case, homogenization methods were used to simplify the mesh without neglecting eddy current, proximity and skin effects, thus allowing accurate simulations of coils with thicker wire gauges and at higher frequencies. In the end, the results of both simulations were briefly discussed to evaluate configurations eligible for construction or assembly.

Key-words: Transcutaneous Energy Transfer. Electromagnetism. Finite Element Method. Optimization.

RESUMO

Esse trabalho estuda um sistema de transferência de energia transcutâneo (TET) que, tal qual um transformador de alta freqüência, usa campos eletromagnéticos para transferir potência de fora do corpo a um órgão artificial dentro do corpo. Assim, a pele passa a ser parte do acoplamento magnético entre o primário (bobina externa) e o secundário (bobina interna). Dessa forma, a bobina externa (transmissor) é excitada por um circuito oscilador, gerando corrente alternada de alta freqüência e transfere energia ao sistema secundário interno (receptor) que contém uma bobina associada a um circuito retificador seguido de amplificadores e reguladores para alimentar o órgão artificial e/ou uma bateria recarregável interna. Devido à diversidade de áreas para pesquisar, esta tese teve as bobinas de TET como objetivo principal, explorando alguns aspectos dos circuitos eletrônicos que afetam diretamente o projeto adequado das bobinas. Simulações de diferentes configurações de bobinas (com diferentes tipos de material magnético e diferentes dimensões geométricas dos núcleos) e diferentes parâmetros elétricos foram realizados através de softwares de Método dos Elementos Finitos (FEM). Essas análises com e sem capacitores de ressonância série (SRCs) observaram o comportamento das bobinas considerando o rendimento, a regulação, a taxa de absorção específica (SAR) e densidade de corrente induzida na pele. Os resultados dessas simulações também facilitou um procedimento de otimização usando o método de Kriging, sem a necessidade de novas simulações via FEM. Em paralelo com o processo de optimização, diferentes protótipos físicos foram criados e testados para validar as simulações e explorar o comportamento das bobinas. O aumento da temperatura nas bobinas e os limites dos circuitos eletrônicos foram observados, sugerindo novas estratégias de otimização. Uma vez que o cálculo da temperatura é demasiado complicado, esta pesquisa sugere o uso de um fator, aqui denominado "fator térmico", para indiretamente considerar esse aumento de temperatura. Além disso, uma vez que o AO requer uma potência constante, a carga do transformador de TET foi modelada como uma resistência variável. Esta tese propõe um algoritmo para calcular este valor de resistência variável diretamente nas simulações com FEM. Assim, foi proposto um outro procedimento de otimização com a nova estratégia mencionada, interagindo diretamente com a aplicação de FEM. Neste segundo caso, os métodos de homogeneização foram utilizados para simplificar a malha sem ignorar correntes de Foucault, e os efeitos pelicular e de proximidade, permitindo simulações precisas de bobinas com fios mais grossos e em frequências mais altas. Os resultados de ambas as simulações foram discutidos brevemente no final para avaliar configurações elegíveis para serem montadas.

Palavras-chave: Transmissão Transcutânea de Energia. Eletromagnetismo. Método dos Elementos Finitos. Otimização.

CONTENTS

1 INTRODUCTION

The researches that aim at the development of devices to support the lives of patients with circulatory diseases are of great importance since these diseases have very high mortality rate. There are different clinical applications for circulatory assist devices such as pre and/or post operation circulatory support, cardiopulmonary bypass (CPB), Ventricular Assist Devices (VAD) as a bridge for cardiac transplant or genetic therapy, and Total Artificial Heart (TAH) which replaces the heart completely.

For these reasons, the foundation for research support of the state of Sao Paulo (FAPESP) approved the thematic project FAPESP 2006/58773-1 that aims to develop components and subsystems for an implantable centrifugal pump for a ventricular assist device (FUNDAÇÃO DE AMPARO À PESQUISA DO ESTADO DE SÃO PAULO, 2007). Different institutions including Sao Paulo University (USP) and the institute Dante Pazzanese of Cardiology (IDPC) among others are involved in this thematic project, part of which is the research of this thesis.

In order for these systems to be fully implantable, they require electric power that can be supplied through the technology of a Transcutaneous Energy Transfer (TET) system. The biggest advantage of this system is its ability to transfer energy to the internal devices through the skin without direct electrical connectivity, thus reducing infections, providing greater comfort and offering greater flexibility to the daily activities of the patient. This system is being strongly studied in different countries, using mainly inductive coupling.

Usually, the TET system has one external coil (transmitter) and one internal coil (receiver), transferring energy like a transformer in which the physical means of magnetic coupling between the primary (external) and secondary (internal) coils includes the skin. The spacing between the coils (coil gap) depends on the thickness of the skin of the patient and can vary from 5 to 20 mm, resulting in higher values of voltage regulation, low coupling and considerable eddy current in the skin with low system efficiency.

The transmission process is performed by a source consisting of an external battery which excites an oscillator circuit, generating high-frequency alternating current, which is applied to the external coil, thus creating a magnetic field. The secondary system (receiver) contains an internal coil immersed in this time-varying magnetic field and a rectifier connected to a regulator circuit, which supplies constant voltage to the VAD and to a rechargeable battery that allows the patient to disconnect from the external system for part of the time.

Therefore, it is noteworthy that a proper design of this system brings a highly efficient and robust system that meets the comfort requirements of the patient.

1.1 TARGETS

The primary targets of this research are to study a more reasonable design, optimization and implementation of methods of energy transmission and create a safe, compact and reliable TET system that supplies power to artificial organs (AOs) – more specifically Ventricular Assist Devices, or VADs – with the least possible discomfort and collateral effect to the patient.

Furthermore, the secondary objectives of this research includes studies that allow the systematization of an optimal design of the electromagnetic equipment, such as numerical methods as well as the operation of electronic systems, to convert continuous voltage (DC) to alternate voltage (AC) and vice versa.

1.2 DOCUMENT STRUCTURE

This document is structured in distinct chapters. Each of the following main chapters contains a brief introduction, a description, and a partial conclusion which may be used in a posterior chapter.

Chapter 2 shows a basic analysis of the TET system in order to support the development of the project with some historical highlights. It introduces the philosophy behind the main principle used to transfer the energy wirelessly, emphasizing biological aspects such as specific absorption rate (SAR) and induced current in the biological tissue, as well as their rules and restrictions.

Next, Chapter 3 presents different methods to acquire the properties of the TET coils, introducing numerical methods such as Finite Element (FE) methods and measurement procedures. Then, it compares the described methods to decide the approach to be used along the design of the project.

Subsequently, Chapter 4 makes several analyses with the methodology attained from Chapter 3, considering physical and virtual prototypes in addition to the use of ferrite cores and serial resonant capacitors (SRCs). The virtual prototypes allow the understanding of the TET system behavior with different geometric and electric construction characteristics. Thus, virtual analyses were performed by varying each characteristic of the TET system individually and then by varying many characteristics simultaneously.

Afterward, Chapter 5 makes a brief outline of electronic circuits which are associated with the TET coils. This chapter presents the observed behaviors of some physically implemented circuits, which are important to define the strategies for the optimization process.

Observing the need for optimization techniques, Chapter 6 then presents different optimization strategies and analyses of the behavior of the chosen configurations of the TET coils.

Lastly, Chapter 7 summarizes the observed remarks and suggests ideas for different future researches related to this project. It also presents the papers and prizes that resulted from this research.

Moreover, some appendixes which may clarify some topics in this research were added to support some readers. They contain:

A. details about the medium between each TET coil;
B. tables with the dielectric properties of some biologic tissues;
C. few basic theories to support the research such as proximity and skin effects, quality factor and its effects on the behavior of the TET system and a deduction of formulas used along the research;
D. details about how some data such as SAR were computed at Flux-2D;
E. extra results comparing the different methods presented in Chapter 3;
F. outlines about the genetic algorithm method.

2 TRANSCUTANEOUS ENERGY TRANSFER AND ITS EFFECTS

2.1 INTRODUCTION

This chapter shows a basic analysis of the TET system in order to support the development of the project. It introduces the philosophy behind the main principle used to transfer the energy wirelessly and outlines biological aspects such as specific absorption rate (SAR) and induced current in biological tissue as well as their rules and restrictions. This chapter also presents some topologies and researches in the area, which have been studied since the 1970s. And lastly, this chapter uses the presented concept to conclude some details that should be contemplated during the design of the TET system.

2.2 TET SYSTEM OVERVIEW

All the studied proposals for TET system development are based on the principle of inductive link through electromagnetic fields, transferring energy from an external coil to a coil inside the body, as represented in Figure 2.1.

Figure 2.1 – Basic Diagram of TET system parts.

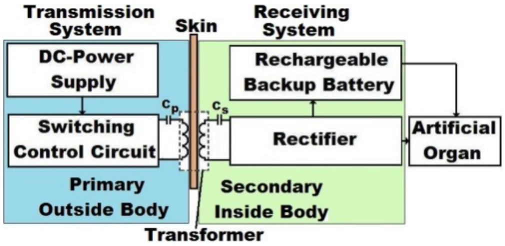

Thus, the TET system is composed of the following distinguished parts:

1. DC Power Supply outside the body, which could be a battery;
2. Switching control circuit outside the body, which converts the DC voltage from the battery into alternating current (AC) to be magnetically induced;

3. Transformer (magnetic transfer device) with the primary coil outside the body to transmit power to a secondary coil inside the body. The coils form a weakly coupled transformer as they usually are not connected by a common ferromagnetic core and they could be misaligned during the movement of the patient. For this reason, in this research, the association of the primary and secondary coils and their respective cores is called transformer;
4. Rectifier inside the body, which converts the AC voltage back to DC so that it can feed an internal battery and power the artificial organ (AO). This rectifier may also be connected to a converter to assure constant DC voltage on the internal battery and the AO;
5. Rechargeable battery inside the body, which is used to energize the AO when the transmitting primary coil is not positioned at the place of transmission;
6. Information Feedback system to convey useful information about the functioning of the internal device to the user. This portion is considered optional since it is not used in many TET systems. But considering that the device is inside the body of a patient, direct access is difficult. Thus, it is important to convey information about the operating condition, among other details.

Given the wide variety of functions of the TET system, its research is quite comprehensive and can deal with different areas. Furthermore, important aspects to the patient such as comfort, flexibility, side effects and electromagnetic influences among other issues should be considered. Thus, one can divide the design of TET system in the following main stages:

1. Transformer considering heating, efficiency and effects of electromagnetic fields on human being.
2. Electronics for the switching circuit outside the body and the rectifier converter inside the body, considering the efficiency.
3. DC voltage sources in and outside the body, considering robustness.

The stages are interrelated and depend on information from each other. However, it is possible to focus only on one specific stage to research. The focus of this thesis is the research of the transformer, exploring different properties and characteristics in order to facilitate the creation of a system that works properly under different conditions with less discomfort to the patient.

2.3 HISTORICAL HIGHLIGHTS

With the introduction of chloroform as an anesthetic agent in the late 1860s, occasional respiratory and cardiac arrest started occurring during medical interventions. In 1872, in the United Kingdom, Green used hand-held electrodes connected to the base of the neck and to the lower left chest of the patient to intermittently apply the output of a 300 V battery. This action could resuscitate five of seven cases of cardiac arrest and it was the beginning of the principle of the defibrillation devices (BRONZINO, 2000).

In 1957, a single myocardial electrode was implanted for the first time in a human being during a surgery to control ventricular rate and thereafter, such electrodes have become frequently used during cardiac surgery. Later, in another patient, an extracorporeal pacemaker was incorporated containing standby techniques, i.e., if a 5 seconds asystole was identified on the ECG monitored patient, the pacemaker was activated. This type of pacemaker was powered by a wire connected to a domestic power outlet and the patient could walk only if he pushed the equipment on a small cart. Then, the quest for portability began (BRONZINO, 2000).

Researchers started thinking about batteries, but several of them were concerned about the battery life. Thus, in 1959, Sennin and Elmqvist described an implantable pacemaker in which the batteries could be recharged through the energy available in a coil placed on the surface of the chest (BRONZINO, 2000).

In 1960, a group from the University of Missouri-Columbia detailed a theoretical rationale for a radio-frequency system involving inductive coupling between a thin, small pancake-shaped coil on the surface of the chest and a similar coil either within the chest or, alternatively, subcutaneously. Their system had a theoretical transfer efficiency of about 95 % and was tested only in dogs (SCHUDER, 2002). It represented the basis to the so called Transcutaneous Energy Transfer (TET) system.

In 1965, (LOUIS C. WALLER, July 20, 1965) patented a power generator for any device implanted in the human body as a pacemaker, containing its own internal power source through which the pacemaker would maintain its normal operation. In this invention, the patient should use a belt coupled to an element external to the body that transmits power to an element internal to the body through loops magnetically coupled and separated by the skin. The coupling between the external and internal loops is done via a permanent magnet present in the external transmitter to create a magnetic field which actuates a proximity switch (sensor) on the internal receiver. This switch closes the circuit indicating that the external device is correctly positioned with the implanted device and allows the external device to transfer power only when it is correctly positioned under great coupling conditions.

Considering that the main objective of Waller was to supply power to a pacemaker, its circuit was intended to generate DC voltage. Thus, the energy transferred by the alternating loops is rectified and can be replaced by the energy of an internal rechargeable battery in a way that the pacemaker works even without the external element coupled. The external element contains an external battery that can be replaced in case of emergency and this battery can be charged by connecting it to the power outlet. In this case, the AC energy is rectified to recharge this external battery and/or power a circuit that has an oscillator that now transforms this energy to AC with the required frequency to transfer energy through the loops.

Furthermore, this invention has current and voltage meters to indicate respectively the operability of the external battery and possible fluctuations in the internal load when the external device is properly positioned with the internal element.

In 1971, Schuder and his group reported the transmission of 1 kW of power for 1 h between an 11 cm diameter water-cooled coil on the surface and a coil implanted subcutaneously in a 31 kg dog (SCHUDER; GOLD; STEPHENSON JR., 1971). They reported that the temperature at the coil tissue interface, as measured just beneath the internal coil, rose from 36.7 ^{o}C to 39.7 ^{o}C.

In 1983, (EMPI, Inc. Donald D. Maurer, Oct. 11, 1983) described a TET device that uses an implanted capacitor whose energy was consumed by the implanted medical device. As Maurer used TET technology to generate an induced voltage to charge the capacitor, he thought having an efficient capacitor was more important than having an efficient TET system and therefore his device had low efficiency. Thus, this patent is related to a very low voltage level, of the order required for a small implantable capacitor.

In 1988, (COCHLEAR PTY. LTD University of Melbourne. James M. Harrison; Peter M. Seligman, May 3, 1988) described a TET system with improved coupling between the internal and external inductive coils. In order to achieve the coupling improvements, Harrison added a circuit electrically coupled to the primary coil configured to boost the quality factor of the primary transmitter circuit which includes the primary coil. His TET system had low power level and therefore had no applications to supply power to an artificial heart.

In 1994, (UNIVERSITY OF OTTAWA, John A. Miller, Sep. 27, 1994) presented a simplified TET device increasing the efficiency of energy transfer by 80 %.

Several researchers continued the studies of TET systems considering auxiliary electronic circuits besides the coils. Some proposed the use of resonant capacitors in series with the primary and the secondary coils to compensate the inductance as shown in Figure 2.2, reducing the voltage regulation and decreasing eddy currents (JOUNG; CHO, 1996; KIM; CHO, 1996).

Figure 2.2 – Circuit showing the induction compensation through resonant capacitors.

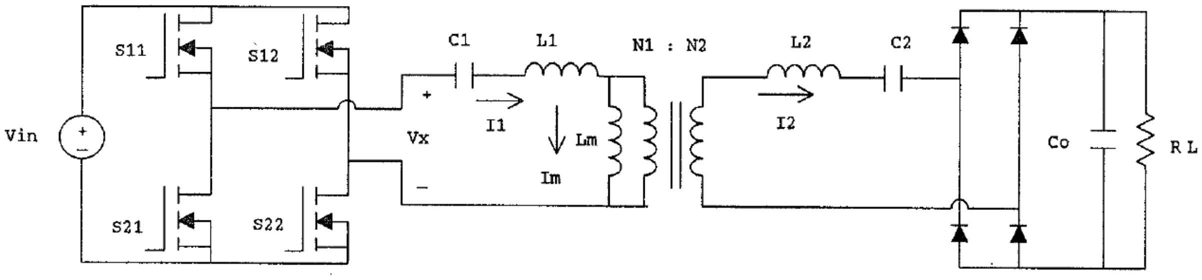

(KIM; CHO, 1996)

The researchers also used close-loop driver topologies, incorporating a telemetry channel and implementing additional control in terms of power management (PUERS; VANDEVOORDE, 2001).

Most of the researches presented coreless TET coils. These topologies of coils have the advantage of a more stable energy supply since the self-inductance of the coils does not change with the variation of the position between the coils. However, such coils have low energy transmission efficiency due to poor electromagnetic coupling between both coils.

The use of ferrite cores was also considered by researchers. (MIURA et al., 2006) proposed new TET coils with thin ferrite cores, which increase the magnetic coupling factor and self-inductance. They replaced the use of resonant capacitor with a synchronous rectifier using a digital phase-locked loop (PLL) technique. However, they reported problems with the heat dissipation capacity. Moreover, continual fluctuation of electromagnetic coupling between both coils caused a disadvantage of unstable operation.

Trying to solve the low coupling problem with the coreless TET coils and the unstable operation problem with the cored TET coils, (OKAMOTO et al., 2009) proposed a hybrid TET system in which the primary coil was coreless, but the secondary coil had a ferrite core.

In 2010, Dissanayake presented her PhD thesis in this subject with a flow diagram of a design methodology for primary and secondary coils, assuring the required transmission power and maximum temperature on the coils. She used ANSYS to simulate the system with different coils diameters obtaining the mutual and self-inductances to compute the maximum transferable power. As soon as she attained the diameters of the coils able to transfer the desired power, she could specify the number of turns and type of Litz wire to fit the simulated data. She used this information in COMSOL software to analyze the temperature on the coils, assuring that it does not exceed a maximum specified value. As soon as all the requirements were fulfilled, she obtained the recommended coil design (DISSANAYAKE, 2010). In her project, she used telemetry to control the frequency in order to make her system less sensitive to the coil movements (DISSANAYAKE et al., 2009).

In summary, the first researches on TET systems, more than five decades ago, did not consider much the effects of the electromagnetic fields in the biologic tissues. But lately, the study of these effects and of the optimization of the TET systems has grown intensively for different applications such as artificial hearts, ventricular assistive devices, and artificial lungs, among others with a wide range of power requirements.

In Brazil, several institutions such as Dante Pazzanese Institute of Cardiology (IDPC), the Heart Institute from Hospital of Clinics (INCOR), the University of Sao Paulo (USP), the Technological Institute of Aeronautics (ITA), and the University of Campinas (UNICAMP), among other institutions have being working together and motivating the technology development in this area with financing from CNPq, CAPES and FAPESP.

In the 90's, IDPC started the research and development of a model of a centrifugal pump to support blood circulation, called Spiral Pump. In 1997, Dr. Aron Andrade worked together with "Baylor College of Medicine" from Houston, Texas, USA to make an auxiliary artificial heart which used a TET system (ANDRADE, 1998).

Trying to analyze the performance of transmission of energy, Lopes Jr. made a research at EPUSP in which he built up coreless TET coils based on (SCHUDER; GOLD; STEPHENSON JR., 1971) with home-made Litz wires that supplied 22 V at 100 kHz to a combination of resistors totaling 20 Ω. During his experiments, he observed current, voltage and temperature in the coils up to 20 mm distance between the coils, getting to reasonable conclusions (LOPES JR., 2003).

2.4 THE TRANSFORMER

2.4.1 Geometry

The coil could have different geometries. However, for the scope of this research, circular geometries with small differences were analyzed due to the shape of the coil winding and the fact that sharp corners could hurt the patient and consequently affect his comfort. Following this premise, the more round the core geometry is, the more comfortable the TET device is for the patient.

Furthermore, a square coil would add an instability problem to the system in regards to misalignment. Considering that the central axes of the coil are lined up, a round core is completely aligned at any rotational position of the cores. In addition, when the axes are displaced, the TET system behaves similarly at any direction of displacement due to the symmetry. A square core, on the other hand, has symmetry only if the relative rotational angle between the cores is a multiple of 90^o. Thus, the behavior of this type of TET system with respect to the displacements between the coils is different if the coil axes displace in different directions. Besides, even if the central axes are lined up, a square TET core would change its behavior at any rotation different than 90^o.

In order to clarify the considered TET coils, Figure 2.3 details all the parts of the transformer considered during the project.

Figure 2.3 – Geometric detail of the considered parts of the TET transformer.

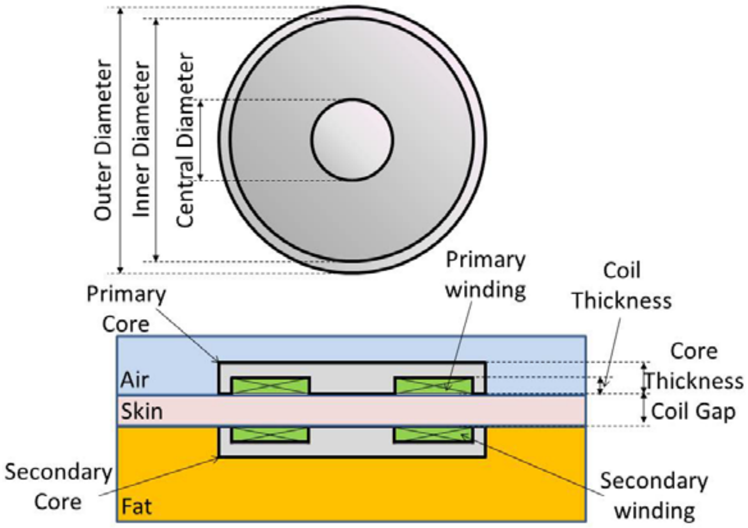

Observe that the primary core, external to the body, is surrounded mainly by air while the secondary core, underneath the skin, is surrounded mainly by fat. As mentioned in APPENDIX A, the thickness of the skin could vary between 5 and 30 mm, thus the value of the coil gap (between primary and secondary coils) affects the TET system design.

During this research, this geometry was used in different configurations considering ferrite cores or coreless coils. In the case of coreless coils, the region defined by the cores assumes properties of air and/or fat.

It is also important to remark that the volume described by the area between the inner and central diameter (the green area) is the space reserved to insert the winding. In these cases, the simulations were performed considering that the winding fills this whole space independent of the number of turns and gauge of wire. This means that the distance between the turns depends on the available space, number of turns and gauge of wire. For example, with less turns and bigger area, the turns are held or coiled less tightly together.

2.4.2 Equivalent circuit

An ideal inductor would have no losses regardless of the amount of current through the winding. However, real inductors have winding resistance depending on the length and cross section of the wire forming the coils. Since the winding resistance appears as a resistance in series with the inductor, it is often called the series resistance and it represents the Joule loss effect of the coil.

Thus, one alternative way to model the parameters of the TET transformer is by using the equivalent circuit model of a regular transformer, a simple circuit composed of resistive elements (r_1 and r_2) representing the Joule loss effect of the coils and other reactive elements (x_1, x_2 and x_m) describing the losses of the magnetic flux, as shown in Figure 2.4.

Figure 2.4 – Equivalent circuit of a TET transformer.

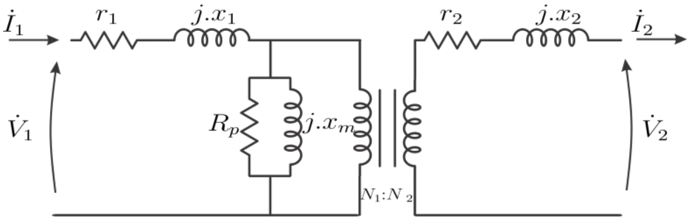

In Figure 2.4, x_1 and x_2 depend on the frequency and the primary and secondary self-inductances, respectively, and x_m depends on the frequency, the mutual inductance and the relation between turns. For frequencies of the order of hundreds of kilohertz, the capacitive effects could be neglected, but the proximity, skin and eddy currents effects should be considered (FAIZ; ASHTIANI; BYAT, 1997). The skin and proximity effects are considered in the values of the frequency dependent parameters r_1, r_2, x_1 and x_2. In the case where the coils have magnetic cores, R_p represents the losses in the core. In case of coreless coils, R_p may be required to represent eddy currents depending on the gauge of the wire. This is better described in the paper “Modeling coreless transformers with relative large wire gauge using an optimization method"[1]. This paper was submitted to COMPUMAG 2013 and is currently under review for posterior publication in the IEEE Transactions on Magnetics. In order to model the eddy currents, this paper proposes the use of a resistance R_p in parallel with x_m which includes the mutual inductance. In this case, even though coreless coils have no magnetic losses in the cores, the equivalent circuit of the TET transformer could be represented by Figure 2.4.

This model is very useful to calculate voltage, current and power with any load without the need to make a time-consuming simulation or implement a physical device. Nevertheless, the values of the elements (parameters) must be accurate or the equivalent circuit model will be unreliable.

2.4.3 Assembly of the TET windings

In this research, the study of the design of TET systems requires the assemblage of physical prototype coils to evaluate the behavior of the system and validate the simulations. In most of the studied literature, the primary and secondary windings are composed of different gauges of Litz wire.

The Litz wire is nothing more than a bunch of copper wire with smaller gauges, individually insulated and twisted to form a single strand. Each copper wire fills each position of Litz wire section in a way that the linkage flux and also the current in each

---

[1] This paper can be found at https://www.conftool.com/compumag2013/index.php?page=browseSessions&form_session=21

wire equalize. Hence, this kind of wire minimizes the AC resistance at high frequencies, reducing the skin effect.

Although the Litz wire is not a standard product, it is not easy to find. For this reason, this research used only solid wires instead.

The shape of the coils must also be considered. Zierhofer and Hochmair (1996) made a geometric analysis to improve the coupling coefficient between two magnetically coupled coils, showing that the coupling coefficient can be significantly improved if the windings of the coils are not concentrated in the outer diameter but distributed along the diameter of the coil forming a planar spiral with only one layer if possible (ZIERHOFER; HOCHMAIR, 1996).

In addition, they suggested that the outer diameter of the secondary winding should be smaller than the outer diameter of the primary winding, which reduces the efficiency but, on the other hand, also reduces the sensitivity to lateral misalignment while the secondary coil stays within the outer diameter of the primary coil. In this configuration, the coupling coefficient is constant in relation to lateral misalignment, but the quality factors of the coils of the transformer at no-load decreases typically by approximately 20 % due to increased wire lengths. However, Zierhofer and Hochmair believe that this would not be a big problem because the coils are part of the transmitter and receiver resonant circuits.

The material that covers the coil also affects its flexibility. There are cases in which researchers uses polypropylene (CHAN; CHENG; SUTANTO, 2000), but most of the references use rubber or Silastic. This research is not dedicated to the study of the best biocompatible material to be used, though this is an important area of research for the implementation of TET devices.

2.5 SERIAL RESONANT CAPACITORS (SRC)

Knowing the values of the self-inductances of the TET coils, serial resonant capacitors (SRC) can be calculated to compensate such inductances. Several researchers used SRC to compensate the leakage inductance, thus its calculation depends on the mutual inductance too (JOUNG; CHO, 1996).

However, as will be seen in Chapter 3, the mutual inductance depends on the geometric properties of the coils and consequently changes with the variation of the displacements and gaps of the coils while the TET device is in use. In the case when the mutual and therefore the leakage inductances change, a SRC calculated to compensate the leakage inductance will no longer be accurate for the chosen frequency. Hence, the frequency must be changed to adjust to the resonance or the system may not be able to transfer the required power; yet, if the system is able to transfer the required power, it will be with less efficiency.

Therefore, in this research, the SRC will be calculated to compensate only the self-inductance (L) at a specific frequency (f):

$$C = \frac{1}{(2.\pi.f)^2.L} \tag{2.1}$$

2.6 HEATING MECHANISMS

The heating is a very important factor to be considered during the design of the TET system and may represent a potential problem. For implantable devices with low power requirement, the rechargeable battery lasts a long time. Therefore, the TET device recharges the battery for a short time duration (<4 hours) without any significant heat generation. However, when the AO requires higher power, the TET device should be used for longer time. In this case, the generation and dissipation of heat becomes very important since excessive heating can lead to tissue damage and discomfort to the patient (LAZZI, 2005).

Many factors could affect the temperature rise during the operation of the TET device. Some of them include the power losses of implanted components, the heat radiated from external components, and the rate of dissipation of heat into the surrounding tissue. Moreover, unpredictable factors such as the ambient temperature and the external clothing of the patient add a complexity to the estimation of the temperature since they contribute to the heat dissipation capacity.

Some researchers detailed the analyses of the temperature rise during the use of bioimplants, considering even the tissue metabolism (LAZZI, 2005). This, however, is not the focus of this project, though it represents a proposal for future work.

Nevertheless, this research does not ignore the fact that the TET coils may affect the temperature in the area of contact. Hence, some factors of temperature rise should be understood.

2.6.1 Heating effects due to dissipated power in the wires

The increase of temperature in the wires is very hard to estimate with accuracy and requires a more dedicated research due to the large amount of unknown factors that affect the temperature.

It is known that, the electric current circulating through the wires and electronics with a certain resistivity releases some Joule losses, which are dissipated in terms of temperature. The amount of heat released is proportional to the dissipated power, i.e., the square of the current as given by the law of Joule.

$$Q \propto r.I^2 \tag{2.2}$$

In this equation, r is the resistance of the winding and I is the net current that cross the winding.

This released heat amount in the copper windings is related to the heat amount in the law of heat transfer of Fourier which postulates that the rate of heat transfer is proportional to the temperature gradient present in a solid.

$$Q \propto A.\left(\theta - \theta_{ref}\right) \tag{2.3}$$

In (2.3), θ is the temperature that the system will get to, θ_{ref} is the ambient temperature considered as initial temperature and A is the surface of heat exchange, i.e., it is the surface area of the winding.

Observe that (2.2) and (2.3) are not exact equations and they indicate only proportionality dependent on an unknown factor. For this reason, in this research, the increase of temperature is indirectly accounted for by the proportional relation between the dissipated power and the coil area. For better reading, this project calls this relation “thermo factor”:

$$\lambda = \frac{r.I^2}{A} \tag{2.4}$$

2.6.2 Electromagnetic effects in biological tissues

As previously mentioned, the TET system is based on the electromagnetic field principle to transfer energy from outside the body to inside the body. This means there is a body part located in the middle of this magnetic field. The question then arises as whether this could result in a detrimental biological effect, which may be characterized by some change in a biological system after the introduction of a specific external stimulus. The electromagnetic waves can generate some kind of biological effect when the frequency of the electromagnetic wave that transfers energy is very high. If this frequency is higher than the emission of light, such as gamma and X-rays (ionizing radiation), the transferred energy would be sufficient to break chemical connections through ionization, which may damage the genetic material of the cells, leading to diseases such as cancer for example.

However, unlike gamma and X-rays, the electromagnetic fields with frequencies lower than the emission of light (non-ionizing radiation) do not have enough energy to cause the breaking of any chemical bonds, though their direct interaction with the tissue can result in thermal or non-thermal effects.

The heating is the result of the absorption of the electromagnetic field in a dissipative medium, where part of the power is reflected by the skin and the other part penetrates and quickly dissipates with the depth (CRUZ, 2005).

The absorption happens mainly due to the rotation of the dipoles of water and dissolved ions induced by the electromagnetic field. Therefore, the amount of water is an important parameter when determining the dielectric properties of the tissue.

The thermal effects have been studied for a long time and, in 1975, Johnson recommended that all researchers in microwave bioeffects portray their radiation conditions in terms of an average absorbed energy per unit of mass from an animal or a tissue sample (JOHNSON, 1975).

Thus, he described a rate that characterizes the absorption of electromagnetic energy in animals and depends on the geometry and size of the animal. This rate is known as *SAR* (Specific Absorption Rate, W/kg) and is given by:

$$SAR = \frac{\sigma . \bar{E} . \bar{E}^*}{2 . \rho} \tag{2.5}$$

in which *E* is the strength of the electric field in biological tissue (V/m); σ is the electrical conductivity of biological tissue in the irradiation frequency (S/m); and ρ is the biological tissue density (kg/m^3).

Particularly at high frequencies, the conductivity is high since the body has a large amount of water and its conductivity can be given by the following expression (BULLA, 2006).

$$\sigma = 2 . \pi . f . \varepsilon'' \tag{2.6}$$

In (2.6), *f* is the frequency in Hz and ε'' is the permissivity of the biologic tissue.

The average SAR and the distribution of SAR can be calculated and estimated through experimental measures and their values depend on the following factors:

1. Parameters of the incident field, such as frequency, intensity, polarization and configuration of the source (near or far field);
2. Characteristics of the exposed body, i.e., its size and geometry and dielectric properties of various tissues;
3. Ground effect and reflection of other objects in the field near the exposed body.

As the total energy imposed in an animal can be measured per amount of heat throughout the body, this factor can also be measured by studying the heat exchanges or through techniques of balance of power (the absorbed power by the tissue is the supplied power less the used power and lost power).

In addition to the thermal effects of non-ionizing waves, there is evidence that induced electromagnetic fields have some biochemical or electro physical effects through direct interaction of oscillatory fields with polar molecules present in the biological fluids and tissues (BULLA, 2006).

Such effects can stimulate the muscles or nerves due to induced current and thus the current density J (A/m^2) must also be considered (SHIBA et al., 2008).

$$J = \sigma . E \tag{2.7}$$

According to (SHIBA et al., 2008), in a TET system, the primary coil current is directly proportional to the voltage of this coil and inversely proportional to the frequency and to the mutual inductance between the coils. (SHIBA et al., 2008) concludes that, by increasing the diameter of the coil, the current density in the skin decreases. Similarly, SAR depends on the voltage at the primary coil which is inversely proportional to the mutual inductance between the coils. Thus, a larger diameter coil reduces the SAR.

Hence, in a first analysis, it is clear that parameters such as frequency, output voltage, mutual inductance between coils, and diameter of the coils are important factors for the development of a secure transmission.

2.6.3 Rules and restrictions for the electromagnetism effects

In order to protect all segments of the population against all damages caused by the identified radio frequency (RF) energy, some international exposure standards have been prepared.

Available experimental evidences indicate that the exposure of human parts for about 30 minutes at a medium-frequency electromagnetic field, producing a whole body SAR of 4 W/kg, results in a temperature rise greater than 1 ^{o}C. Exposure to higher intensity fields, producing SAR values greater than 4 W/kg, can overcome the thermo regulatory capacity of the body and produce levels of body heat even more dangerous.

Several studies with rodents and primate models have demonstrated the wide range of tissue damage as a result of temperature rise in excess of 1 to 2 °C of a certain part of the body ("Local") or the whole body ("Whole-Body"). The sensitivity to thermal damage to different types of tissue varies, but the limit for irreversible effects under normal conditions is greater than 4 W/kg, even for the most sensitive tissues (INTERNATIONAL COMMISSION ON NON-IONIZING RADIATION PROTECTION, 1998).

Thus, in each country, committees formed by governmental and non-governmental organizations developed their rules and regulations proposing certain safety limits.

In the United States, the standard C95.1 developed by the IEEE (Institute of Electrical and Electronics Engineers) was adopted by the North American ANSI (American National Standard Institute) for the first time in 1966, and it has been periodically reviewed since. Its last review, in 1999, evaluated over 1400 articles (DIAS; SIQUEIRA, 2002). The committees that developed the standard consisted of members from universities, industry and government.

Based on data obtained in the revision of 1982, the IEEE added a safety factor of 10, placing a limit for the "Whole-Body Average SAR" at 0.4 W/kg and the peak value of the "Local SAR" at 8 W/kg.

The “Whole-Body Average SAR” is the average value of SAR obtained in the whole body for a period of 30 minutes. The peak value of the “Local SAR” is the average value obtained by any SAR in any 1 g of tissue for the same time period.

In 1991, IEEE established a difference between occupational exposure (controlled) and the general public (uncontrolled), adding greater security for the latter. Therefore, the “Whole-Body Average SAR” and the peak value of the “Local SAR” for "uncontrolled" exposure were 0.08 W/kg and 1.6 W/kg, respectively (CRUZ, 2005).

Table 2.1 shows the SAR limits established by the IEEE for a frequency range between 100 kHz and 6 GHz for a period of 30 minutes.

Table 2.1 – SAR basic restrictions established by IEEE and based on the standard ANSI/IEEE C95.1 for a frequency range between 100 kHz and 6 GHz for a period of 30 minutes.

Characteristic of the Exposure	**Whole-body Average SAR (W/kg)**	**Local SAR (head and trunk) (W/Kg/1g)**	**Local SAR (members) (W/kg/10g)**
Occupational Exposure	0.4	8	20
General Public	0.08	1.6	4

Similarly, the International Commission on Non-Ionizing Radiation Protection (ICNIRP), with worldwide acceptance and permission from several other organizations such as the WHO (World Health Organization) and ILO (International Labor Organization), set some limits for SAR, current density and power density according to Table 2.2. These limits provide a wide margin of safety for other boundary conditions such as high temperature, humidity, and level of physical activity.

Table 2.2 - SAR basic restrictions established by ICNIRP for a frequency range between 100 kHz and 10 GHz for a period of 6 minutes.

Characteristic of the Exposure	**Whole-body Average SAR (W/kg)**	**Local SAR (head and trunk) (W/Kg in 10g)**	**Local SAR (members) (W/kg in 10g)**
Occupational Exposure	0.4	10	20
General Public	0.08	2	4

The limit for SAR is the same as IEEE C95.1 for the "Whole-Body Average SAR" exposure, but with only 6 minutes of exposure. For "Local SAR" exposure, the ICNIRP uses a sample of 10 g rather than 1 g for the IEEE (CRUZ, 2005).

As the measurement of SAR in an animal or human being is very difficult or imprecise to pursue, some methods that relate the values of accepted SAR inside the body with measurements performed outside the body were established. For the microwave range, the external measurements were the power density of equivalent plane wave whose more usual unit of measure is W/m^2 or mW/cm^2.

Table 2.3 - ICNIRP basic restrictions for the frequency between 100 kHz and 10 MHz.

Characteristic of the Exposure	**Current Density (mA/m^2) (RMS)**	**Average SAR (W/Kg)**	**Power Density (W/m^2)**
Occupational Exposure	f/100	0.4	50

In (BRASIL, Lei no 11.934, 2009), the republic presidency signed the law 11,934, which amended the law 4,771 from September 1965 to make other arrangements on the limits of human exposure to electric, magnetic and electromagnetic fields in the frequency range up to 300 GHz in order to ensure protection of the general health and the environment.

This law adopts the limits recommended by the World Health Organization (WHO), which recommends the limits of ICNIRP (BRASIL, Lei no 11.934, 2009).

As mentioned, according to ICNIRP rules, a patient that knows the risk of the exposure to this magnetic field and is oriented to follow the right procedure to minimize the risks can be exposed at a maximum value of the induced RMS current density in mA/m^2 not exceeding the value of the frequency divided by one hundred, i.e., $\mathrm{J_{max}} = {}^{\mathrm{f}}/_{100}$.

Therefore, this research works with the concept of relative current density in the skin in percentage, which is the induced current density divided by its limit at the frequency of the induction and multiplied by one hundred (J/Jmax.100 %). Since the acceptable limit by ICNIRP is the frequency divided by 100, the relative current density is the induced current in mA/m^2 divided by the frequency and multiplied by 10000.

2.7 CONCLUSIONS

The difficulty of the design of a TET system is related to the large amount of parameters that could affect its behavior. The main idea is to attain a TET system that provides more comfort and reliability to the patient.

In this way, a good alternative would be trying to minimize the volume or weight of the TET device, taking in consideration the restrictions of the project and all the unusual situations to which the TET system is submitted.

Thus, the design of the TET system may contain the following restrictions:

1. Relative induced current density in the skin;

2. SAR;
3. Output voltage/power between the required range;
4. Increase of temperature of the wires of the coil.

As mentioned in Section 2.6.1, in this research, the increase of temperature is indirectly accounted for by the “thermo factor”, i.e., relation of the dissipated power by the coil area.

Furthermore, since part of the TET system will be positioned in the body of the patient, it will be subjected to different kinds of coupling situations, such as:

1. Distance between the coils (coil gap): the skin thickness could vary according to the patient;
2. Distance between the axes of the coils (coil misalignment): since the secondary coil is positioned inside the body, the alignment between the coils is very hard to achieve.

Hence, all the mentioned restrictions should be fulfilled in all these coupling situations. The parameters of the TET system that could help to provide the requirements of this project (maximum efficiency, minimum volume, low relative induced current density) could be:

1. Parameters related to the magnetic properties, such as number of turns as well as relative permeability of the ferromagnetic material, inner and outer diameters, and geometry of the cores.
2. Parameters related to the electric system, such as applied voltage and frequency.

2.7.1 Parameters related to the physical properties of the coils

This case considers the primary (L_1) and secondary (L_2) self-inductances, which depend on:

- Number of turns.

- Wire cross section: affects the outer diameter of the coil, thus affecting the inductance. Moreover, the cross section affects the skin and proximity effects, depending on the frequency.
- Relative permeability of the ferromagnetic material of the core.
- The inner and outer diameters of the cores.

In this project, the coil is cylindrical and the turns are uniformly distributed. Otherwise, the number of parameters would be even higher.

The mutual inductance also depends on the coupling factor *k* and the relative position between the coils, what is called disturbance in this project.

The use of ferromagnetic material as the core of the coils also makes the design process more complex and more susceptible to the aforementioned disturbances because, in this case, the self-inductance is also affected by the relative position between the coils, requiring more calculation for reliable results.

2.7.2 Parameters related to the electric system

The electric part of the TET system depends on:

- Applied voltage;
- Frequency;

The voltage and frequency are control parameters to try to fix the disturbances due to the variation of the relative position between the coils.

Lastly, it is important to cite that the results and conclusions of this chapter were partially submitted in the following papers to the following conferences and journal:

1. “Screening a Transcutaneous Energy Transmitter”, accepted for oral presentation at MOMAG 2012 in Joao Pessoa, Brazil. The presentation of this paper got a prize of second best presenting paper.

2. “An accurate model with lumped parameters for coreless transformers with relative large wire gauge”, accepted for poster presentation at EMF 2013 in Bruges, Belgium.
3. “Modeling coreless transformers with relative large wire gauge using an optimization method”, accepted for poster presentation at COMPUMAG 2013 in Budapest, Hungary. The full paper was accepted on October 3rd 2013 for publication in the IEEE Transactions on Magnetics.
4. “A Systematic Sensitivity Analysis of the Performance of a Transcutaneous Energy Transmitter for Design Purposes”, accepted in August 2013 for publication in the Journal of Microwaves, Optoelectronics and Electromagnetic Applications (JMOe).

3 OBTAINING THE TET COILS PROPERTIES

3.1 INTRODUCTION

This chapter introduces different concepts to compute the lumped parameters of the TET transformer (self and mutual inductances and joule losses resistances), including analytic calculations, method of experimental measurements and simulations through Finite Element Method.

It also discusses different Finite Element approaches, proposing the use of homogenization techniques to minimize the computational cost of dense meshes needed for configurations where the penetration depth of the electromagnetic wave at the specific frequency is smaller than the gauge of the wire.

At the end, it compares the proposed methods with experimental measurements considering their variation with misalignment and frequency.

3.2 ANALYTIC CALCULATION OF THE INDUCTANCES OF THE CORELESS COILS

In order to simplify the explanation of how to analytically calculate the self and mutual inductances of a coreless coil, consider first two single-turn coils, i.e. with only one turn each. The self-inductance of each coil could be calculated, according to (ZIERHOFER; HOCHMAIR, 1996), by:

$$L = \mu_0 . a \left(ln \left(\frac{8.a}{r_w} \right) - 2 \right) \tag{3.1}$$

For a coil composed of N_1 concentric circular loops with different inner radii, the mutual inductance between the loops is part of the self-inductance of the coil. This mutual inductance can be calculated as in the situation of multiple loops aligned with distance d = 0, as will be explained in Section 3.2.4.

The single turn coils could be positioned at three different arrangements as shown in Figure 3.1 – (a) with the center aligned and coils separated by distance d, (b) with lateral misalignment Δ, (c) with angular misalignment α.

Figure 3.1 – Position arrangements between primary and secondary coils:
(a) coils aligned and separated by distance d; (b) lateral misalignment Δ; (c) angular misalignment α.

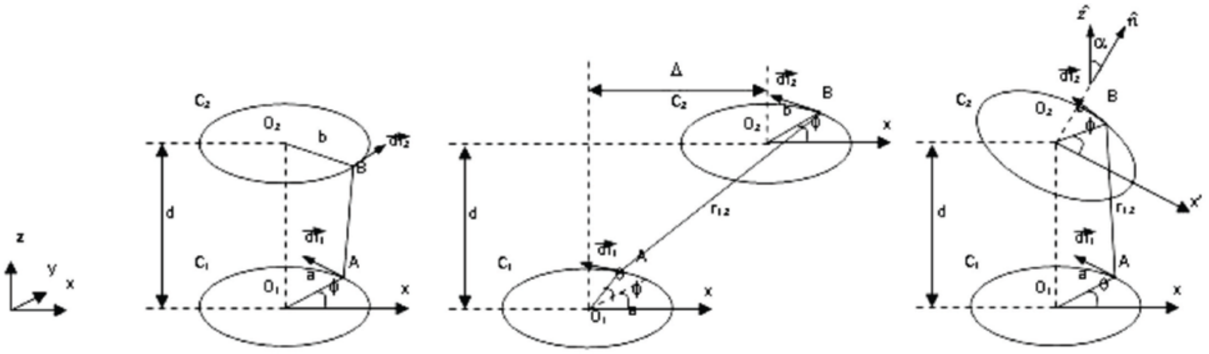

(a) (b) (c)

3.2.1 Turns aligned and separated by distance d.

The mutual inductance of two single-turn coils separated by a distance *d* with their centers aligned can be calculated by (see proof in (SOMA; GALBRAITH; WHITE, 1987; ZIERHOFER; HOCHMAIR, 1996)):

$$M = \mu_0 . \sqrt{a.b} . G(r) \tag{3.2}$$

in which μ_0 is the vacuum magnetic permeability $4.\pi.10^{-7}$ H/m, *a* and *b* are the inner diameters of the coils 1 and 2, respectively and

$$G(r) = \left(\frac{2}{r} - r\right) . K(r) - \frac{2}{r} . E(r) \tag{3.3}$$

in which *K(k)* and *E(k)* are the complete elliptic integrals of the first and second kind, respectively and

$$r = \sqrt{\frac{4.a.b}{(a+b)^2 + d^2}} \tag{3.4}$$

3.2.2 Lateral misalignment ∆.

In the cases where there are a misalignment ∆, (SOMA; GALBRAITH; WHITE, 1987) shows that the mutual inductance can be calculated through the integral

$$M = \frac{\mu_0.a.b}{2.\pi}.\oint \frac{\cos\beta}{\sqrt{a.b_L}}.G(r).d\varphi \tag{3.5}$$

in which φ is defined in Figure 3.1, *G(r)* is already defined by (3.3) and

$$r = \sqrt{\frac{4.a.b_L}{(a+b_L)^2 + d^2}} \tag{3.6}$$

$$b_L = \sqrt{b^2 + \Delta^2 + 2.\Delta.\cos\varphi} \tag{3.7}$$

$$tg\beta = \frac{\Delta.\sin\varphi}{b + \Delta.\cos\varphi} \tag{3.8}$$

3.2.3 Angular misalignment α.

When the coils are misalignment by an angle α, (SOMA; GALBRAITH; WHITE, 1987) shows that the mutual inductance can be calculated through the integral

$$M = \frac{\mu_0.\sqrt{a.b}}{\pi\sqrt{cos\alpha}} \int_0^{\pi} \sqrt{\left(\frac{cos\vartheta}{cos\emptyset}\right)^3}.G(r)d\emptyset \tag{3.9}$$

in which ϕ is shown in Figure 3.1, *G(r)* is already defined by (3.3) and

$$r = \sqrt{\frac{4.a.b.cos\emptyset.cos\alpha/cos\vartheta}{a^2 + b^2 + d^2 - 2.b.d.cos\emptyset.sin\alpha + 2.a.b.cos\emptyset.cos\alpha/cos\vartheta}} \tag{3.10}$$

$$tg\vartheta = \frac{sin\emptyset}{cos\emptyset.cos\alpha} \tag{3.11}$$

3.2.4 Coils with more than one turn.

Since the turns of the spiral coils are circularly concentric, the inner diameter of each turn increases at least by the wire diameter of the previous turn. Nevertheless, it is possible to approximately represent this special coil by a set of single-turn coils. Figure 3.2 shows this approximated model.

Figure 3.2 – Approximated model of the spiral coil.

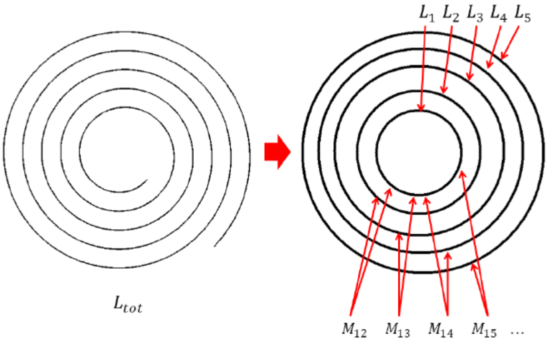

Thus, in order to consider all the loops of the coils, it is necessary to make the integration of mutual inductance for each turn:

$$M = \sum_{i=1}^{N_1} \sum_{j=1}^{N_2} M\left(a_i, b_j, \Delta, d\right) \tag{3.12}$$

Following the same trend of thought, the self-inductance of a coil with more than one turn can be calculated by:

$$L = \sum_{i=1}^{N_1} L(a_i, r_w) + \sum_{i=1}^{N_1} \sum_{j=1}^{N_1} M\big(a_i, a_j, \Delta = 0, d = 0\big) \tag{3.13}$$

It is noteworthy that the sum of the mutual inductance should not be account when *i=j*.

3.3 CALCULATION THROUGH VOLTAGE AND CURRENT DATA

The procedure described in Section 3.2 is fast and accurate for aligned coreless coils and in situations where the proximity, skin and eddy currents effects are negligible. However, as already mentioned in Section 2.4.2, the proximity, skin and eddy currents effects should be considered at frequencies of the order of hundreds of kilohertz and the equivalent circuit, that could model the TET transformer with the losses, is the circuit shown in Figure 2.4. In this figure, r_1 and r_2 represent the joule loss resistances already considering the skin and proximity effects, while x_1 and x_2 are the reactances that consider the leakage inductances of the primary and secondary coils, i.e., they consider the self-inductance (L_1 and L_2) and the mutual inductance (M).

Hence, special no-load and short-circuit tests may be performed to calculate the parameters of the equivalent circuit. In this case, the voltage and current at the primary ($\dot{V}_1$, $\dot{I}_1$) and secondary ($\dot{V}_2$, $\dot{I}_2$) coils with their respective phases must be acquired for both tests: no-load ($\dot{V}o_1$, $\dot{I}o_1$, $\dot{V}o_2$ and $\dot{I}o_2$) and short-circuit ($\dot{V}cc_1$, $\dot{I}cc_1$, $\dot{V}cc_2$ and $\dot{I}cc_2$). Note that in the no-load test, $\dot{I}o_2 = 0$, and in the short-circuit test, $\dot{V}cc_2 = 0$. However, these variables were also considered in order to systematize the acquisition of data.

Then, the lumped parameters could be calculated by observing Figure 2.4.

When the equivalent circuit is at no-load, the voltage in the parallel branch containing *x_M* and *R_p* is $a.\dot{V}o_2$, where $\omega = 2.\pi.f$ in which *f* is the frequency, and *a* is the transformer ratio which can be calculated by using the currents from the short-circuit test as:

$$a = \left|\frac{\dot{I}cc_2}{\dot{I}cc_1}\right| \tag{3.14}$$

Thus, the impedance in this parallel branch is given by $a.\dot{V}o_2 / \dot{I}o_1$. Since separating the real and imaginary parts of a parallel impedance is complicated, the admittance of this branch, given by $\dot{I}o_1 / a.\dot{V}o_2$ is considered instead. The real part of this admittance is due to the eddy current losses (R_p) and the imaginary part is due to the mutual ($x_M = \omega.M$). Thus,

$$M = \frac{-1}{Im\left(\frac{\dot{I}o_1}{a.\dot{V}o_2}\right)}.\frac{1}{\omega} \tag{3.15}$$

$$R_p = \frac{-1}{Re\left(\frac{\dot{I}o_1}{a.\dot{V}o_2}\right)} \tag{3.16}$$

Observing that x_1 and x_2 of Figure 2.4 are dependent on the self and mutual inductances as $x = j.\omega.(L - M)$, the parameters of the primary coil can be calculated from the no-load data as:

$$r_1 = Re\left(\frac{\dot{V}o_1 - a.\dot{V}o_2}{\dot{I}o_1}\right) \tag{3.17}$$

$$L_1 = Im\left(\frac{\dot{V}o_1 - a.\dot{V}o_2}{\dot{I}o_1}\right).\frac{1}{\omega} + M \tag{3.18}$$

In the same way, the secondary coil parameters can be calculated from the short-circuit data as:

$$r_2 = Re\left(a.\frac{\dot{V}cc_1 - (r_1 + j.\omega.L_1).\dot{I}cc_1}{\dot{I}cc_2}\right) \tag{3.19}$$

$$L_2 = Im\left(a.\frac{\dot{V}cc_1 - (r_1 + j.\omega.L_1).\dot{I}cc_1}{\dot{I}cc_2}\right).\frac{1}{\omega} + M \tag{3.20}$$

However, in a bad coupled system, this equation for the transformer ratio is not always precisely valid. Thus, another way of obtaining these parameters without the use of the transformer ratio is by separating completely the coils, i.e., making them electrically or magnetically uncoupled. In this case, the equivalent circuit of each coil can be modeled as shown in Figure 3.3.

Figure 3.3 – Equivalent circuit of one coil separately.

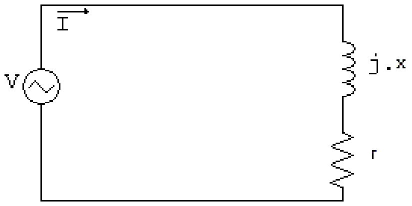

Thus, the self-inductance and the joule loss resistance can be obtained separately by the voltage ($\dot{V}$) and current ($\dot{I}$) at each coil, as:

$$r = Re\left(\frac{\dot{V}}{\dot{I}}\right) \tag{3.21}$$

$$L = \frac{Im\left(\frac{\dot{V}}{\dot{I}}\right)}{\omega} \tag{3.22}$$

Once both coils are measured and their parameters (L_1 and L_2) and (r_1 and r_2) are known, the mutual inductance and the proposed parallel resistance can be obtained by considering the equivalent circuit from Figure 2.4. For this purpose, the coils should be properly placed and the modulus and phase of the voltage and current should be measured.

Since there is no current on the secondary coil when it has no-load, its measured voltage is exactly on the branch containing the mutual inductance in parallel with the resistance that models the eddy currents. Thus, the mutual inductance and the parallel resistance can be calculated by using (3.15) and (3.16), respectively.

In this way, the parameters are directly calculated without the use of the transformer ratio.

It is noteworthy that the proposed equivalent circuit model can be enhanced to better consider all the relevant effects for high frequencies, including capacitive effects if needed. Then, the equations presented here are not sufficient to compute all the parameters which could then be computed via optimization techniques, as described in the paper "Modeling coreless transformers with relative large wire gauge using an optimization method"[2] mentioned in Section 2.4.2.

---

[2] This paper can be found at https://www.conftool.com/compumag2013/index.php?page=browseSessions&form_session=21

3.4 ACQUISITION THROUGH MEASUREMENTS

3.4.1 Measurements with IA (Impedance Analyzer)

If the coil is already built, it is possible to measure the physical self-inductance of the coil by using an impedance analyzer (IA), but the mutual inductance is a parameter that cannot be measured directly with only one measurement.

The IA supplies data of frequency (*f*) in Hz, modulus ($|Z|$) in ohms and phase (φ) in degree. Thus, considering that the circuit is composed of an inductance in series with a resistance, the inductance for each frequency can be calculated by using:

$$L = \frac{|Z|.\sin\left({}^{\varphi.\pi}/_{180}\right)}{2.\pi.f} \tag{3.23}$$

When the coil is not electrically or magnetically coupled to any other coil, the self-inductance of each coil could be easily identified at any frequency by this measurement process.

However, the mutual inductance requires a little more sophisticated procedure. It can be derived from two sets of inductance measurements while the coils are magnetically coupled with the desired coupling to obtain the mutual inductance. Besides the magnetic coupling, the coils should be electrically coupled in series in two different configurations as shown in Figure 3.4. First, the coils should be connected in a way that the magnetic field created by one coil opposes the magnetic field created by the second coil, measuring $L_o = L_1 + L_2 - 2M$. Second, they should be connected in a way that the magnetic fields of both coils are in the same direction (non-opposing configuration), measuring $L_a = L_1 + L_2 + 2M$. Then, the mutual inductance is calculated as $M = (L_a - L_o)/4$.

Figure 3.4 – Configuration used to measure the mutual inductance through the Impedance Analyzer.

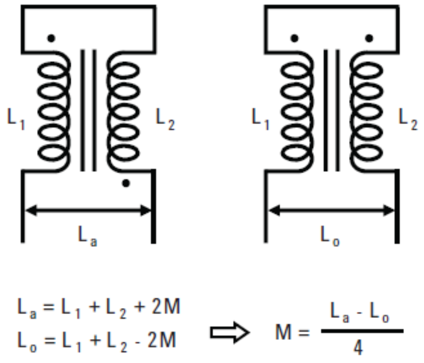

3.4.2 Using Vector Network Analyzer

Another way to obtain the mutual inductance is by using the Vector Network Analyzer (VNA).

This instrument has a built in signal generator that supplies the input voltage to the primary coil and measures the supplied input current. Thus, the other channel of this device measures the current on the short-circuited secondary.

To perform the measurements with VNA, channel 1 can be connected to measure current on the primary and channel 2, to measure current on the secondary, as shown in Figure 3.5. Then, the primary coil is supplied with the signal supplier from VNA. The secondary coil should be short-circuited and VNA should be configured to calculate the current on the secondary coil (channel 2) divided by the current on the primary coil (channel 1) for a frequency range from 20 kHz to 1 MHz.

Figure 3.5 – Test configuration for the measurements with VNA.

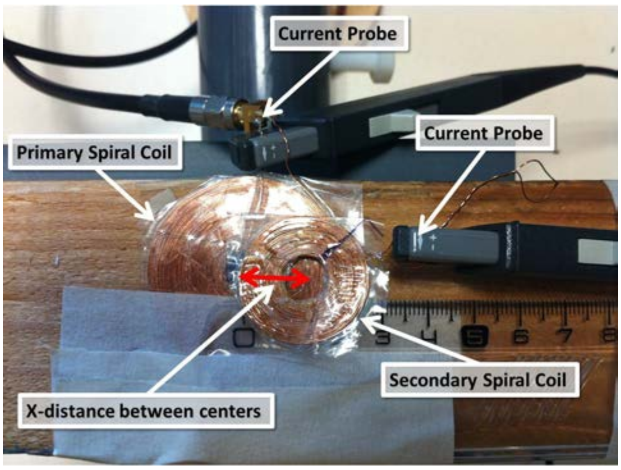

Note that VNA supplies the data in dB. Thus the collected data from VNA is:

$$VNA = 20.log\left(\frac{I_2}{I_1}\right) \tag{3.24}$$

In this case, there are some considerations, such as:

- there is no magnetic nonlinearity or core loss;
- there is no eddy current losses;
- the distributed capacitances of the windings are neglected;
- the quality factor of the short circuit coil must be very high;
- the joule loss resistance is much smaller than the inductive reactance $j.\omega.L$.

Thus, the mutual inductance can be calculated by the coupled-circuit voltage equations.

$$\left(\frac{I_2}{I_1}\right) = \left(\frac{M_{12}}{L_2}\right) \tag{3.25}$$

For the correctness of the measurements, a calibration data (deviation of channel 1 to channel 2) must be acquired before starting any measurements. This data is obtained by connecting channel 1 to channel 2. What is read in channel 2 should be the same as in channel 1. Otherwise, this deviation should be used to correct the measurements on the TET coils.

As observed from (3.25), in order to compute the mutual inductance with this method, the knowledge of the self-inductance is necessary. Thus, the usage of the IA prior to the VNA measurements is also required. Moreover, with this method, the losses due to eddy current cannot be computed.

3.5 SIMULATIONS THROUGH FINITE ELEMENT METHOD

Another procedure to compute the properties of the TET coils before it is even assembled is through simulations by Finite Element (FE) method. In this case, besides the joule loss resistance and the self and mutual inductance, other properties such as the current density among others may also be achieved while considering different influences such as magnetic core and presence of biological tissue around the TET coils.

In this research, two different software applications were used, considering distinct situations: Flux and Gmsh/GetDP.

3.5.1 CEDRAT - Flux

Flux-2D/3D is a numerical simulation software developed (in collaboration with the G2ELab) and distributed in France by CEDRAT SA. It uses the FE method and allows the calculation of electrical or thermal magnetic states, arrangements for permanent, transient and harmonic systems with the functionality of extended multi-parametric analysis, circuit couplings and kinematics.

Flux-2D/3D solves a variety of equations: Maxwell's equations, heat, law of behavior of materials. Due to the difficulty of the simultaneous solution of these equations, the

Flux code is divided into a set of modules which are responsible for solving a given type of problem.

Hence, this research used the axisymmetric approach from Flux-2D to develop the presented geometry, create the triangular FE mesh and simulate the magnetic transfer from a power supply connected to the primary coil to a resistive load connected to the secondary coil.

Figure 3.6 shows half of the geometry with the FE generated by Flux-2D. The top and bottom dark blue regions simulate respectively the primary and secondary cores. The pink and yellow parts simulate respectively the skin and fat with their material properties according to the characteristics for all studied frequencies, as defined in APPENDIX A. The top and bottom green regions represent the primary and secondary stranded windings, respectively, and the light blue part simulates the air.

Figure 3.6 - Magnetic geometry of TET coils implemented in Flux-2D with mesh.

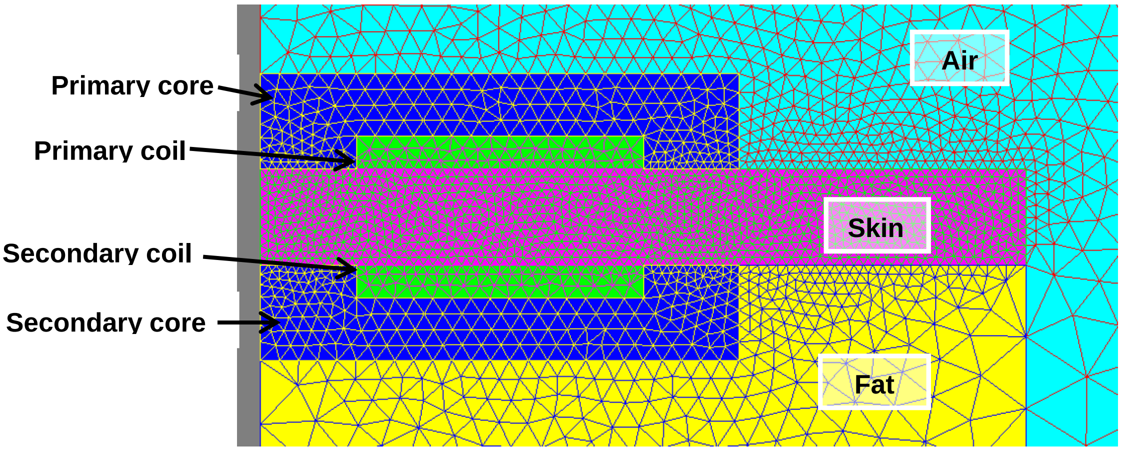

In order to simulate the voltage of the primary coil (considered sinusoidal) and the connection to the load, this geometry was associated with the electrical circuit shown in Figure 3.7.

Figure 3.7 – Electric circuit implemented in Flux-2D for association with the magnetic simulation.

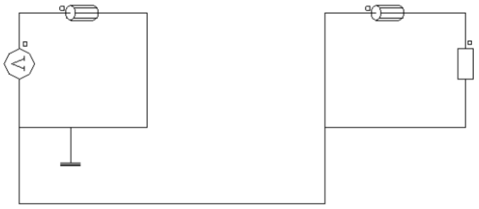

All the simulations in Flux-2D were performed considering that copper wire AWG 28 fill the whole space of the green regions independently of the number of turns. This means that the distance between the turns is variable and depends on the available space between the inner and central diameter and the number of turns. Moreover, the turns were not represented individually in the simulation since stranded coils were considered. This means that each green region has a distributed uniform current density given by the total current density of all the turns of each winding averaged all over the region.

Thus, the electrical resistance of the stranded conductor coupled with the FE geometrical regions in Flux-2D depends on the length of the wire and the resistance per unit length of the solid wire AWG 28, i.e., 0.212872 Ω/m. The length of the wire (l) was calculated based on the number of turns (N) and considering the average distance between the inner (D_{inner}) and central ($D_{central}$) diameter, i.e.

$$l = N.\pi.\left(\frac{D_{central} + D_{inner}}{2}\right) \tag{3.26}$$

The electrical properties of the skin between both coils and the fat around the secondary core, defined by (INSTITUTE FOR APPLIED PHYSICS NELLO CARRARA) as described in APPENDIX A, were used to account for their losses during the simulation of the system.

Other losses considered in these simulations were the iron losses in the ferromagnetic core (the magnetic properties of the core were set with isotropic analytic saturation, relative permeability and saturation magnetization) when coils with cores were considered. In fact, in order to evaluate the performance of the TET coils, some simulations modeled the ferromagnetic material (dark blue regions in Figure 3.6) with different values of relative permeability. Other simulations modeled the top dark blue region as air and the bottom dark blue region as fat in the case of coreless coils. The analyses of these simulations will be presented in Chapter 4.

Finally, Flux-2D/3D attained the voltage and current at the primary ($\dot{V}_1$, $\dot{I}_1$) and secondary ($\dot{V}_2$, $\dot{I}_2$) coils with their respective phase: i) when the secondary has no-load ($\dot{V}o_1$, $\dot{I}o_1$, $\dot{V}o_2$ and $\dot{I}o_2$); ii) when the secondary is short-circuited ($\dot{V}cc_1$, $\dot{I}cc_1$, $\dot{V}cc_2$ and $\dot{I}cc_2$). Then, the parameters could be calculated by (3.15) through (3.20). Again, in the no-load test, $\dot{I}o_2 = 0$, and in the short-circuit test, $\dot{V}cc_2 = 0$. However, these variables were also considered here in order to systematize the acquisition of data.

3.5.2 Gmsh and GetDP

Gmsh is an open source Finite Element (FE) software application developed by Christophe Geuzaine and Jean-François Remacle to generate three-dimensional FE grid with a build-in CAD engine and a post-processor (GEUZAINE; REMACLE, 2009). It provides a fast, light and user-friendly meshing tool with parametric input and advanced visualization capabilities, containing four modules: geometry, mesh, solver and post-processing, that can be developed interactively using the graphical user interface (GUI) or with instructions in text files using Gmsh's own scripting language. External solvers can be interfaced with Gmsh, but its default solver is GetDP.

GetDP is a general one, two and three dimensions FE solver. Its input data used for defining discrete problems (written by the user in ASCII data files) closely resembles the symbolic mathematical expressions of these problems (DULAR; GEUZAINE).

Hence, the TET transformer can be simulated by using Gmsh. In this software, the magnetic geometry was implemented by drawing the parts of the system (coil, core, air, skin, fat) and defining the electrical and magnetic properties at each region.

The design of the coil in this software was done in two different approaches: first, by simply drawing a coil box where all the wires of the coil would fit and consider that the coil is stranded as shown in Figure 3.8(a) and second, by drawing every individual turn of the solid coil as shown in Figure 3.8(b).

Figure 3.8 – Possibilities of magnetic geometry of TET coils to be implemented in Gmsh.

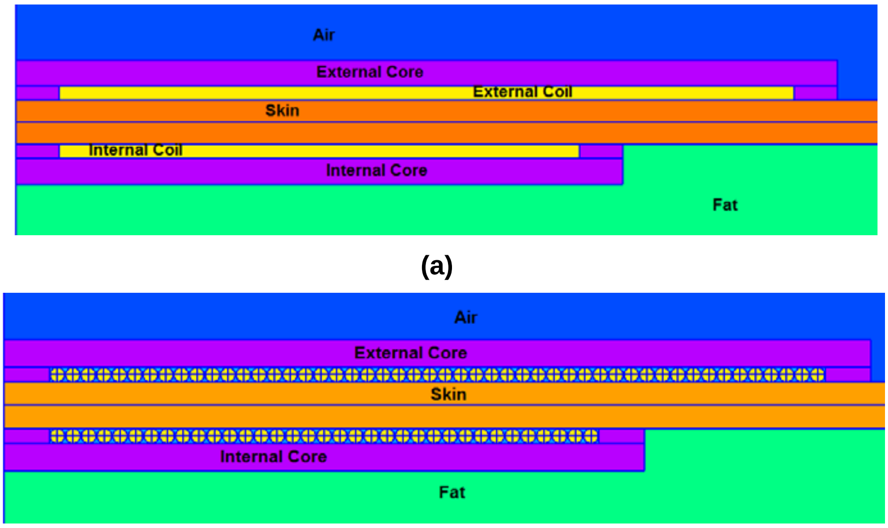

(a)

(b)

The main difference between them is that since the solid conductor is meshed, the FE method can compute skin and proximity effects, what cannot be computed in the stranded case. The geometry was associated with an electrical circuit to simulate the voltage of the primary coil (considered sinusoidal) and the connection to the load, similar to what was done with the simulation in Flux-2D/3D.

The association of Gmsh with GetDP simulated a sinusoidal input signal at the primary coil with the chosen frequency and amplitude, attaining voltage and current at the primary ($\dot{V}_1$, $\dot{I}_1$) and secondary ($\dot{V}_2$, $\dot{I}_2$) coils with their respective phases. Moreover, Gmsh/GetDP were used to simulate the designated coil considering two different situations – when the secondary has no-load (very high resistance) and when the secondary was short-circuited (very small resistance, tending to 0).

In this way, the voltages and currents (modulus and phase) in the primary and secondary obtained by the simulation in short-circuit and at no-load were used to calculate the parameters of the equivalent circuit of the TET transformer as already described.

3.5.2.1 Defining the problem in Gmsh and GetDP

Initially, the project was defined as two coreless coils with air all around. Some variable files were created with some parameterized variables to support future optimization.

In this way, the points, lines and surfaces were created to make half of the two-dimensional geometry as shown in Figure 3.8(b). In this figure, the circles were defined as solid conductors, configuring the primary coil (the circles on the top) and the secondary coil (the circles on the bottom). All the other surfaces in the geometry were configured as air, though the geometry is already prepared to consider ferromagnetic core. The line in the center between the top and bottom coil was inserted only to smooth the mesh in that region. The vertical line on the left configures the symmetric axis of the problem. Note that, in this configuration, it is possible to increase the coil gap, but any misalignment of axis would require the use of 3D geometry.

Once the geometry and the mesh were created, the axisymmetric problem could be solved using GetDP, which was programmed to couple the magnetic simulation with an electrical simulation. For that, functions were defined to associate each circle from Figure 3.8(b) with an inductor by assigning electrical nodes. Then, in the constraints of the circuit, those electrical nodes were configured as if each coil turn is in series with each other. In the same way, a source of voltage was assigned in series with the primary coil and a resistor was assigned in series with the secondary coil. The existing libraries from other projects were used to complete the GetDP program.

Making the geometry in this kind of detail is the most precise way to consider the skin and proximity effect, but it has a bigger computational cost, because it requires a finer mesh. An alternative possibility is an approximation as stranded coils, as shown in Figure 3.8(a). The geometry and mesh contain only a rectangle in place of all the circles and therefore has the current density distributed in the rectangular region instead of in each circular turn associated in series. In this case, the FE equations consider the amount of turns directly in the function for the imposed current density.

In addition to the information about magnetic vector (A), magnetic field (B) and current density (J), the post-processing was configured to create files with the information about voltage, current and power of the power supply, load resistor and each coil. Figure 3.9, Figure 3.10 and Figure 3.11 show an example of the continuous map of A, B and J obtained from a simulation.

Figure 3.9 – Magnetic vector (*A*) simulated by Gmsh/GetDP.

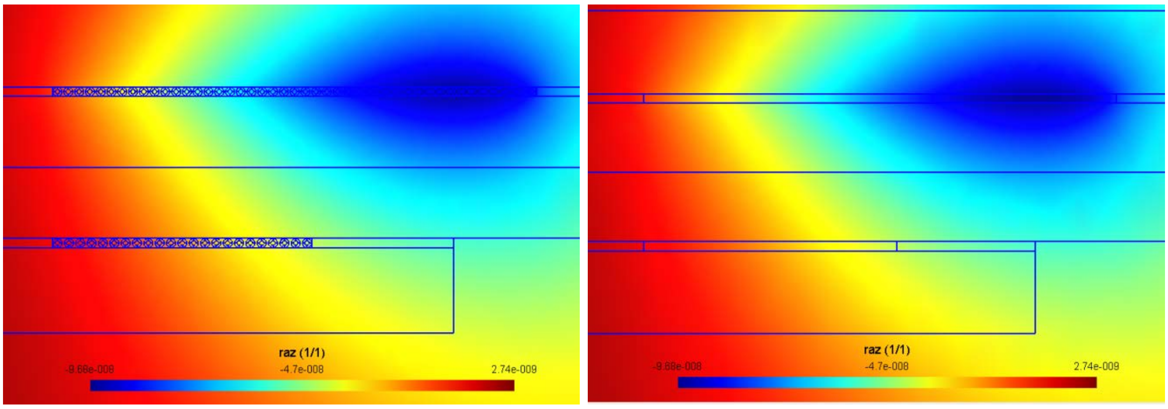

Figure 3.10 – Magnetic field (*B*) simulated by Gmsh/GetDP.

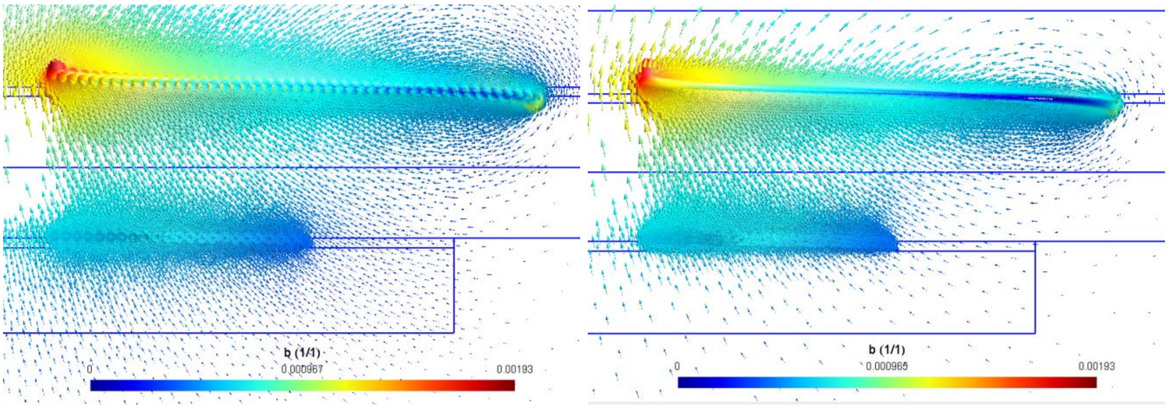

Figure 3.11 – Current Density (*J*) simulated by Gmsh/GetDP.

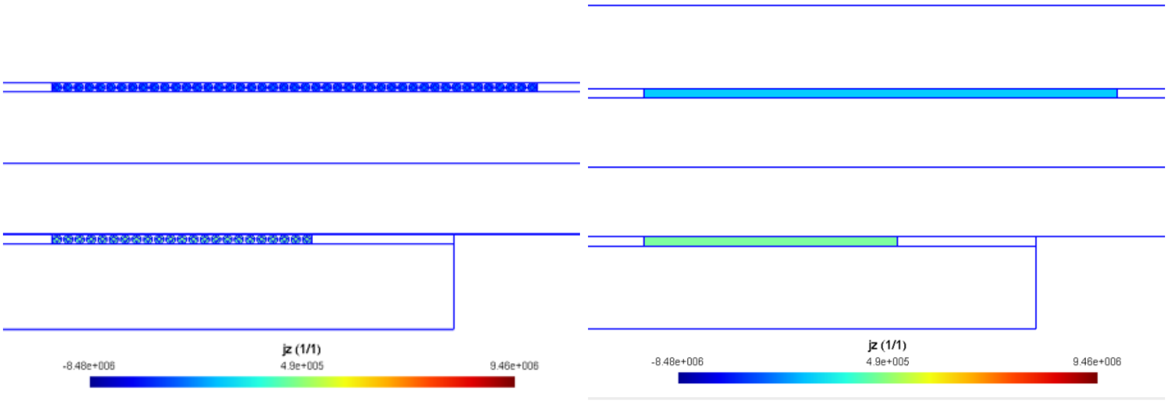

In order to better visualize the details of each conductor, a zoom in the winding is shown in Figure 3.12, Figure 3.13 and Figure 3.14.

Figure 3.12 – Zoom of the magnetic vector (*A*) simulated by Gmsh/GetDP.

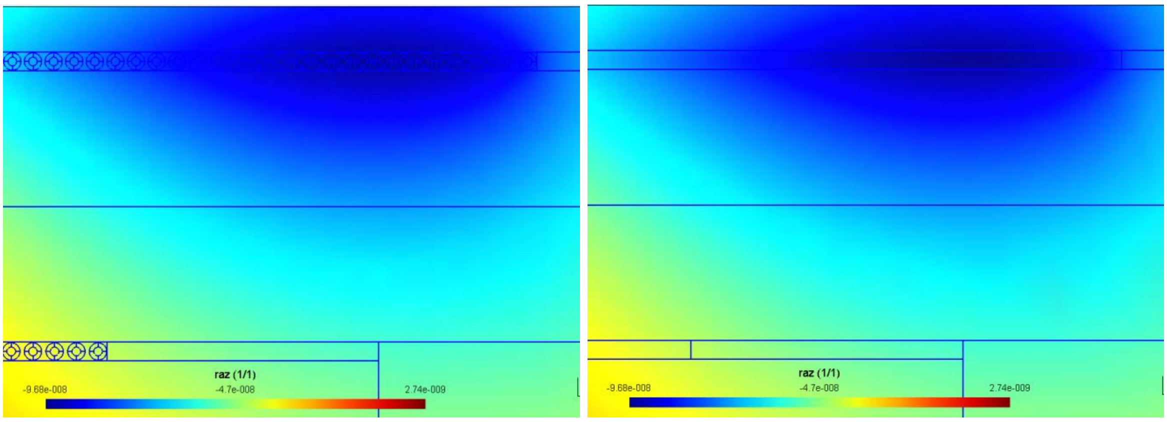

Figure 3.13 – Zoom of the magnetic field (*B*) simulated by Gmsh/GetDP.

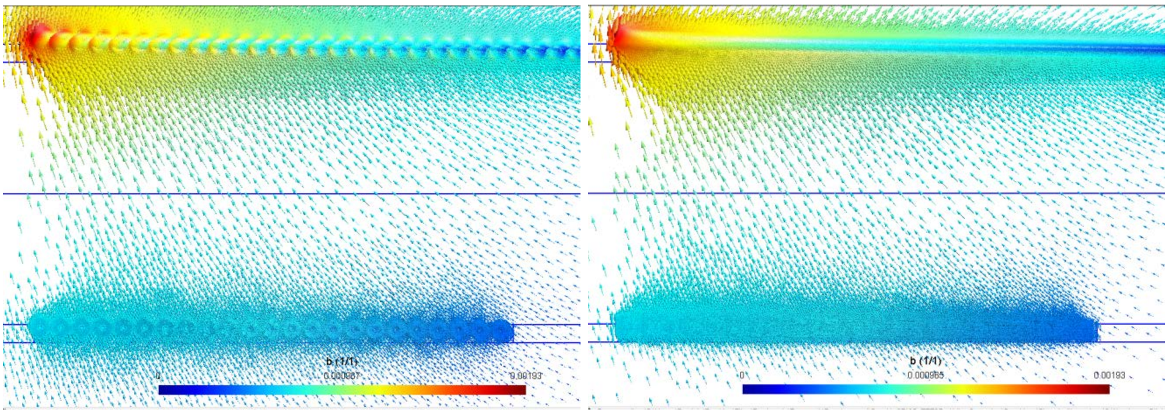

Figure 3.14 – Zoom of the current Density (*J*) simulated by Gmsh/GetDP.

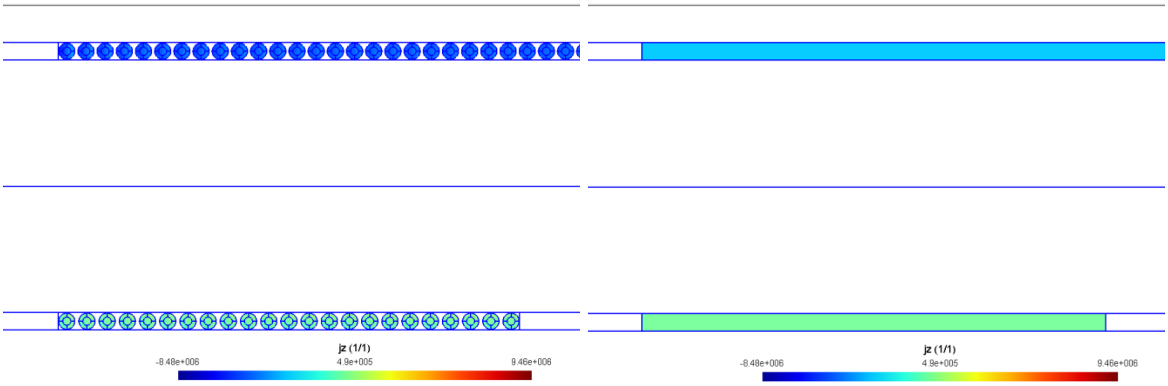

Comparing the results between the simulations of stranded and solid conductor windings, it can be observed that the magnetic vectors are very similar, but the magnetic fields and current densities on the coils show a very small difference due to the distance between each turn.

Therefore, the use of the approximation of stranded windings should be evaluated whether the type of problem has penetration depth smaller than the wire radius. If the problem has a slight penetration depth in a way that the current density is not distributed along the whole section of the wire, the approximation of stranded windings cannot be used at the expense of the computation cost of the simulation of solid conductor windings.

3.5.3 Axisymmetric versus 3-Dimensional Simulation

The presented simulations in Flux-2D and Gmsh/GetDP considered the coils aligned and separated by a certain distance. Thus, the 2D axisymmetric simulation could be performed. However, in order to analyze the displacement between the coils, a three-dimensional (3D) simulation is required.

The 3D geometry was implemented in both software applications, Flux-3D and Gmsh/GetDP. However, due to the increase of complexity in the geometry, the 3D simulation takes much longer time to be computed. For this reason, the 3D simulations were used only in cases of misalignments leaving the axisymmetric approach to be used in all the other cases (coils aligned).

Moreover, in the 3D simulations, the use of solid wires is computationally too costly to be simulated with the available machines. Thus, in all cases where 3D was required, the stranded approach was used with the lack of the proper calculation of the proximity and skin effects. For this reason, the technique of homogenization was proposed, as will be shown in Section 3.5.4.

3.5.4 Homogenization method

Considering that the design of the TET coils may assume different ranges of wire gauge at different frequencies, the skin and proximity effects cannot be ignored. Thus, the use of the stranded model is not accurate enough since the stranded approach disregards these effects and estimates the losses a posteriori by computing them individually through, e.g. analytical approaches (DOWEL, 1966; FERREIRA, 1994).

Since the eddy current effects may significantly alter the performance of the TET system, their direct inclusion in the FE simulations is mandatory. In principle, this can be done through the use of the solid conductors, but even such model should be very finely meshed inside each conductor in order to have a good estimation of the skin and proximity effects. Usually, the characteristic length of the discretization of the conductors has to be at least three times smaller than the skin depth and that may cause a mesh with high computational cost, mainly at higher frequencies.

Dedicated homogenization methods are then essential to reduce the computational cost while considering all the mentioned effects in the FE equations. In the frequency domain, they usually amount to the use of complex frequency-dependent reluctivity and impedance, the values of which are obtained analytically (MOREAU; POPIEL; PAGES, 1998) or numerically via an elementary FE method (PODOLTSEV; LEBEDEV, 2003).

Several authors have presented homogenization methods in the frequency (PODOLTSEV; LEBEDEV, 2003; GYSELINCK; DULAR, 2005) and time domains (GYSELINCK; SABARIEGO; DULAR, 2007). 3D simulations with homogenization methods have also been studied in frequency (MEUNIER et al., 2010) and time

(SABARIEGO; DULAR; GYSELINCK, 2008) domains. This method has also been used in a 3D FE model of a coil with a magnetic core (SIBUÉ et al., 2012; SIBUÉ et al., 2013). However, all of the above mentioned researches deal with the study of multi-turn windings in the abscissa (x direction) and ordinate (y direction), i.e. with a quite periodic and homogeneous geometry.

The homogenization method characterizes the general skin and proximity effect of the winding by a representative FE model consisting of only one wire surrounded by air.

In the frequency domain, the eddy current effects can be characterized by adopting a complex skin-effect impedance in the source electric circuit, and a complex proximity-effect permeability (or reluctivity) in each homogenized winding volume (GYSELINCK; DULAR, 2005; GYSELINCK; SABARIEGO; DULAR, 2007). The values of these parameters are determined by simulations of a representative FE model.

Taking advantage of the spatial orthogonality between the net current in the inductors (complex representation I**)** and the transverse magnetic induction (complex representation B), two decoupled effects are identified and the associated losses are simply added: the skin effect (when net current $I \neq 0$ and induction field $B = 0$) and the proximity effect ($I = 0$ and $B \neq 0$). Then, the associated losses are simply added. Therefore, the key quantities of the method are the net current in the conductors, I, and the two components of the average induction, $\{B_x, B_y\}$.

The idea of this method is to characterize the general skin and proximity effect of the winding by a representative FE model consisting of one wire surrounded by air. Hence, two steps are necessary to simulate the system:

1. This representative FE model is simulated in three situations (with $\{I, B_x, B_y\}$ equal to {1,0,0}, {0,1,0} and {0,0,1}) for a wide frequency range. At each frequency, three elementary solutions are obtained and the complex power absorbed by the representative wire is computed. The first case allows the determination of a complex impedance Z_{skin} due to skin effect, while the last two allow the computation of a complex and frequency dependent reluctivity tensor υ_{prox} that accounts for proximity effects (GYSELINCK; DULAR, 2005). Thus, a set of data is attained for Z_{skin} and υ_{prox} at the simulated frequencies, which allows the interpolation for other frequencies that may be considered in the complete TET device.
2. The complete TET coil geometry is then simulated without the fine discretization of the solid wires to include the skin depth. This means the windings are simulated as stranded conductors in which a uniform current density, with the number of conductors and the overall surface area, is adopted. At the voltage terminals of the winding in the electrical circuit equation, the DC resistance has to be replaced by a component with impedance Z_{skin} and the homogenized volume should be simulated with the proximity-effect reluctivity υ_{prox}, defined by the previously mentioned simulated curves, which will be explained next.

In order to detail the way to obtain Z_{skin} and υ_{prox}, a non-dimensional parameter X, referred as reduced frequency is defined by

$$X = \frac{r}{\delta} = \sqrt{f}.r.\sqrt{\pi.\sigma.\mu_0} \tag{3.27}$$

In (3.27), r is the radius of the conductor, $\delta = \sqrt{2/(\sigma.2.\pi.f.\mu_0)}$ is the skin depth at frequency f and σ is the conductivity of the conductors.

Figure 3.15 shows some solutions obtained with the representative FE model in all three situations for three different reduced frequencies X. Note that, as the frequency increase, the flux pattern is less and less homogeneous with flux lines concentrating near the boundaries.

Figure 3.15 – Elementary flux patterns obtained by Gmsh/GetDP for skin (left) and proximity effect (right) at different frequencies *X*.

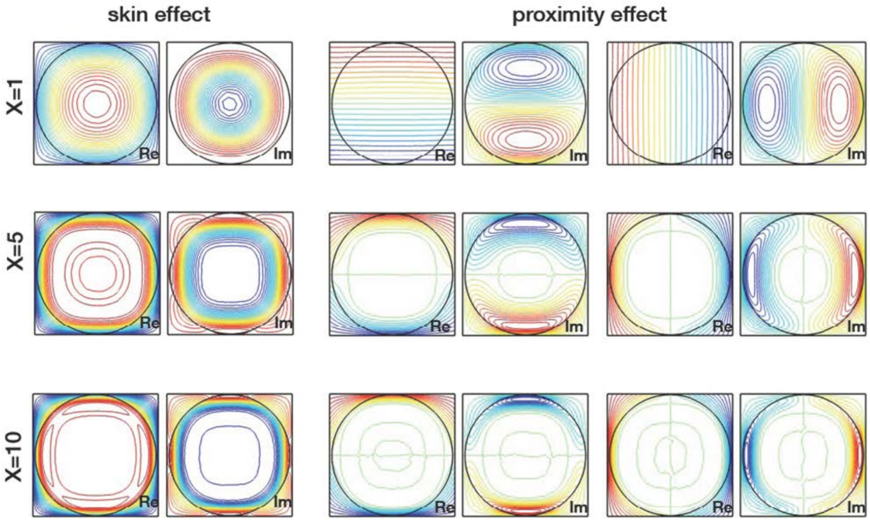

The complex impedance ($Z_{skin}(X)$) can be calculated as:

$$Z_{skin} = \frac{S_{skin}}{\frac{1}{2}I^2} = p_I(X).R_{dc} + j.q_I(X).\omega.\frac{\mu_0.l}{8.\pi.\lambda} \tag{3.28}$$

In (3.28), $R_{dc} = \frac{l}{\sigma.S}$ is the direct current (DC) resistance of the conductor. The factor $\frac{\mu_0.l}{8.\pi.\lambda}$, usually negligible, is based on the DC inductance of a round conductor (internal field only). The non-dimensional factors p_I and q_I depend on the winding type and the reduced frequency *X*. As evidenced in (GYSELINCK; SABARIEGO; DULAR, 2007), the skin-effect losses and the coefficient are practically independent of the fill factor. They can be calculated as:

$$p_I(X) = \frac{R_{ac}}{R_{dc}} = \frac{X}{2}.Re\left((1+j).\frac{J_0((1+j).X)}{J_1((1+j).X)}\right) \tag{3.29}$$

$$q_I(X) = \frac{R_{ac}}{R_{dc}} = \frac{X}{2}.Im\left((1+j).\frac{J_0((1+j).X)}{J_1((1+j).X)}\right) \tag{3.30}$$

with J_α the Bessel function of the first kind and order α.

By imposing a zero net current and a unit average horizontal induction, a pure proximity effect flux pattern is produced in the representative cell. The same happens by imposing a unit average vertical induction. The tensor υ_{prox} is given by the corresponding complex reluctivity calculated in both situations (horizontal and vertical induction). In the case of round conductors and a symmetric representative cell, the tensor becomes a scalar.

$$\upsilon_{prox} = q_B(X).\upsilon_0 + j.p_B(X).\omega.\frac{\lambda.\sigma.r^2}{4} \tag{3.31}$$

In (3.31), $\omega.\frac{\lambda.\sigma.r^2}{4}$ follows from the analytical expression for low-frequency proximity losses in a round conductor (PODOLTSEV; LEBEDEV, 2003). The non-dimensional factors q_B and p_B are calculated from the energy absorbed by the cell as:

$$p_B(X) = \frac{4}{X^2}.Im\left(\frac{J_2\big((1+j).X\big)}{J_0\big((1+j).X\big)}\right) \tag{3.32}$$

$$q_B(X) = \frac{4}{X^2}.Re\left(\frac{J_2\big((1+j).X\big)}{J_0\big((1+j).X\big)}\right) \tag{3.33}$$

For round conductors, this tensor υ_{prox} can be reduced to a scalar quantity.

In this way, the data set mentioned in step 1 represents a group of curves attained for the six non-dimensional but frequency-dependent factors p_I and q_I, and q_B and p_B (note that in the general case both x and y directions need to be considered). Thus, Z_{skin} and υ_{prox} can be estimated by the interpolation of these curves at the frequency considered in the complete TET device.

3.6 COMPARISON AMONG THE METHODS

3.6.1 Coils with thin wires

For the validation of the simulation method, a first set of coils of 45 and 23 turns with wire AWG 28 were built and the different methods – analytic, experimental measurement and FE simulation – were compared. This type of wire was selected due to the thickness being smaller than the penetration depth and therefore the skin and proximity effect can be neglected. For the purpose of comparing the self-inductance values among the methods, Table 3.1 was created.

Table 3.1 – Comparison of the self-inductance and joule effect loss between measurements, Flux-2D, Gmsh/GetDP and obtained analytically.

	Measured	**Flux-2D**	**Gmsh/GetDP**	**Analytical**
r_1	0.96 Ω	0.81 Ω	0.89 Ω	0.72 Ω
L_1	51 µH	47.3 µH	48.79 µH	37.22 µH
r_2	0.55 Ω	0.41 Ω	0.314 Ω	0.26 Ω
L_2	10.72 µH	10.1 µH	10.44 µH	7.996 µH

When comparing the results of the mutual inductance of the measurements with the simulation from Flux-2D and the analytically calculated values for the coils aligned and with different gaps, Figure 3.16 was obtained.

Figure 3.16 – Comparison between the modulus of the mutual inductance measured and calculated analytically and via FE method for the coils aligned with different gaps at different frequencies.

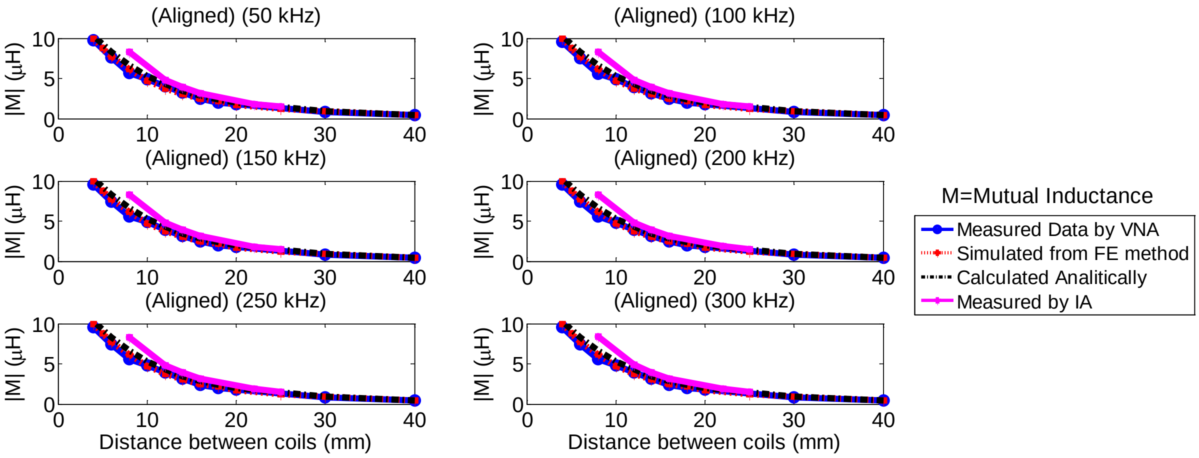

For the specific frequency of 100 kHz, Figure 3.17 shows more details of this comparison.

Figure 3.17 – Comparison between the data measured and calculated analytically and via Flux-2D for the coils aligned with different gaps at 100 kHz.

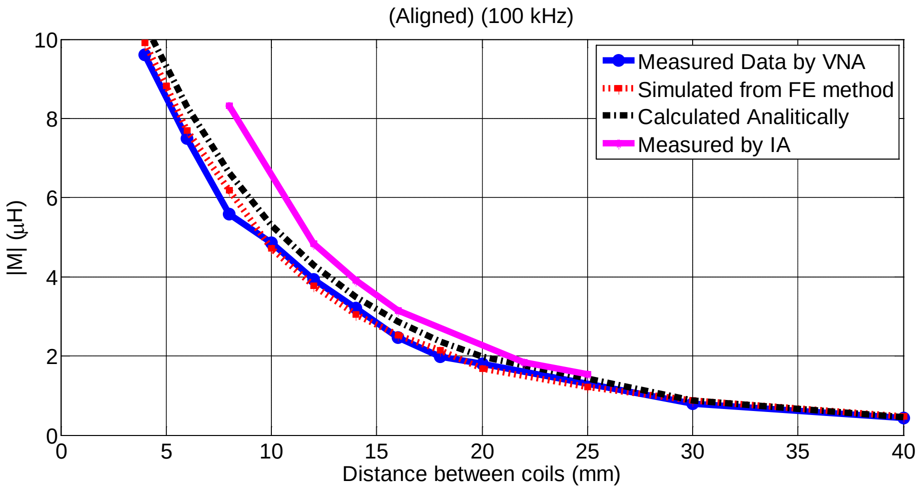

When comparing the results from the measurements with the simulation from Flux-3D and the analytically calculated values for the coils with different misalignments, Figure 3.18 was obtained. Note that the ordinate of the graphs is showing the modulus of the mutual inductance which can have negative values for higher misalignments, as will be seen in the next section.

Figure 3.18 – Comparison between the modulus of the mutual inductance measured and calculated analytically and via FE method for the coils with different misaligning at different frequencies.

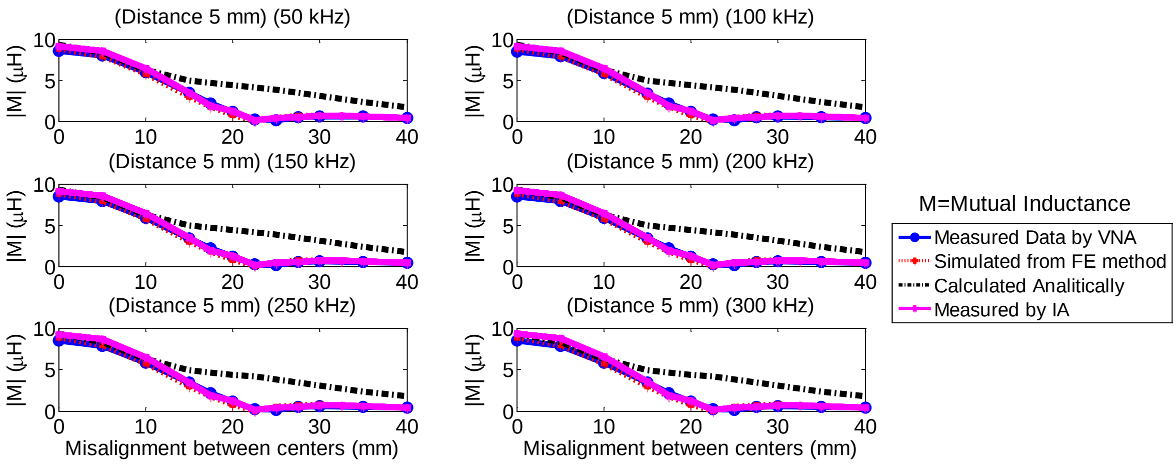

Figure 3.19 shows more details of this comparison at 100 kHz.

Figure 3.19 – Comparison between the data measured and calculated analytically and via Flux-3D for the coils misaligned at different values at 100 kHz.

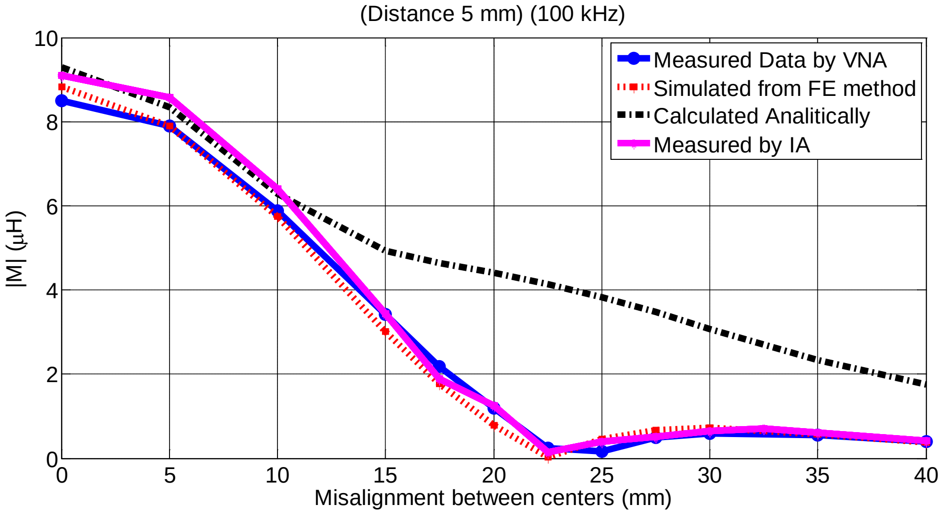

As observed, the analytical calculation presents considerably accurate values for misalignments below 15 mm. Although the analytical method is very fast when compared to FE method, the latter is very accurate for any position of the coils, whereas the analytical method is valid only for small misalignments.

3.6.2 Coils with thick wires

In order to verify the behavior of the proximity and skin effects, a new set of coils was built with thicker wires. Due to the availability of this gauge of wire in the laboratory, two coils with 35 and 50 turns of wire AWG 15 were created, as shown in Figure 3.20.

Figure 3.20 – Built coils with wire AWG 15.

Note that the coils considered in this section were difficult to assemble and the turns were not precisely positioned in the same ordinate (some turns are a little bit higher than other), as shown in Figure 3.20. However, the simulations were performed as if all the turns were precisely allocated at the same level and separated by a constant distance.

The self-inductances of the coils were compared among the methods, considering 2D and 3D approaches, solid conductors and stranded windings and homogenization technique.

Initially, the case of aligned coils was considered. This research performed five different simulations at ninety different frequencies in the range [10^4, 10^6] Hz. A new mesh was generated for each new simulation and frequency. Following is the list of the considered FE models and their computational time:

1. 2D axisymmetric with solid conductors (1 hour);

2. 2D with stranded windings (25 minutes);
3. 2D with the homogenization method (11 minutes);
4. 3D with the homogenization method (7.2 hours); and
5. 3D with stranded windings (14.35 hours).

Observe that, although the simulation with homogenization technique uses the stranded approximation with the complex impedances and reluctivities, it was faster than the stranded winding simulation. That happens because the stranded winding simulation was more finely meshed in order to minimize the errors. With the homogenization technique, the mesh does not need to be that fine and thus the simulation is faster.

Figure 3.21 analyzes this set of coils separated by 5 mm, showing the impedance (real and imaginary part) of the primary coil aligned with the no-load secondary coil. Other simulations at different coupling situations with slight differences were also computed and validated:

- “Uncoupled”: the coil is individual (magnetically and electrically uncoupled from the second coil);
- “No-load coupled”: the coil is magnetically coupled with the second coil at no-load;
- “Short-circuited coupled”: the coil is magnetically coupled with the second coil in short-circuit.

These results can be seen in APPENDIX E.

Figure 3.21 – Comparison of the real and imaginary impedance (coil of 35 turns with wire AWG 15; coil gap of 5 mm; coil of 50 turns with wire AWG 15 at no-load) between the data measured and calculated via Gmsh/GetDP with full model and with homogenization.

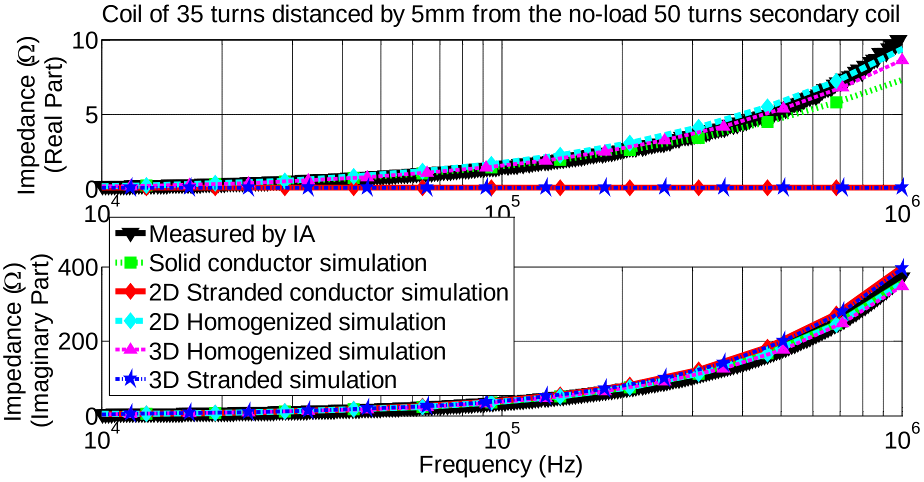

Observe that the results obtained from the stranded simulations (curves 2 and 5) start diverging from the reference at few dozen kilohertz. In fact, the skin depth of round copper conductors at 10 kHz is 0.66 mm, i.e. smaller than the radius of the conductor (0.725 mm). When using the proposed homogenization method (curves 3 and 4), the results follow the measured reference tightly.

It is noteworthy to remember that the used FE magnetodynamic models disregard the capacitive effects. This fact explains why the simulation curves deviate from the measured curves for frequencies greater than 2 GHz. The impedance of this set of coils was measured through the IA for a larger range of frequencies than shown in this figure. These measurements showed that the resonant frequency due to capacitive effects is around 2.8 GHz. This range of frequencies, however, is not shown in this figure; otherwise, the quality of the figure would be degraded. Not using capacitive effects in this research does not represent a problem since the frequency range used in this design is much smaller than 2 GHz.

Looking at the computational time data, one could say that the 2D method is faster than the 3D method for the same accuracy. However, there are some important situations where the 2D method cannot be used, such as when the coils are misaligned.

Then, this research used the mutual inductance to analyze the 3D method for the coils misaligned at different distances. Figure 3.22 compares the 3D stranded windings simulations, the 3D windings with homogenization method simulations, and the experimental measurements of this set of coils at 105 kHz.

Figure 3.22 – Mutual inductance of the set of coils (coil of 35 turns with wire AWG 15; coil of 50 turns with wire AWG 15) with gap of 5 mm and different conditions of misalignments.

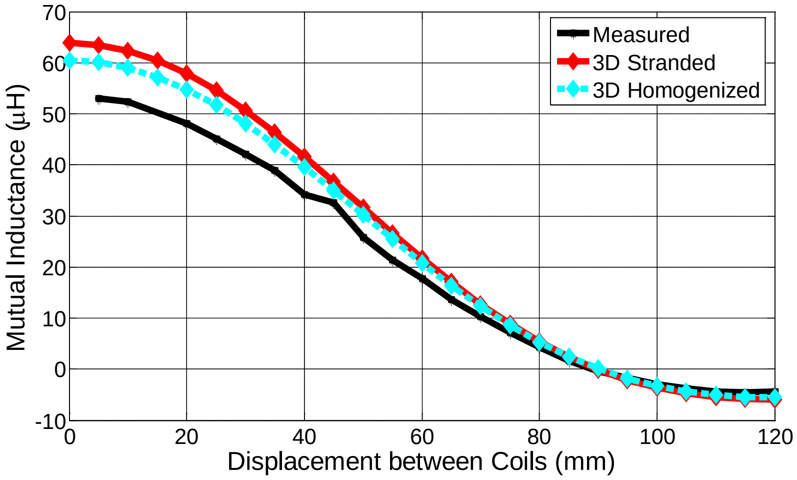

Observe that in this figure, the error from the measurements and the simulations is smaller than 10%. However, in this figure, the homogenization does not show much advantage compared to the stranded simulation. This occurs because the main reason to use the homogenization technique is due to the skin and proximity effects. However, these effects affect mainly the resistance and not the self and mutual inductances. For this reason, different measurements considering two coupling situations were compared with the 3D simulations at different misalignment positions. In both situations, the coils were electrically connected in series and were positioned in such a way that:

1. the flux of the first coil is in the same direction of the flux of the second coil;

2. the flux of the first coil opposes the flux of the second coil.

The impedance of the first situation is expected to be higher than the impedance of the second situation.

Figure 3.23 and Figure 3.24 compare the simulations with the measurements, thus showing that the homogenization method is more reliable than the stranded model.

Figure 3.23 – Impedance of the set of coils, separated by 10 mm at different conditions of misalignment. Coils positioned such that the flux of one coil complements the flux of the other coil.

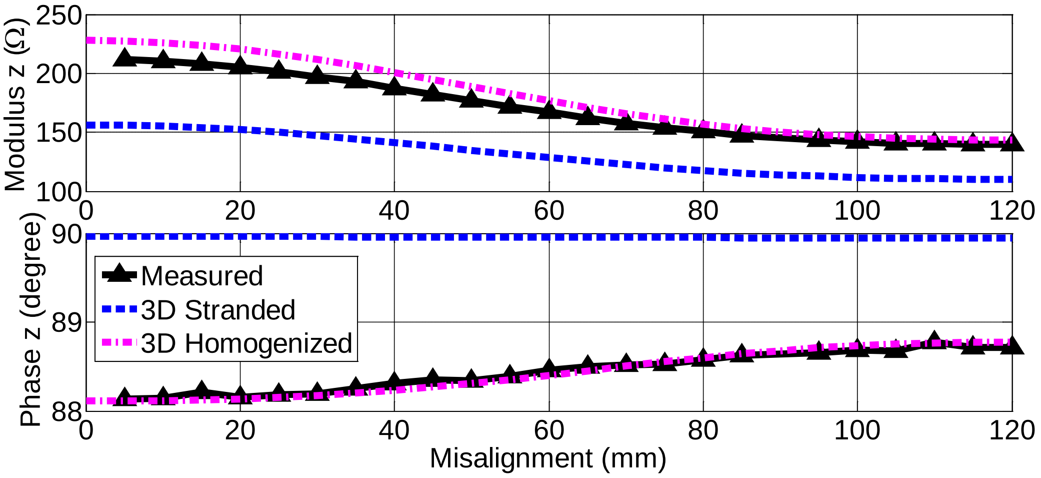

Figure 3.24 – Impedance of the set of coils, separated by 10 mm at different conditions of misalignment. Coils positioned such that the flux of one coil opposes the flux of the other coil.

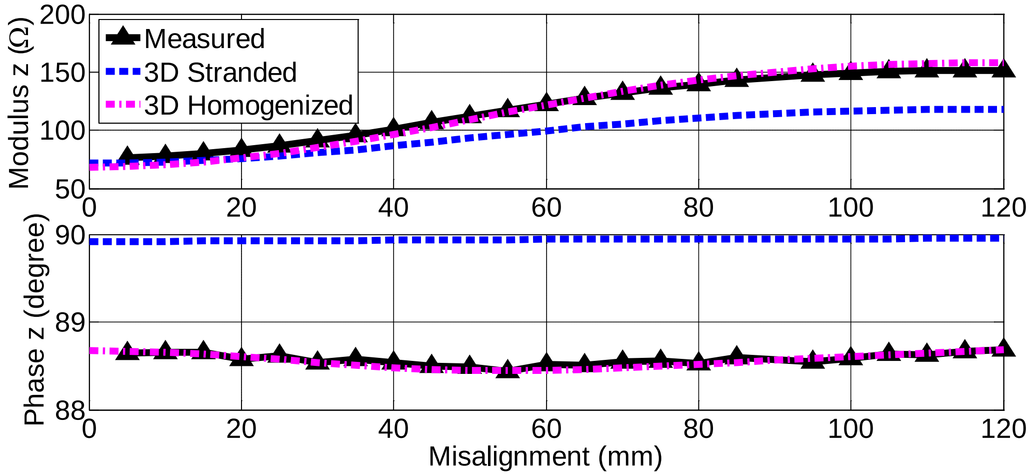

The small difference between the impedance measured and simulated with the homogenization technique in Figure 3.23 is probably due to the bad assemblage of the coils as mentioned earlier and shown in Figure 3.20.

3.6.3 Coils with thin and thick wires

The same analysis was performed on a set of coils in which the primary coil has large wire gauge, but the secondary coil has small wire gauge. Therefore, a primary coil with 62 turns of wire AWG 19 and a secondary coil with 24 turns of wire AWG 26 were created.

Figure 3.25 analyzes this set of coils separated by 5 mm, showing the impedance (real and imaginary part) of the primary coil aligned with the no-load secondary coil. Again, other simulations at different situations were also performed with slight differences and can be seen in APPENDIX E.

Since the coils have different gauges, the behavior of the TET system when the coils have their functions inverted is shown in Figure 3.26.

These coils present analogous behavior as observed for the set of coils with wire AWG 15. The difference is that, in Figure 3.25 and Figure 3.26, the stranded data start diverging from the reference at around 30 kHz and 80 kHz, respectively. At these frequencies, the skin depths of the round copper conductor are 0.38 mm and 0.23 mm, respectively, which are comparable to the 0.456 mm and 0.202 mm radii of these respective conductors.

The resonant frequency is around 2.4 GHz and 12 GHz for the first and second combination of coils, respectively. Again, it is much higher than the range of frequency in which the TET coils might operate. This is the reason why, in Figure 3.25, the solid conductor and homogenized simulations (curves 1, 3 and 4) start diverging from the measurement data for frequencies above 350 kHz.

Figure 3.25 – Comparison of the real and imaginary impedance (coil of 62 turns with wire AWG 19; coil gap of 5 mm; coil of 24 turns with wire AWG 26 at no-load) between the data measured and simulated via Gmsh/GetDP with full model and with homogenization.

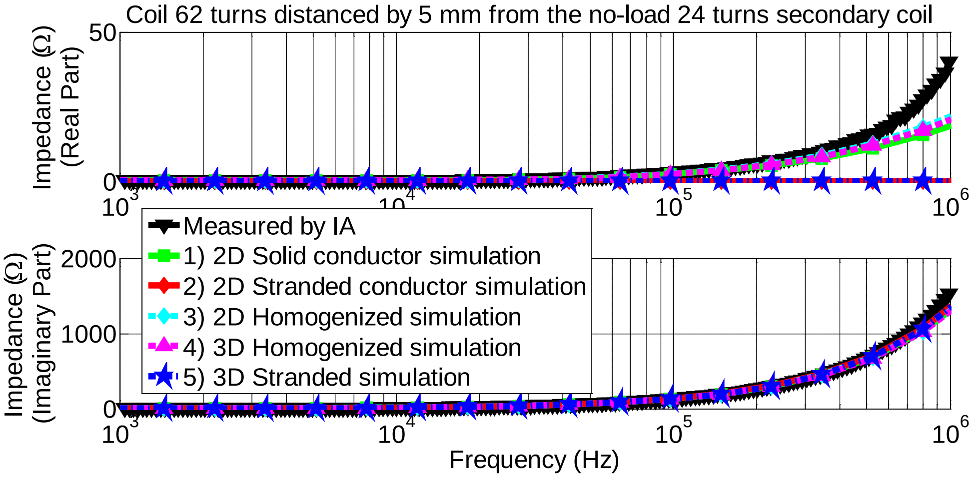

Figure 3.26 – Comparison of the real and imaginary impedance (coil of 24 turns with wire AWG 26; coil gap of 5 mm; coil of 62 turns with wire AWG 19 at no-load) between the data measured and simulated via Gmsh/GetDP with full model and with homogenization.

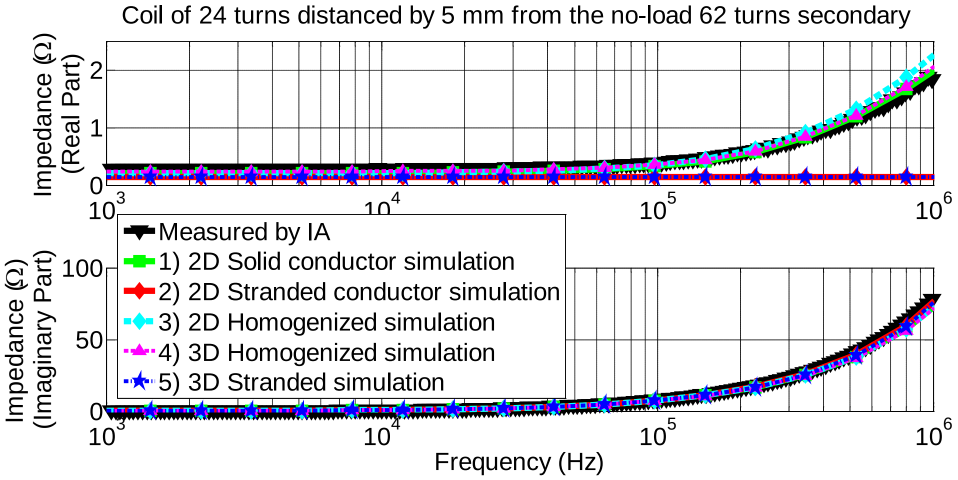

The misalignments of the coils were also analyzed in the 3D approach for this set of coils at 213 kHz in the same way as performed for the set of coils with wire AWG 15 (Section 3.6.2). Figure 3.27 compares the mutual inductance simulated in 3D stranded windings, simulated in 3D using the homogenization method, and measured physically.

Figure 3.27 – Mutual inductance of the set of coils (coil of 62 turns with wire AWG 19; coil of 24 turns with wire AWG 26) with gap of 5 mm and different conditions of misalignments.

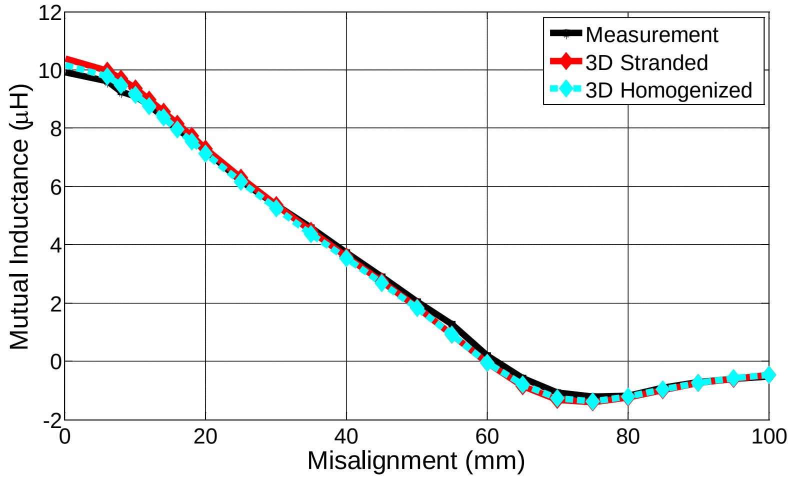

Again, for the same reasons already mentioned, the mutual inductance does not present very big difference between the homogenized and stranded simulations. Thus, Figure 3.28 and Figure 3.29 used the aforementioned coupling of the coils electrically connected in series to compare the impedances between the simulations and the measurements at different misalignments.

Figure 3.28 – Impedance of the set of coils, separated by 5 mm at different conditions of misalignment. Coils positioned such that the flux of one coil complements the flux of the other coil.

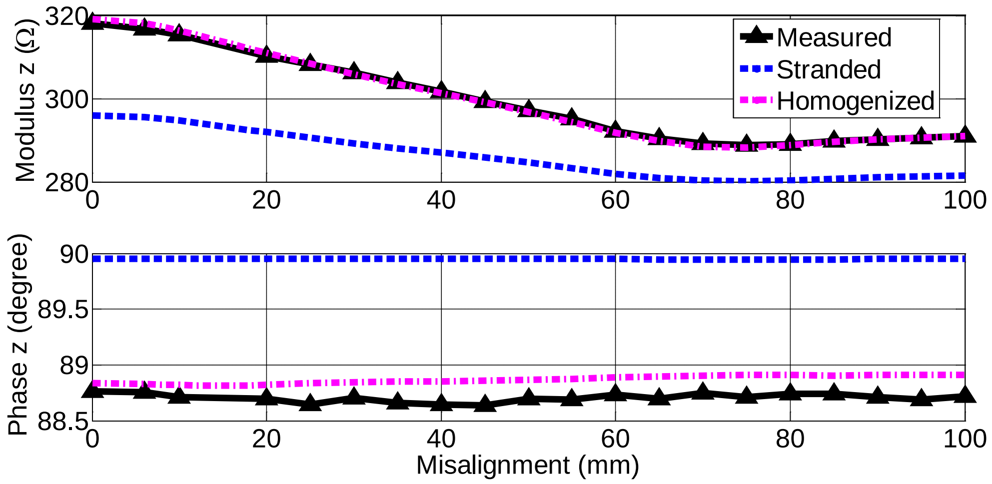

Figure 3.29 – Impedance of the set of coils, separated by 5 mm at different conditions of misalignment. Coils positioned such that the flux of one coil opposes the flux of the other coil.

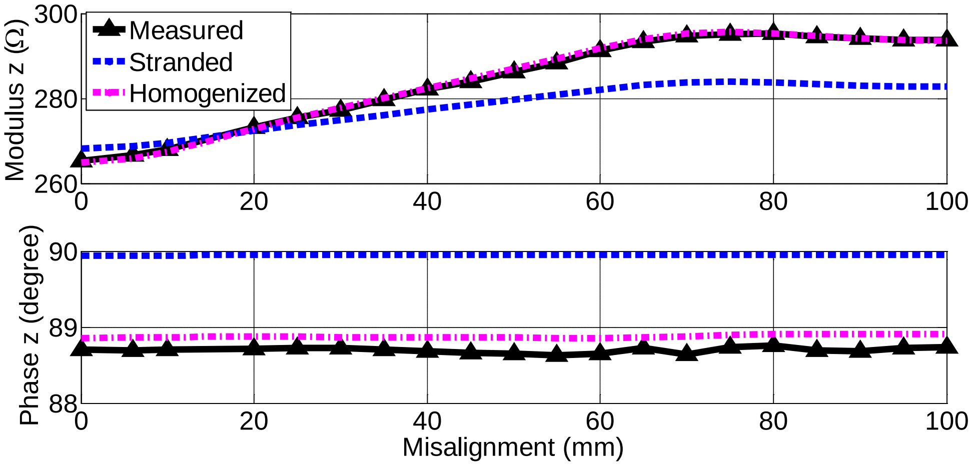

Note that, for the stranded case, the impedance phase stays very close to 90°. On the other hand, for the homogenization case, the phase is correctly simulated for all misalignments.

Moreover, the coils built with these configurations were better assembled and all their turns were in the same ordinate, unlike what happened with the coils in Section 3.6.2. Hence, the simulations with the homogenization technique presented the curve of the modulus of the impedances very close to the measured values. Thus, the proposed 3D frequency domain method provides very accurate results even for coils with a planar geometry.

3.7 UNCOUPLED AND COUPLED SIMULATIONS AT NO-LOAD AND SHORT-CIRCUIT

Figure 3.30 and Figure 3.31 show the results of measurements at the three different coupling situations mentioned in Section 3.6.2 (“Uncoupled”, “No-load coupled”, “Short-circuited coupled”).

Figure 3.30 – Impedance of the coil of 50 turns with wire AWG 15 measured at the three different coupling situations with the coil of 35 turns with wire AWG 15 and coil gap of 5 mm.

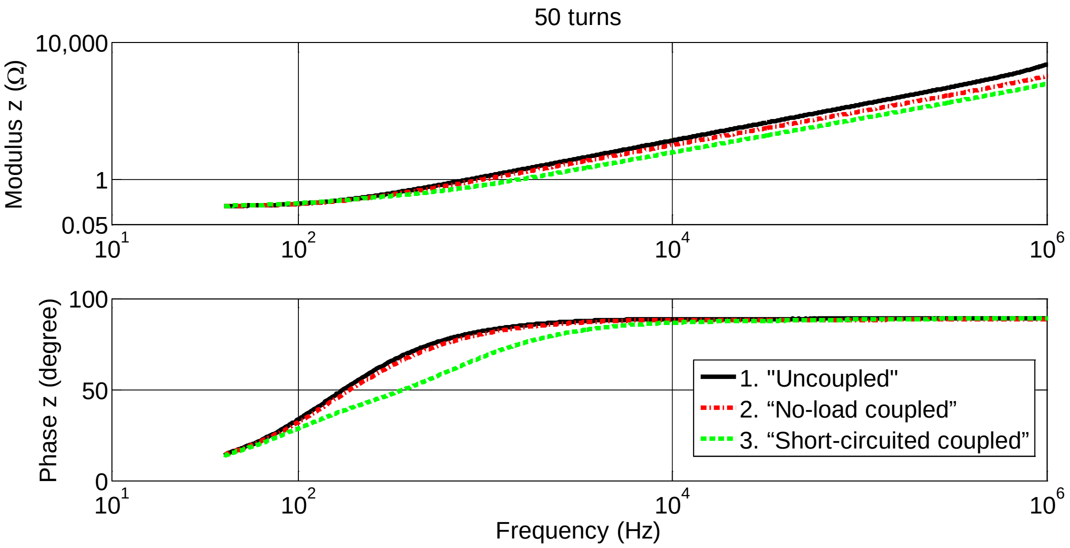

Figure 3.31 – Impedance of the coil of 35 turns with wire AWG 15 measured at the three different coupling situations with the coil of 50 turns with wire AWG 15 and coil gap of 5 mm.

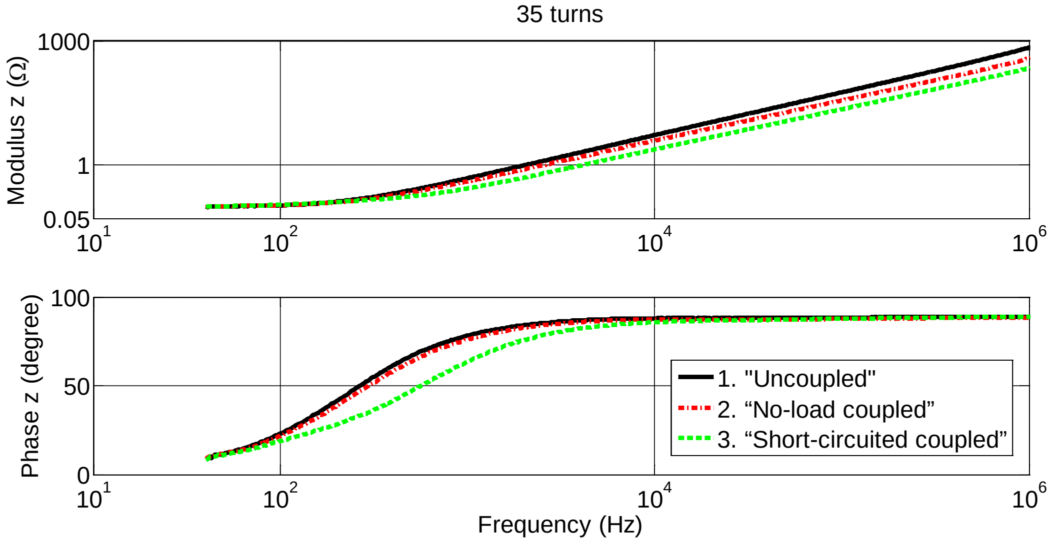

Observe that, as expected, when the secondary coil is in short-circuit (“Short-circuited coupled”), the impedance seen by the source is strongly affected. However, the difference between the primary coil impedance at the “Uncoupled” or “No-load coupled” situations observed in these figures is not expected. Thus, Figure 3.32 and Figure 3.33 were created in order to have a better visualization of this behavior.

Figure 3.32 – Impedance of the coil of 35 turns with wire AWG measured at the three different coupling situations with the coil of 50 turns with wire AWG 15 and coil gap of 5 mm.

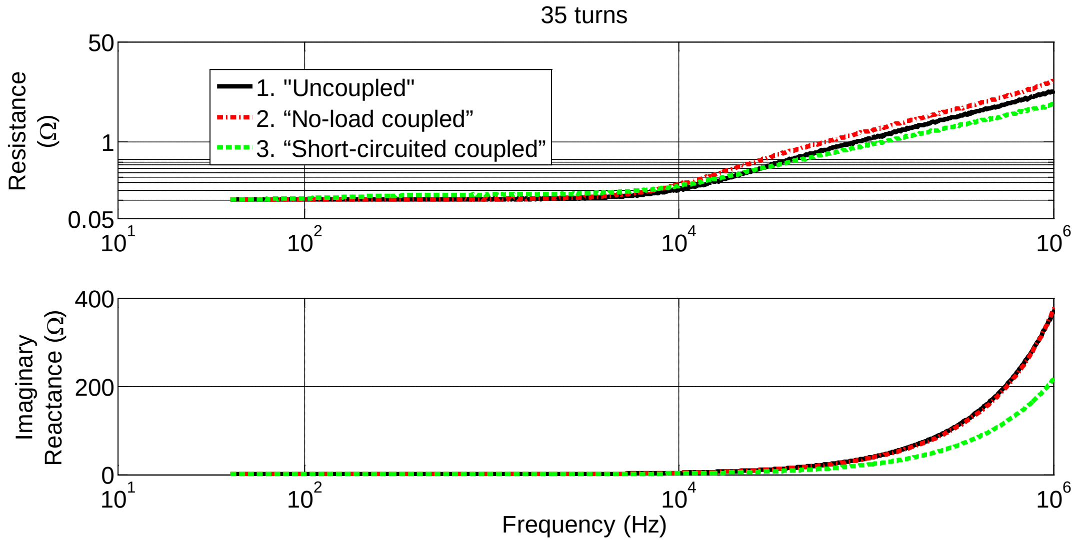

Figure 3.33 – Impedance of the coil of 50 turns with wire AWG measured at the three different coupling situations with the coil of 35 turns with wire AWG 15 and coil gap of 5 mm.

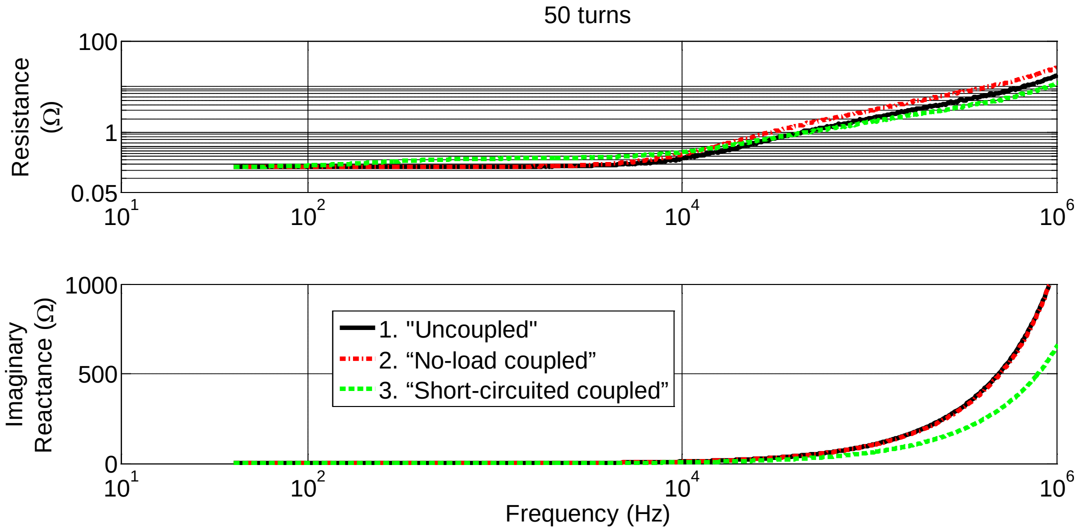

Again, Figure 3.32 and Figure 3.33 show that the reactance of the primary coil is, for all practical reasons, not affected by the secondary coil. On the other hand, the AC resistance of the primary coil is affected by the presence of the secondary coil even if the secondary coil has no-load (“No-load coupled” situation), mainly at frequencies higher than 10 kHz.

It is important to mention that the same behavior can be observed in simulations which does not account for the capacitive effects. Thus, the effect of the secondary coil on the primary coil, even at no-load, is not due to capacitive effect and might be due to something else such as eddy currents in the secondary coil near the primary coil.

This observation is very important, because in these cases, the calculation of the lumped parameters via special short-circuit and no-load tests, as presented in Section 3.3, would not work properly. In these cases, the lumped parameters could be calculated through individual tests as presented in the same section.

3.8 CONCLUSIONS

This chapter compared an analytical method to obtain lumped parameters of the TET transformer with proposed FE methods. When the circuit model is properly chosen, the calculation through the FE method is very precise though slower than the analytical method.

The FE method can be used even in situations where other type of material such as ferrite core is used around the coils, whereas the analytical method should be readapted to work in such situations.

Moreover, this chapter explained two different methods to measure the mutual inductance. Although the VNA is a powerful tool, it still requires the knowledge of the self-inductance to assess the mutual inductance. The IA measures the mutual inductance without the knowledge of the self-inductance, yet requiring more data from multiple configurations.

The use of FE homogenization techniques provides an excellent approximation for accurately accounting for eddy current, proximity and skin effects, while minimizing the computational cost linked to a dense mesh in simulations with detailed solid wires.

The proposed frequency domain 3D homogenization method provides very accurate results even for coils with a single layer planar geometry, as the case of most of the TET systems, where the geometry is periodic and homogeneous in one direction only.

In this way, the simulation of the displacements between the TET coils, which must be performed in 3D, can be simulated as simple stranded windings together with the homogenization technique to decrease the simulation time while keeping the accuracy of the frequency dependent effects.

In situations where the coils are aligned, the 3D approach is not necessary and the 2D axisymmetric is sufficient to compute any data with quality. Even with the 2D axisymmetric, the homogenization technique may be also needed to reduce dense meshes of a detailed model with solid wires in case the gauge of the wire is larger than the magnetic wave penetration depth.

Lastly, it is important to cite that the results and conclusions of this chapter were partially submitted in the following paper to the following conferences:

1. “Simulations of Transcutaneous Energy Transmitters by using Homogenization Method”, accepted for poster presentation at EMF 2013 in Bruges, Belgium.
2. “Analysis on Methods to obtain Lumped Parameters for an Inductive Coupling Device”, accepted for poster presentation at COMPUMAG 2013 in Budapest, Hungary.

3. “Homogenization Methods in Simulations of Transcutaneous Energy Transmitters”, accepted for poster presentation at COMPUMAG 2013 in Budapest, Hungary. The full paper was accepted on September 29th 2013 for publication in the IEEE Transactions on Magnetics.

4 SENSITIVITY ANALYSIS

4.1 INTRODUCTION

In order to better understand and visualize the behavior of the TET coils under different conditions, this chapter makes different analyses, considering virtual and physical prototypes.

First, the behavior of the TET coils was analyzed with virtual prototypes for a wide range of load resistance in order to establish a pattern and propose a computational procedure to obtain a load resistance value that consumes a specific power.

Second, physical prototypes were built and the secondary voltage, current and power, efficiency, and winding temperature were observed while:

- supplying different primary voltages and frequencies;
- using different load resistances;
- placing ferrite cores near the coils;
- moving the coils relative to each other.

Third, sensitivity analyses were performed by simulating virtual prototypes while varying some geometrical and electrical aspects as proposed in Chapter 2. These analyses were done by following two different approaches:

1. The efficiency, regulation and SAR were analyzed using aligned coils with or without serial resonant capacitors (SRCs) in four different topologies for the TET transformer referenced as “Coreless” (both primary and secondary coils are coreless), “Ferrite cored” (both primary and secondary coils have ferrite core), “Hybrid PFSA” (primary coil has ferrite core and secondary coil is coreless) and “Hybrid PASF” (primary coil is coreless and secondary coil has ferrite core).
2. The efficiency and relative current density were analyzed with the coils aligned to choose a core geometry. Then, a ferrite core geometry was chosen and

simulated with SRCs and with the coils misaligned to evaluate the impact of the variation of the mentioned parameters on the efficiency and relative current density. In this analysis, the value of relative core permeability was also studied.

All the discussed observations at the end of this chapter were important to ratify some decisions for the continuation of this research.

4.2 THE LOAD WITH THE REGULATOR

In order to make a proper design of the TET system, the knowledge of the AO to which the TET system will be connected is necessary. Thus, Professor Ivan Eduardo Chabu[3] stated that the AO is driven by a 12 W DC motor that should be supplied with constant voltage of around 15 V, thus implying a current of around 0.8 A. For this reason, a regulator might be inserted between the motor of the AO and the secondary coil of the magnetic transformer that transfer power inside the body. For practical reasons, this section considered supplying the power of 13 W in order to support any need for extra power, e.g. to compensate for the efficiency of the converter.

If the voltage is enough to supply the required power, this regulator will try to maintain a constant voltage on the AO. This means that if the secondary coil voltage is higher than the required AO voltage, the regulator will decrease the secondary coil current to maintain the required constant voltage and power on the AO. In case the

---

[3] Information attained in 2010 from Professor Ivan Eduardo Chabu, the person partly responsible for the development of a propulsion motor for the pump in the thematic project from FAPESP.

secondary coil voltage is less than the required AO voltage, the regulator would increase the secondary coil current as long as the secondary coil voltage is above the input voltage threshold of the regulator.

This behavior can be modeled as a resistance that varies its value according to the supplied voltage, consuming always the same power. However, what is this value of resistance?

In order to answer this question, it is good to understand how the TET system works with the variation of this load (in this case, the regulator with AO). Hence, one configuration of TET transformer (62 turns of wire AWG 19 in the primary coil and 24 turns of wire AWG 26 in the secondary coils, both with SRCs) was simulated with different values of load resistance and its behavior can be seen in Figure 4.1.

Figure 4.1 – Load voltage, current and power with different load resistance values of a TET system with 62 turns of wire AWG 19 in the primary coil and 24 turns of wire AWG 26 in the secondary coils, both with SRCs.

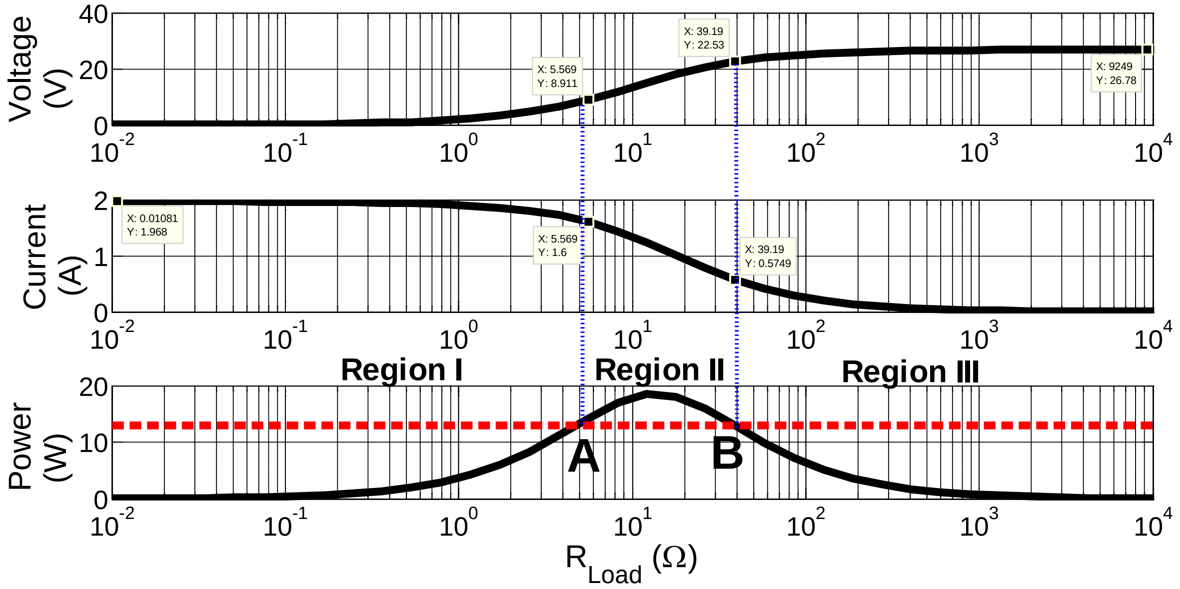

The red dashed line on the power graph in Figure 4.1 represents the desired power $P_{desired}$. As the graphs depicts, there is a range of load resistance (Region II) in which the TET coils can supply more than the desired power; for all other resistances outside of this range (regions I and III), this configuration of TET coils supplies less than the desired power.

From Figure 4.1, depending on the maximum power that the system can transfer, there could be up to two values of load resistance which consume exactly the desired power (A and B in Figure 4.1). These values could be computed through analytical calculations deduced from the equivalent circuit model of Figure 2.4. However, this deduction is very complicated and, in the configurations where this model is not accurate, the computed resistance values would supply wrong information about the system.

There are two other ways to compute the load resistance (R_{Load}) from the desired power $P_{desired}$ without the need for an equivalent circuit model: either by using the load voltage (V):

$$R_{Load} = \frac{V^2}{P_{desired}} \tag{4.1}$$

or by using the load current (I):

$$R_{Load} = \frac{P_{desired}}{I^2} \tag{4.2}$$

Observe that, if (4.1) uses the no-load voltage to compute the load resistance, the latter may not be exactly the load resistance that consumes the required power. This may happen due to the high regulation of this transformer, making the load voltage for the calculated resistance smaller than the no-load voltage and thus the load power also smaller than the required power. If this happens, it is possible to compute a new load resistance value by using (4.1) with the new load voltage acquired at this load resistance value. Of course, the second computed load resistance may have the same problem of having smaller load voltage than the previous resistance and consequently not having the required power. The same may happen if (4.2) is used to compute the load resistance from the short-circuit current. Thus, multiple new iterative computations may be needed to eventually converge to the value of the load resistance that consumes the required power.

Moreover, observe that (4.1) will always compute a value of the load resistance R_{Load} that is smaller than or equal to the resistance that is associated with the voltage V since it is always dividing by the desired power. In the same way, (4.2) will always compute a value of load resistance that is bigger than or equal to the resistance that is associated with the current I because it is multiplying by the desired power.

For these reasons, in order to compute the load resistance that absorbs the required power, the voltage and current of the system should be known for an initial value of resistance, which could be either no-load or short-circuit. The choice of (4.1) or (4.2) should be done by analyzing in which region of the curve (shown in Figure 4.1) the actual known data is located.

Since the no-load voltage is the highest voltage that the system can supply and a limit for maximum voltage is necessary as will be shown in Chapter 5, this research chose to compute the load resistance by using the no-load data. Then, the computed load resistance that consumes the required power is the one at point B in Figure 4.1. This resistance is not necessarily the one that achieves the highest efficiency of the system, but is the one that produces the least amount of problems to the regulator connected to the secondary coil because it attains higher voltage and lower current when compared with the second resistance at point A.

Therefore, the procedure used to search for the load resistance that absorbs the desired power is the following:

1. Simulate the system at no-load and observe the load power and voltage.
2. Calculate a new load resistance with (4.1).
3. Simulate the system with the new load resistance and observe the load power and voltage.
4. If the modulus of the load minus required power (|load power - required power|) exceeds the tolerance limit, compute the new load resistance according to steps 4.a to 4.c and return to step 3; otherwise, the value of the load resistance is reached and then the procedure is exited.
    - 4.a. If the actual load power is bigger than the required power (Region II), compute a new load resistance with (4.1).
    - 4.b. If the actual load power is smaller than the required power and the computation of (actual power – previous power)/(actual resistance – previous resistance) is smaller than zero (Region III), compute a new load resistance with (4.1).
    - 4.c. If the actual load power is smaller than the required power and the computation of (actual power – previous power)/(actual resistance – previous resistance) is larger than zero (Region I), compute a new load resistance with (4.2).

This procedure was implemented in Gmsh/GetDP.

4.3 THE FIRST MEASUREMENTS

For a qualitative analysis with experimental data, an initial physical prototype with coils of 45 and 23 turns, both with solid wire AWG 28 was built and tested as shown in Figure 4.2.

Figure 4.2 – Test configuration.

In this Figure:

- The primary coil has 45 turns and the secondary coil has 23 turns of copper wire AWG 28 which has diameter equal to 0.32004 mm.
- SRCs were calculated for 100 kHz to be connected in series with the primary and secondary coils. Since the measured primary and secondary inductances are 51 μH and 11 μH, respectively, the calculated capacitors were 50 nF and 230 nF. The capacitances used in this experiment were 47 nF and 220 nF, respectively, connected in series with the primary and secondary coils.
- The coils were aligned and initially separated by 3 mm.
- The primary coil was supplied by an amplifier fed by a signal generator.
- The secondary coil was connected to three parallel resistances of 33 Ω, totaling a resistive load of 11 Ω.
- Two oscilloscopes measured the RMS voltages and currents in the primary and secondary coils.

Since the capacitors used in this experiment are not exactly the calculated ones, the resonant frequency is different than 100 kHz. Thus, the frequency had to be adjusted to the resonant frequency by observing when the voltage was in phase with the current.

4.3.1 Aligned coreless coils

The signal from the generator was then increased to reach around 10 V in the secondary coil with the SRC, what equates to 9 W in the load. At this point, the currents and voltages in the primary and secondary coils were noted.

This procedure was repeated by changing the coil gap in different steps as shown in Table 4.1. Since the coils were in the resonant frequency for practical reasons, the voltage of the primary coil with the SRC was in phase with its current. Thus the power is simply the product of the voltage and current. Of course, the voltage and current of the secondary coil with the SRC are always in phase because they are connected to a resistive load.

Table 4.1 – Results from the tests without ferrite cores.

	Coil gap [mm]	**Frequency [kHz]**	**Primary coil with the SRC**			**Secondary coil with the SRC**			**Efficiency [%]**
			Voltage [V]	**Current [A]**	**Power [W]**	**Voltage [V]**	**Current [A]**	**Power [W]**	
1	3	105	5.2	1	5.2	6.4	0.55	3.52	67.7
2	3	105	8.2	1.7	13.94	10.2	0.9	9.18	65.8
3	3	105	8.6	1.73	14.9	10.6	0.9	9.5	64
4	5	105	8.6	2.33	20.04	11	0.96	10.56	52
5	7	105	8.6	3.2	27.5	12	1.04	12.5	45
6	7	105	4.1	1.5	6.15	5.6	0.5	2.8	45.5
7	7	104	4.2	1.7	7.14	6.2	0.53	3.29	46
8	5	104	4.4	1.3	5.72	6.2	0.54	3.35	58.5
9	3	104	4.6	1	4.6	5.8	0.51	2.96	64.3

Table 4.1 shows that, for the same coil gap and the same frequency, when the primary coil power is increased by amplifying the signal generator voltage, the secondary coil power increases, but the efficiency decreases and the primary coil current increases (see rows 1, 2 and 3).

Furthermore, rows 3, 4 and 5 show that for the same input voltage (primary coil voltage), when increasing the coil gap, the secondary coil power increases at the cost of the efficiency. In this case, the primary coil current also increases.

This can be explained as follows. When the coil gap is slightly increased, the mutual inductance decreases. As the load resistance is fixed, this fact makes the equivalent resistance seen by the power supply smaller. Thus, the primary coil current increases because the power supply voltage is fixed. Consequently, the powers of both primary and secondary coils increase. In this experiment, the load resistance is fixed, thus an increase in the secondary coil power means an increase in the secondary coil voltage. Nevertheless, the efficiency decreases because the coupling coefficient also decreases.

This experiment simulates a system design where the RMS source voltage and the load resistance are always constant. By increasing the coil gap, the secondary coil voltage and thus the secondary coil power increases, while the efficiency decreases and the primary coil current increases. Thus, during the coil design, the high currents of both coils must be taken into consideration when the coil gap is higher.

Nevertheless, an AO supplied by a regulator cannot be exactly modeled by a fixed resistance. As already mentioned, it can be modeled by a variable resistance that consumes certain amount of power. This situation was not initially tested, but in order to keep the secondary coil power constant for a fixed resistance, the primary coil voltage should decrease with the increase of the coil gap.

Trying to express this phenomenon mathematically:

$$R_{eq} = \frac{V}{I} = \frac{V^2}{P} \tag{4.3}$$

If the voltage of the secondary coil with the SRC increases with the coil gap, a variable load resistance would increase to maintain constant power while the secondary coil current would decrease. This implies that the maximum secondary coil current in such a system occurs at the smallest coil gap.

With a regulator between the secondary coil and the AO, the load voltage may change when the load impedance changes to try to maintain the constant power. Thus, this transitory situation may be difficult to analyze by manually changing the load resistance.

Moreover, an increase in the wire temperature was observed in this wire for currents above 1 A. Thus, the currents were limited to values not higher than 2 A, most of the time.

4.3.2 Temperature measurements

Since the temperature increases with the current, its variation was measured for a current of 1 A at 105 kHz in a coil of 45 turns. The results are shown in Table 4.2 and Figure 4.3.

Table 4.2 – Results from the temperature test.

Time	**Temperature [^{o}C]**
16:05:02	28.2
16:05:14	30.7
16:05:33	37.8
16:06:03	45.8
16:06:32	51.1
16:07:03	55.3
16:07:33	58.7
16:08:03	60.3

Figure 4.3 – Temperature measured in the 3 minutes of applying a current of 1A in a coil of 45 turns of wire AWG 28.

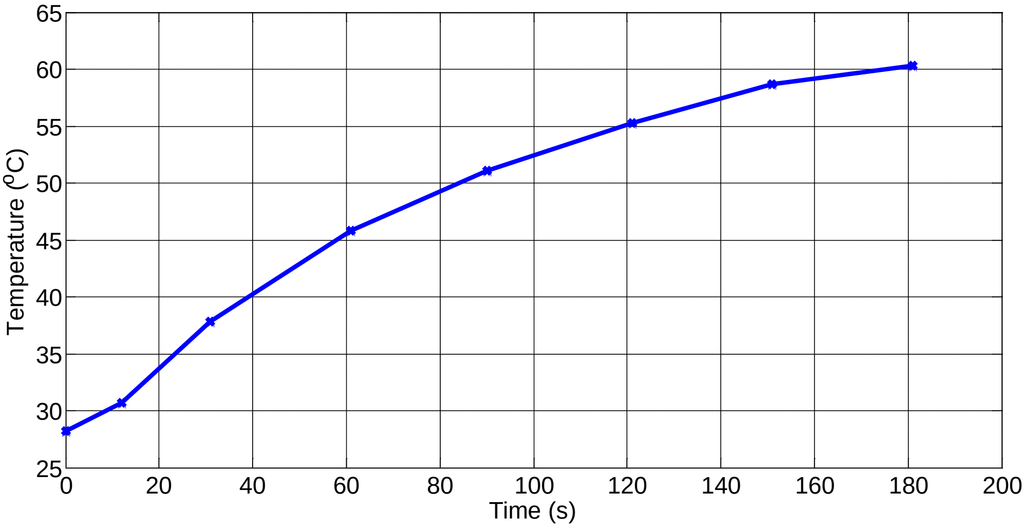

The temperature increase rate slowed down after 61 ^oC. This temperature is uncomfortable for the human body and therefore this amplitude of temperature should be avoided.

The coil from these measurements had approximately L_1=51 μH and r_1=0.96 Ω and its surface area was delimited by an external circumference with 22 mm of radius and an internal circumference with 5 mm of radius. Therefore, in an area of 1442 mm^2, the joule effect power dissipated was

$$P = r.I^2 = 0.96.1^2 = 0.96\,W \tag{4.4}$$

The measurements were performed with Fluke Thermal Imagers Ti10 at no forced ventilation or anything touching the coil and the temperature images were collected as shown in Figure 4.4.

Figure 4.4 – Temperature measured after 3 minutes of applying a current of 1A in the coil of 45 turns of wire AWG 28.

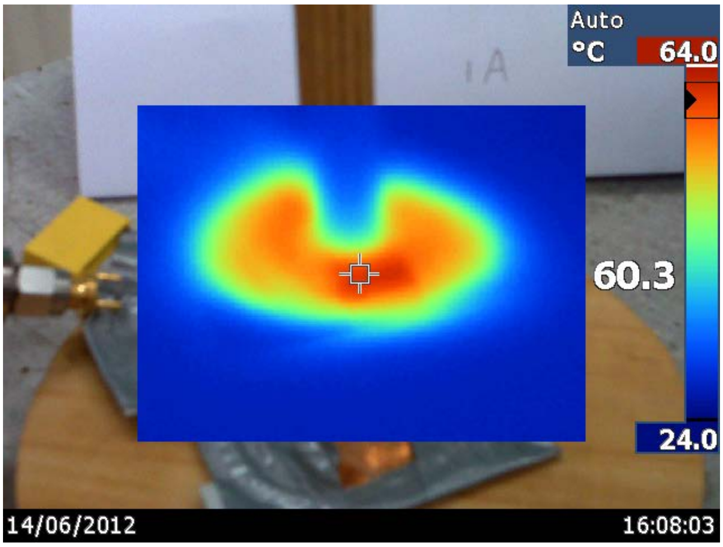

Two coils were created with different type of wires (shown in Figure 4.5) in order to test the effect of the temperature with different conductors.

Figure 4.5 – The two new coils developed to evaluate the temperature behavior.

(a) Coil 1 (b) Coil 2

The characteristics of those coils are:

- Coil 1: 2 layers of 20 turns each, solid wire AWG 22 (0.64 mm diameter), area equal to 996.7 mm^2 (10 mm inner diameter and 37 mm outer diameter) [4], L_1=33.5 µH, r_1=0.405 Ω at 50 kHz and r_1=0.838 Ω at 100 kHz.
- Coil 2: 2 layers of 20 turns each, multi-wire cable (0.7 mm diameter) with insulation (1.12 mm diameter), area equal to 2563.5 mm^2 (10 mm inner diameter and 58.5 mm outer diameter) [4], L_1=33.5 µH, r_1=0.286 Ω at 50 kHz and r_1=0.356 Ω at 100 kHz.

On each coil, 1 A at 100 KHz, 0.8 A at 100 kHz and 0.8 A at 50 kHz were applied, measuring respectively 68 ^oC, 58 ^oC and 45 ^oC on coil 1 and 49 ^oC, 40 ^oC and 37 ^oC on coil 2. This data is organized in Table 4.3.

Table 4.3 – Results from the temperature test with different coils.

Coil	**Current [A]**	**Frequency [kHz]**	**Dissipated Power [W]**	**ΔTemperature [^{o}C]**	**$P_{dissipated}/\Delta T$ [W/ ^{o}C]**	**$P_{dissipated}/A$ [W/m^2]**	**$P_{dissipated}/A/\Delta T$ [W/m^2/ ^{o}C]**
Initial Coil	1	105	0.96	61 – 24 = 37	0.026	665.74	17.99
Coil 1	1	100	0.84	68 – 28 = 40	0.021	840.77	21.02
Coil 1	0.8	100	0.54	58 – 28 = 30	0.018	538.10	17.94
Coil 1	0.8	50	0.26	45 – 28 = 17	0.015	260.06	15.30
Coil 2	1	100	0.36	49 – 28 = 21	0.017	138.87	6.61
Coil 2	0.8	100	0.23	40 – 28 = 12	0.019	88.88	7.41
Coil 2	0.8	50	0.18	37 – 28 = 09	0.020	71.40	7.93

Observe that, for practical reasons, when the “thermo factor” ($P_{dissipated}/A$) for each particular coil increases, the temperature rise increases, as expected from Section 2.6.1.

---

[4] Observe that here the coils are coreless. In this case, what is called inner diameter and outer diameter represent respectively the core central diameter and the inner diameter from Figure 2..

4.3.3 The effect of the ferrite core on the aligned coils

Afterwards, the influence of the ferrite cores on the coils was examined by measuring the voltages and currents in the primary and secondary coils separated by gaps of 3 and 7 mm. Unfortunately, there was no ferrite core with the same geometry as the coils. Thus, in order to evaluate only the qualitative effect, two rectangular ferrite pieces were added over the primary coil and/or below the secondary coil, as shown in Figure 4.6.

Figure 4.6 – Addition of ferrite cores to verify the influence of the transmission – (a) only on the primary; (b) on both; (c) only on the secondary.

(a) (b) (c)

The performed measurements with ferrite pieces are shown in Table 4.4. The addition of the ferrite pieces increases the inductance of the coil. As the SRCs have fixed values, the resonant frequency decreases, what is clearly understandable by (2.1). For all situations tested, the resonant frequency was adjusted to always have voltage in phase with the current, allowing the calculation of the power to be voltage times current.

Table 4.4 – Results from the tests with ferrite. The column “Ferrite on” shows N (no ferrite), P (ferrite on the primary coil), S (ferrite on the secondary coil) and B (ferrite on both coils).

	Ferrite on	Coil gap [mm]	Frequency [kHz]	Primary coil with the SRC			Secondary coil with the SRC			Efficiency [%]
				Voltage [V]	Current [A]	Power [W]	Voltage [V]	Current [A]	Power [W]	
1	N	3	104	5	1	5.00	6.17	0.53	3.27	65.4
2	P	3	83	5	0.7	3.50	5.3	0.5	2.65	75.7
3	P	3	83	5.6	0.8	4.48	6.11	0.5	3.06	68.2
4	B	3	76	5.6	0.6	3.36	5.4	0.46	2.48	73.9
5	B	3	76	6.4	0.7	4.48	6.1	0.52	3.17	70.8
6	S	3	100	6.4	0.96	6.14	7.2	0.6	4.32	70.3
7	S	7	102	6.4	1.9	12.16	8.9	0.75	6.68	54.9
8	B	7	79.4	6.2	1.3	8.06	7.9	0.7	5.53	68.6
9	B	7	79.4	5	1.1	5.50	6.17	0.53	3.27	59.5
10	P	7	83.2	4.8	1.4	6.72	6.31	0.55	3.47	51.6
11	P	7	83.2	4.6	1.3	5.98	6.15	0.53	3.26	54.5
12	N	7	104	4.4	1.6	7.04	6.2	0.5	3.10	44.0

Comparing the first two rows of Table 4.4, it is possible to analyze the addition of ferrite piece only on the primary coil at the resonant frequency and at a fixed coil gap while maintaining the primary coil voltage fixed. In this case, the efficiency increases, but the secondary coil voltage and current and consequently its power decrease. It would be necessary to increase the primary coil voltage and current in order to obtain higher secondary coil power though at lower efficiency, yet higher than without the ferrite pieces as can be observed by comparing the two last rows of Table 4.4.

If the primary coil voltage is maintained, the addition of the ferrite pieces also on the secondary coil (compare rows 3 and 4) increases the efficiency even more, while decreasing the load power. Again, the increase of primary coil voltage in this case increases the secondary coil power and decreases the efficiency, however with higher efficiency than without the ferrite pieces on the secondary coil.

For a specific secondary coil power, having ferrite pieces on both coils (primary and secondary) improves the efficiency even more (compare rows 9 and 11).

Previously, it was observed that, for coreless TET coils, increasing the coil gap increases the secondary coil voltage unless the primary coil voltage is decreased which in turn decreases the efficiency. Again, rows 6 and 7 show that this behavior happens on TET coils with ferrite pieces, but the decrease of efficiency is less intensive in the TET coils with ferrite pieces than coreless.

4.4 THE SELECTED COIL BUILT WITH THE SRC

According to the simulations, the built coils make a configuration that can transfer up to 24 W when the primary coil of 35 turns is supplied by a source voltage of 12 V at 50 kHz. Thus, the built coils from Figure 3.20 were connected with two SRCs, calculated to compensate the self-inductances at 50 kHz as described in (2.1). Following this equation, the calculated values of the SRCs to compensate the primary and secondary coil self-inductances were respectively 171 and 62.6 nF. For practical reasons, the secondary coil was connected in series with a combination of three capacitors of 21 nF in parallel and the primary coil was connected in series with a combination of six capacitors in parallel (one 100nF, three 21 nF and one 10 nF).

The resulting capacitances were not exactly resonant at 50 kHz. Therefore, in order to detect the resonant frequency, the impedance of the primary coil was measured in the IA. This measurement was executed when the secondary coil was connected to different values of load resistances: no-load, 11 Ω, 33 Ω and 66 Ω. Moreover, the coils were connected to their respective SRCs and the secondary coil was aligned with the primary coil with a coil gap of 5 mm.

Figure 4.7 shows all these results when these loads are directly connected to the secondary coil with a SRC and Figure 4.8 shows the same results, but with a rectifier between the secondary coil and the load resistance. The resonance frequency may be observed at the local minimum of the modulus of the impedance.

Observe that when having the rectifier, the resonant frequency appears to happen at almost 50 kHz (49.5 kHz more specifically). In this case, the change of the load almost does not affect the resonance. In fact, only at frequencies above 100 kHz, the impedance is different for the situation when there is no-load.

On the other hand, observing the behavior of the impedance when there is no rectifier (the load is directly connected to the secondary coil with a SRC), the behavior of the impedance changes significantly with the variation of the load. Even the resonant frequency apparently changes in this situation although all the graphs of each load condition cross the zero phase at the same frequency of 49.5 kHz.

Figure 4.7 – Impedance of the input of the TET system with SRCs that connects to load resistance of different values.

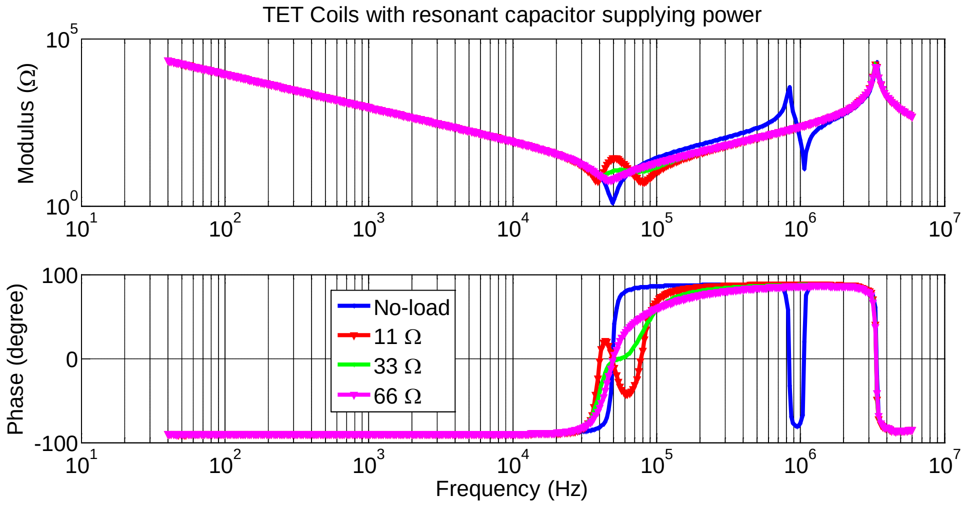

Figure 4.8 – Impedance of the input of the TET system with SRCs connected to a rectifier that connects to load resistance of different values.

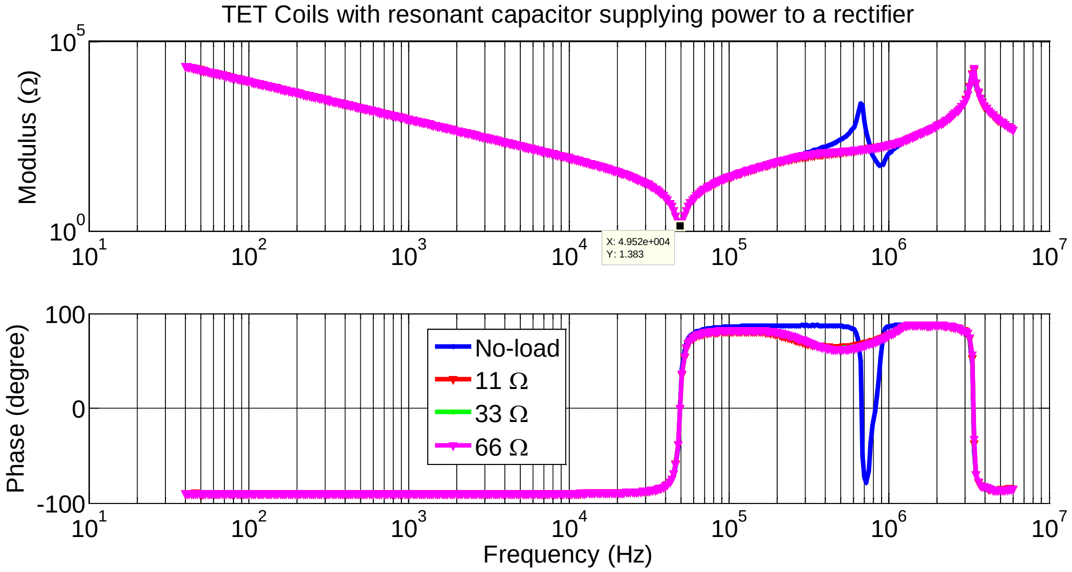

This difference between the measurement of the impedance of the system with and without rectifier is probably due to the signal generated by the IA being not enough to make the diodes switch. Then, the impedance of the system with rectifier behaves as if the system is at no-load.

Making the simulation of these different load conditions with Gmsh/GetDP, the same behavior ensued, as shown in Figure 4.9. Observe that the “Phase” curves in Figure 4.9 have the same phase as the “Phase” curves in Figure 4.7. The difference is that Figure 4.9 shows the phases from 0^{o} to 360^{o} and Figure 4.7 shows the phase from -180^{o} to 180^{o}. Knowing that -90^{o} is the same as 270^{o}, both figures present the same results in different scale.

Figure 4.9 – Impedance of the input of the TET system obtained from Gmsh/GetDP simulation while using SRCs and connected to load resistance of different values.

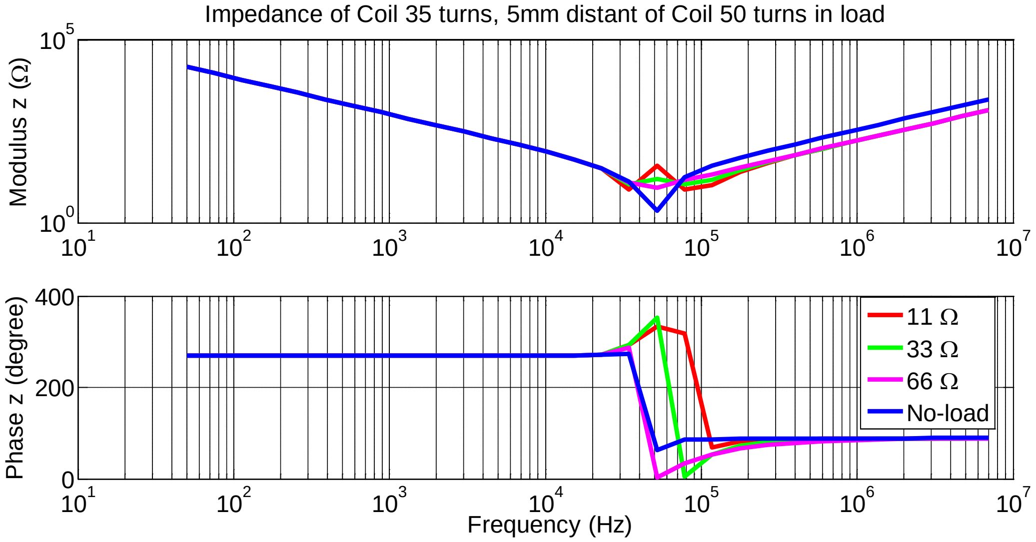

This behavior is easily explained by the analytical formulation when considering the simplified model of Figure 4.10 with SRCs.

Figure 4.10 – Simplified equivalent circuit model without considering *Rp*.

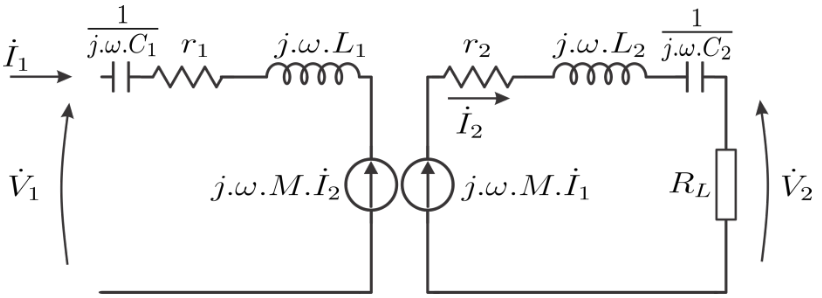

From this model,

$$Z = \frac{\dot{V}_1}{\dot{I}_1} = \left(r_1 + j.\omega.L_1 + \frac{1}{j.\omega.C_1}\right) - j.\omega.M.\frac{\dot{I}_2}{\dot{I}_1} \tag{4.5}$$

Then, replacing $\dot{I}_2$, the equation of the impedance becomes:

$$Z = \left(r_1 + j.\left(\omega.L_1 - \frac{1}{\omega.C_1}\right)\right) + \frac{\omega^2.M^2}{R_L + r_2 + j.\left(\omega.L_2 - \frac{1}{\omega.C_2}\right)} \tag{4.6}$$

These formulas were applied considering:

- the joule loss resistance obtained when the coil is magnetically and electrically uncoupled from any other coil;
- the self and mutual inductances when the coil is 5 mm distant from the other coil (as done with the measurements and simulation);
- the use of SRCs.

Thus, the obtained curve was similar to the curve obtained by measurement (Figure 4.7) and by simulation (Figure 4.9) as shown in Figure 4.11.

Figure 4.11 – Impedance of the input of the TET system obtained from the analytical equations while using SRCs and connected to load resistance of different values.

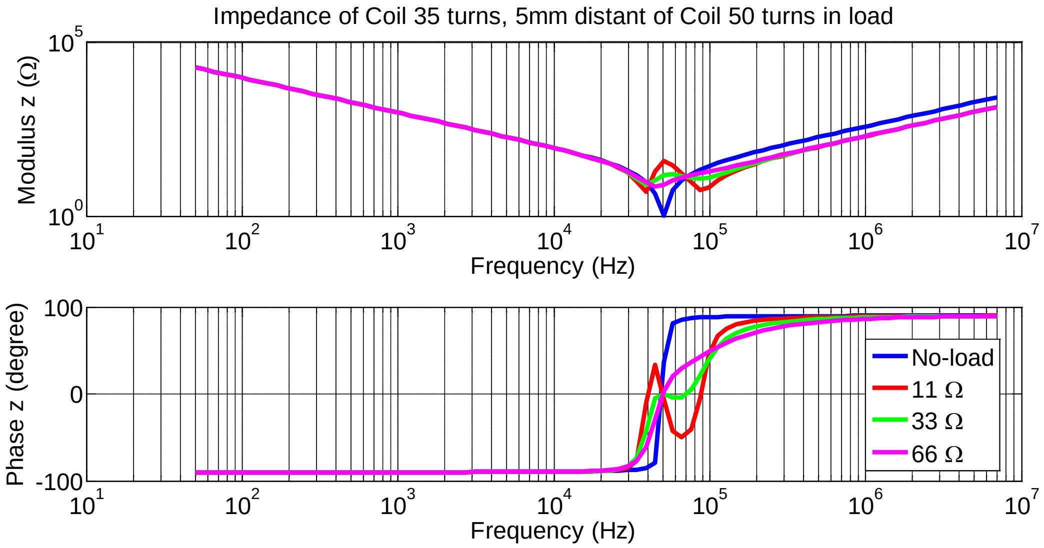

As elucidated in (4.6), the system impedance is strongly dependent on the load resistance. If the SRCs of both primary and secondary coils were exactly the values that compensate their self-inductance for a given frequency, this frequency would be the only point of resonance. However, since the primary SRC is resonant at a frequency different than the resonant frequency of the secondary SRC, the impedance may have two different points of resonance depending on the load resistance.

If the load resistance is much bigger than the error of the resonance of the secondary coil $\left(\omega . L_2 - \frac{1}{\omega . C_2}\right)$, then this error of resonance is negligible and the denominator of

(4.6) is mostly a real value. However, if the load resistance is small compared to this error of the secondary resonance impedance, then the total impedance of the system is going to have a second resonant frequency defined by the imaginary part of the denominator of (4.6).

4.5 ANALYSIS OF EFFICIENCY, REGULATION AND SAR

Having completed the analyses with physical prototypes, few observations were still missing. Then, virtual prototypes were implemented in FE applications in order to continue with further analyses.

Using the parametric tool of Flux-2D, the same simulation can be executed repeatedly while varying different parameters to make a sensitivity analysis and observe the response of the efficiency, regulation and SAR according to the parameters. Moreover, the simulations can be performed with different core materials as well as considering configurations with and without SRCs.

Hence, the geometry of Figure 2.3 was simulated in Flux-2D with the default dimensions and the same properties as described in Section 3.5.1., and several scenarios were created in Preflu (input modulus of Flux-2D), varying individual geometrical and physical parameters as shown in Table 4.5. Each scenario was changing one of the parameters at a time while keeping the remaining parameters fixed. In order to obtain the equivalent circuit of the TET transformer, each scenario was simulated with different load conditions, representing short-circuit, nominal load (18.75 Ω) and no-load tests.

Table 4.5 – Implemented scenarios for simulation and analysis.

Variable	**Default Value**	**Minimum Value**	**Maximum Value**	**Variation Step**
AC Frequency	100 kHz	100 kHz	300 kHz	50 kHz
Number of turns of primary coil	23	23	45	3
Number of turns of secondary coil	45	23	45	3
Coil Thickness	1.75 mm	1 mm	4 mm	0.75 mm
Core Central Diameter	10 mm	8 mm	24 mm	4 mm
Core Inner Diameter	40 mm	20 mm	45 mm	5 mm
Core Outer Diameter	50 mm	45 mm	70 mm	5 mm
Coil gap	5 mm	5 mm	30 mm	5 mm
Core Thickness	5 mm	5 mm	15 mm	5 mm
Power Supply Voltage	24 V	16 V	30 V	4 V

These simulations were performed considering four different topologies for the TET transformer according to the types of cores present:

1. “Coreless”: the regions designed for both primary and secondary cores have air properties.
2. “Hybrid PASF”: the region designed for the primary core has air properties (coreless coil), but the secondary coil has ferrite core.
3. “Ferrite cored”: both primary and secondary cores have ferrite properties.
4. “Hybrid PFSA”: the primary coil has ferrite core, but the region designed for the secondary core has fat properties (coreless coil).

The geometry of Figure 3.6 was also simulated with a combination of each parameter, as shown in Table 4.5, making a multiparametric analysis, which is presented in Section 4.6.

Since the simulated TET configurations were assumed to have thin wires with no significant skin and proximity effects, the self-inductance could be calculated through the short-circuit tests performed with stranded windings simulations. Then, the SRC could be calculated as described in Section 2.5 and the same simulations could be performed again, but this time considering SRCs.

The first parameter to be evaluated was the frequency of transmission. Assuming that it is possible to vary the frequency up to 300 kHz with the data from Table 4.5, the primary coil was fed with a source voltage of 24 V at frequencies ranging from 100 kHz to 300 kHz. The results are shown in Figure 4.12.

Figure 4.12 – Behavior of efficiency, regulation and SAR with frequency variation.

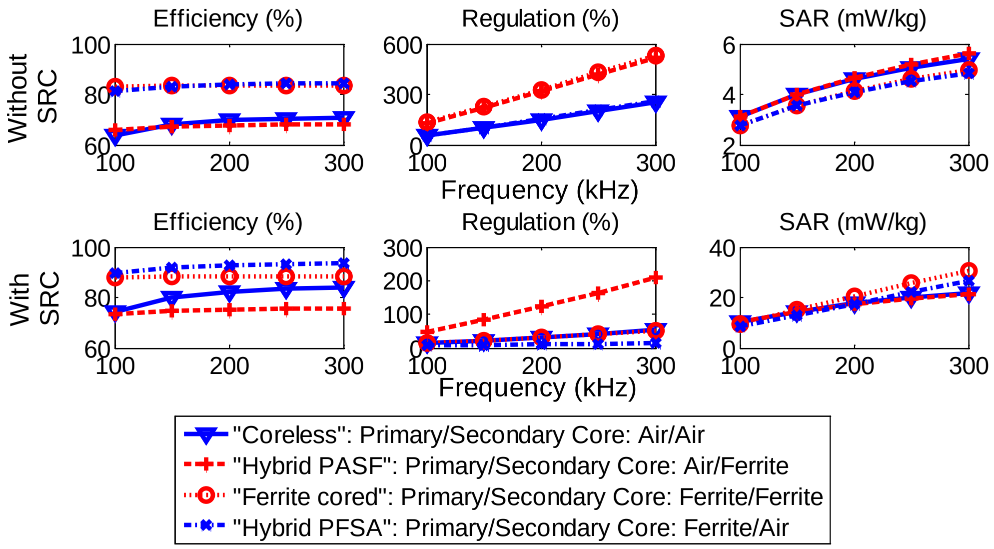

Remember that, for each simulated frequency, the associated SRC value is different and is dependent on the parameters of the TET transformer as mentioned in Section 2.5.

Observe that the qualitative behavior of the TET coils with respect to frequency variation is almost the same regardless of the presence of SRCs, except for the topologies in which the primary coil has a ferrite core. In this latter case, although the efficiency and regulation have similar performance, apparently the behavior of the SAR with respect to frequency variation becomes linear in the observed frequency range.

Despite the type of core used, the regulation increases with the frequency although the regulation increases less when the secondary coil is coreless. The SAR also increases with the frequency similar to what could be modeled by a quadratic function. However, this increase is smaller when the primary coil is coreless and the TET coils are connected to SRCs. Moreover, the smallest values of SAR happen when the primary coil has a ferrite core.

The “Hybrid PFSA” topology (in which the primary coil has a ferrite core and the secondary coil is coreless) is the topology that gives the best values of efficiency and regulation. However, if this topology has SRCs, it does not instigate the best SAR value. Thus, the decision on the type of core should be evaluated cautiously because it depends on the frequency used in addition to whether SRCs are used.

With SRCs, the SAR value more than doubled. Moreover, when the primary coil has a ferrite core, the SAR values exceed its values for the topologies in which the primary coil is coreless. This does not occur when SRCs are not used.

In contrast, the inclusion of SRCs caused a small improvement in the efficiency and a much larger improvement in the regulation. Note that this improvement in the efficiency was higher in the topologies in which the secondary coil is coreless. In addition, the regulation improved more strongly in the topologies in which the primary coil has a ferrite core.

With the default geometry values of TET coils, the increase of frequency helped to improve only the efficiency, especially in the configurations with SRCs. Even though, the gain of the efficiency is only significant at frequencies below 200 kHz and when at least one of the coils is coreless. According to Figure 4.12, for the “Ferrite cored” topology, the efficiency remains almost independent of the frequency variation.

This analysis suggests an optimization to observe how much the enhancement of an attribute worsens the others and also to obtain the best frequency and topology of core to be implemented. Nevertheless, the “Hybrid PFSA” topology graphically appears to be the best choice.

Moreover, this simulation allowed a mapping of the SAR in the skin. Figure 4.13 shows the mapping of the power density in the skin around the TET coils configured as “Hybrid PFSA”, at 200 kHz. This is apparently the configuration with the best values of efficiency and reasonable values of SAR and regulation.

The power density is concentrated in a region near the external area of the skin and has its maximum value near the core central diameter of the primary coil. Therefore, the maximum SAR in 10 g of skin is located in this region of contact with the coil.

Figure 4.13 – Power density mapping in the skin at 200 kHz.

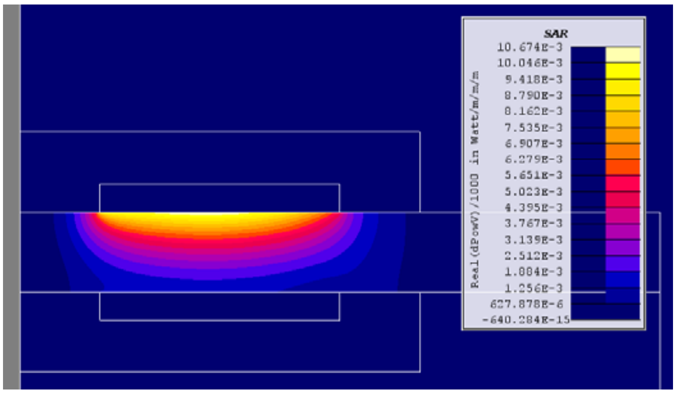

The frequency is not the only parameter that can improve the efficiency, SAR and regulation. Hence, a similar analysis varying the number of turns in the primary and secondary coils were performed, according to Table 4.5. Figure 4.14 and Figure 4.15 show the results of these simulations.

Figure 4.14 – Behavior of efficiency, regulation and SAR with primary coil number of turns variation.

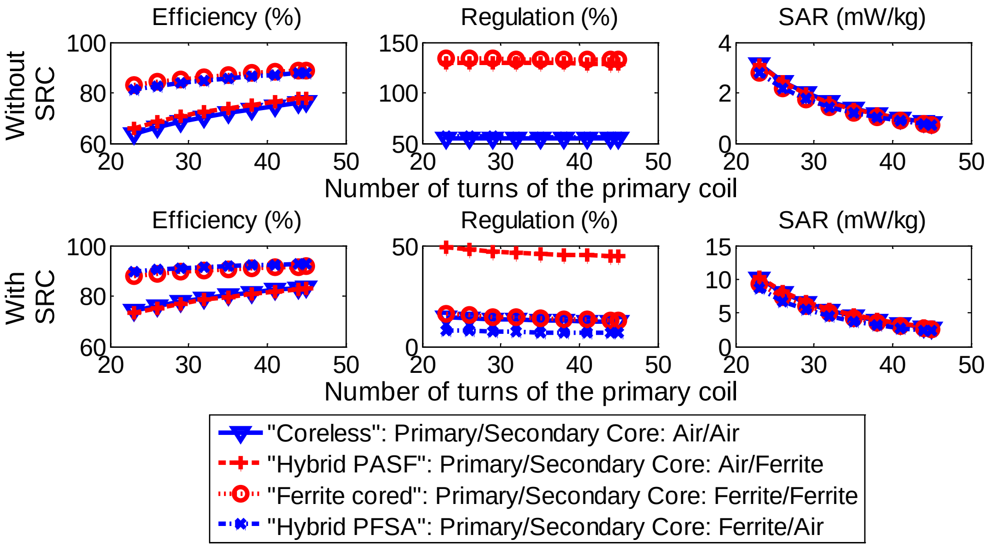

Figure 4.15 – Behavior of efficiency, regulation and SAR with secondary coil number of turns variation.

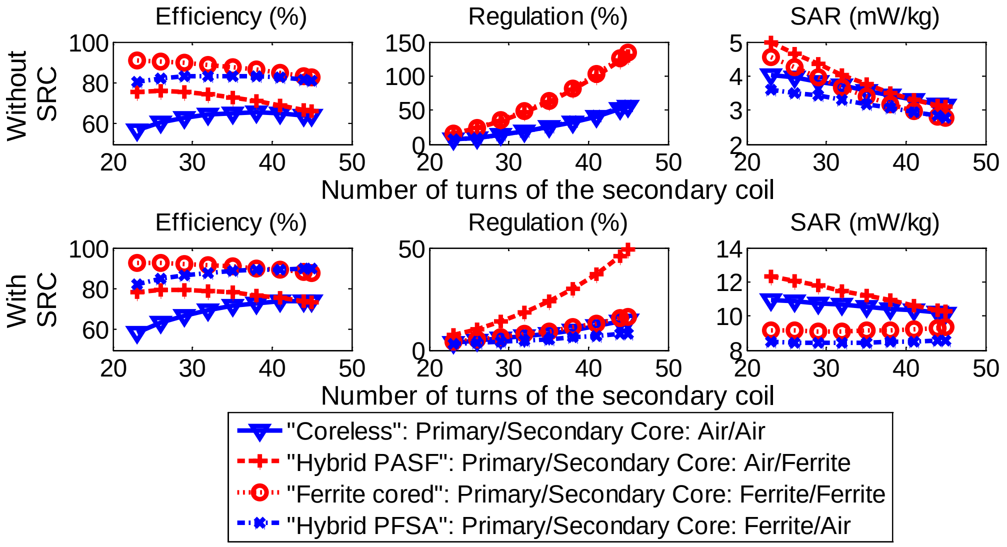

By reducing the number of turns of the secondary coil and increasing it for the primary coil, the efficiency increases and the regulation decreases even though the regulation almost does not change when the primary coil has more turns. This means, the higher the ratio between the coils, the better efficiency and regulation are. However, the ratio can impact the final secondary voltage supplied to the AO.

On the other hand, SAR decreases with the increase of the number of turns of both coils, i.e., the number of turns of the secondary coil might also be increased to improve SAR, unlike the efficiency and regulation.

Regarding the presence of a core, when the primary coil has ferrite core, the efficiency and SAR values are better. When the secondary coil is coreless, the regulation is better. Thus in the default configuration, it seems that the best choice would be the “Hybrid PFSA” topology with more turns in the primary coil and fewer turns in the secondary coil.

In order to analyze the variation of the coil thickness, it was varied from 1 to 4 mm, considering that this variation is feasible while maintaining the default parameters of Table 4.5. The results of efficiency, regulation and SAR are shown in Figure 4.16. Note that when the coil is coreless, the increase in the coil thickness means that the coil occupies more space in air, yet with no variation in reluctance.

Figure 4.16 – Behavior of efficiency, regulation and SAR with coil thickness variation.

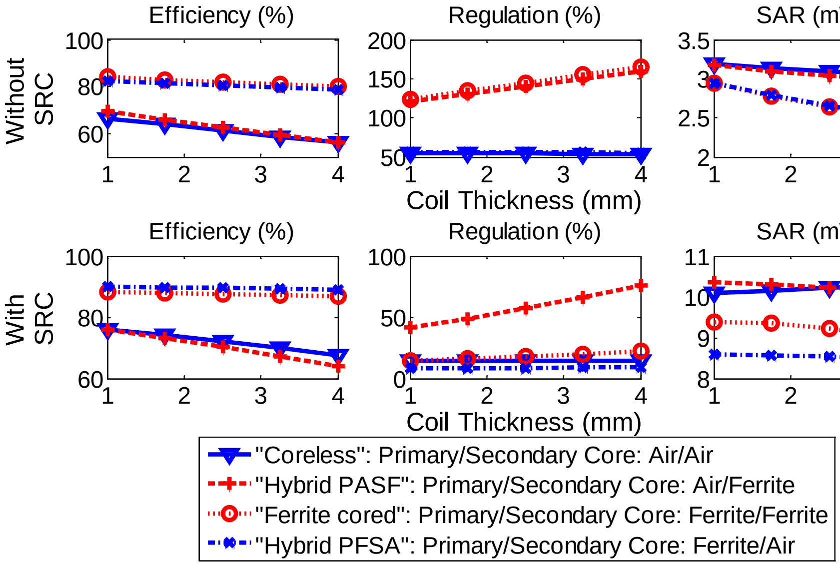

Figure 4.16 shows that the efficiency and regulation worsen almost linearly when increasing the coil thickness regardless of the presence of magnetic cores or SRCs.

The efficiency has its worst value when the primary coil is coreless and the regulation has its worst value when the secondary coil has ferrite core.

On the other hand, the behavior of SAR differs greatly when comparing the configurations with and without SRCs. By adding capacitors in the “Coreless” topology, the SAR increases almost linearly with the coil thickness. Without SRCs, the SAR decreases with increasing thickness even though, for coreless coils, the SAR has its higher values regardless of the presence of SRCs.

In the “Ferrite cored” topology, the SAR decreases. This decrease follows a quadratic trend for configurations with SRCs and a linear trend for configurations without SRCs. In the hybrid topologies (“Hybrid PFSA” and “Hybrid PASF”), the SAR slightly decreases with the increase of coil thickness, following different decrease rates depending on the use of SRCs. Moreover, the SAR has its lowest value in the “Hybrid PFSA” topology with large coil thickness.

The next parameter to be analyzed according to Table 4.5 was the core central diameter. The results are shown in Figure 4.17.

Figure 4.17 – Behavior of efficiency, regulation and SAR with core central diameter variation.

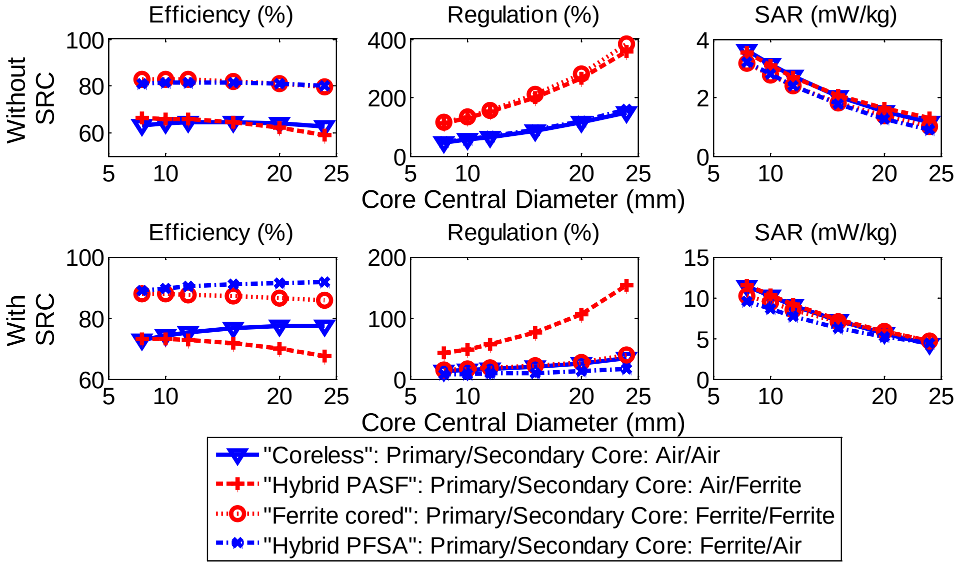

Observe that in the configurations without SRCs, the efficiency decreases with the increase in the core central diameter. But in the configurations with SRCs, if the secondary coil is coreless, the efficiency increases with the core central diameter. In order to control the regulation, the tendency is to reduce the core central diameter regardless of the presence of cores or SRCs. Thus, the regulation has better values with the presence of SRCs and when the TET system is configured as “Hybrid PASF”. On the other hand, to reduce the SAR value, the core central diameter must be increased and a SRC should not be used.

In the same way, the core inner diameter was evaluated by varying its values as shown in Table 4.5. The results are depicted in Figure 4.18.

Figure 4.18 – Behavior of efficiency, regulation and SAR with core inner diameter variation.

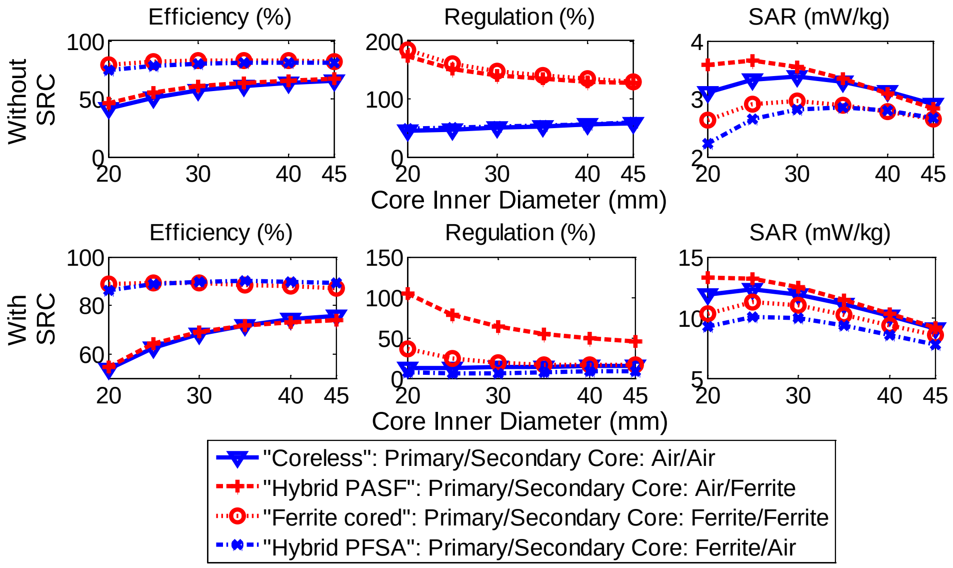

The efficiency increases very little by increasing the core inner diameter while the SAR increases to a maximum value for a given value of inner diameter and then decreases subtly, almost following a quadratic trend. On the other hand, the regulation decreases with the increase of this diameter when the secondary coil has ferrite core, but slightly increases when the same is coreless. This probably occurs because the cross-sectional area of the core through which the flux circulates decreases with the increase in the core inner diameter while keeping the core outer diameter fixed. Therefore, the reluctance of the magnetic circuit increases.

It is noteworthy that the best values of efficiency and SAR occur when the primary coil has a ferrite core. However, the best values of regulation occur when the secondary coil is coreless, regardless of the presence of a SRC, even though the use of the latter improves efficiency and regulation, but worsen the SAR.

Continuing with the systematic analysis, several simulations were performed while varying the core outer diameter as shown in Table 4.5. Figure 4.19 shows the results of these simulations.

The efficiency, regulation and SAR almost do not change their values with the core outer diameter even though this variation represents a variation in the reluctance. However, they improve their values with the presence of SRCs, depending on the presence of a core.

Even though, Figure 4.19 shows that the best values of efficiency and SAR occur when the primary coil has a ferrite core while the best values of regulation happens when the secondary coil is coreless.

It is noteworthy that similar analysis was performed by varying the core outer thickness from 5 to 15 mm while keeping the coil thickness fixed. However, this approach did not have any impact in terms of efficiency, regulation and SAR. Thus, the figure associated with this analysis was not included in this text.

Figure 4.19 – Behavior of efficiency, regulation and SAR with core outer diameter variation.

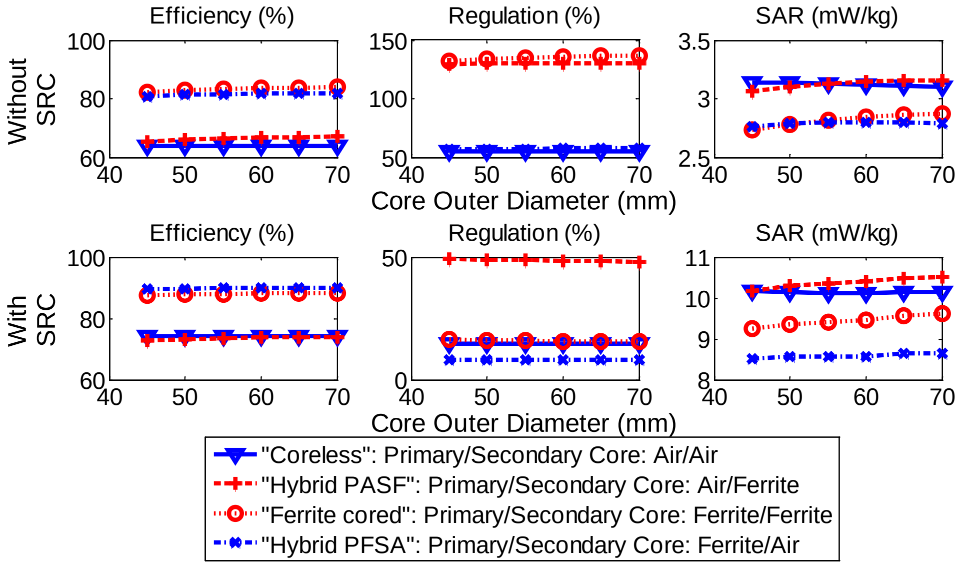

Since, the value of the power supply voltage should change depending on the turn ratio between the coils, the same analysis was performed to determine the sensitivity of TET coils with the variation of the source voltage from 16 to 30 V as can be seen in Figure 4.20.

Figure 4.20 – Behavior of efficiency, regulation and SAR with source voltage variation.

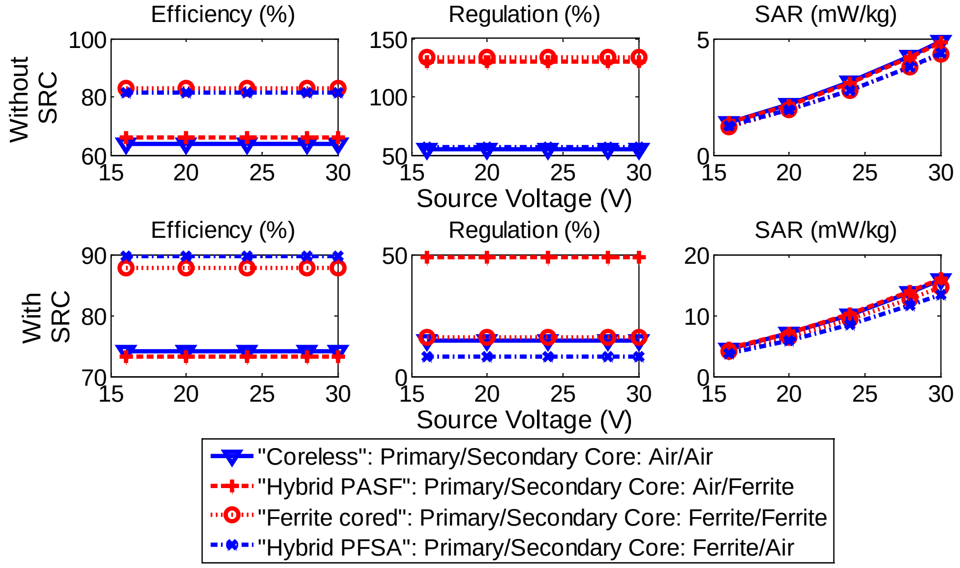

As expected, the efficiency and regulation do not vary but the SAR increases significantly with voltage. This is expected since less power is transferred with less voltage and thus less energy is absorbed. However, a reduction in voltage is not always possible, particularly if the turn ratio between the coils is too large.

It is noteworthy that, as observed with the variation of frequency, the behavior of the TET transformer with and without SRCs, regardless of the variation of any parameter, follows the same trend, except when the primary coil has a ferrite core. Moreover, the values of efficiency and regulation are better and the values of the SAR are worse with the insertion of SRCs, having more emphasis in the topologies where the primary coil has a ferrite core. In the “Hybrid PFSA” topology, the TET transformer has the best values of efficiency, regulation and SAR.

Furthermore, the analyses of most of the parameters (such as coil thickness, number of turns and core central diameter) suggest an optimization to better assess the values of these parameters which minimizes SAR and regulation while maximizing efficiency. Although SAR was smaller than the limits established by ICNIRP for all the analyzed configurations, it is not certain that it would still be smaller for configurations different than the analyzed ones. Thus, an optimization that also minimizes SAR could support this sensitivity analysis.

4.6 MULTIPARAMETRIC ANALYSIS

From the previous sensitivity analysis, it is clear that the efficiency, SAR and regulation have different behaviors according to the variation of each mentioned parameter. However it is unclear whether such behavior would remain the same for other non-default parameter settings. Thus, in order to analyze whether the behavior of the parameters differs when the rest of the parameters have non-default values, other simulations for the “Ferrite cored” topology and different values of number of turns, frequency, coil thickness, core central diameter and voltage were performed according to Table 4.6:

Table 4.6 – Limits of parameters variations simulated in Flux-2D for multiparametric analysis.

Parameters	**Limits**
Core Central Diameter	[8 24] mm
Coil Thickness	[1 4] mm
Number of turns of the Primary Coil	[23 45] turns
Number of turns of the Secondary Coil	[23 45] turns
AC Frequency	[100 300] kHz
Source Voltage	[16 30] V

Therefore, a matrix of variable data (parameters) was created with six columns which represent the variation of each of the following parameters: core central diameter, coil thickness, number of turns of the primary and secondary coil, transmission frequency and source voltage. Another matrix was created with the values of efficiency, regulation, SAR and load power resulting from the simulations of each specific configuration defined by the combination of all the parameters of the first matrix.

These matrices were used in the data analysis and interpolation tool of Matlab, the *Response Surface Tool* (RSTool), in order to obtain the trend curves of efficiency, regulation, SAR and load power related with the different configurations of TET coils.

Hence, the responses of efficiency, regulation, SAR and load power with the variation of the mentioned parameters were interpolated by a quadratic polynomial, as shown in Figure 4.21.

Figure 4.21 shows that in order to obtain the best efficiency, the TET coils should have:

- more turns in the primary coil,
- thinner slot for the coil thickness,
- less turns in the secondary coil,
- a small, but not too small, core central diameter,
- high frequency,
- any value of voltage.

On the other hand, in order to improve the regulation, the source voltage and number of turns of the primary coil have no influence. However, the coil thickness, the number of turns of the secondary coil and the core central diameter should apparently be small. Since the variation of the frequency resembles a parabola, the frequency should be neither too high nor too low in order to improve the regulation.

All parameters affect the SAR, but the coil thickness, number of turns of the secondary coil and frequency have little effect. According to Figure 4.21, in order to minimize the SAR, the voltage and frequency should be minimized and the number of turns of the primary and secondary coils, the coil thickness and the core central diameter should be maximized.

In order to maximize the load power, the voltage should be maximized and the number of turns of the primary and secondary coils, the coil thickness, the core central diameter and frequency should be minimized. Note that at the cursor point of Figure 4.21, the load power is less than 12 W. Thus, the number of turns of the primary coil or the frequency should be reduced to obtain values above 12 W.

Figure 4.21 – Tendency curve, generated by RSTool of Matlab, for the “Ferrite cored” TET systems without SRCs.

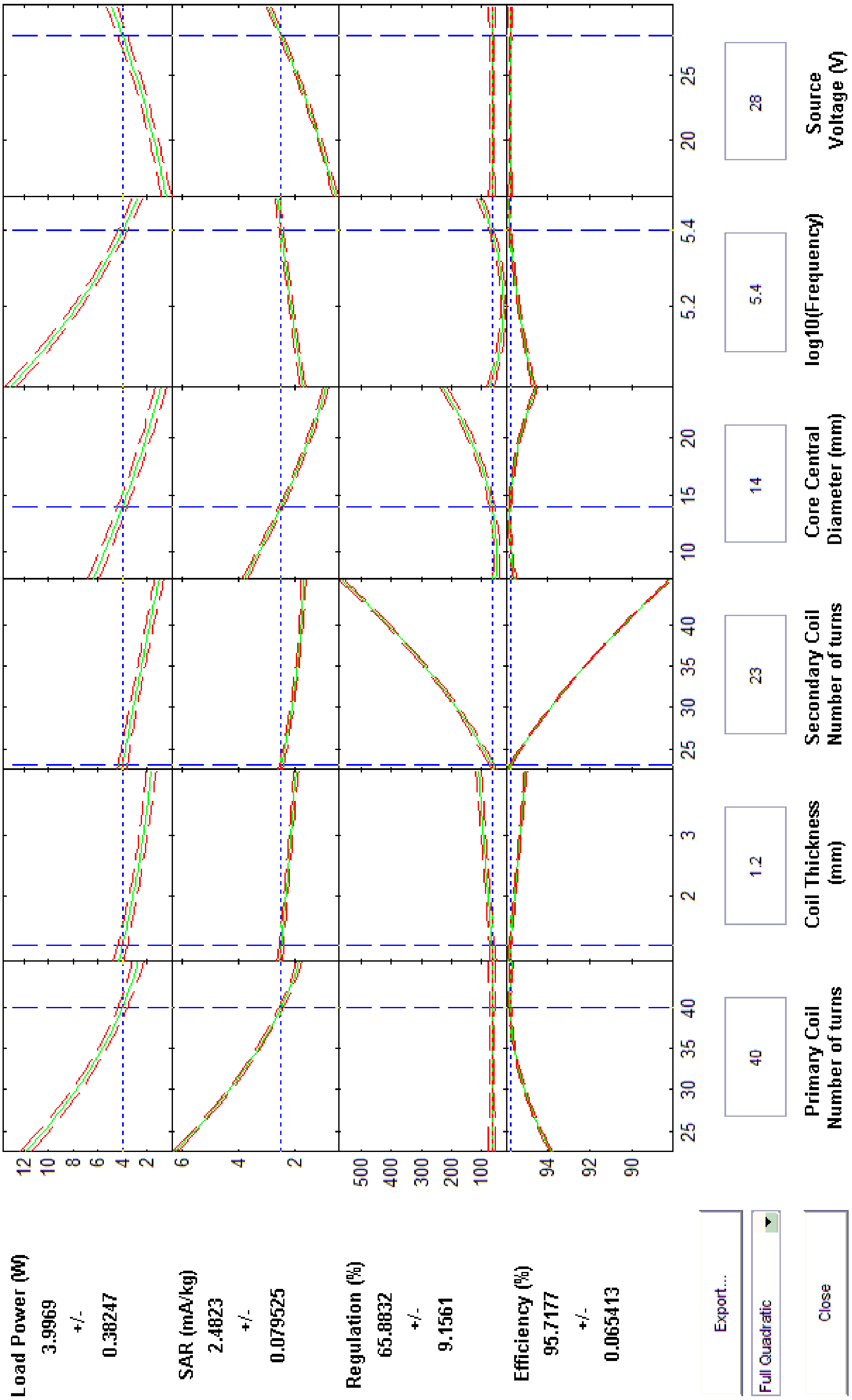

Load Power (W)
3.9969
+/-
0.38247

SAR (mA/kg)
2.4823
+/-
0.079525

Regulation (%)
65.8832
+/-
9.1561

Efficiency (%)
95.7177
+/-
0.065413

Primary Coil Number of turns: 40

Coil Thickness (mm): 1.2

Secondary Coil Number of turns: 23

Core Central Diameter (mm): 14

log10(Frequency): 5.4

Source Voltage (V): 28

It is noteworthy that when the cursor of any parameter moves to another value, the slopes of the curves of the other parameters change, i.e., the behavior of efficiency, regulation, SAR and load power vary according to the chosen parameters configuration.

Thus, this multiparametric analysis shows that there is a need to provide systematic analysis in order to find the best configuration of TET coils that maximizes efficiency while minimizing regulation and SAR, and while supplying a power equal to or greater than the power of 12 W required by the load. This implies a technique of multi-objective optimization, which is described in Chapter 6. Therefore, other requirements may be added.

A second analysis was performed after the insertion of SRCs to compensate the self-inductances of the primary and secondary coils as described in Section 2.5. Similar to the previous analysis, the chosen interpolation is modeled by quadratic curves, as shown in Figure 4.22.

Comparing Figure 4.22 (with SRCs) with Figure 4.21 (without SRCs), the load power and the efficiency are larger and the regulation is much smaller. The SAR, on the other hand, is much worse though always smaller than the limits established by ICNIRP.

In this case, again the slopes of the curves of all the responses change with the variation of the parameter cursor. For comparison purpose, the cursors of both figures were positioned at the same configuration.

Figure 4.22 – Tendency curve, generated by RSTool of Matlab, for the “Ferrite cored” TET systems with SRCs.

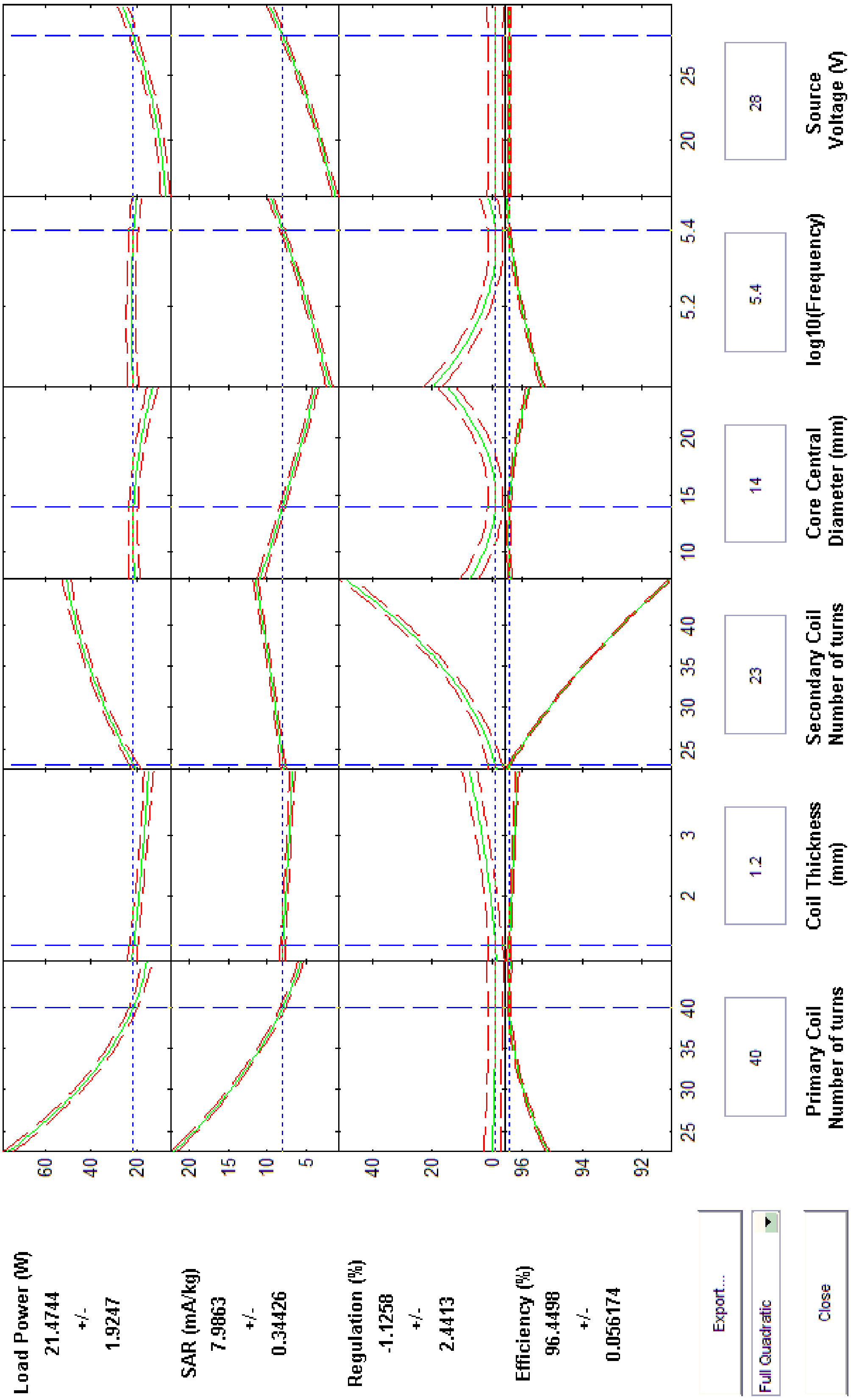

Load Power (W)
21.4744
+/-
1.9247

SAR (mA/kg)
7.9863
+/-
0.34426

Regulation (%)
-1.1258
+/-
2.4413

Efficiency (%)
96.4498
+/-
0.056174

Primary Coil Number of turns: 40

Coil Thickness (mm): 1.2

Secondary Coil Number of turns: 23

Core Central Diameter (mm): 14

log10(Frequency): 5.4

Source Voltage (V): 28

The same observations mentioned for the configuration without SRCs are still valid for this case with SRCs, except for the SAR and load power in relation to the number of turns of the secondary coil. Without SRCs and with more turns in the secondary coil, the SAR and load power decrease while, with SRCs, they increase.

The sensitivity analysis of Section 4.5 implied that a “Hybrid PFSA” TET topology would be the most recommended. Thus, this multiparametric analysis was also performed with the mentioned topology, obtaining Figure 4.23.

Comparing this “Hybrid PFSA” topology with the “Ferrite cored” topology from Figure 4.21 (both figures do not consider SRCs), the tendency curves have similar trend. However, in the “Hybrid PFSA” topology, the SAR is slightly smaller and the regulation is much smaller (almost half) than for the “Ferrite cored” topology. On the other hand, the load power for “Hybrid PFSA” topology is also smaller, yet not by much. This observation agrees to what was observed with physical prototypes in Section 4.3.3.

Thus, the “Hybrid PFSA” topology without SRCs can be better or worse than the “Ferrite cored” topology. In order to choose the best topology of TET coils, the optimization of this “Hybrid PFSA” topology must be performed first and then compared with the best configurations of the “Ferrite cored” topology, what will be discussed in Section 6.3.

Figure 4.23 – Tendency curve, generated by RSTool of Matlab, for the “Hybrid PFSA” TET system without SRCs.

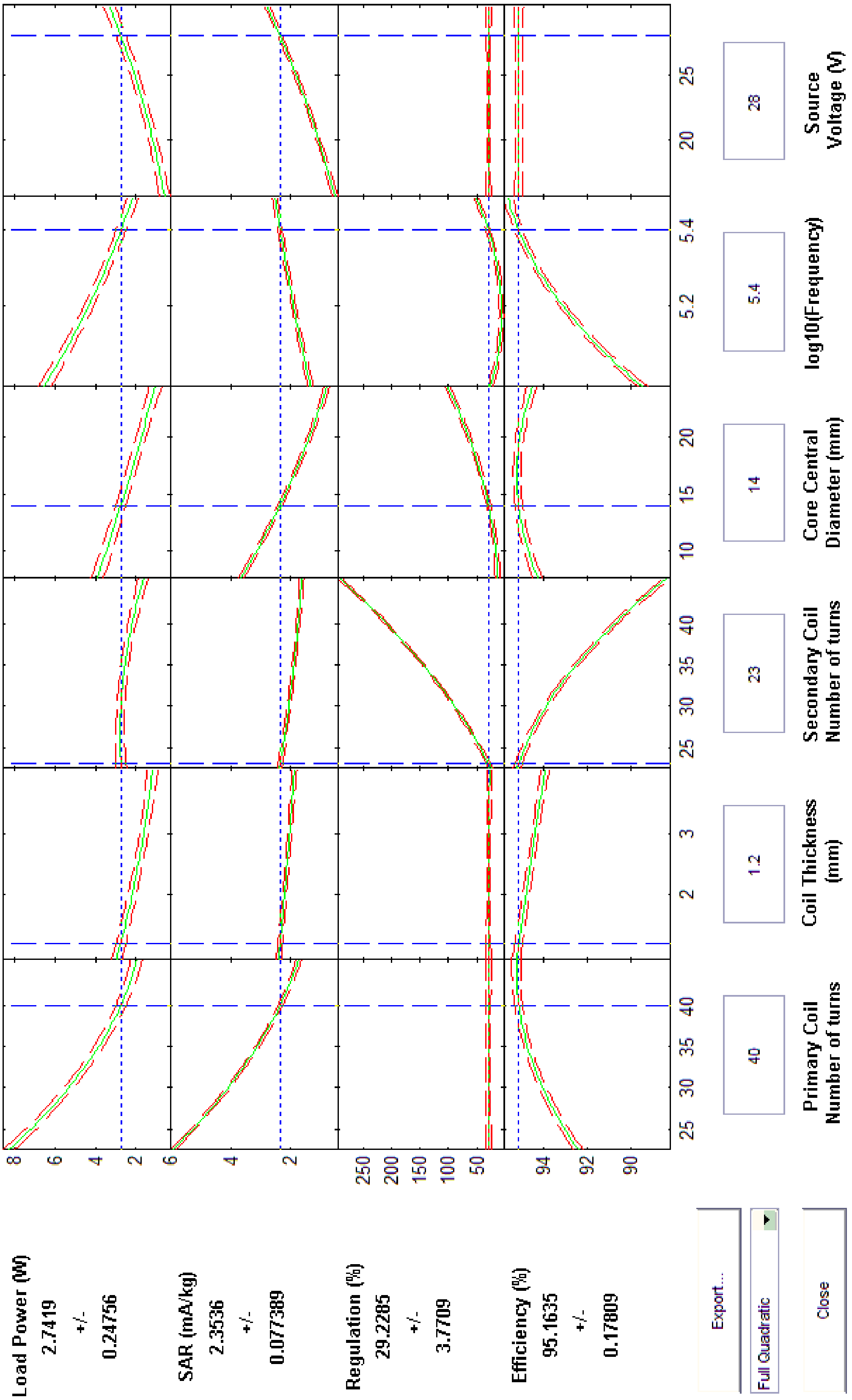

Load Power (W)
2.7419
+/-
0.24756

SAR (mA/kg)
2.3536
+/-
0.077389

Regulation (%)
29.2285
+/-
3.7709

Efficiency (%)
95.1635
+/-
0.17809

Primary Coil Number of turns: 40

Coil Thickness (mm): 1.2

Secondary Coil Number of turns: 23

Core Central Diameter (mm): 14

log10(Frequency): 5.4

Source Voltage (V): 28

The configuration of Figure 4.23 has no advantage when compared to the configuration of Figure 4.22, in which the TET coils are connected to SRCs. However, this “Hybrid PFSA” topology should be analyzed by also considering SRCs. Hence, the SRCs for the previous simulated configurations with this topology were calculated and the system was again simulated with all the mentioned combinations of configuration, obtaining the data shown in Figure 4.24.

Observe that the efficiency, regulation and SAR improved with the addition of the SRCs.

Regardless of the topology, the load power becomes larger with the use of SRCs, thus satisfying the power requirement needed for the application considered in this research.

However, once again, in order to choose the best configuration for the TET coils, optimization techniques must be performed with this “Hybrid PFSA” topology. Then, the best configurations chosen with “Hybrid PFSA” topology with SRCs should be compared with the best configurations chosen with “Ferrite cored” topology with SRCs.

Figure 4.24 – Tendency curve, generated by RSTool of Matlab, for the “Hybrid PFSA” TET system with SRCs

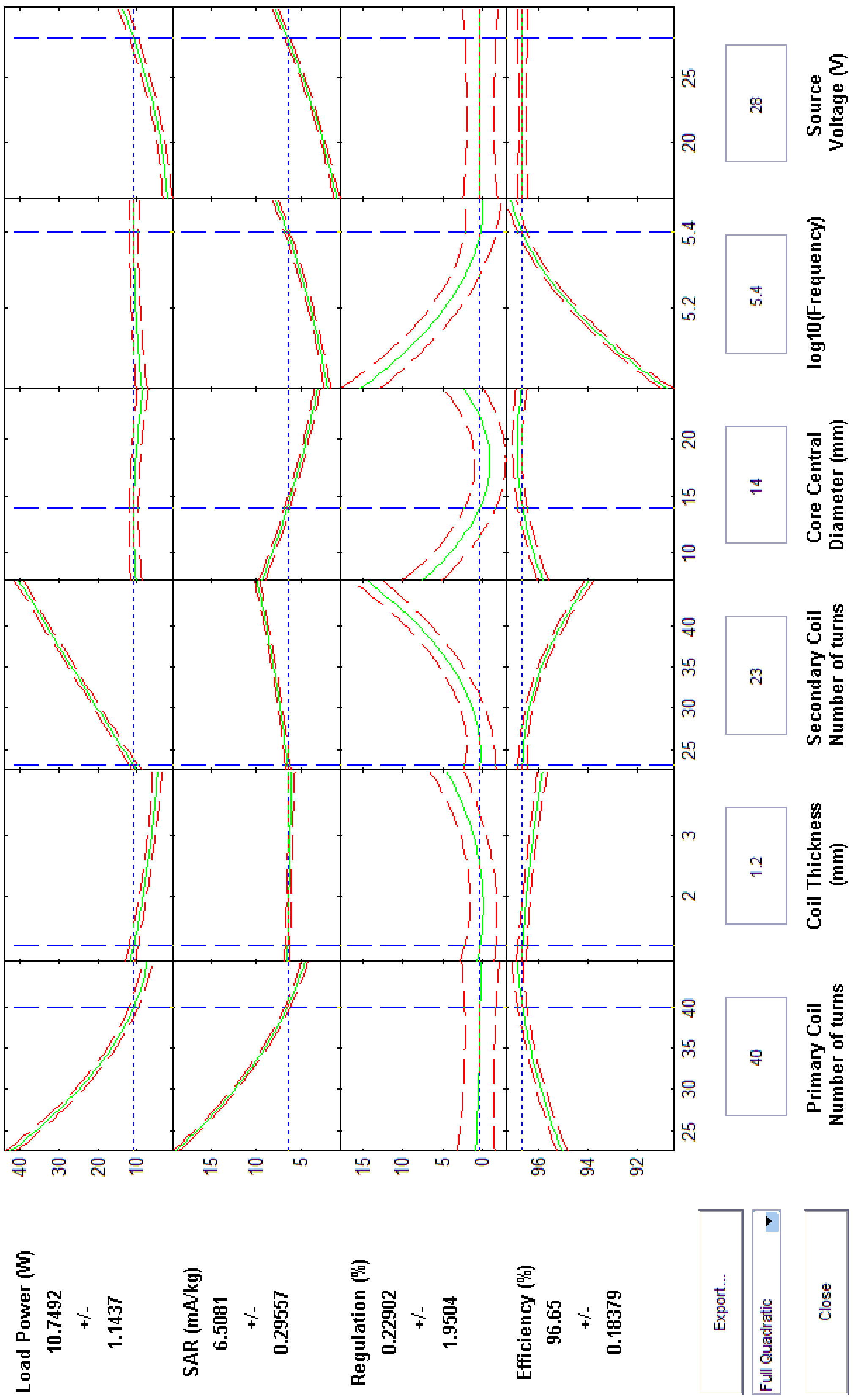

Load Power (W)
10.7492
+/-
1.1437

SAR (mA/kg)
6.5081
+/-
0.29557

Regulation (%)
0.22902
+/-
1.9504

Efficiency (%)
96.65
+/-
0.18379

Primary Coil Number of turns: 40

Coil Thickness (mm): 1.2

Secondary Coil Number of turns: 23

Core Central Diameter (mm): 14

log10(Frequency): 5.4

Source Voltage (V): 28

4.7 ANALYSIS OF EFFICIENCY AND RELATIVE CURRENT DENSITY

In order to make a more specific analysis of the efficiency and relative current density, the TET coils were implemented in Flux-2D considering coreless coils as well as cores with the five different geometries shown in Figure 4.25. The Flux-2D software performed a set of simulations with the coils aligned for the range of dimensions shown in Table 4.7 and with the same properties as described in Section 3.5.1. All the geometrical parameters are shown in Figure 2.3.

Figure 4.25 – Different analyzed geometries of TET cores.

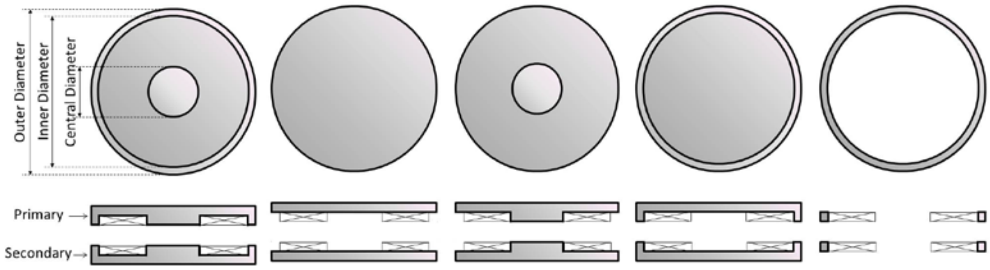

(I) (II) (III) (IV) (V)

Table 4.7 – Dimensions with their default values and range of simulation.

Dimensions	Default	Range
Frequency	100 kHz	[50 300] kHz
Core Outer Diameter	50 mm	[45 70] mm
Core Inner Diameter	40 mm	[20 45] mm
Core Central Diameter	10 mm	[8 24] mm
Primary Coil Number of turns	23 turns	[23 45] turns
Secondary Coil Number of turns	45 turns	[23 45] turns
Relative Core Permeability	3400	[2 4000]

4.7.1 Evaluating geometry type and size when coils are aligned

The simulation of the different core types was performed using Flux2D with both coils aligned while varying the geometry according to Table 4.7. The results are explicit in Figure 4.25, which shows the efficiency and the relative current density as functions of each dimension for all core types.

Note that the worst configuration is when the coil has no magnetic core – the relative current density is the highest and the efficiency is one of the smallest. The configuration with core type V is as bad as coreless since this type of core entails in low efficiency (some cases even lower than coreless) and the relative current density induced in the skin from this kind of core is one of the worst.

From Figure 4.25, the most recommended type of core is number I, which implies the best values of efficiency and lowest values of relative current density. All the other type of cores (II, III and IV) has similar performance with comparable values of efficiency for any size of geometry.

It is also possible to observe in Figure 4.25 that when the coils are aligned, the efficiency improves for most of the core types while:

1. Increasing the number of turns of the primary coil.
2. Decreasing the number of turns of the secondary coil. Although for core type V and coreless coils, the efficiency increases a little bit up to 35 turns and then starts decreasing again, for the other types of core, the efficiency improves with less turns in the secondary coil.

Figure 4.26 – Performance of TET transformer with different geometry types and sizes. Each graphic is the variation of one of the parameters while the other parameters remain at the default values, i.e., frequency of 100 kHz, core outer diameter of 50 mm, core inner diameter with 40 mm, core central diameter with 10 mm, primary coil with 45 turns and secondary coil with 23 turns.

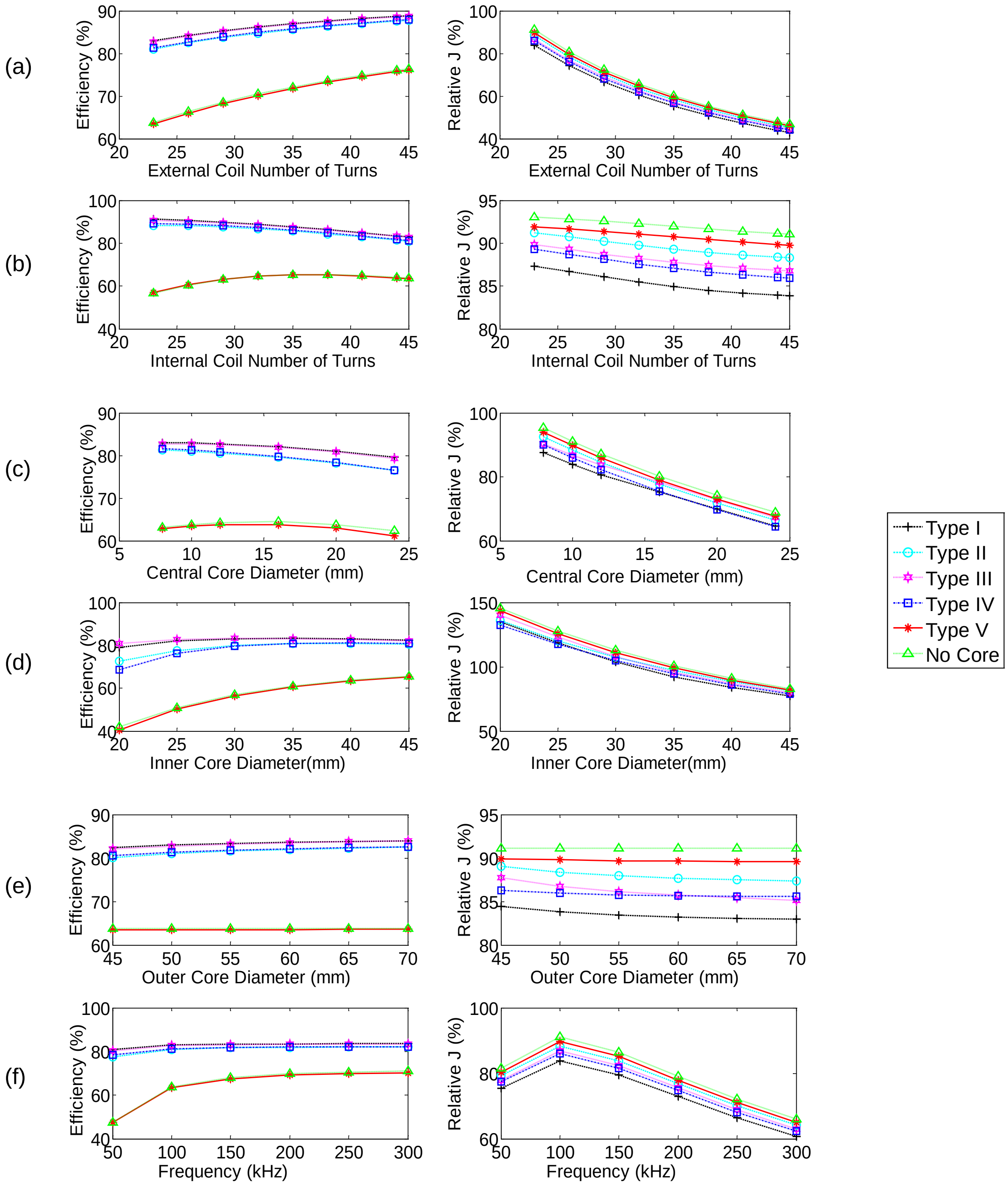

3. Decreasing the size of the core central diameter. Observe that as the core central diameter tends to zero, core type I looks similar to core type IV. However, there is a conceptual difference: making the core central diameter of core type I tend to zero implies that the windings must have the core central diameter tending to zero, which is very difficult to obtain. Core type IV has no core in the center of the windings, yet it has an inner diameter different than zero. Thus, Figure 4.25 shows that core type I is the best core type and has better results as the core central diameter is smaller.
4. Having the core inner diameter between 25 mm and 40 mm (though with values out of this range, the efficiency is not much worse). Note that for core type V and coreless coils, the bigger the core inner diameter is, the higher the efficiency is. The meaning of this parameter for coreless TET coils comes from the spacing between the turns of the coil. This observation shows that the wider is the coreless coil, the more efficient power it will transfer.
5. Increasing the core outer diameter. This parameter has no meaning for the coreless TET coils and very little influence on core type V. This is the reason why, for those geometries, the efficiency and induced current are constant with the change of this parameter.
6. Increasing the frequency. Although the improvement of efficiency is negligible for frequencies higher than 100 kHz, the relative current density decreases at higher frequencies, having its worst value at 100 kHz for the default configuration shown in Table 4.7.

The behavior of the relative current density improves while:

- increasing the number of primary and secondary turns;
- increasing the size of the core central and inner diameters;
- increasing the frequency. The current density has its worst value when the frequency is 100 kHz. Here, there is a strong relation to the conductivity of the biologic tissues. As the frequency increases, the conductivity of the biologic tissues also increases, increasing the induced current. Looking at Table A.2 in APPENDIX A, it is possible to notice that the increase rate of the tissue conductivity is smaller after 100 kHz. Since the limit allowed by ICNIRP increases linearly with frequency, the relative current density becomes smaller

for frequencies at which the tissue conductivity increasing rate is smaller (at 100 kHz).

The variation of the core outer diameter did not change the value of the relative current density. Note that changing most of the parameter to improve the efficiency induces more current density in the body of the patient.

In addition to the core geometry, different core permeabilities were also analyzed for the different types of geometry. Similarly, the results identify core type I as the recommended type. Moreover, Figure 4.27 shows that the relative permeability of the material of the core affects very little the efficiency of the TET coils for values above 50, which means that the use of materials different than ferrite with lower relative permeability but still above 50 could be pertinent.

Figure 4.27 – Response of the TET transformer with different core material and type.

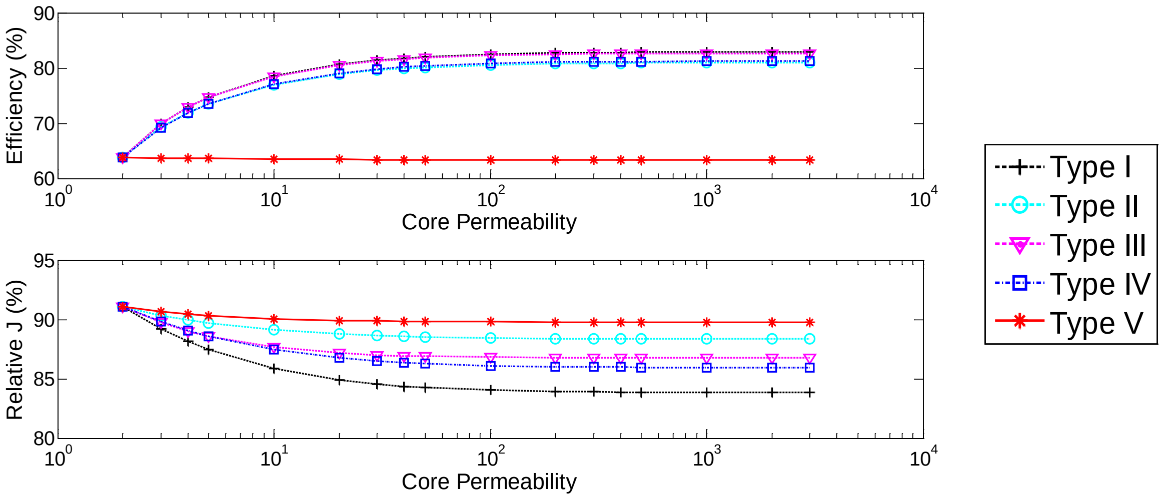

The behavior of the different core types with the variation of the thickness of the core was also analyzed, observing that the values of efficiency and relative current density were almost the same for all simulated thicknesses and that the behavior with the change of core type is similar to what was observed with the other dimensions – type I best results, type V worst results, and type II, III and IV similar results.

The evaluation of efficiency and relative current density with variation of core permeability was performed by varying the permeability of both primary and secondary cores. Thus, as the relative permeability tends to zero, the behavior of all core types might tend to the same behavior of the configuration with coreless coils. Since type I was appointed as the best core, it was simulated with different relative permeability of each core, keeping the permeability of the other core constant at the low value of 20, as shown in Figure 4.28.

Figure 4.28 – Variation of the relative permeability only in one of the cores, keeping the other core with relative permeability = 20 (Simulation only for type I).

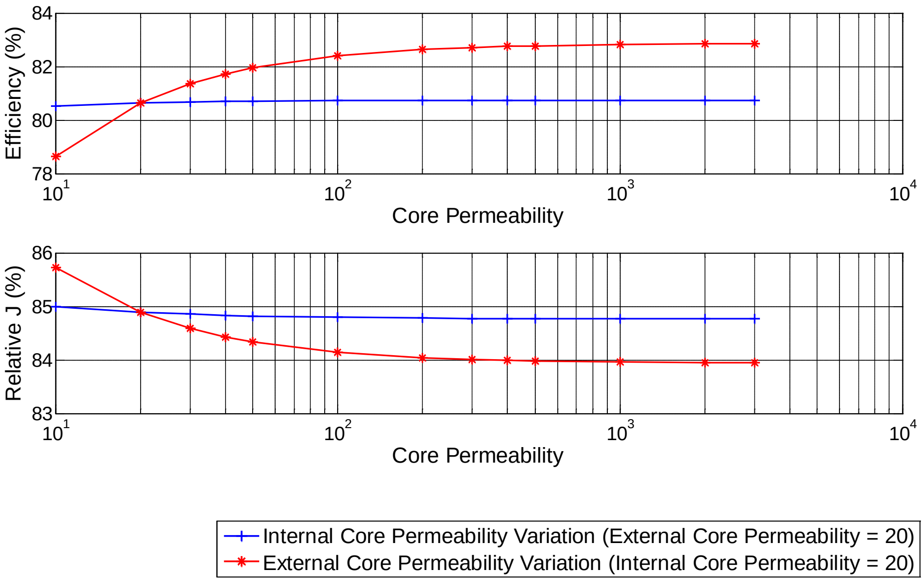

Note that, when the relative permeability of the primary core is constant at low value, the variation of the relative permeability of the secondary core almost does not change the behavior of the system. However, when the secondary core has low constant relative permeability, the curve of Figure 4.28 is similar to the curve of type I from Figure 4.27. That means that the effect observed in Figure 4.27 is mainly due to the variations on the relative permeability of the primary core. This observation suggests a configuration where the secondary coil has very low permeability (eventually even no core) and the primary coil has a core type I with permeability larger than 50, similar to the “Hybrid PFSA” topology already suggested in the previous section.

4.7.2 Evaluating stability with misalignment

Seeking to analyze the behavior of the TET coils when the primary coil is not aligned with the secondary coil, simulations with core type I (the most recommended configuration from the Section 4.7.1) were performed with 45 turns in the primary coil and 23 turns in the secondary coil.

Figure 4.29 shows the results of those simulations, presenting the response of the efficiency and relative current density at different misalignments for all the configurations in the range depicted by Table 4.7. Observe that the default values from Table 4.7 are still the same except for the primary and secondary number of turns which are now 45 and 23, respectively.

It can be seen that, regardless of the change of the geometrical dimensions of the TET transformer, the efficiency declines about 20% when the misalignment is up to 10 mm and then sinks to very low values for misalignments up to 20 mm. By further increasing the misalignment, the efficiency slightly improves, stabilizing at similar values between 25 and 30 mm. Above 30 mm of misalignment, the efficiency devaluates again.

The decline of the efficiency is strongly influenced by the size of the core inner diameter. By analyzing Figure 4.29(d), the efficiency improves at different values of misalignment depending on the size of the core inner diameter. If it is too small, the efficiency worsens even with misalignments smaller than 10mm.

Figure 4.29 – Response of TET coils to the misalignment between coils at each configuration. (primary coil = 45 turns; secondary coil = 23 turns).

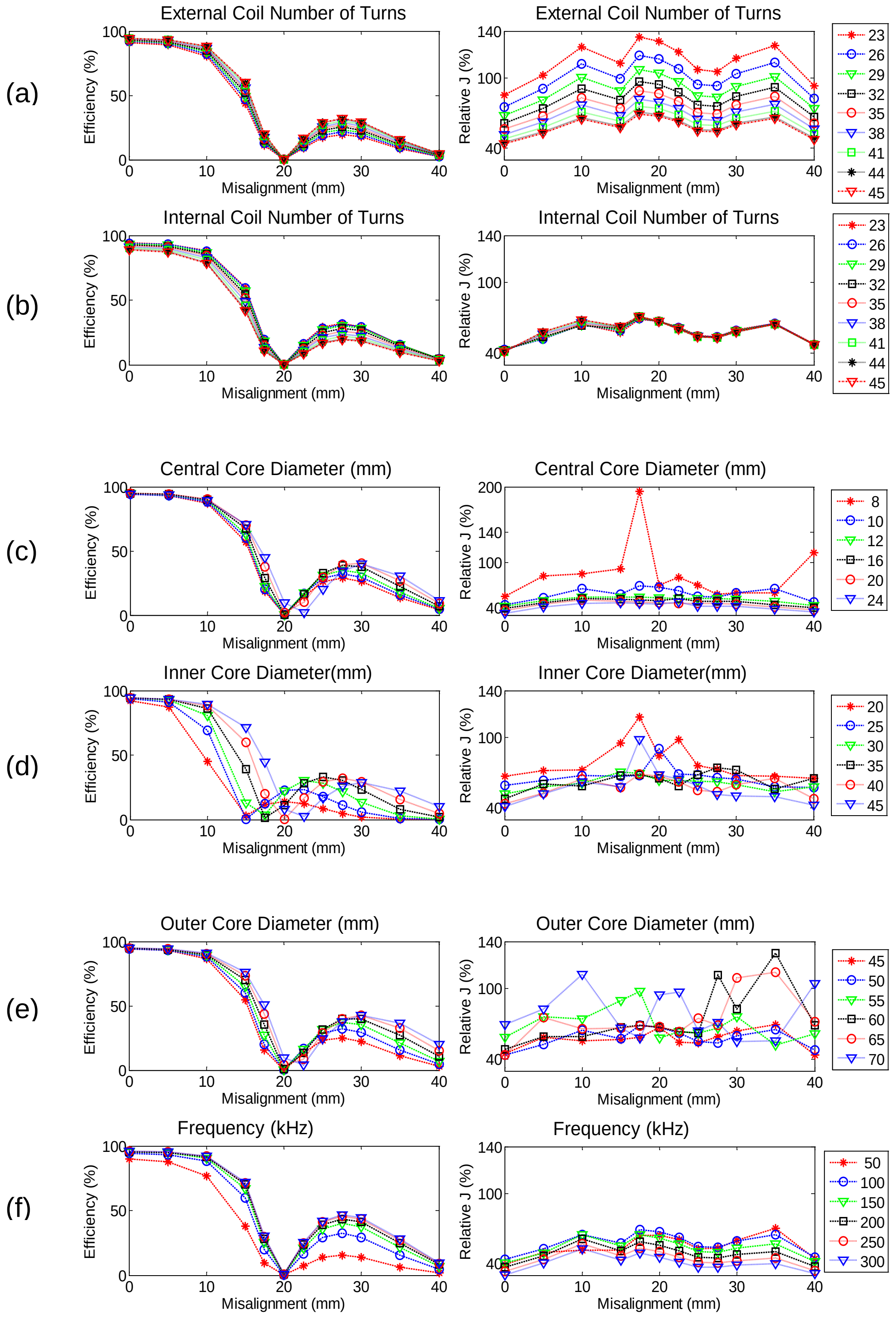

Observe that, when the inner diameter is 20 mm, the TET transformer reduces its efficiencies in about 40% by increasing its misalignment from 5 to 10 mm. This shows that the core inner diameter is determinant in the stability of the TET transformer.

Unlike the efficiency, in most of the cases, the relative current density deteriorates greatly with small misalignments of approximately 5 mm and then varies slightly with larger misalignments, even improving at larger misalignments. It is not easy to find a pattern of the behavior of the relative current density. However, Figure 4.29 shows that for misalignment of 17.5 mm, the relative current density is extremely high – the highest for most of the simulated configurations. This probably happens because the flux starts changing its direction at this misalignment.

Despite this value of misalignment, observe that the variation of the relative current density follows the same trend independent of the number of turns in the primary and secondary coils, frequency, and core central diameter. This trend cannot be observed when varying the inner and core outer diameter. Indeed, Figure 4.29(d) and Figure 4.29(e) show different curves following different trends depending on the size of the core inner and outer diameters.

This behavior can be understood by analyzing the chosen geometry at certain specific misalignment positions. For better perception, Figure 4.30 shows the qualitative effect of the induced current density in the skin for the default values of the dimensions when the coils are aligned as well as misaligned at the specific positions where the trend changes – 10 mm, 17.5 mm and 30 mm.

Figure 4.30 – Isovalues of the Induced Current Density when the coils are with different misaligning situations, such as (a) 0 mm; (b) 10 mm; (c) 17.5 mm; (d) 30 mm. TET transformer with 45 turns in the primary coil supplied by 24 V at 100 kHz and 23 turns in the secondary coil connected to a resistance of 18.75 Ω. Primary and secondary coils contain core type I with relative permeability 3000, 10 mm in the core central diameter, 40 mm in the inner diameter and 50 mm in the outer diameter.

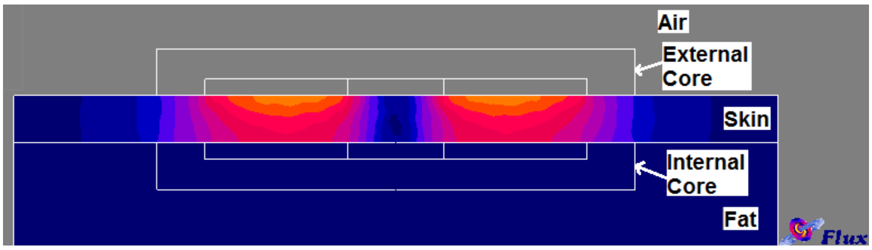

(a) 0 mm

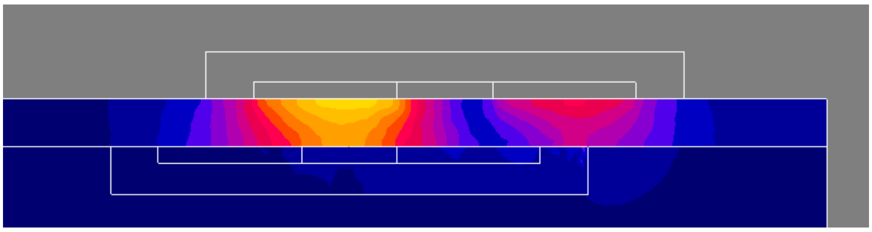

(b) 10 mm

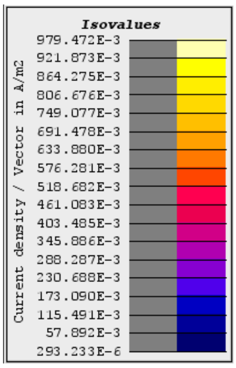

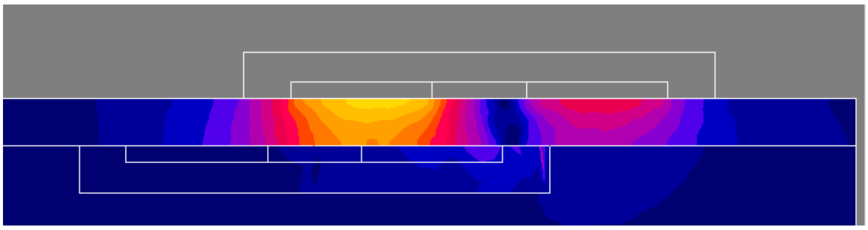

(c) 17.5 mm

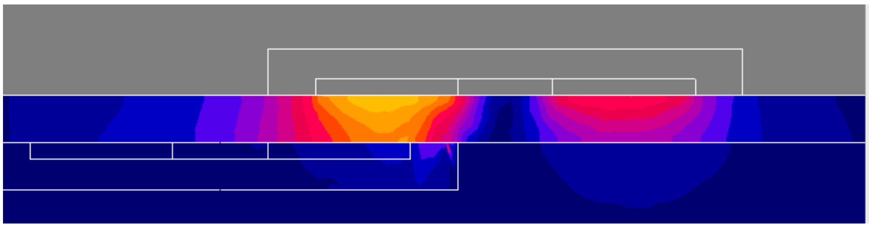

(d) 30 mm

Observe that, when aligned, the coils make the best coupling for this application, and thus lower induced current and higher efficiency are expected. When the misalignment starts, the coupling starts weakening thus worsening the efficiency and the current density induced in the skin. When the misalignment is just after 10 mm, the primary core has just finished facing the secondary core, as shown in Figure

4.30(b). For this reason, it is expected that the efficiency and relative current density at the skin deteriorate more by increasing this misalignment.

Nevertheless, as the central part of the primary core loses connection with the central part of the secondary core, it gets closer to make a better coupling with the outside edges (defined by the area between the inner and outer diameter). When the misalignment is close to 17.5 mm the central part begins to align with the outside edges, as shown in Figure 4.30(c). Thus, the TET transformer start having a different new magnetic circuit with smaller reluctance and, consequently, an improvement in the performance of the TET transformer is expected as can be observed in Figure 4.29 and Figure 4.30.

While the central part of the primary core is aligned with any magnetic part of the secondary core, the values of the efficiency should maintain similar values, depreciating again when the primary core loses magnetic coupling with the secondary core, what happens at 30 mm. This explanation also justifies why the worst values of relative current density occur when the core inner diameter is smaller than 30 mm or larger than 45 mm, what can be observed in Figure 4.29 by analyzing the performance of the TET transformer with the change of the core inner diameter.

It is noteworthy to mention that when the coils are misaligned, the value of the current density exceeds the limit established by ICNIRP only for some configurations and mainly when the primary coil has less than 32 turns.

Moreover, it can be concluded that the core outer diameter should not be larger than 55 mm because such configurations result in higher relative current density, even though better values are achieved when the misalignment is 17.5 mm. It is noteworthy to remember that, these analyzes are being performed only for core type I, as mentioned in the beginning of this section.

In addition to this analysis with geometric dimensions, this research also studied the sensitivity of the efficiency and induced current density at configurations with different core permeability in the range described by Table 4.7. Figure 4.31 shows this result.

Similarly, from Figure 4.31, the efficiency changes with the misalignment for core relative permeability above 30. For core permeability smaller than 30, the sensitivity of the efficiency with respect to the misalignment is slightly different, affecting more the efficiency at misalignments higher than 20 mm.

Figure 4.31 – Response of TET coils to the misalignment between coils at each simulated permeability. (TET transformer with 45 turns in the primary coil supplied by 24 V at 100 kHz and 23 turns in the secondary coil connected to a resistance of 18.75 Ω. Primary and secondary coils contain core type I with relative permeability 3000, 10 mm in the core central diameter, 40 mm in the inner diameter and 50 mm in the outer diameter.).

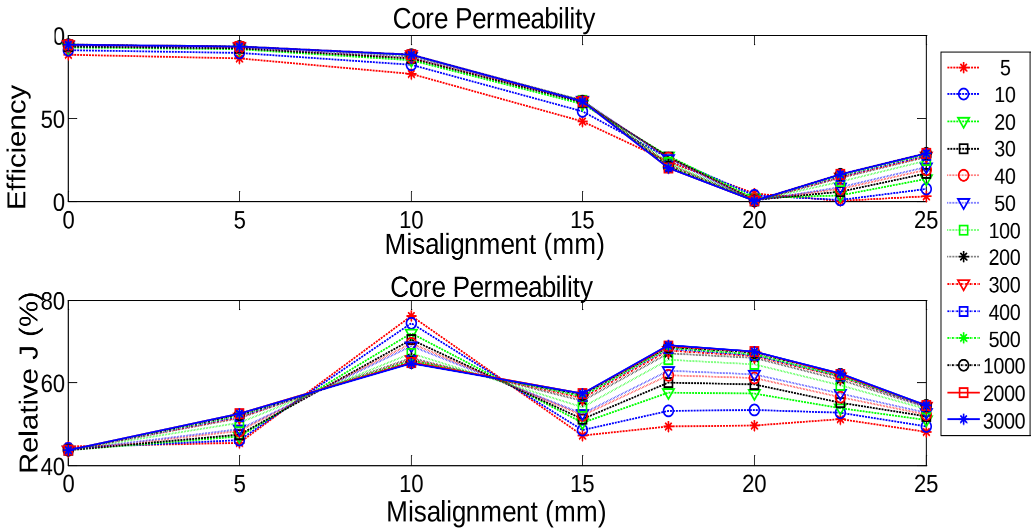

Regarding the relative induced current density, it has the highest variations with the misalignment when the core permeability has the lowest values. This means that the lower the core permeability is, the more sensitive the induced current density is to misalignments.

4.8 MISALIGNED COILS AT DIFFERENT COIL GAPS

Section 4.7 showed the behavior of the efficiency and relative current density according to the misalignments between the coils. The efficiency especially presents an interesting behavior when its value increases for misalignments slightly greater than the misalignment that nullifies it. However, this was analyzed at a specific coil gap while considering ferrite cores in both coils.

Here, several simulations considering coreless coils at different position situations, i.e., coil gaps and misalignments, were performed. The procedure described in Section 3.3 was used to compute the mutual inductance for each coupling position.

Figure 4.32 shows that, when the misaligned coils are separated by a certain distance, they have the same mutual inductance as when they are aligned at further distance.

Figure 4.32 – Mutual inductance of a TET transformer with 62 turns of wire AWG 19 in the primary coil and 24 turns of wire AWG 26 in the secondary coil at different coil gaps.

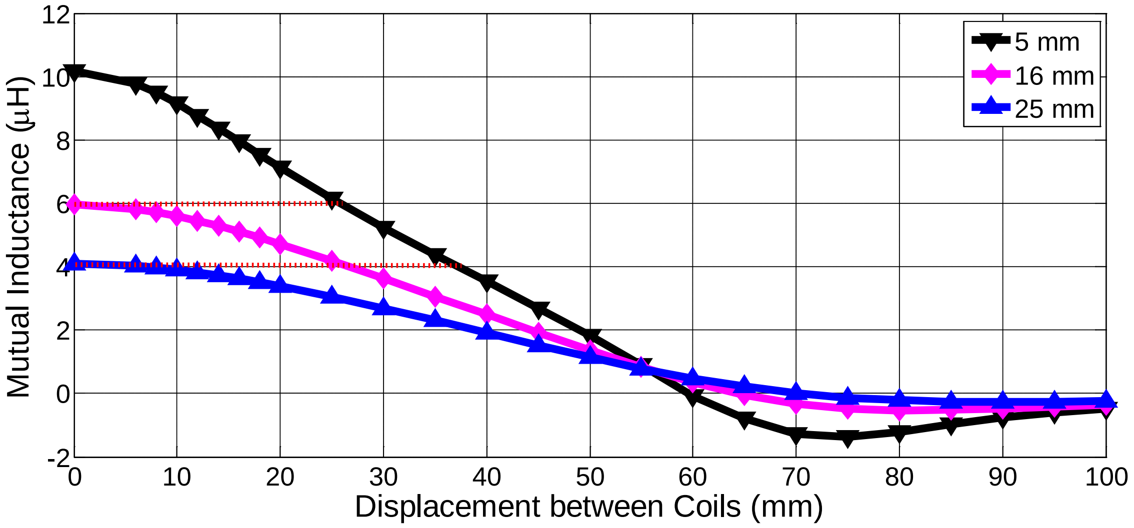

Observe the red dotted lines in Figure 4.32. They show that the mutual inductance and thus the coupling factor of the coils aligned and separated by 25 mm is the same when the coils are separated by 5 mm and misaligned by 37 mm. Moreover, this mutual inductance is also the same when the coils are separated by 16 mm and misaligned by 27 mm.

This observation can simplify the design process since the TET coils can be simulated through FE in axisymmetric 2D when the coils are aligned, avoiding the expensive computations of the FE 3D to simulate the misalignment.

Indeed, as mentioned in (LI et al., 2009), the coupling affects the maximum transference of power. Thus, if the coupling of the coils misaligned at certain gap is the same as the coupling of the coils aligned at larger gap, then the maximum transference of power is also going to be the same.

4.9 CONCLUSIONS

This chapter made different analyses considering virtual and physical prototypes.

The analysis of the behavior of the TET system related to the variation of load resistance facilitated a procedure to determine the value of the load resistance that would model the system composed of the AO and the regulator, i.e., the load resistance that consumes the power that would be consumed by the mentioned system.

The use of this variable resistance is very important during the design of the TET system because, as shown in the analyses with the physical prototypes, the use of a fixed resistor as the load is not enough to verify the complete behavior of the TET system.

This chapter also discussed the behavior of the temperature in the winding, pointing out that it cannot be ignored. Then, the use of larger wire gauge may be considered to try to minimize the effects of the temperature.

Moreover, for some configurations of the TET coils, the regulation is very high and thus the voltage at no-load is much higher than the voltage at the load resistance that consumes the required system power. This is another reason why the system should be designed at this value of load resistance, which would be the “nominal load”; otherwise, the voltage at this “nominal load” might not be within the limits required by a regulator converter.

The sensitivity analysis of the virtual prototype recommends the use of SRCs to improve the efficiency and mainly the regulation at the cost of higher SAR values that are still smaller than the maximum limit defined by ICNIRP.

However, when the SRCs do not exactly compensate the self-inductances of the coils, this load resistance also affects the behavior of the TET coils. Unfortunately, a SRC with the calculated value to precisely compensate the self-inductance is usually not a standard manufactured product, and thus the variation of the load resistance affects the resonant frequency of the system.

Analyses of physical and virtual prototypes suggested ferrite cores as a good option to increase the performance of the TET coils. The virtual sensitivity analysis recommended the “Hybrid PFSA” topology for having the best values of efficiency with acceptable values of regulation and SAR. These analyses led to the following observations:

- When increasing the frequency, the efficiency improves, but the regulation and the SAR get worse. However, it happens only for frequencies up to 200 kHz.
- The efficiency and the regulation improve with more turns in the primary coil and less turns in the secondary coil. The SAR improves with more turns in both coils.
- When the coil thickness and the core central diameter decrease, the efficiency and regulation improve, but the SAR worsens.
- The SAR improves, but the regulation and efficiency are not affected by decreasing the outer diameter of the core.
- With the increase of the core inner diameter, the efficiency improves. In this case, the regulation improves only if the secondary coil has a ferrite core. The SAR has a quadratic behavior with the variation of this diameter.
- The stability of the efficiency regarding misalignments is strongly dependent on the core inner diameter, getting worse as the diameter gets smaller.

All these analyses suggest the use of optimization methods to seek the best parameters that improve efficiency, regulation, SAR and relative current density.

However, a ferrite core with the desired geometry and dimensions is not always feasible. Trying to overcome this problem, a virtual sensitivity analysis studied the effects of the variation of the ferrite permeability in the efficiency and relative current density. A comparison among the performances of different types of core geometry of TET systems suggested that the use of a round core with the flat coil inserted in the core, as shown in Figure 4.25(I), brings the best efficiency at the lowest values of relative induced current density, which is one of the constraints for a safe use of the device. It was also observed when comparing the different geometries with different permeability of the material, what makes this type of geometry possible to construct even with materials that are not ferrite, such as plastic ferrites or magnetorheological fluids (SIMON et al., 2001).

In addition, a more thorough analysis of the recommended geometry investigated the behavior of this configuration in different sizes and for different positions of misalignment between the coils, observing the following:

- The stability of the efficiency is strongly dependent on the core inner diameter, getting worse as the diameter gets smaller.
- In order not to exceed the limits of the induced current density in the skin in the analyzed cases, the default primary coil must have more than 32 turns if the secondary core has 23 turns.
- The relative permeability of the core does not affect much the efficiency for values above 50, but the induced current density is more sensitive to misalignments when the relative permeability of the core is lower. Thus, the use of new materials with relative permeability as low as 50 is acceptable in this case.

Furthermore, this chapter studied the mutual inductance between coreless coils related to different misalignment values at different coil gaps. It was important to show that when the coils are misaligned and separated by some specific distance, they have the same mutual inductance that when they are aligned and separated by further distance. This observation may eliminate some use of 3D simulations if 2D simulations with larger coil gaps are performed.

In summary, this chapter pointed the following:

- The load resistance that accurately models the system composed of a regulator converter and the AO should follow the procedure presented in Section 4.2.
- The value of the load resistance affects the resonant frequency if the considered SRCs do not precisely compensate the self-inductances of the TET coils.
- The increase of temperature due to Joule losses in the windings cannot be ignored and can be indirectly included by the “thermo factor” introduced in Section 2.6.1.

- Different gauges of wire could support the minimization of temperature rise at the cost of the size of the coil.
- The use of SRCs improves the efficiency and mainly the regulation of the TET coils, but it worsens the SAR though the SAR values are still within the limits established by ICNIRP.
- TET systems with “Hybrid PFSA” showed to have the best values of efficiency and regulation with acceptable values of SAR.
- During the design of the TET system, the efficiency, regulation, SAR and relative current density could be improved by using optimization techniques with different geometrical and electrical attributes in the variables of decision (variables to be changed in order to get the optimal solution).
- Ferrite cores matching precisely the presented geometry are very difficult to find in practical applications, but other magnetic cores with different relative permeability, such as composites, plastic ferrite or magnetorheological fluids, could also be considered. According to the sensitivity analysis, the relative permeability of the core does not affect much the efficiency for values above 50, but the induced current density is more sensitive to misalignments at lower values of the relative permeability. Thus, the use of new materials with relative permeability as low as 50 is acceptable in this case.
- The 3D simulation may be replaced by 2D axisymmetric simulation during the optimization procedure if it considers coil gaps further than required.

Lastly, it is important to cite that the results and conclusions of this chapter were partially submitted in the following papers to the following conferences and journal:

1. “Screening a Transcutaneous Energy Transmitter”, accepted for oral presentation at MOMAG 2012 in Joao Pessoa, Brazil. The presentation of this paper got a prize of second best presenting paper.
2. “A Design Proposal for Optimal Transcutaneous Energy Transmitters”, accepted for poster presentation at COMPUMAG 2013 in Budapest, Hungary. The full paper was accepted on September 10th 2013 for publication in the IEEE Transactions on Magnetics.
3. “A Systematic Sensitivity Analysis of the Performance of a Transcutaneous Energy Transmitter for Design Purposes”, accepted for publication in the

Journal of Microwaves, Optoelectronics and Electromagnetic Applications (JMOe) in August 2013.

5 THE POWER ELECTRONIC CIRCUIT

5.1 INTRODUCTION

Three electronics converter systems are inspected in this research:

1. DC/AC converter: also called inverter. It is the circuit that transforms the DC power of the external battery to AC in order to transfer the energy through the coils.
2. AC/DC converter: also called rectifier. It is the circuit that transforms the AC power from the secondary coil to DC in order to recharge the internal battery and supply power to the AO.
3. DC/DC converter: also called regulator. It is a circuit to regulate the DC voltage on the AO and battery.

These converters will be briefly commented in this chapter, focusing on the electronic circuit components that were physically implemented to test the TET coils. However, this is a very deep subject which may require a lot of study. Hence, a more detailed research to improve these electronic circuits for the specific application of TET systems is recommended as future work.

Here in this chapter, only the basic simple electronic circuits to make a TET device work with a set of coils in the required conditions were implemented. These circuits were tested individually and with the coils in order to verify their behavior and rectify any problems that might arise.

It is also noteworthy that, since the AO requires 15 V, the DC voltage source must be able to operate over a range between 12 and 45 V. One feasible option of power supply would be 24 V which is the voltage used in electric wheelchairs, for example, and could be supplied by two 12 V batteries. This voltage would be converted by an electronic circuit to achieve constant AC voltage at the required level at the input of the primary coil. A hot-swappable system could be considered to aid in the process of replacing the battery. Moreover, additional functionalities such as protections against overvoltage, undervoltage or short-circuit could be proposed. However, this is also not the focus of this project, suggesting again another interesting line of research that seeks the best topology of source voltage and the protection for the equipment and patient.

5.2 ELECTRONIC CIRCUITS

Using many techniques in their design, the electronic circuits can be followed by regulators and/or amplifiers, also known as DC-DC converters, in order to maximize the transfer efficiency. Some techniques used in the literature include the use of amplifiers of class D (GALBRAITH; SOMA; WHITE, 1987) or E (MIZANNOJEHDEHI; SHAMS; MUSSIVAND, 2006; TANG; ZHAO; CHEN, 2010) or PWMs (Pulse Width Modulation) (DISSANAYAKE et al., 2009).

One proposal of a block diagram of a TET system using converters is shown in Figure 5.1.

Figure 5.1 – Basic Diagram of a TET system with converters.

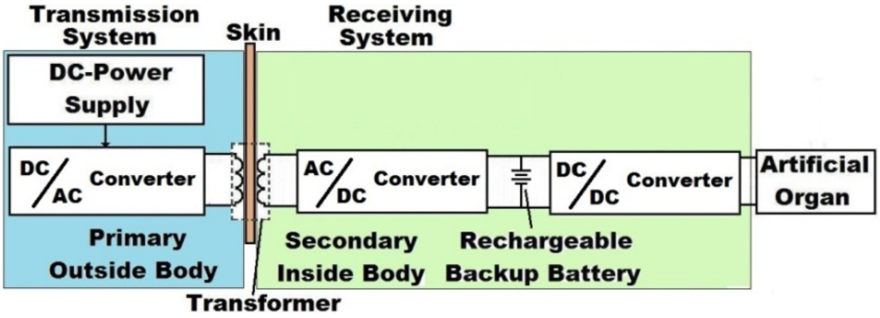

PWM is a technique of power control devices made of modern electronic power switches. The average voltage feeding the load of the inverter is controlled by fast switching. The voltage supplied to the load increases or decreases proportionally to the time that the switch remains enabled for the same time period.

The advantages of the PWM converters is the low component amount, high efficiency, constant frequency operation, relatively simple control and commercially available integrated circuits, and the ability to achieve high conversion rates for step-up and step-down voltage applications.

However, their disadvantages are the rectangular voltages and currents caused by the on and off switching of the semiconductor devices since switching losses often limit the operational applications to hundreds of kilohertz of frequency.

5.2.1 The DC/AC Converter - Inverter

Single-phase inverters can be found in topology of half or full bridge. Although its power range is low, they are widely used in voltage power supplies or single phase UPS. In this research, the full bridge topology, more specifically H-bridge, is analyzed.

The H-bridge topology consists of 4 switching elements (MOSFET, for example) as two half bridges in parallel, with the second bridge operating at 180^o out of phase.

There are several possible strategies to control 4 switches (H-bridge). This research used the strategy of doubling a half bridge and using the single command element of one half bridge inverted in relation to the single command element of the other half bridge, as shown in Figure 5.2.

Figure 5.2 – Implemented H-bridge inverter.

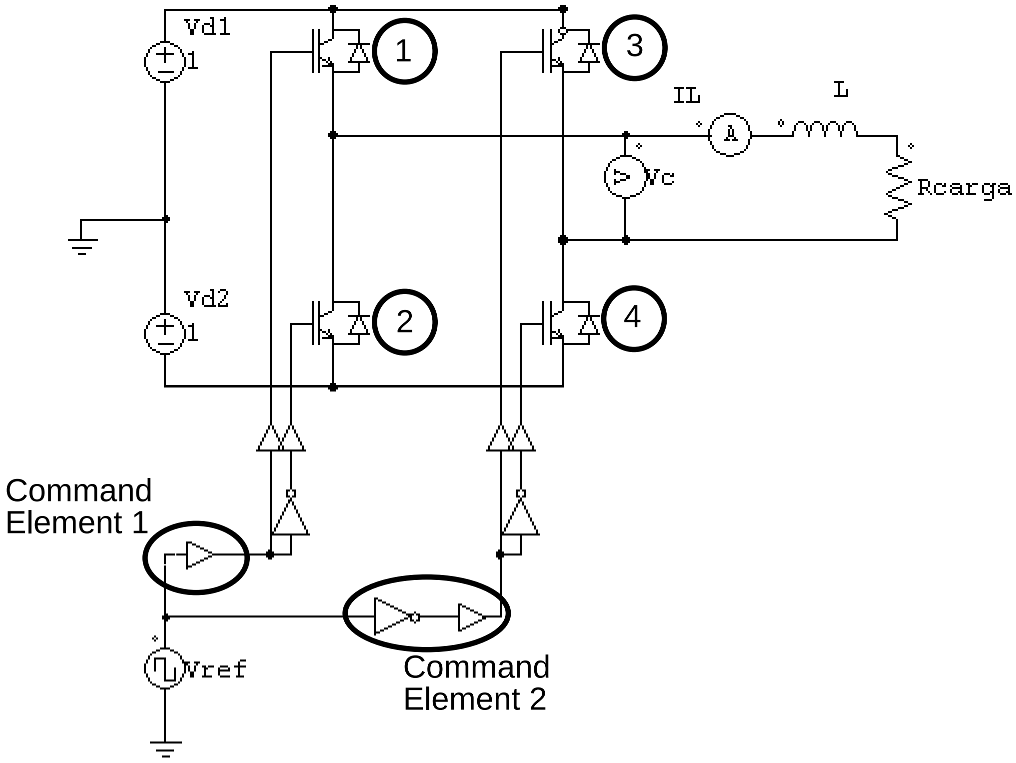

In the way how the command elements were used, the MOSFETs are triggered alternately depending on whether the reference signal is high or low. The continuous voltage V_{DC} at the input of the H-bridge allows the square output of the H-bridge to have two levels of voltage, $+V_{DC}$ (when the reference signal is high and the MOSFETs 1 and 4 are on) and $-V_{DC}$ (when the reference signal is low and the MOSFETs 2 and 3 are on). In this way, the value of the fundamental of the output voltage can be controlled.

In this research, the IRS20124(S)PbF was used for both command elements and the power MOSFETs IRLL2705 were used for the switching elements.

5.2.2 The AC/DC Converter – Rectifier

The AC to DC conversion must be done very carefully, because rectifiers or stages of regulation normally produce several harmonics and can represent an undesired source of energy loss. The diode rectifiers are usually full wave rectifiers and the use of capacitive or inductive filters to improve the voltage in its output is common. Those filters can be:

- DC filter inductor, preferred in high power applications because it reduces the form factor of the current of the rectifier making the transformers more efficient;
- DC filter capacitor that can provide a more efficient operation, but it is more suitable only for systems with low power consumption, wherein a more accurate regulation is normally achieved by an electronic regulator in cascade.

In this research, a full wave rectifier with a DC filter capacitor was used.

5.2.3 The DC/DC Converter - Regulator

The main functions of a regulator are:

- Convert an input DC voltage V_S to an output DC voltage V_o;
- Regulate the output DC voltage against variations in the source or the load;
- Reduce the ripple AC voltage on the output DC voltage to values lower than required;
- Isolate the input source from the load (not always necessary);
- Protect the provided system and the input source from electromagnetic interference.

The regulation is performed by measuring the output DC voltage, which generate a control signal to maintain the output signal as constant as possible.

A transistor regulator can act in its active region (linear voltage regulator) or as a switch in its cutoff or saturation region (switched voltage regulator).

The switched voltage regulator can be used in different configurations – Bulk, Boost, Buck-Boost, and Cuk. Those configurations can be isolated by combining the following classifications – Flyback, Forward, Push-pull (RASHID, 2001).

5.2.3.1 The driver SG3525A PWM

As observed in Section 4.2, the TET transformer may have no-load voltage much higher than the load voltage. In addition, during the switching of a regulator circuit, this circuit may present very high impedance. Thus, connecting the regulator to the secondary coil with the SRC in close loop may create situations in which the close loop would send a command to switch the regulator circuit in a way that its equivalent impedance could instigate a voltage on the secondary coil with the SRC higher than the maximum threshold limit of the regulator (if the no-load voltage is higher than this limit).

Thus, an optional DC/DC converter electronic circuit was developed with an open loop in order to verify its behavior with safety. The SG3525A PWM control circuit was used because it offers improved performance and lower external parts count when implemented for controlling all types of switching power supplies. Its representative block diagram is shown in Figure 5.3.

Figure 5.3 – Representative block diagram of the regulating PWM SG3525A.

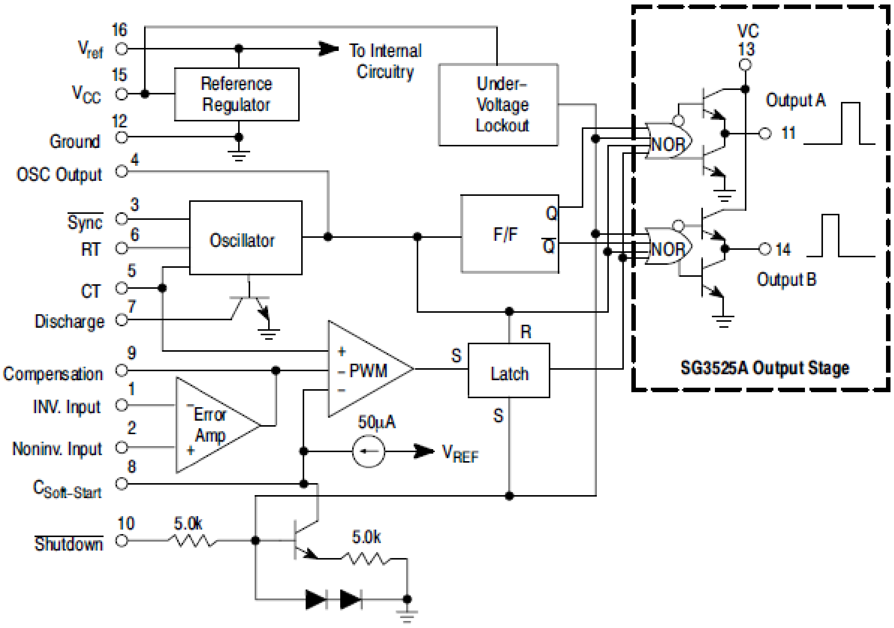

With this configuration, it is possible to control the duty cycle of the PWM by a potentiometer connected between the non-inverting input of the error amplifier and the reference signal. This allows changing the output of the converter manually as an open loop.

The SG3525A has a dual alternating output, which allow either single ended or push-pull applications. These outputs have complimenting output stages, allowing the control of two different switches and assuring that these switches would not be on at the same time. Since this research used SG3525A to control a buck regulator topology, which has only one switch, both outputs could be connected in parallel.

The recommended SG3525A operating supply voltage is between 8 and 35 V, even though its maximum voltage rating is 40 V. In this research, the SG3525A was connected to the output of the rectifier that converts the AC voltage from the TET coil to DC. Thus, the design of the coils should consider these limits in order to assure the perfect operation of the whole system.

The threshold voltage to trigger the MOSFET IRFP250N is 20 V, but the normal operation of the TET coil (*Vcc*) may reach up to 35 V (the recommended operating supply voltage of the driver SG3525A). Thus, the supply of voltage that will be transferred to the output of the driver (*Vc*) cannot be directly supplied by the TET secondary coil. Hence, a voltage regulator LM7812A was connected to the secondary coil with the SRC in order to convert its voltage into 12 V, supplying 12 V to the *Vc* input and the voltage of the secondary coil with the SRC to the *Vcc* input of the SG3525A.

The electronic diagram of the driver is shown in Figure 5.4.

Figure 5.4 – Driver electronic with SG3525A to command a buck converter with regulator for the input voltage.

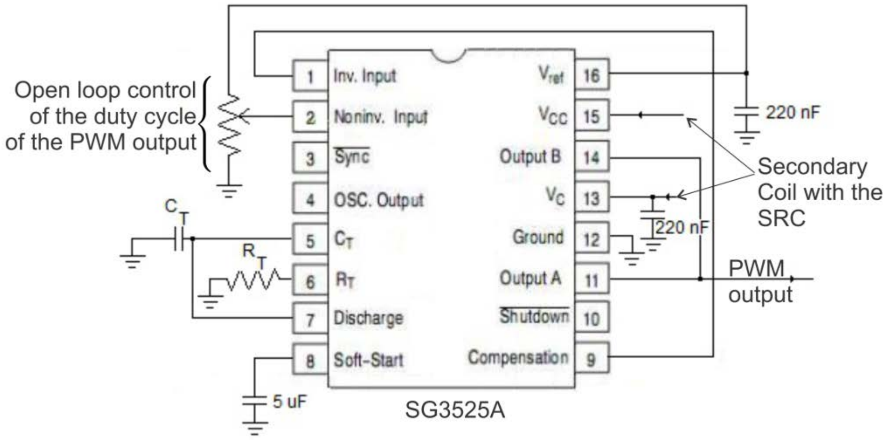

5.2.3.2 The buck converter

The described driver in Section 5.2.3.1 is the command element (PWM) to the gate of the MOSFET IRFP250N in the buck topology, shown in Figure 5.5.

Figure 5.5 – Buck topology.

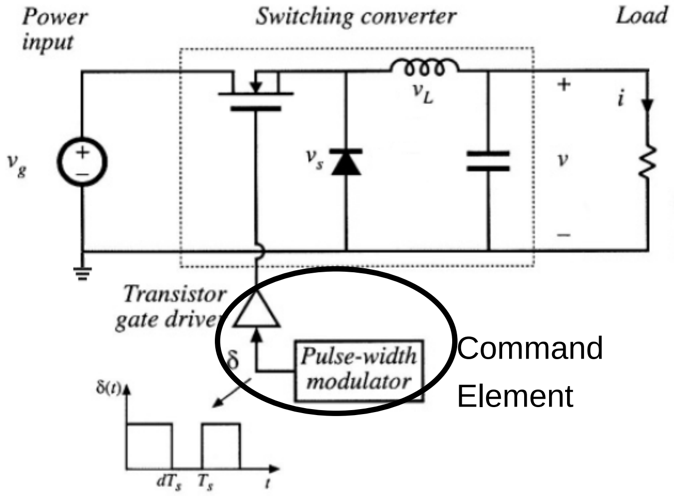

(ERICKSON; MAKSIMOVIC, 2004)

The PWM command element triggers the MOSFET, making it conduct for some time and not conduct for the compliment of the time. This MOSFET associated with the diode works as a switch that produces a rectangular waveform as shown in Figure 5.6(a).

Figure 5.6 – Voltage signal on (a) the diode; (b) inductor.

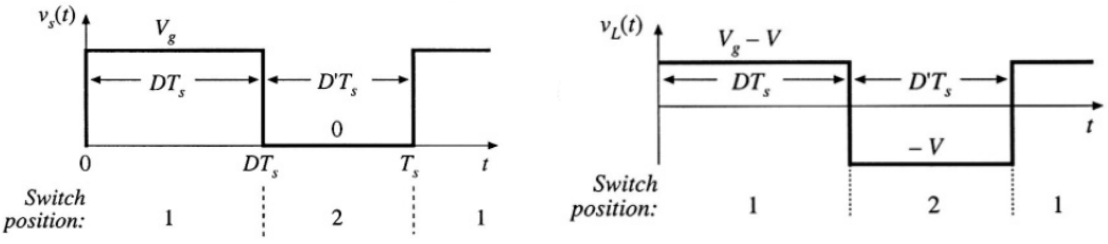

(a) (b)

(ERICKSON; MAKSIMOVIC, 2004)

When the MOSFET conducts (triggered by the PWM), the voltage on the diode (V_s) is equal to the DC input voltage *Vg* and thus the diode does not conduct. When the MOSFET is off, the diode conducts, thus connecting the inductor to ground (voltage equals zero).

5.3 BEHAVIOR OF THE BUILT INVERTER

The built inverter needs 3 inputs:

1. Input with 12 V to feed the components,
2. Input voltage depending on the value of the desired voltage in the output of the inverter,
3. TTL input with the frequency set point at which the output voltage of the inverter should oscillate.

In order to decrease the number of sources and make the manipulation easier, only one 12 V_{DC} power supply was used to feed the components and supply the voltage to be converted to high frequency voltage. A signal generator supplied the TTL input. Figure 5.7 shows the montage of the inverter system test.

Figure 5.7 – Inverter System Test.

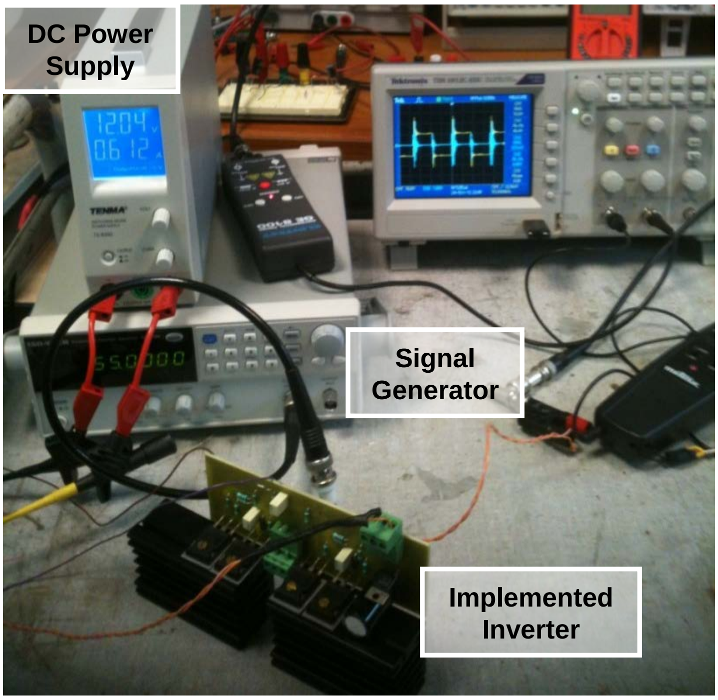

In this way, applying 12 V at the input of the inverter and 55 kHz in the inverter TTL input, the output of the inverter was a square wave of 55 kHz with 10.8 V_{RMS}, as shown in Figure 5.8.

Figure 5.8 – Voltage in the input (blue) and output (yellow) of the built inverter with no-load.

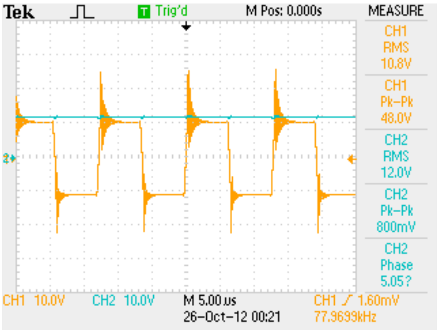

The blue line is the input of the inverter (12 V_{DC}) and the yellow line is the square wave output of the inverter (10.8 V_{RMS}).

5.4 BEHAVIOR OF THE BUILT COIL WITH THE RECTIFIER

Before connecting the rectifier to the output of the secondary coil of the TET transformer of Figure 3.20, the primary coil with SRC was connected to a signal generator with an amplifier to have its voltage controlled. In order to have neither too high voltage at the secondary coil nor too large current in the primary coil, the voltage at the primary coil was adjusted by measuring the voltage at the secondary coil when it had no-load. Therefore, 1.07 V_{RMS} was applied on the primary coil, as shown in Figure 5.9.

Figure 5.9 – Voltage (yellow) and current (blue) of the TET coils at no-load, measured at (a) the primary coil (35 turns with wire AWG 15 with a SRC of 170 nF) supplied by a signal generator with a linear amplifier and (b) the secondary coil (50 turns with wire AWG 15 with a SRC of 66 nF).

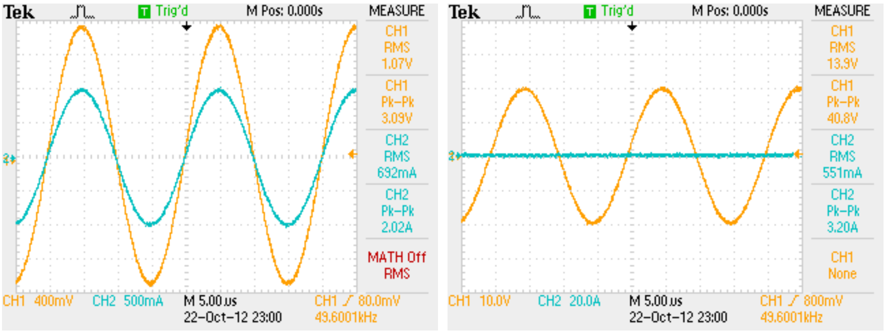

(a) Primary coil with the SRC

(b) Secondary coil with the SRC

Observe that, when the described TET primary coil was submitted to 1.07 V_{RMS}, its current was 0.7 mA and the voltage in the secondary coil at no-load was 14 V_{RMS}.

Then, the secondary coil with a SRC was connected at first to the rectifier with no-load and then to a resistance of 99 Ω, obtaining Figure 5.10.

Figure 5.10 – System with SRCs connected to the primary coil of 35 turns of wire AWG 15 and the secondary coil of 50 turns of wire AWG 15 supplied voltage to a rectifier (.1) at no-load and (.2) connected to 99 Ω. (a) Primary coil measurements (voltage (yellow) and current (blue)); (b) Secondary coil measurements (voltage (yellow) and current (blue)); (c) Rectifier measurements (voltage in the input (yellow) and output (blue)).

Primary coil with the SRC

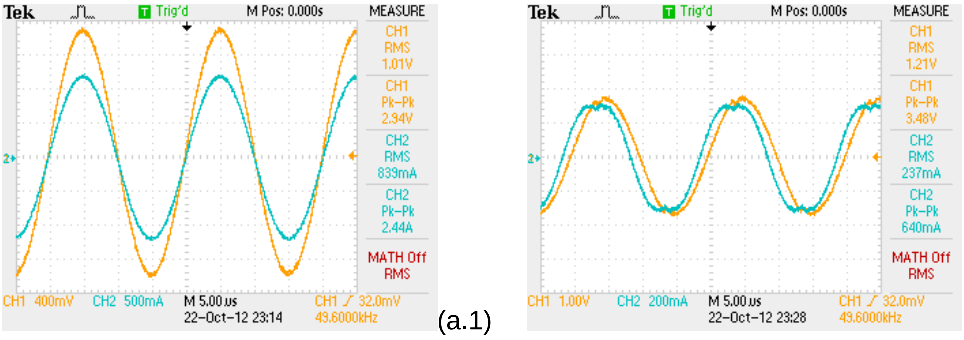

(a.1) (a.2)

No-load 99 Ω

Secondary coil with the SRC

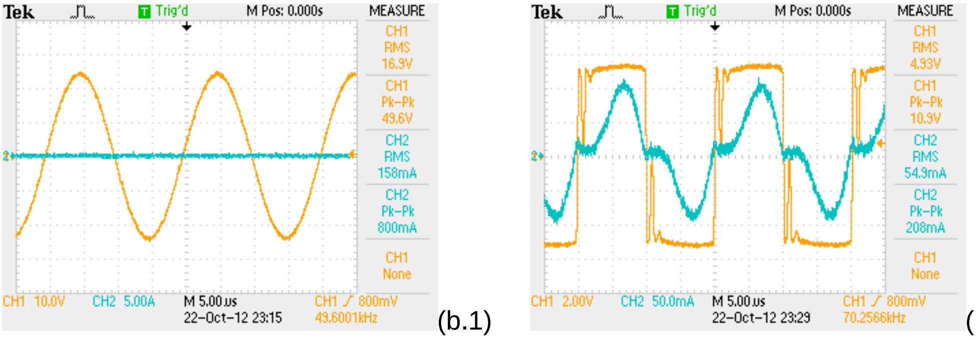

(b.1) (b.2)

No-load 99 Ω

Rectifier

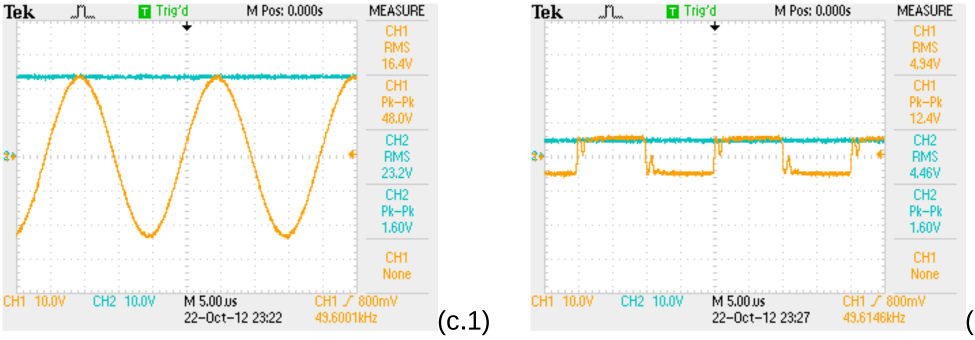

(c.1) (c.2)

No-load 99 Ω

Observe that, although the voltage at the primary coil is the same voltage used to feed the coils without rectifier, the secondary coil has no current and its voltage increased together with the current of the primary coil (Figure 5.10(a.1) and (b.1)). This can be explained by the filter capacitor connected at the output of the rectifier that represents a capacitive load.

When adding the resistive load of 99 Ω, the secondary coil (input of the rectifier) presents a square voltage and a current with undefined shape (Figure 5.10(b.2)), due to the harmonics created by the diodes. Even the voltage at the primary coil was slightly affected (Figure 5.10(a.2)). It is noteworthy that when the rectifier is supplied with an amplified signal from a regular signal generator instead the TET coils, the voltage at the input of the rectifier as can be seen in Figure 5.11 does not behave in the same way as shown in Figure 5.10(a).

Figure 5.11 – Rectifier supplied with an amplified signal from a signal generator and (a) at no-load (voltage (yellow) and current (blue) at the input of the rectifier); (b) at no-load (voltage in the input (yellow) and output (blue) of the rectifier); and (c) connected to 99 Ω (voltage (yellow) and current (blue) at the input of the rectifier) (d) connected to 99 Ω (voltage in the input (yellow) and output (blue) of the rectifier).

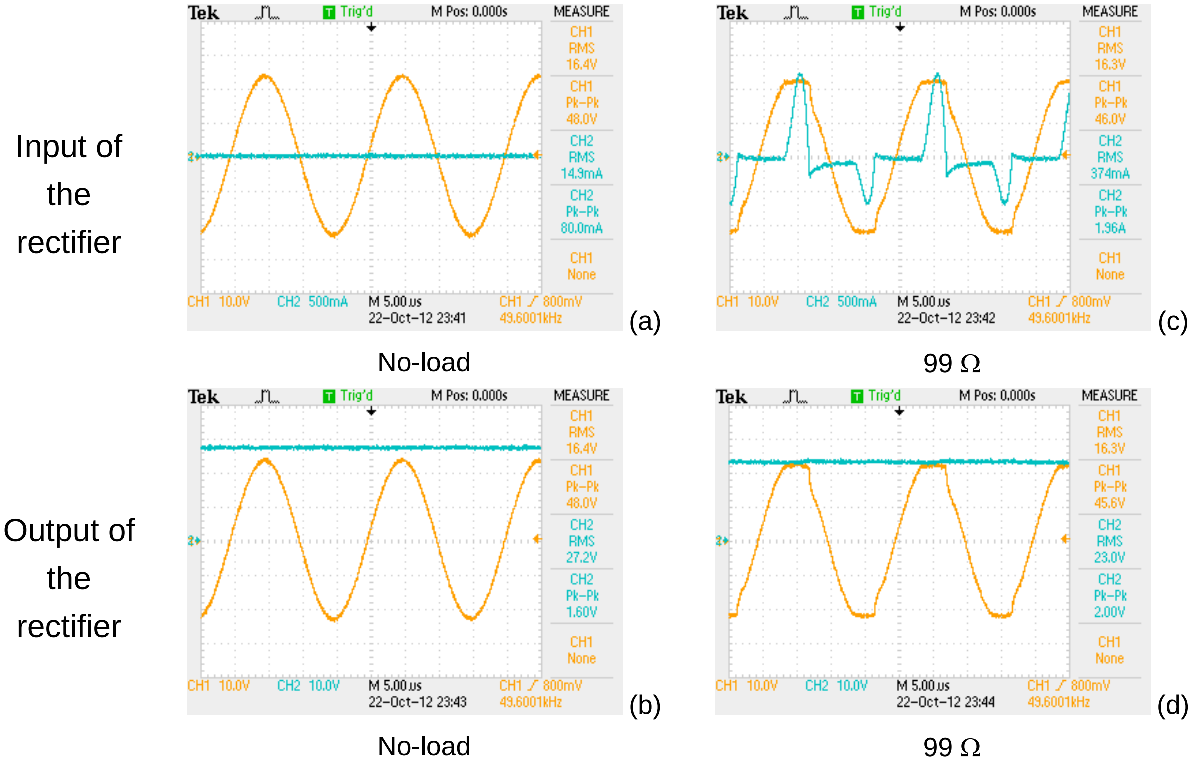

There is a small change in the load voltage (Figure 5.11(c)) when compared with the no-load voltage (Figure 5.11(a)), but this change is not as big as the change that happened when the rectifier is supplied by the TET coils with SRCs. That happened due to the fact that the signal generator amplifier is a voltage source and does not have the strong inductive effect present in the TET coils. When the rectifier was supplied by the coils, it had the mutual inductive effect that works as a filter when associated with the capacitor that was in the output of the rectifier. Thus, the input current was smoother and the voltage was squarer.

It is possible to calculate the capacitor value to be added at the output of the rectifier in order to make the current as sinusoidal as possible, however this strongly depends on the load resistance.

The previous measurements did not supply the required power. Thus, the voltage of the linear amplifier was increased to an RMS value of a square wave with peak equal to 12 V, implying a fundamental voltage equal to $12.\frac{4}{\pi}.\frac{1}{\sqrt{2}} = 10.8$ V_{RMS}. A load resistance of 66 Ω was then added to the output of the rectifier. Figure 5.12 shows this result.

Observe that although the input current of the rectifier was not completely sinusoidal, it was closer to a sinusoidal wave for this load value and its input voltage was even squarer in this case as well. In this situation, the output voltage of the rectifier was around 30 V_{DC}.

Figure 5.12 – System with SRCs connected to the primary coil of 35 turns of wire AWG 15 and the secondary coil of 50 turns of wire AWG 15 supplied voltage to a rectifier connected to 66 Ω. (a) Primary coil with the SRC measurements (voltage (yellow) and current (blue)); (b) Secondary coil with the SRC measurements (voltage (yellow) and current (blue)); (c) Rectifier measurements (voltage in the input (yellow) and output (blue)).

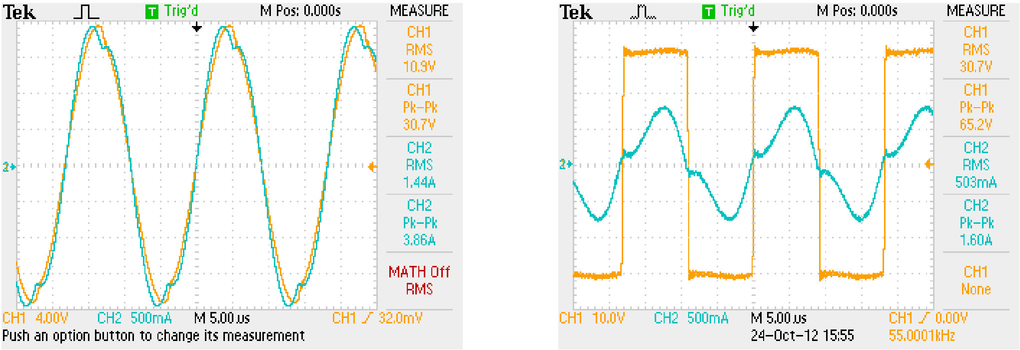

(a) Primary coil with the SRC (b) Secondary coil with the SRC

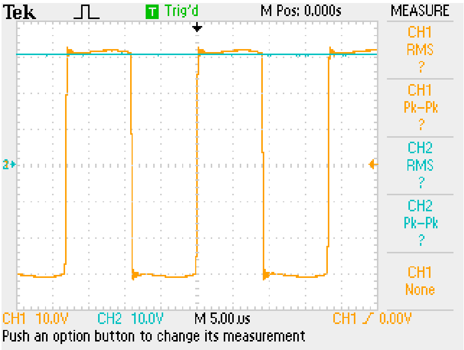

(c) Rectifier

5.5 THE COMPLETE SYSTEM WITHOUT REGULATOR

The whole system with inverter and rectifier but without the regulator was mounted together. Figure 5.13 shows the montage of the complete system test without regulator.

Figure 5.13 – Complete system test without regulator.

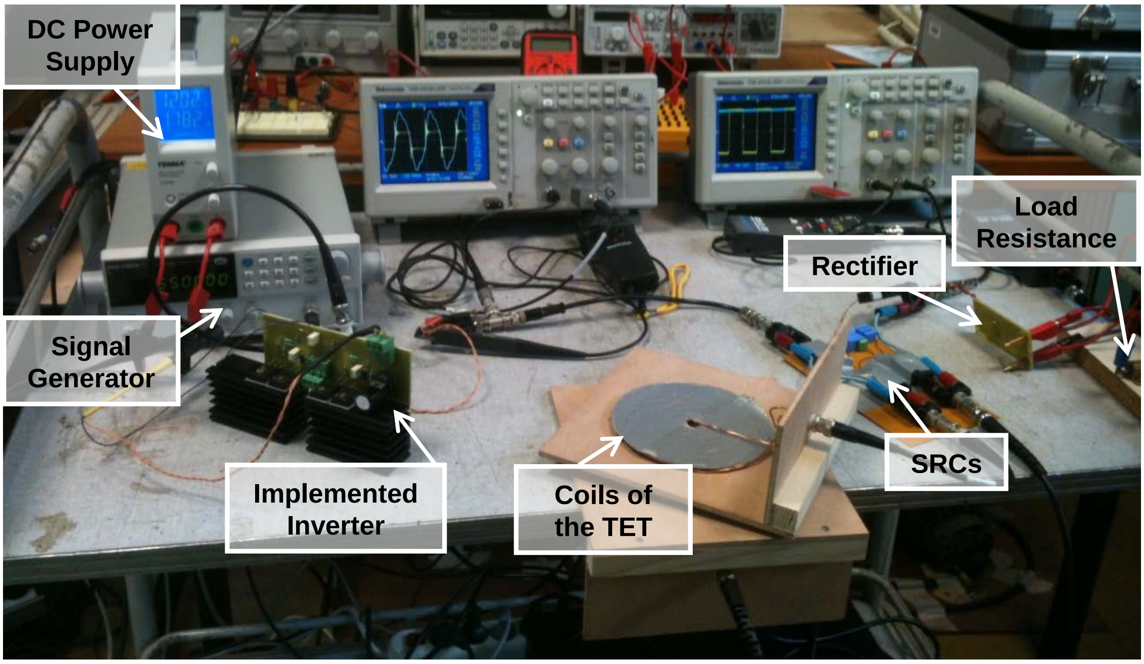

In this way, applying 12 V at the input of the inverter and 55 kHz in the inverter TTL input, the input of the primary coil was a square wave of 55 kHz with 10 V_{RMS} and the output of the secondary coil was a square wave with 26.4 V_{RMS}, as shown in Figure 5.14.

Figure 5.14 – Voltage (yellow) and current (blue) measured (a) in the input of the primary coil with the SRC (same as the inverter) and (b) in the output of the secondary coil with the SRC and with 66 Ω connected after the rectifier.

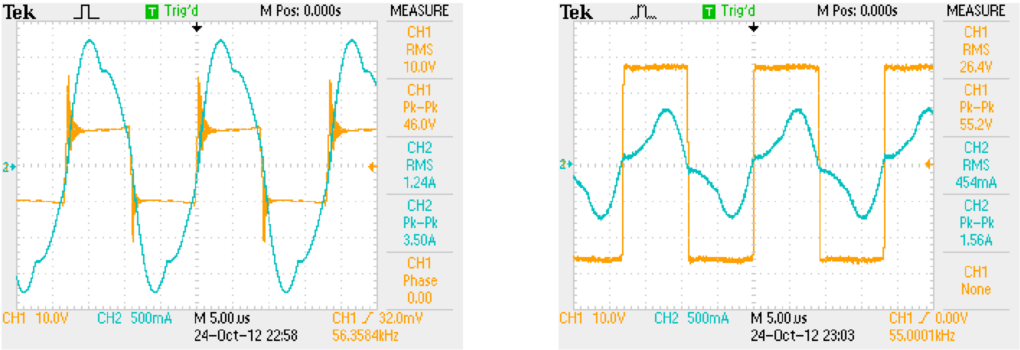

(a) Primary coil with the SRC (b) Secondary coil with the SRC

Note that with the whole system connected (excluding the regulator), the current supplied by the DC power supply to the inverter was 1.72 A at 12 V_{DC} and the voltage used by the resistance of 66 Ω was 25.9 V. Hence, the power supplied was 20.64 W and the power used by the resistance was 10.16 W, what means the system was working at 49 % efficiency when the coils were aligned with 5 mm distance.

It is also possible to define the efficiency of each element. The voltage at the input of the primary coil was square in phase with its almost sinusoidal current, as shown in Figure 5.14(a) (phase equal 0). For a square voltage, the RMS voltage value is the maximum voltage *Vmax*. Then, the RMS value of the sinusoidal fundamental voltage is $\frac{4}{\pi}.\frac{1}{\sqrt{2}}.Vmax \cong 0.9.Vmax$. From Figure 5.14(a), the RMS voltage at the primary coil with a SRC was 10 V, i.e., the fundamental voltage was 9 V_{RMS}. And the RMS current at the primary coil was 1.24 A. Hence, the power at the primary coil is 11.16 W. Thus, the efficiency of the inverter is 54 %. This low efficiency may be due to the dissipated power in the MOSFETs. In fact, MOSFETs dissipate a lot power into heat, reason why this circuit needs a very big cooler as shown in Figure 5.7. Therefore, inverters with higher efficiency for this application open another line of research for future work.

Following the same philosophy, the power at the secondary coil is 10.78 W. Hence, the efficiency of the inverter is 54 %, the efficiency of the TET transformer is 96.6 % and the efficiency of the rectifier is 94 %, what makes the total efficiency of the system equal to 49 %.

5.6 THE SYSTEM WITH REGULATOR IN OPEN LOOP

Since the built coil has an extremely high no-load voltage, a regulator in close loop may get damaged. This may happen because in close loop, the regulator may show extremely high impedance in some situations and this impedance creates a voltage higher than what may be acceptable by the regulator.

For this reason, a regulator in open loop was mounted. First, as described in Section 5.2.3.1, a driver was created and tested. Then, it was connected to trigger a buck DC/DC converter as described in Section 5.2.3.2. After testing and verifying that it works fine, the regulator was connected to the TET coils. Hence, after applying 12 V to the primary coil, the duty cycle of the PWM was adjusted by changing the potentiometer connected to the SG3525A till the load voltage achieved 15 V.

It is noteworthy that by changing the duty cycle of the PWM, the impedance seen by the coil changes and thus the resonant frequency is affected. For this reason, the system frequency was always adjusted to follow the resonance together with the duty cycle of the PWM.

Figure 5.15 shows the results of the voltage and current at the input of the primary coil and output of the secondary coil when the PWM was adjusted with a duty cycle that supplies 15 V to the load resistance of 16.5 Ω.

Note that the voltage of the primary coil with the SRC was sinusoidal at 12.1 V_{RMS} in phase with its current which was sinusoidal at 2.01 A_{RMS}. Hence, the power of the primary coil was 24.32 W. The secondary coil with the SRC had square voltage of 17.6 V_{RMS} (i.e., the fundamental voltage of this coil was 15.84 V_{RMS}) in phase with its sinusoidal current of 1.24 A_{RMS}. Thus, the power of the secondary coil with the SRC was 19.64 W. This means that the coils had an efficiency of 80.8 % when they were aligned with 5 mm distance.

Figure 5.15 – Voltage (yellow) and current (blue) measured (a) in the input of the primary coil with the SRC; (b) in the output of the secondary coil with the SRC; and (c) voltage in the in (yellow) the input of the buck converter after the rectifier and (green) in the 16.5 Ω connected after the open loop regulator.

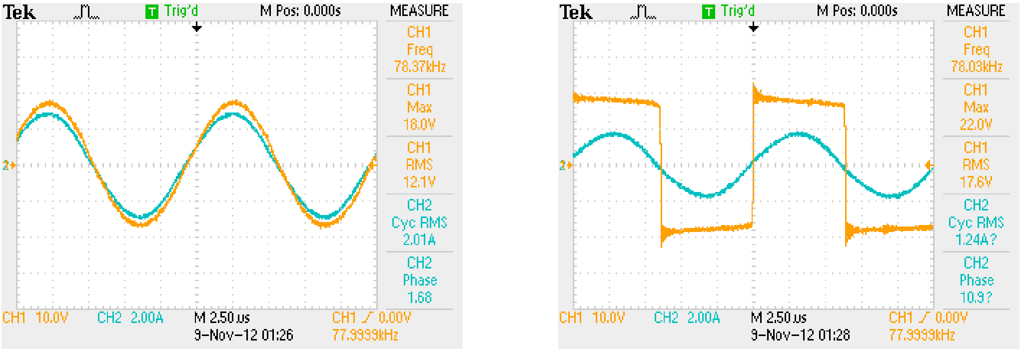

(a) Primary coil with the SRC (b) Secondary coil with the SRC

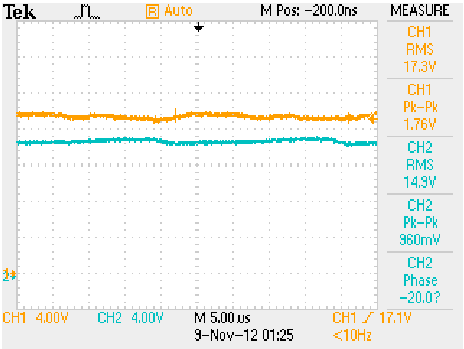

(c) Buck converter

Moreover, the voltage at the load resistance of 16.5 Ω was 14.9 V, as shown in Figure 5.15(c). Hence, the resistor was dissipating 13.4 W, what means that the rectifier plus converter group had an efficiency of 68.5 %. This efficiency is lower than expected for this regulator. This is due to the fact that the LM7812 dissipates a lot of power as heat. This should be investigated in future work.

Thus, the efficiency of the TET coils is 80.8 % and the efficiency of the rectifier plus converter is 68.5 %. Thus the total efficiency of the system is around 55 %.

Note that this efficiency does not include the inverter. In order to have the sinusoidal fundamental of 12 V_{RMS}, the inverter would need to supply 13.3 V square, what is more than what was tested in Section 5.5. However, if the efficiency of the inverter to convert 13.3 V square is the same as to convert 10 V (54 %), then the total efficiency of the system would be around 30 %.

5.7 CONCLUSIONS

This chapter discussed some aspects of electronic circuits which may be considered in a TET project. It briefly outlined the main blocks of electronic converters such as DC/AC, AC/DC and DC/DC converters, emphasizing the electronic components used in this research.

It was observed that all the electronic circuits have input thresholds and thus the design of the coils should consider them. The coils used for the measurements had a very high no-load voltage, much higher than the maximum threshold limit of the considered regulator. Thus, connecting the regulator in close loop with the secondary coil with the SRC could instigate voltage higher than the threshold limit of the regulator resulting in damaging it. For this reason, this research studied the behavior of a regulator in open loop instead of close loop.

With all the observations of this chapter, the following important aspects should be contemplated during the design of the TET system:

1. The voltage of the secondary coil that will be supplied to the regulator must be within the threshold limits of 8 and 35 V.
2. The no-load voltage of the secondary coil must not exceed the maximum acceptable voltage of the regulator, which is 40 V.
3. Since the regulator has an efficiency of 68.5 %, the coils should be designed for supplying a power of 19 W.

The graphs and results from the measurements showed that the selected coils with the implemented electronics were able to supply more than the power required by the

AO, but with low efficiency of approximately 30 % for the complete system or 55 % excluding the inverter.

Note that the efficiency is low, mainly due to the converters. The losses due to the DC/AC converter are outside the patient. Thus, although it has low efficiency and must be improved, it does not cause heating in the body of the patient. However, the losses in the DC/DC converter are more problematic since the converter is inside the body of the patient and any heating losses create discomfort.

The built inverter presented an efficiency of about 54 % while the regulator presented an efficiency of around 68 %, both being very low efficiencies. Thus, among all observations, this chapter suggested interesting future lines of researches since it was not the focus here:

- DC/AC electronic circuits with higher efficiency for the application of the TET system.
- DC/DC electronic circuit without another DC/DC element (LM7812A) to use different levels of voltage in the circuit, trying to improve the efficiency of the complete regulator circuit of the TET system. The close loop DC/DC converter is also part of this future work since, in this research, the regulator used was in open loop.
- Electronic circuits with alternative source voltage and protection for the equipment and the patient, as mentioned in the introduction of this chapter.

6 OPTIMIZATION

6.1 INTRODUCTION

As remarked in Chapter 4, the design of the TET system can be expressed as an optimization process. For this reason, this chapter explores two different philosophies of optimization with different software applications, Flux-2D and Gmsh/GetDP.

First, this chapter summarizes the data that are important to be considered, according to what was presented in the previous chapters, explaining and justifying the optimization methods utilized.

Then, this chapter introduces the first optimization procedure implemented to work with simulations in Flux-2D. This procedure used the Kriging method (LEBENSZTAJN et al., 2004) to interpolate functions that model the attributes to be optimized. In this case, configurations with “Ferrite cored” topologies considering small gauge wire and the use of SRCs were optimized in order to attain the best efficiency, regulation and SAR while supplying power to a constant resistance of 18.75 Ω. The power of 12 W was one of the constraints of this optimization and the results, along with the relative current density, were then analyzed.

Afterwards, configurations of “Coreless” topology are optimized via Gmsh/GetDP. In this case, different wire gauges were evaluated considering the proximity and skin effects. The optimization was directly executed with FE interaction without the need for Kriging approximations. Then, this optimization minimized the volume and “thermo factor” by searching for configurations that supply constant power of 19 W, while considering the limits of the studied electronic circuits from Chapter 5 and the concept of variable resistance introduced in Section 4.2. This optimization also considered different coil gaps as constraints.

At the end, this chapter makes a brief conclusion, reiterating the analyses that were already made for each optimization procedure, showing their advantages and disadvantages.

6.2 STRATEGY OF OPTIMIZATION

Considering all the analyses from the previous chapters, there are many factors that may affect the behavior of a TET system and thus should be examined during its design. Table 6.1 summarizes:

- the variables of decision – variables of the TET system that affect its behavior and could be changed during its design in order to support the decision of choosing a configuration;
- the criteria of decision – attributes which should be evaluated during the design of the TET system and that may be affected by changing any variable of decision;
- the variables of disturbance – variables that may be expectedly or unexpectedly modified during the operation of the TET device affecting the proper behavior of the chosen configuration.

For the process of optimization, the genetic algorithm (GA) (GOLDBERG, 1989) from the optimization tool of Matlab version 7.6.0.324 (R2008a) was used since it is a reliable method for solving both constrained and unconstrained optimization problems. Although this stochastic algorithm never produces the same results, it has some inherent mechanisms to escape from local minima.

Table 6.1 – Variables to consider in the process of the design.

Variables of decision	Criteria of decision	Variables of disturbance
Number of turns (Primary Coil) Number of turns (Secondary Coil) Primary Coil Wire Gauge Secondary Coil Wire Gauge Frequency Source Voltage Primary Core Permeability Secondary Core Permeability Primary Core Outer Diameter Secondary Core Outer Diameter Primary Core Central Diameter Secondary Core Central Diameter Coil Thickness	Weight Volume Relative induced current density SAR “Thermo factor” Required load and no-load voltage Load power	Coil gaps Coil misalignments Angle between coil plans

This algorithm repeatedly modifies a population of individual solutions. At each step, it selects random individuals from the current population to be parents and uses them to produce the children for the next generation. Over successive generations, the population "evolves" towards an optimal solution.

The genetic algorithm, which is more detailed in APPENDIX F, uses three main operators at each step to create the next generation from the current population:

- Selection operator selects the individuals, called parents, which contribute to the population of the next generation.
- Crossover operator combines two parents to form children for the next generation.

- Mutation operator applies random changes to individual parents to form children. It provides genetic diversity and enables the genetic algorithm to search a broader space.

6.3 OPTIMIZATION WITH KRIGING AND FLUX-2D

Initially, the optimization was performed with multiple objectives trying to maximize the efficiency while minimizing the SAR and regulation, and assuring that the power delivered to a load resistance of 18.75 Ω is greater than or equal to the desired power of 12 W. It is noteworthy that, as observed in Section 4.5 and Section 4.6, the improvement of one requirement in general results the degradation of the other requirements. This is a typical behavior of optimization problems with multiple objectives.

Here in this section, the optimization process used the same geometry shown in Figure 3.6 and the limit values depicted in Table 4.6 to vary the number of turns of the primary and secondary coils, coil thickness, core central diameter, source voltage and frequency.

The design of a TET system through the optimization methods of this section required some of the criteria of decision to be optimized and some to be used as constraints for the different configurations chosen from the variables of decisions. In the first approach, the optimization process used:

- efficiency, regulation and SAR as criteria of decision;
- load power as constraint;
- number of turns of the primary and secondary coils, coil thickness, core central diameter, source voltage and frequency as variables of decisions.

Note that, although in the previous sensitivity analysis from Chapter 4, the SAR was observed to always be below the limits established by ICNIRP, it was used as criteria of decision in order to minimize its value. By minimizing the SAR, the current density is also expected to be indirectly minimized.

In the case of this research, the use of the Flux-2D application together with Matlab proved to be slow and difficult to implement. Thus, one way to overcome this numerical problem is via approximation functions, a technique widely studied in the electromagnetism community. One of the most popular approximation functions is called Kriging (LEBENSZTAJN et al., 2004).

Kriging is a technique used for minimum error variance estimation, which employs concepts of interpolation and radial basis functions. It uses:

- a set of polynomials ($p(x)$) which is intended to follow the general tendency of the function to be modeled;
- a set of Gaussians ($h(x)$) that makes it possible to follow the fluctuations around the general tendency.

Therefore, the model can be mathematically written by

$$\mathrm{y(x)} = \mathrm{c}^T \mathrm{p(x)} + \mathrm{w}^T \mathrm{h(x)} \tag{6.1}$$

In this equation, w^T and c^T are the weights for each Gaussian and polynomial respectively, which could be found by processing a set of data.

In this section, this research used the Universal Kriging which allows an improvement in the accuracy of the model as compared to Ordinary Kriging which imposes a constant value to $p(x)$. The Universal Kriging assumes that the trend ($c^T\, p(x)$) can be written as a linear combination of known functions, determined by the physics of the problem being dealt with. Since this is not easy to achieve, a second-order polynomial (full quadratic model, for example) is performed. Then the stochastic portion of (6.1) ($w^T\, h(x)$) could be calculated.

Hence, all the configurations simulated in Section 4.6 could be used as inputs (set of data) of the Kriging algorithm to create a model to be used in the optimization process. However, since the amount of simulated data was too large, a specific number of randomly chosen samples were used as the input of the Kriging algorithm to evaluate the model of efficiency, regulation, SAR and load power with the respective parameters varied during the multiparametric analysis.

The RSTool from Matlab can be configured to model the supplied data as a second order polynomial function and provide the parameters of this function together with its deviation from the supplied data. Hence, this research used the *RSTool* from Matlab to aid the Kriging method process. This was done by first inserting the chosen sample data (simulated by Flux-2D) into *RSTool* from Matlab to obtain a full quadratic model and its residuals for efficiency, regulation, SAR, and load power. Then, the full quadratic model from *RSTool* represented c and $p(x)$ of (6.1) and the residuals from *RSTool* were used to obtain the Gaussian tendency parameters, w^T and $h(x)$ of (6.1).

The two data sets for “Ferrite cored” TET systems with and without SRCs collected in Section 4.6 were used in this section to perform optimization searches.

In order to ascertain the attained models, the efficiency, regulation, SAR, and load power of both configurations (with and without SRCs) were estimated through this Kriging approximation functions for all the simulated configurations and compared with their simulated values in the data set. It was expected that the estimation through the Kriging functions match the simulated values for all configurations randomly chosen to create the Kriging functions. However, it was uncertain that it would be the same for the other simulated configurations.

Figure 6.1 shows the relative estimated errors from the efficiency, regulation, SAR, and load power for all configurations, with and without SRCs. Each point represents a simulated configuration even if it was not used to support the Kriging model.

Figure 6.1 – Percentual error of the Kriging model compared to the simulation with Flux-2D for efficiency, regulation, SAR and load power. Each point on the abscissa represents each configuration of a sample combining parameters according to Table 4.6.

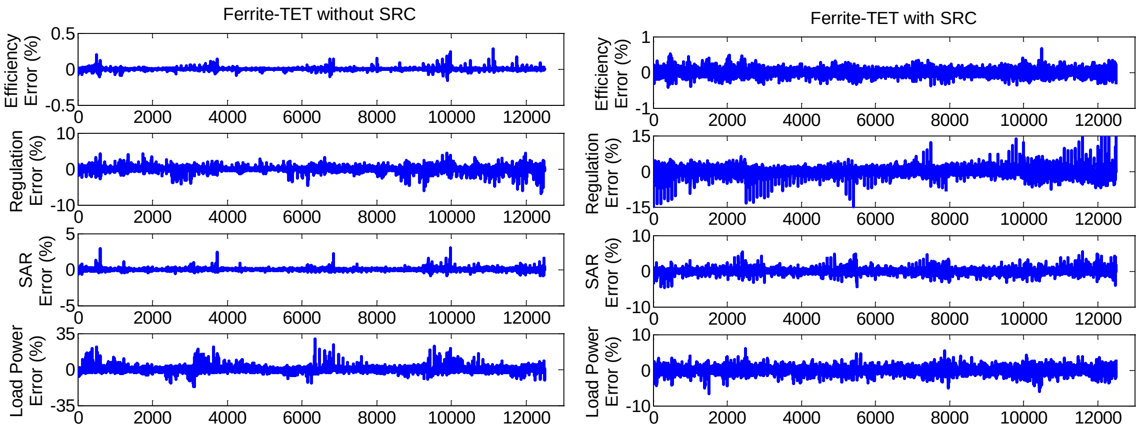

It is noteworthy that in both cases, with and without SRCs, the model of the efficiency, regulation, SAR and load power did not necessarily use the same simulated configurations to be created. Since the configurations used to generate the model were randomly chosen, such configurations may have been chosen different for each model yet with the same amount of samples.

Observe that the Kriging approximation model was very accurate, mainly for the efficiency in the configurations without SRCs, in which the errors were smaller than 0.5 %. The worst model was for the load power in the configurations without SRCs, in which some errors reached 35 %. However, since this model is used only for constraints in the optimization process (as will be seen ahead), this error did not represent a big issue. In the configuration with SRCs, the worst model was for regulation, in which some errors reached 15 %, but even in this case, the average error was smaller than 10 %. Therefore, the model is consistent and can be used to support the objective function in the optimization process.

After the model was created, the multiobjective genetic algorithm (MGA) from Matlab was used to optimize the efficiency, regulation and SAR with less computational cost. Here, constraints such as minimal load power and coil area were inserted by the use of penalty functions as in (VIEIRA et al., 2004):

1. the load power should always be bigger than 12 W;
2. the region reserved to allocate the primary and secondary coils (the green region in Figure 2.3) should have space enough to fit all the turns of the coils.

Thus, the objective functions of the MGA were to minimize:

$$\begin{cases} F1 = -Efficiency\ Model + 10.(Penalty\ Function) \\ F2 = Regulation\ Model + 10.(Penalty\ Function) \\ F3 = SAR\ Model + 10.(Penalty\ Function) \end{cases} \tag{6.2}$$

In (6.2), the efficiency, regulation and SAR models are the respective models attained from the Kriging method and the penalty function is the sum of the following functions:

- Penalty function for the load power: if the estimated modeled load power was smaller than the desired power (12 W), the difference between both was the penalty function. Otherwise, the penalty function was zero. This value was normalized by dividing it by 12.
- Penalty function for the available region to allocate the primary coil (the top green region in Figure 2.3): the available area ((core inner diameter – core central diameter)*coil thickness) should be bigger than the number of turns times the cross-section of the considered wire (0.08 mm^2). Hence, if the available area is smaller than the coil area, the difference between both areas was the penalty function. Otherwise, the penalty function was zero. This function was also normalized by dividing its value by the area of the coil.

- Penalty function for the available region to allocate the secondary coil (the bottom green region in Figure 2.3): the same procedure used for the primary coil was used here by considering the parameters from the secondary coil instead the primary coil.

Moreover, since the regulation values were extremely high, an extra penalty function was added in order to strength its minimization. If the estimated modeled regulation was bigger than 100 %, this penalty function was the excess of 100 %; otherwise, it was zero.

Thereby, a set of 32 different configurations for TET systems with and without SRCs was the result from the MGA technique. In the optimization literature, these configurations are called non-dominated set or Pareto set.

As the optimal set of parameter was obtained using a surrogate function and the numbers of turns from these results were not integer, there was uncertainty in the validity of these data. Thus, the configurations recommended by the non-dominated set was analyzed through new simulations in the Flux-2D, considering the integer numbers of turns and the fewer decimal cases on the geometric parameters in order to verify the actual value of the efficiency, SAR, current density and load power.

Figure 6.2 presents the values of the efficiency, regulation, and SAR obtained from the Kriging model and the Flux-2D application for all individuals in the non-dominated set. Observe that the Kriging model had very good reliability even for the non-dominated set that contains configurations which were not used to create the Kriging function model.

Figure 6.2 – SAR, efficiency and regulation - Comparison between data calculated in Flux and estimated from Kriging model. Each point on x axis represents each configuration on the non-dominated set, selected by MGA.

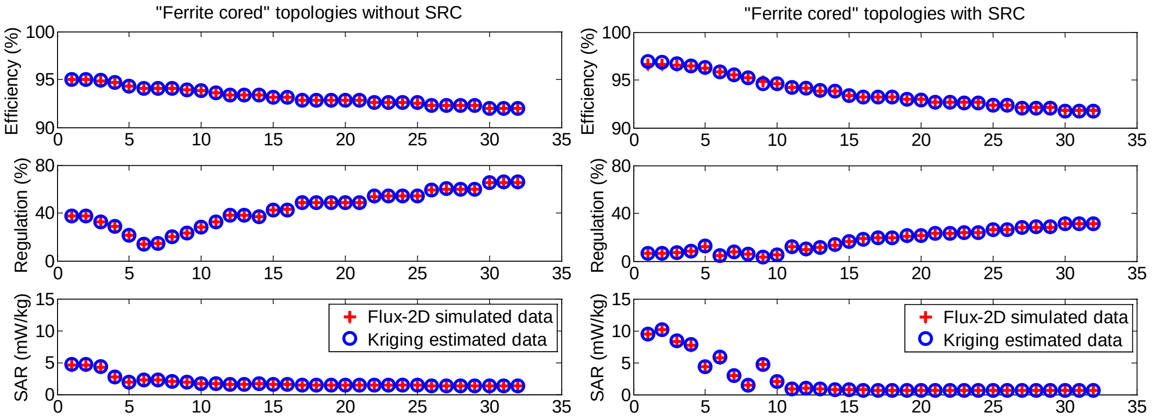

All these configurations fulfill the 12 W power requirement and are possible to be constructed mechanically, but each one has different results of efficiency, regulation, SAR and current density. For some configurations, the efficiency is better, whereas for others, regulation and/or SAR are better.

Observe that, in the non-dominated set with SRCs, the efficiency is slightly higher and the regulation is much smaller compared with the non-dominated set without SRCs, in which the best regulation is 15 %. However, the SAR is much smaller in the configurations without SRCs than in the set with SRCs. Even though, no configuration exceeded the SAR limit of 0.4 W/kg established by ICNIRP, as presented in Section 2.6.3.

Figure 6.3 shows the correlation between the efficiency and each of the SAR, regulation and relative current density for all configurations of the non-dominated sets found by the optimization algorithm that was executed for TET systems with and without SRCs.

Figure 6.3 – Values of SAR, regulation, and relative current density comparing with efficiency for the configurations of the non-dominated sets attained from MGA with and without SRCs.

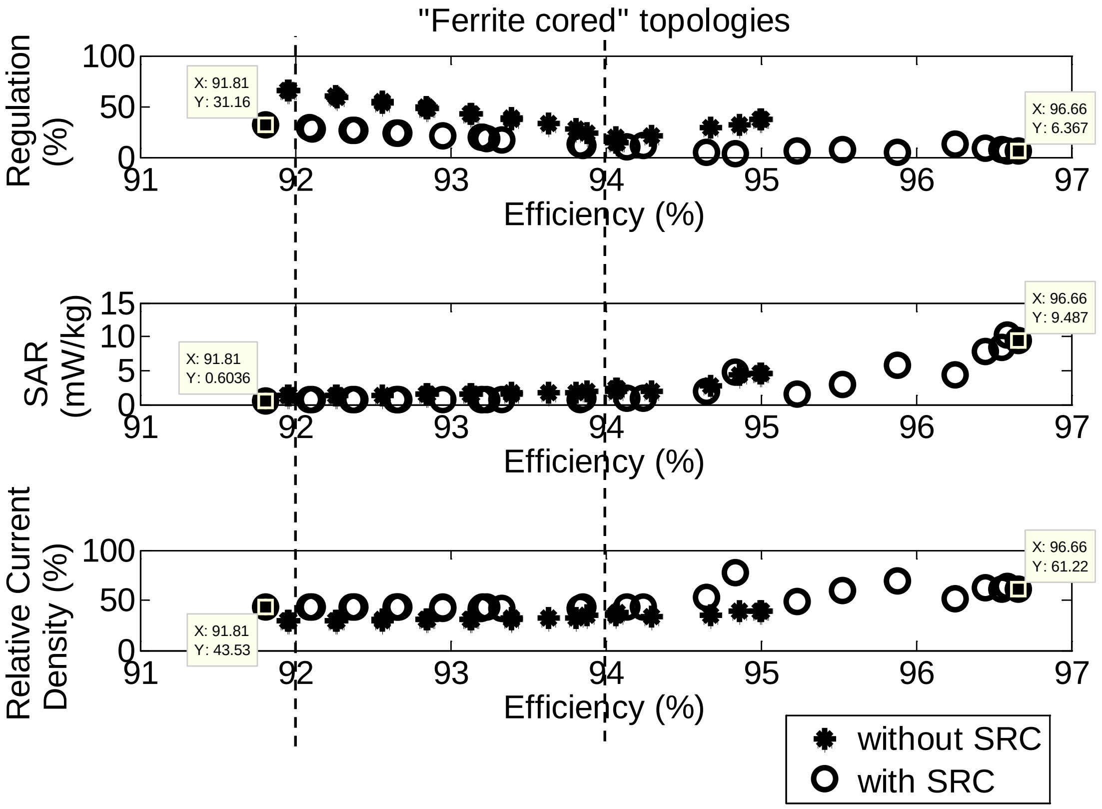

According to the results attained from the configurations chosen by the optimization method, the efficiency improves together with regulation (efficiency increase as regulation decreases) and the SAR improves together with the induced current density (both decreases together), but each pair improves with the depreciation of the other.

The best regulation values of the non-dominated sets with and without SRCs are respectively higher than 3 and 10 % and they attain worst regulations at values even higher than 50 %. This can be understood due to the high inductive behavior of the TET transformer, since it contains a very big gap between the coils. For TET coils with SRCs, this inductive behavior is compensated by the capacitors.

All the induced values of SAR and current density are also within the limits proposed by ICNIRP and they maintain their lower values for the configurations with efficiency smaller than 95 %. However, the regulation is higher in these configurations.

The best obtained efficiency is 96.7 % for a configuration with SRCs which attained 6.4 % of regulation, 9.5 mW/kg of SAR and 61.2 % of relative current density. However, the best SAR value was 0.6 mW/kg for a configuration with SRCs that attained the worst efficiency (91.8 %) with 31.2 % of regulation and 43.6 % of relative current density.

It is possible to perform an analysis with the non-dominated sets results, since these sets are chosen to have the best values of the efficiency, regulation and SAR concomitantly. This means that a configuration that is too different than any of those in the non-dominated sets should not be used because it may represent a better value of one of the efficiency, regulation or SAR, but it is not a compromised solution.

Figure 6.4 shows the correlation between the efficiency and the constructive (core central diameter, coil thickness and number of turns of primary and secondary coils) and electrical (voltage and frequency) parameters. The regulation can also be observed in this figure in order to evaluate its behavior with the variation of the mentioned parameters and efficiency. Figure 6.5 shows similar correlation but between SAR and relative current density in place of efficiency and regulation.

Figure 6.4 – Values of the parameters chosen by MGA (frequency, number of turns of primary and secondary coil, core central diameter and coil thickness) resulting in configurations for TET system with and without SRCs which attain the shown values of efficiency and regulation.

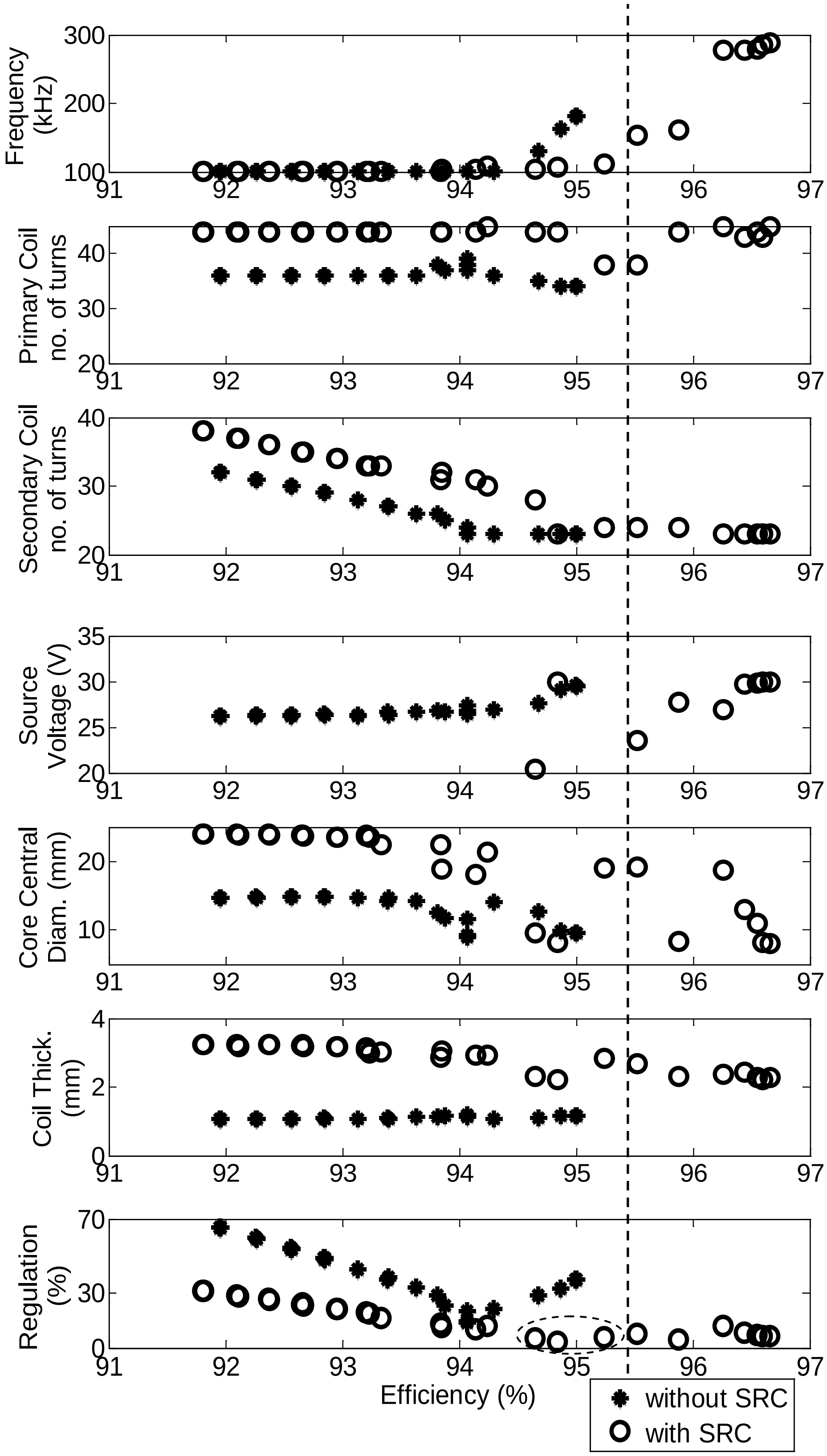

Figure 6.5 – Values of the parameters chosen by MGA (frequency, number of turns of primary and secondary coil, core central diameter and coil thickness) resulting in configurations for TET system with and without SRCs which attain the shown values of SAR and relative current density.

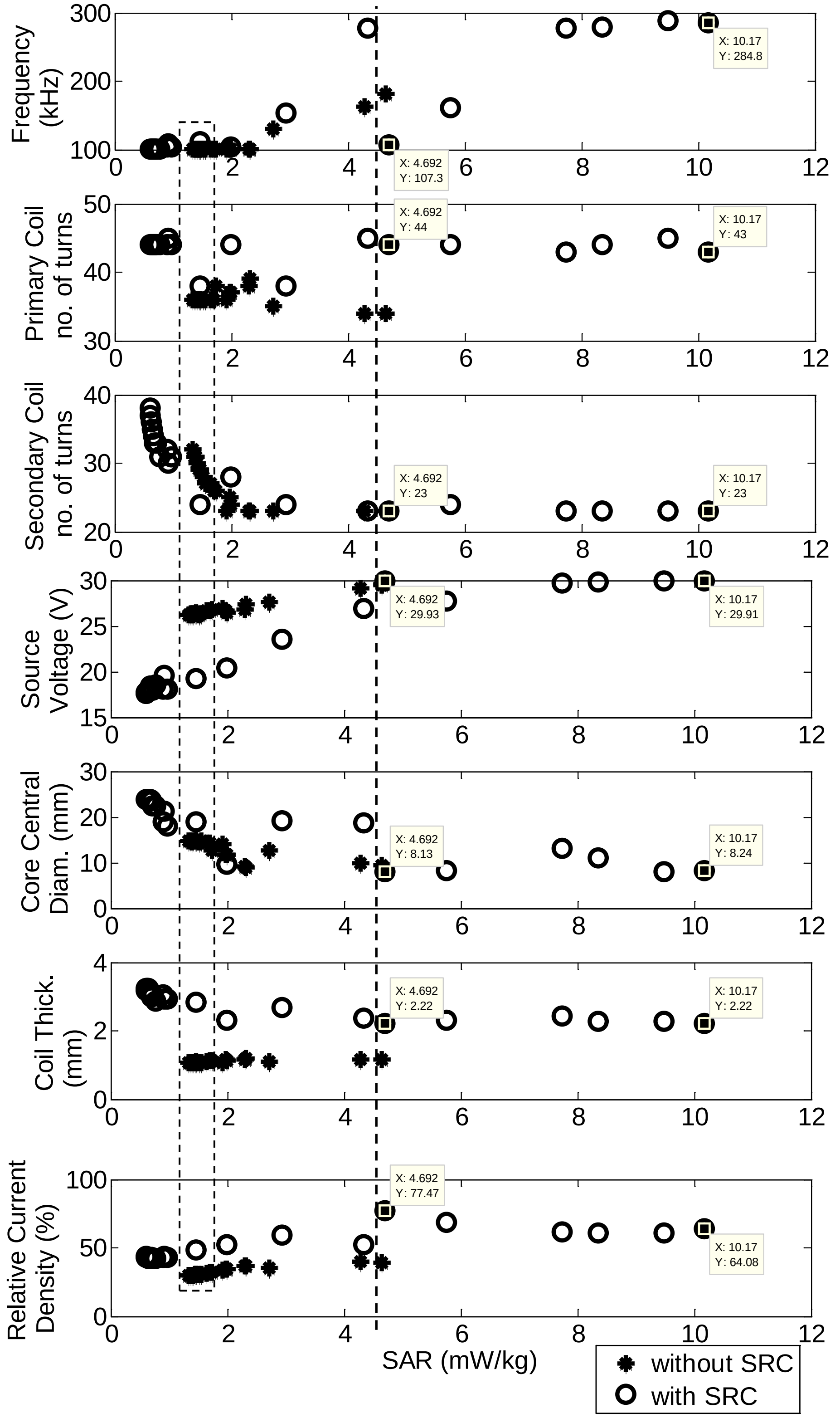

The non-dominated set for the TET system without SRCs recommended that

- the coil thickness should be as small as 1.2 mm,
- the core central diameter should be limited within 8 and 15 mm,
- the supplied voltage should be higher than 26 V,
- the secondary coil should not contain too many turns (less than 32 turns),
- the primary coil should have around 36 turns, and
- the frequency should not be much more than 100 kHz.

On the other hand, the non-dominated set for the TET system with SRCs recommended that

- the coil thickness is larger, being between 2.22 and 3.2 mm,
- the core central diameter should be bigger (up to 24 mm),
- the supplied voltage should be smaller (even around 16 V),
- the primary and secondary coils should contain more turns, and
- now frequencies above 200 kHz are acceptable.

The vertical dashed line on Figure 6.4 shows that the configurations on the right result in the best values of efficiency and regulation, although there are some configurations with better values of regulation on the left side as encircled. The vertical dashed line on Figure 6.5 shows that the configurations on the left result in the best values of SAR. Note that the non-dominated sets of configurations acquired from MGA present differences according to the use of the SRC.

Both non-dominated sets of configurations provide good efficiency, but the best values of efficiency and regulation are achieved with the configurations that have SRCs, as shown on the right side of the dashed line on Figure 6.4. These selections are combinations of the parameters as follows:

- the frequency is high (about 280 kHz);
- the secondary coil has less than 28 turns;
- the source voltage is around 30 V in spite of good values of regulation with voltage around 20 V;
- the core central diameter is smaller than 13 mm;

- the coil thickness is between 2.22 and 2.4 mm.

The left side of the dashed line in Figure 6.5 shows that there are some configurations with and without SRCs that also culminate in good values of SAR, whereas:

- the frequency is around 100 kHz;
- the secondary coil is between 30 and 40 turns;
- the source voltage is around 18 V;
- the core central diameter is between 16 and 24 mm;
- the coil thickness is around 3 mm.

These configurations with SRCs are also the ones that resulted in efficiency between 92 and 94 %, regulation between 10 and 31 %, SAR around 0.6 mW/kg and relative current density around 43 %, as shown in between the lines in Figure 6.3.

However, the configurations that attained the best values of relative current density and with very low SAR are the configurations without SRCs located within the dashed rectangle in Figure 6.5, whereas:

- the frequency is about 100 kHz;
- the primary coil is about 36 turns;
- the source voltage is around 26 V;
- the center core diameter is about 15 mm;
- the coil thickness is nearly 1 mm.

It is noteworthy that, from all the configurations of the non-dominated sets, the maximum effective values of SAR and induced current density were 10.2 mW/kg and 1.83 A/m^2, respectively, at 284.8 kHz for a configuration with SRCs as demarked in Figure 6.5. This particular value of current density implies a relative current density of 64 %. However, the configuration, that implies the worst relative current density of 77.5 % at 107.3 kHz, has effective current density of 0.83 A/m^2, which is smaller than the above mentioned maximum effective value of 1.83 A/m^2. For all the other configurations, the relative current density is lower than 77.5 % even if their effective values are greater than 0.83 A/m^2.

The selected number of turns of the primary coil from MGA is between 38 and 45 for configurations with SRCs and between 34 and 39 for configurations without SRCs. This parameter affects the efficiency, regulation, SAR and current density depending on the combination with the other parameters. This means, the same amount of turns in the primary coil may present worst TET performance if the other parameters in combination are not well chosen.

These analyses are very important at the time of choosing the configuration to implement since the MGA returns a set of non-dominated configurations. For example, the space to better allocate the coils can be a strong point to consider when selecting the final decision. In this case, the chosen configuration would be with SRCs at 104.2 kHz frequency, 44 turns in the primary coil, 18 turns in the secondary coil, 20 V power supply, 9.6 mm core central diameter and 2.3 mm coil thickness. If the available power supply is the issue at the time of the choice, then the configuration may be different.

6.4 OPTIMIZATION WITH GMSH AND GETDP

As already remarked in Chapter 5, in order to supply the required power of 12 W to the AO with the denoted electronic circuits,

1. the voltage of the secondary coil that will be supplied to the regulator must be within the threshold limits of 8 and 35 V;
2. the no-load voltage of the secondary coil must not exceed the maximum acceptable voltage of the regulator, which is 40 V;

3. the coils should be designed for supplying a power of 19 W since the regulator has an efficiency of 68.5 %.

Although these requirements seem trivial, they add strong constraints to the process of designing the TET coils.

As previously mentioned, the considered TET coils with SRCs to compensate the self-inductances has an optimal coupling position different than the highest coupling that entails the maximum transfer of power (LI et al., 2009). This enforces the need to simulate the constraints in different positions instead of only the largest coil gap because the worst case can be at any position. The concept introduced in Section 4.8 was used in order to simplify the optimization procedure and use 2D axisymmetric instead of 3D simulations. Using this concept, the coil gap must be simulated at higher values to also consider the displacements between the coils. For this reason, all the constraint and objective functions have to be calculated for a set of coil gaps from 5 to 25 mm. This chosen set of coil gaps included 4, 8, 12, 16, 20 and 25 mm.

Furthermore, this power, consumed by the system composed of the AO with the DC/DC converter, should be implemented within the simulations of the TET coils as a variable resistance according to the procedure described in Section 4.2.

With all said and done, it is desired to find the smallest TET coils with the smallest “thermo factor” that supply the required power within the required voltage limits for a range of specified coupling situations. However, as the coil area decreases, the “thermo factor” increases (MATSUKI et al., 1992). That suggests the use of multi-objective optimization algorithms with the coil volume and “thermo factor” as objective functions.

Observe that volume (*Vol*) and “thermo factor” (λ) are not actually single functions because each coil has its own volume and “thermo factor”. Moreover, although the volume is independent of the coil gap, the “thermo factor” in each coil depends on this gap. Since the optimization procedure considers different coil gaps, the “thermo factor” objective function is composed of the “thermo factor” calculated for each coil at each simulated coil gap.

Minimizing only the coil inside the body of the patient may result in bigger coils outside the body of the patient. Since the optimization searches for the least discomfort of the patient, the volumes of both coils should be minimized. In addition, it is not interesting to have coils with very large size difference, because it would also create discomfort. Likewise, the “thermo factor” should also be considered in both coils and for all coil gaps.

Thus, in order to transform these functions in single-objective functions, the square root of the sum of the square function was used, as in

$$\mathrm{OF}_1 = \sqrt{{Vol_1}^2 + {Vol_2}^2} \tag{6.3}$$

and

$$\mathrm{OF}_2 = \sqrt{\sum_{i=4}^{25\,mm} {\lambda_{1,i}}^2 + {\lambda_{2,i}}^2} \tag{6.4}$$

In (6.4), *i* is the distance between the primary and secondary coils at which the TET coils were simulated. Thus, the optimization procedure searches for configuration that fulfills the requirements and has the minimum “thermo factor” for a range of coil gap from 4 to 25 mm.

As aforementioned, the constraints of load power (P_L), load voltage (V_L) and no-load voltage (V_o) must be maintained for all coupling condition defined by coil gaps up to 25 mm. Hence, the non-linear constrained inequalities are computed for each simulated distance as

$$\begin{cases} \mathrm{g}_1 = 19 - P_L < 0 \\ \mathrm{g}_2 = 8 - V_L < 0 \\ \mathrm{g}_3 = V_L - 35 < 0 \\ \mathrm{g}_4 = V_o - 40 < 0 \end{cases} \tag{6.5}$$

Usually, when MGA is used, the constraints are handled by using penalty techniques. However, good values for the penalty weights are unknown most of the time, adding complexity to this approach. Thus, the constraints were considered in the procedure here as a third objective function that counts the number of constraints that has been violated, as suggested in (VIEIRA et al., 2004). Hence, an extra objective function is added to the optimization process:

$$\mathrm{OF}_3 = \sum_{i} \sum_{k=1}^{4} \gamma(g_{k,i}), \quad \begin{cases} \gamma(g_{k,i}) = 1, & if \quad g_{k,i} > 0 \\ \gamma(g_{k,i}) = 0, & otherwise \end{cases} \tag{6.6}$$

Again, *i* is the distance between the primary and secondary coils at which the TET coils were simulated and k defines each of the constrained inequalities of (6.5).

Since this optimization is considering coreless coils, the variables of decision proposed in Table 6.1 should not be in any way related to magnetic cores. Therefore, the optimization strategy used here is as shown in Table 6.2.

Table 6.2 – Simplified optimization strategy.

Variables of Decision	**Constraints**	**Disturbances**	**Objective Function**
Primary Coil Number of turns Secondary Coil Number of turns Wire gauge (cross section) of Secondary Coil Wire gauge (cross section) of Primary Coil Frequency Power Supply Voltage	Load voltage within range ($8 < V_L < 35$ V) No-load voltage ($V_o < 40$ V) Load Power bigger than the required ($P_L > 19$ W)	Coil gaps (4, 8, 12, 16, 20, 25 mm)	Minimize volume And Minimize “Thermo factor”

The limits used for the variables of decision are depicted in Table 6.3. These variables, except for the voltage and frequency, should be integer numbers, but the genetic algorithm from this version of Matlab works with floating numbers. For this reason, special mutation function and initial population function were created to generate populations satisfying the range and integer constraints on the variables of decision.

Table 6.3 – Limits of the variables of decision.

Variables of Decision	**Limits**
Primary Coil Number of turns	[20 – 65] turns
Secondary Coil Number of turns	[20 – 65] turns
Wire gauge (cross section) of Secondary Coil	AWG [14 – 32]
Wire gauge (cross section) of Primary Coil	AWG [14 – 32]
Frequency	[50 – 400] kHz
Power Supply Voltage	[12 – 36] V

Mutation options specify how the genetic algorithm makes small random changes in the individuals in the population to create mutation children. In these functions, similar to the number of turns and type of wire of the coils, the supply voltage and frequency were also defined as integers since there is no practical advantage in specifying them with several decimal places.

The type of wire used was based on the standard table of AWG properties for copper wires. Thus, the optimization generates the GA individual with integer values for the AWG numbers which correspond to the diameters of the wires that affect the geometries, inductances, resistances and the volumes of the TET coils.

The selected individual was then virtually implemented in the software Gmsh (GEUZAINE; REMACLE, 2009) and its FE equations were simulated by the software GetDP (DULAR; GEUZAINE) as already described in Section 3.5.2.1, using the homogenization techniques as in Section 3.5.4. This simulation generated information such as voltage, current and power at the source and load.

The constraints were computed as a non-linear function for all gap positions and were used by the MGA algorithm to calculate new individuals.

The TET system to be optimized here was considered to use SRCs to compensate the self-inductances of the coils. In this way, for each individual created by the optimization software, it is necessary to determine the values of the new SRCs. This enforces the optimization to know the complete equivalent circuit for each individual before simulating the TET coils with the proper SRCs.

Thus, for each individual, the optimization executed the following procedure:

1. GetDP calculates the equivalent circuit parameters of TET transformer at the initial coil gap;

2. Matlab calculates the value of the SRCs;
3. GetDP simulates the TET coils with these SRCs, obtaining the value of constraints and the dissipated power to compute the “thermo factor”;
4. Matlab stores the results;
5. If the coil gap is the last to be analyzed, the data is supplied to GA and the calculation for this individual ends; otherwise, GetDP calculates the new mutual inductance at the next coil gap and steps 3, 4 and 5 are executed again.

This process resulted in a non-dominated set with 8 individuals shown in Table 6.4.

Table 6.4 – Non-dominated individuals from the multi-objective optimization.

N1	AWG1	N2	AWG2	V	Freq (kHz)	Diam1 (mm)	Diam2 (mm)	OF_1 (cm^3)	OF_2 (W/m^2)	OF_3
60	21	23	26	25	146	103.99	32.14	6.27	427.30	0
59	20	23	26	25	154	112.91	32.14	8.28	339.70	0
60	20	23	25	25	144	114.66	34.47	8.54	284.32	0
60	19	23	25	25	150	126.54	34.47	11.65	232.33	0
61	19	24	24	25	142	128.49	38.23	12.02	173.01	0
61	15	25	23	27	152	194.18	42.58	43.44	128.33	0
62	15	24	22	26	137	197.20	44.69	44.80	92.99	0
62	15	25	22	26	137	197.20	46.14	44.81	87.74	0

Observe that even though the limits of the optimization for the source voltage were up to 36 V, the non-dominated set selected voltages around 26 V. This probably happened due to the overvoltage at the secondary coil with no-load when the source voltage is too big.

Moreover, as already seen in the sensitivity analysis, even though the frequency was limited within 50 and 400 kHz, the non-dominated set from MGA resulted in configurations at frequencies between 100 and 200 kHz.

All the individuals from the non-dominated set have the primary coil with more turns and thicker wire (around 60 turns with AWG between 15 and 21) than the secondary coil (around 23 turns with AWG between 22 and 26), resulting in a primary coil bigger than the secondary coil. Indeed, Table 6.4 shows that the primary coils are three to four times bigger than the secondary coils. This result is also discussed in (ZIERHOFER; HOCHMAIR, 1996) and is expected in order to decrease the sensitivity of the system with respect to coil gaps and misalignments.

Figure 6.6 shows the current, voltage, “thermo factor” and power of these individuals according to the variation of coil gap.

Observe that the primary coil has higher current in order to transfer the required power to the secondary coil. Since one of the objective functions of MGA is the "thermo factor" that is inversely proportional to the area, it is expected that bigger coils would have smaller “thermo factors”.

Since the optimization process considered coil gaps up to 25 mm, the load power is exactly 19 W at all the coupling conditions where the coil gap is up to this value. The power did not exceed 19 W because the simulation was set to change the resistor value in order to maintain constant power as recommended in Section 4.2.

Even though the optimization process was considering coil gaps only up to 25 mm, there are configurations able to supply 19 W even at gaps larger than 25 mm, however with higher currents and “thermo factor” in the secondary coil. As typical in multi-objective problems, Figure 6.6 shows that the smallest individuals (1-black, 2-red and 3-blue) are the ones that have the highest "thermo factor" and vice versa.

Figure 6.6 – All Individuals from the non-dominated set obtained from MGA.

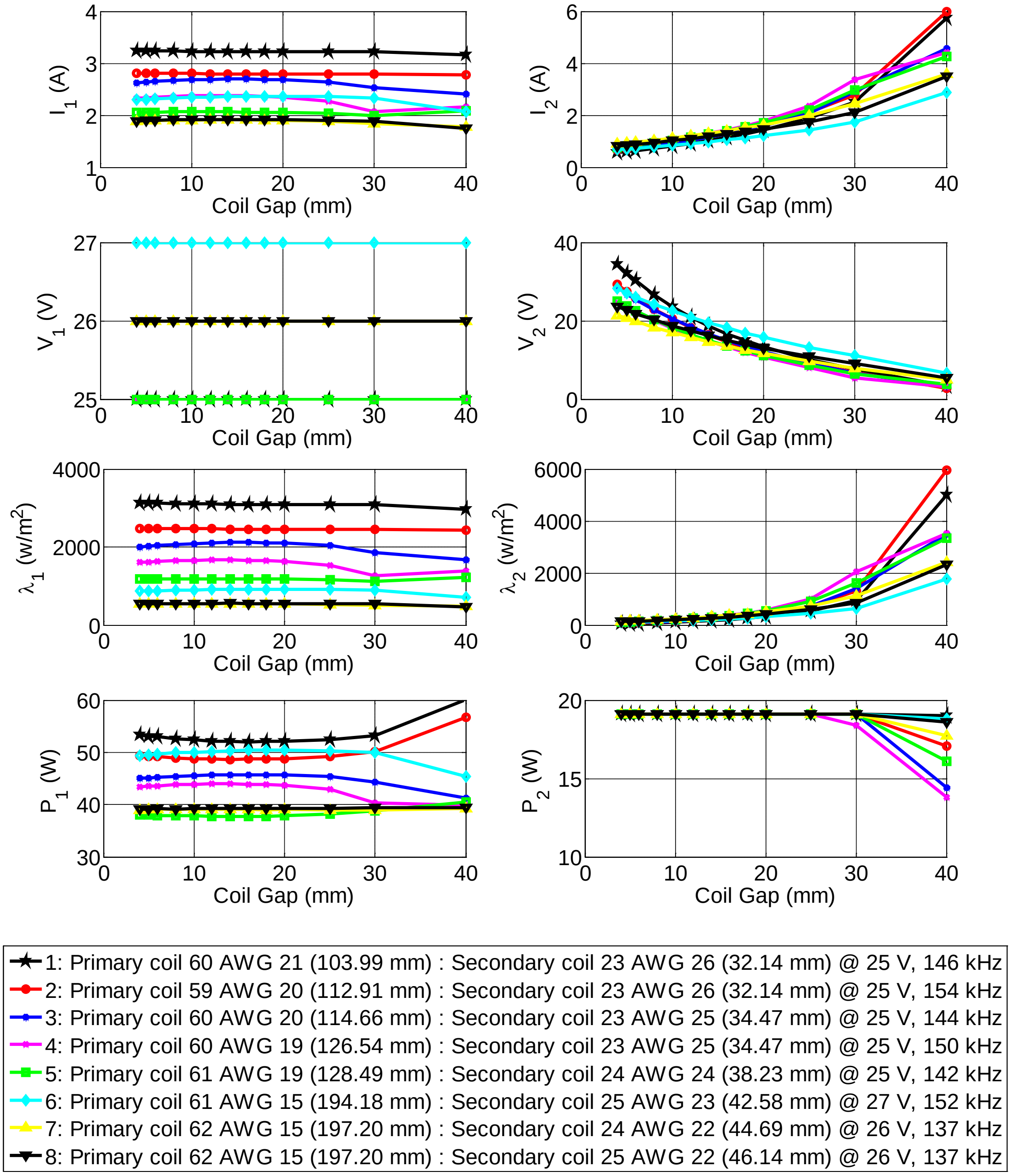

Note that the “thermo factor” in the primary coil is almost constant when increasing the coil gap. On the other hand, the "thermo factor" in the secondary coil increases exponentially with the coil gap. This occurs because when the coil gap is small, the mutual inductance is higher and consequently the voltage in the secondary coil is higher. Since the load consumes constant power, it has smaller current at higher voltage and thus the power dissipated in the secondary winding is smaller.

Hence, the choice of the TET coils to assembly should be performed carefully, considering other project needs. For example, with these performed analyzes, the configuration with 23 turns of wire AWG 26 in the secondary coil and 60 turns of wire AWG 21 in the primary coil supplied by 25 V at 146 kHz seems to have reasonable size (primary and secondary coils have respective diameters of 10.4 cm and 3.2 cm) and it is apparently very stable up to 30 mm of coil gap. This configuration entails temperature rise in the secondary coil similar to the temperature rise entailed by the other configurations. However, it entails temperature rise in the primary coil higher than the other configurations. Thus, among other factors, this temperature rise should be evaluated in order to certify if it is satisfactory.

Moreover, the choice of the TET coils to assemble should also consider the SAR and current density induced in the skin, what was not analyzed here.

6.5 CONCLUSIONS

This chapter performed two multi-objective optimization procedures with different approaches.

First, random simulations were chosen from the results of the different “Ferrite cored” topologies virtually simulated through Flux-2D in Section 4.5 for the two situations, with and without SRCs, to be the inputs of the Universal Kriging algorithm. This algorithm created reliable models for efficiency, regulation, SAR and load power as function of center core diameter, coil thickness, primary and secondary coil number of turns, source voltage and frequency.

These models were used by the MGA to find a set of 32 good configurations (non-dominated set) that resulted in high efficiency with low regulation and SAR. All the attained configurations generated acceptable values of SAR and relative induced current density with efficiencies between 92 and 97 % and regulations between 3.4 and 31 % for configurations with SRCs, and efficiencies between 92 and 95 % and regulations between 14 and 66 % for configurations without SRCs.

It was also noticed that although the SAR and current density follow a similar trend, the relative current density may be different since the current density limit depends on the frequency. The efficiency and regulation also follow the same trend, but they are contradictory to the SAR and current density.

Since the SAR and current density presented acceptable values within the ICNIRP limits for the entire non-dominated set, the choice of better efficiency and regulation might prevail at the final choice for implementation.

Second, this chapter proposed the usage of an optimization process interacting directly with Gmsh/GetDP without the need for Kriging approximation. In this case, the procedure tried to define the smallest TET coils with the smallest “thermo factor”, meeting the requirements of power transfer and load voltage at different coil gaps.

Since the load absorbs a constant active power when energized, the results of the selected optimal configuration presented the required power at all coil gaps within the constraints of the optimization. This procedure achieved configurations with secondary coils as small as 3.2 cm in diameter, but with primary coils of sizes greater than 10 cm in diameter.

It is noteworthy that the “thermo factor” is just a parameter that is known to be directly proportional to the temperature in the windings. However, it is an important indicator to track and indirectly minimize the increase of temperature of the windings, though it is not enough to report the temperature itself without further information. The computation of temperature is also another interesting line of research for future work.

Lastly, it is important to cite that the results and conclusions of this chapter were partially submitted in the following papers to the following conferences:

1. “Improving the Efficiency of a Transcutaneous Energy Transmitter and the influence of the Specific Absorption Rate”, accepted for poster presentation at COMPUMAG 2011 in Sidney, Australia.
2. “Optimization of Efficiency, Regulation and Specific Absorption Rate of a Transcutaneous Energy Transmitter with Resonant Capacitor”, accepted for oral presentation at BIODEVICES 2012 in Vila Moura, Portugal. This paper can be found in the proceedings of the International Conference on Biomedical Electronics and Devices, pp. 224-229.
3. “Resonant Capacitors and the Performance of Transcutaneous Energy Transmitters”, accepted for oral presentation at IASTED 2012 in Innsbruck, Austria. This paper can be found in the proceedings of the 9th IASTED International Conference on Biomedical Engineering, BioMed 2012, pp. 470-477.
4. “A Design Proposal for Optimal Transcutaneous Energy Transmitters”, accepted for poster presentation at COMPUMAG 2013 in Budapest, Hungary. The full paper was accepted on September 10th 2013 for publication in the IEEE Transactions on Magnetics.

7 FINAL REMARKS

The subject of this research is quite broad and has already been researched outside Brazil for a considerably long time. This makes it a challenge to make a contribution to this subject, even though the Laboratory of Applied Electromagnetism of the University of Sao Paulo had already performed some research in this area.

It is an extensively comprehensive project able to explore various lines of research and can be used even for other artificial organs besides the ventricular assist device. This research focuses mainly on the coils of the TET system, briefly touching on some electronic circuits, to achieve a systematic approach that can be represented mathematically as an optimization procedure that searches for good configurations of the TET system.

Some parameters related to the physical properties of the coils and to the electric part of the TET system were compiled from an initial examination in the academic literature and the restrictions that govern the effects of electromagnetic fields in a biological body.

Subsequently, investigations of some methods to compute the properties of the TET coils were performed, including the use of two FE software applications (Flux-2D/3D from CEDRAT and Gmsh with GetDP) to simulate the system. As described in this document, an alternative technique in the FE method (homogenization method) was inspected to whether it succeeds in simulating pancake coils that have non-symmetric geometry in one of the directions. After proving the validity of this method, which cannot be found in the academic literature yet, this technique was applied to the TET device in order to simulate different geometries with fewer mesh problems and less computational cost. Moreover, two different measurement methods (using VNA and IA) were explored.

Having chosen the methodology to measure and simulate the system, physical and virtual experiments were performed and their results, analyzed. These analyses suggested the use of optimization methods to seek the best parameters that improve efficiency, regulation, SAR and relative current density.

A procedure to determine the value of the load resistance that would model the system composed of the AO and the regulator was defined through the analysis of the behavior of the TET system related to the variation of load resistance. This procedure is another contribution of this work to future research; a load with a known active power is used instead of an impedance with a fixed value.

The use of SRCs to improve the efficiency and specifically the regulation by compensating the self-inductance was recommended by the sensitivity analysis of the virtual prototype; even though its use increases the SAR, the latter is still smaller than the maximum limit defined by ICNIRP. However, a capacitor with the exact calculated value is usually not a standard manufactured product, and thus the variation of the load resistance may affect the resonant frequency of the system.

Moreover, analyses of physical and virtual prototypes suggested ferrite cores as a good option to increase the performance of the TET system. In order to have the best values of efficiency with acceptable values of regulation and SAR, the virtual sensitivity analysis also recommended TET coils in which the primary core has ferrite properties and the secondary coil is coreless (“Hybrid PFSA” topology). This observation was not found in any revised literature and requires better analysis, especially in relation to misalignments of the coils, before finalizing any conclusions.

A virtual sensitivity analysis of the effects of the variation of the ferrite permeability in the efficiency and relative current density suggested that other types of core materials such as composites, plastic ferrite or magnetorheological fluids could be considered since materials with core relative permeability as low as 50 are acceptable. There are some authors that propose a hybrid TET transformer equivalent to the presented “Hybrid PASF”. Nevertheless, this interesting result with different permeability was not reported in any other work found in the academic literature. Moreover, plastic ferrite and magnetorheological fluids could represent interesting solutions since they are flexible and therefore increase the level of comfort of the patient. Thus, they should be investigated more deeply in order to evaluate their usage in TET systems.

A ferrite core with the desired geometry and dimensions is not always feasible. Thus, coreless TET coils were analyzed, including their mutual inductance related to different misalignments at different coil gaps. This analysis showed that when the coils are misaligned and separated by some specific distance, they have the same mutual inductance as when they are aligned and separated by further distance. This important observation eliminated the use of some 3D simulations which were replaced by 2D simulations with larger coil gaps.

The exploration of the electronic circuits through physical measurements inferred that the design of the TET coils must consider the load voltage within the limits of values defined by the threshold of the DC/DC converter and the no-load voltage at a maximum limit. Moreover, since the DC/DC converter is not 100 % efficient, the design of the TET coils should compensate this lack of efficiency by increasing the power requirements of the secondary coil.

The built inverter presented an efficiency of about 54 % while the built regulator presented an efficiency of around 68 %, both being very low efficiencies. The graphs and results from the measurements showed that the physical prototype can supply more than the power required by the AO, but with low efficiency of about 30 % for the complete system or 61 % when excluding the inverter.

With all this knowledge, two multi-objective optimization procedures were performed considering Flux-2D with Kriging techniques and Gmsh/GetDP using homogenization techniques. The former procedure optimized TET coils with ferrite cores and SRCs by changing some geometrical dimensions of the core, number of turns and some electrical parameters. It reached a non-dominated set of 32 good configurations that has the maximum efficiency with minimum regulation and SAR.

However, due to the difficulty to find ferrite cores with the specifications defined by the optimization, a second optimization with coreless coils was executed. In this latter case, coreless coils with SRCs were optimized by evaluating the number and gauge of turns and some electrical parameters, achieving a non-dominated set of 8 good configurations that has the smallest coils with the smallest “thermo factors”.

Although the structure of this document presented individual chapters, the chapters complemented each other. An initial multi-parametric analysis supported the development of physical prototypes which, in turn, supplied extra details not considered in the first optimization, allowing new optimization procedures with better strategies to be performed. Therefore, a procedure using optimization was performed in parallel with the implementation of TET coils that were not yet well optimized in order to better understand the needs of the electronic circuits and define new optimization strategies.

Therefore, this research was able to reach its main targets by using optimization techniques to propose a systematic design for TET coils, considering all the aforementioned electronic circuits and issues. At this moment, it is possible to state that the Laboratory of Applied Electromagnetism of the University of Sao Paulo has improved the know-how about TET systems and how they are being researched internationally in a way that future lines of research can be proposed.

7.1 SUGGESTION FOR FUTURE ACTIVITIES

In the previous chapters, some topics were proposed as future researches. Among these topics and others not yet mentioned, important topics that need special attention and particular research could be cited as follows:

- Investigate the application of ferromagnetic material core and the possibility of hybrid configurations, i.e. TET coils with different core types. Composite or magnetorheologic materials could be used due to the easy molding of the desired geometry.
- Research better models to represent the TET coils even when having proximity effects, skin effects and induced eddy currents.
- Create a model in the FE software that considers the electromagnetic effects in the biologic tissue, such as Specific Absorption Rate and Induced Current Density.
- Explore models for evaluating, with adequate accuracy, the temperature in the skin of the patient as well as on the surface of the coil that is in contact with this skin.
- Engineer a circuit to protect the patient as well as the internal electronic system against overvoltage and/or short-circuits.
- Analyze an inverter that converts DC voltage to AC voltage at a desired frequency with better efficiency.
- Study voltage rectifiers (with regulators) transform the AC voltage transferred to the secondary coil and control the DC voltage supplied to the VAD.

- Consider a close loop system to maintain the input regulator voltage at necessary levels. The close loop system can significantly simplify the hardware of the internal electronic circuit.
- Evaluate alternative sources that include rechargeable batteries as a source for the inverter, e.g., piezoelectric transducers.

7.2 OTHER ACTIVITIES

During this research, the PhD student spent six months in France as part of a knowledge exchange program, submitted papers, participated in events and received prizes.

Following are the approved conference papers:

1. First author of a paper entitled “Improving the Efficiency of a Transcutaneous Energy Transmitter and the influence of the Specific Absorption Rate”, accepted for poster presentation at COMPUMAG 2011 in Sidney, Australia.
2. First author of a paper entitled “Optimization of Efficiency, Regulation and Specific Absorption Rate of a Transcutaneous Energy Transmitter with Resonant Capacitor”, accepted for oral presentation at BIODEVICES 2012 in Vila Moura, Portugal. This paper can be found in the proceedings of the International Conference on Biomedical Electronics and Devices, pp. 224-229.
3. First author of a paper entitled “Resonant Capacitors and the Performance of Transcutaneous Energy Transmitters”, accepted for oral presentation at IASTED 2012 in Innsbruck, Austria. This paper can be found in the proceedings of the 9th IASTED International Conference on Biomedical Engineering, BioMed 2012, pp. 470-477.
4. First author of a paper entitled “Screening a Transcutaneous Energy Transmitter”, accepted for oral presentation at MOMAG 2012 in Joao Pessoa, Brazil. The presentation of this paper got a prize of second best presenting paper.

5. First author of a paper entitled “Simulations of Transcutaneous Energy Transmitters by using Homogenization Method”, accepted for poster presentation at EMF 2013 in Bruges, Belgium.
6. Second author of a paper entitled “An accurate model with lumped parameters for coreless transformers with relative large wire gauge”, accepted for poster presentation at EMF 2013 in Bruges, Belgium.
7. First author of a paper entitled “Analysis on Methods to obtain Lumped Parameters for an Inductive Coupling Device”, accepted for poster presentation at COMPUMAG 2013 in Budapest, Hungary.
8. First author of a paper entitled “Homogenization Methods in Simulations of Transcutaneous Energy Transmitters”, accepted for poster presentation at COMPUMAG 2013 in Budapest, Hungary. On September 29th 2013, the full paper was accepted for publication in the IEEE Transactions on Magnetics.
9. First author of a paper entitled “A Design Proposal for Optimal Transcutaneous Energy Transmitters”, accepted for poster presentation at COMPUMAG 2013 in Budapest, Hungary. On September 10th 2013, the full paper was accepted for publication in the IEEE Transactions on Magnetics.
10. Second author of a paper entitled “Modeling coreless transformers with relative large wire gauge using an optimization method”, accepted for poster presentation at COMPUMAG 2013 in Budapest, Hungary. On October 3rd 2013, the full paper was accepted for publication in the IEEE Transactions on Magnetics.

It is noteworthy that the PhD student presented all the papers except the first one.

Moreover, in August 2013, a paper entitled “A Systematic Sensitivity Analysis of the Performance of a Transcutaneous Energy Transmitter for Design Purposes” was accepted for publication in the Journal of Microwaves, Optoelectronics and Electromagnetic Applications (JMOe).

While in France, the PhD student also wrote two papers for the workshop “II Simpósio Dispositivos de Assistência Circulatória Uni e Bi-Ventricular Coração Artificial” related to the thematic project of FAPESP 2006/58773-1 in Brazil. Those papers were nominated as “Avaliação do tipo de geometria e tamanho de um Transmissor de Energia Transcutâneo” and “Avaliação da estabilidade de um Transmissor de Energia Transcutâneo com desalinhamentos”. Since the PhD student was not in Brazil at the time of the workshop, her advisor, Professor Luiz Lebensztajn, substituted for her and presented these papers. The paper “Avaliação do tipo de geometria e tamanho de um Transmissor de Energia Transcutânea” received a prize of Featured Work in this workshop.

Lastly, during the research activities, the PhD student had the opportunity to participate for two semesters in a program to improve teaching called “Programa de Aperfeiçoamento de Ensino”.

REFERENCES

ANDRADE, A. **Projeto, protótipo e testes "in vitro" e "in vivo" de um novo modelo de coração artificial total (TAH) por princípio eletro-mecânico de funcionamento**. 1998. Tese (Doutorado). Faculdade de Engenharia Mecânica, Universidade Estadual de Campinas, Campinas, 1998.

BRASIL. Lei no 11.934, de 5 de maio de 2009. Dispõe sobre limites à exposição humana a campos elétricos, magnéticos e eletromagnéticos; altera a Lei no 4.771, de 15 de setembro de 1965; e dá outras providências. Disponível em: <http://www.planalto.gov.br/ccivil_03/_Ato2007-2010/2009/Lei/L11934.htm>. Acesso em: 24 ago. 2011.

BRONZINO, J. D. **The biomedical engineering handbook**. 2nd ed. Boca Ratón: CRC, 2000. 3189 p.

BULLA, G. **Cálculo de taxa de absorção específica e aumento de temperatura em modelos de cabeça de adulto e criança**. 2006. 97p. Dissertação (Mestrado). Universidade Federal do Rio Grande do Sul, Porto Alegre, 2006.

CHAN, H. L.; CHENG, K. W. E.; SUTANTO, D. A simplified Neumann's formula for calculation of inductance of spiral coil. **IEEE Power Electronics and Variable Speed Drives**, New York, n. 475, p. 69-73, Sept. 2000.

COCHLEAR PTY. LTD University of Melbourne. James M. Harrison; Peter M. Seligman. **Power transfer for implanted protheses**. U.S. 4.741.339, Oct. 21, 1985, May 3, 1988.

CRUZ, S. D. D. **Verificação dos níveis de radiação emitidos pelas antenas das ERBs e a percepção das comunidades próximas**. 2005. 165p. Dissertação (Mestrado). Pontifícia Universidade Católica do Rio de Janeiro, Rio de Janeiro, 2005.

DIAS, M. H. C.; SIQUEIRA, G. L. Considerações sobre os efeitos à saúde humana da irradiação emitida por antenas de estações rádio base de sistemas celulares. **Revista Telecomunicações - Inatel**, Santa Rita do Sapucaí, v. 5, n. 1, p. 41-54, jun. 2002.

DISSANAYAKE, T. D. **An effective Transcutaneous Energy Transfer (TET) system for artificial hearts**. 2010. 210p. Thesis (PhD). University of Auckland, New Zealand, 2010.

DISSANAYAKE, T. D. et al. Experimental study of a TET system for implantable biomedical devices. **IEEE Transactions on Biomedical Circuits and Systems**, New York, v. 3, n. 6, p. 370-378, Dec. 2009.

DOWEL, P. Effects of eddy currents in transformer windings. **Proceedings of the Institution of Electrical Engineers**, London, v. 113, n. 8, p. 1387-1394, 1966.

DULAR, P.; GEUZAINE, C. GetDP: a general environment for the treatment of discrete problems. Disponível em: <http://geuz.org/getdp/>. Acesso em: 15 jun. 2012.

EMPI, Inc. Donald D. Maurer. **Capacitive energy source and circuitry for powering medical apparatus**. U.S. Pat. No. 4.408.607, Apr. 13, 1981, Oct. 11, 1983.

ENDERLE, J. D.; BLANCHARD, S.; BRONZINO, J. **Introduction to biomedical engineering**. 2nd ed. [S.l.]: Elsevier, 2005. 1144 p.

ERICKSON, R. W.; MAKSIMOVIC, D. **Fundamentals of power electronics**. 2nd ed. New York: Kluwer Academic/Plenum, 2004. 883 p.

FAIZ, J.; ASHTIANI, A.; BYAT, M. R. Lumped complete equivalent circuit of a coreless high-frequency transformer. **IEEE Transactions on Magnetics**, New York, v. 33, n.1, p. 703-707, Jan. 1997.

FERREIRA, J. A. Improved analytical modeling of conductive losses in magnetic components. **IEEE Transactions on Power Electronics**, New York, v. 9, n. 1, p. 127-131, 1994.

FUNDAÇÃO DE AMPARO À PESQUISA DO ESTADO DE SÃO PAULO. **Sistemas propulsores eletromagnéticos implantáveis para dispositivos de assistência circulatória sanguínea uni e biventricular**. Sao Paulo: 2007. Projeto Temático.

GALBRAITH, D. C.; SOMA, M.; WHITE, R. L. A wide-band efficient inductive transdermal power and data link with coupling insensitive gain. **IEEE Transactions on Biomedical Engineering**, New York, v. 34, n. 4, p. 265-275, Apr. 1987.

GEUZAINE, C.; REMACLE, J. -F. Gmsh: A 3-D finite element mesh generator with built-in pre- and post-processing facilities. **International Journal for Numerical Methods in Engineering**, Chichester, v. 79, n. 11, p. 1309-1331, 2009.

GOLDBERG, D. E. **Genetic algorithms in search, optimization, and machine learning**. Reading: Addison-Wesley, 1989.

GYSELINCK, J.; DULAR, P. Frequency-domain homogenization of bunbundles of wires in 2D magnetodynamic FE calculations. **IEEE Transactions on Magnetics**, New York, v. 41, n. 1, p. 1416-1419, 2005.

GYSELINCK, J.; SABARIEGO, R. V.; DULAR, P. Time-domain homogenization of windings in 2-D finite element models. **IEEE Transactions on Magnetics**, New York, v. 43, n. 4, p. 1297-1300, 2007.

INSTITUTE FOR APPLIED PHYSICS NELLO CARRARA. An Internet resource for the calculation of the dielectric properties of the body tissues in the frequency range 10 Hz–100 GHz. Disponível em: <URL:http://niremf.ifac.cnr.it/tissprop/.>. Acesso em: 24 ago. 2011.

INTERNATIONAL COMMISSION ON NON-IONIZING RADIATION PROTECTION. **Guidelines for limiting exposure to time-varying electric, magnetic, and electromagnetic fields (up to 300 GHz)**. [S.l.]: p. 494–522. 1998.

JOHNSON, C. C. Recommendations for specifying EM wave irradiation conditions in bioeffects research. **Journal of Microwave Power**, Mechanicsville**,** v. 10, n. 3, p. 249-250, 1975.

JOUNG, G. B.; CHO, B. H. An energy transmission system for an artificial heart using leakage inductance compensation of transcutaneous transformer. In: POWER ELECTRONICS SPECIALISTS CONFERENCE, 27, 1996, Baveno. **Proceedings**. New York, IEEE, 1997. v. 1, p. 898-904.

KIM, C. G.; CHO, B. H. Transcutaneous Energy Transmission with double tuned duty cycle control. In: INTERSOCIETY – ENERGY CONVERSION ENGINEERING CONFERENCE, 31, 1996, Denver. **Proceedings**. New York, IEEE, 1997. v. 1, p. 587-591.

LAZZI, G. Thermal effects of bioimplants: power dissipation characteristics and computational methods. **IEEE Engineering in Medicine and Biology Magazine**, New York, v.24, n.5, p. 75-81, 2005.

LEBENSZTAJN, L. et al. Kriging: a useful tool to electromagnetic devices optimization. **IEEE Transactions on Magnetics**, New York, v. 40, n. 2, p. 1196-1199, 2004.

LI, H. L. et al. Optimal coupling condition of IPT system for achieving maximum power transfer. **Electronics Letters**, London, v. 45, n. 1, p. 76-77, 2009.

LOPES JR., D. **Análise de desempenho de um sistema transcutâneo de transmissão de energia**. 2003, 61p. Dissertação (Mestrado). Escola Politécnica da Universidade de São Paulo, São Paulo, 2003.

LOUIS C. WALLER. **Power supply for body implanted instruments**. U.S. Pat. 3.195.540, Mar. 29, 1963, July 20, 1965.

MATSUKI, H. et al. Investigation of coil geometry for transcutaneous energy transmission for artificial heart. **IEEE Transactions on Magnetics**, New York, v. 28, n. 5, p. 2406-2408, 1992.

MCINTOSH, R. L.; ANDERSON, V. A. comprehensive tissue properties database provided for the thermal assessment of a human at rest. **Biophysical Reviews and Letters**, Singapore, v. 5, n. 3, p. 129-151, June 2010.

MEUNIER, G. et al. Homogenization for periodical electromagnetic structure: which formulation? **IEEE Transactions on Magnetics**, New York, v. 46, n. 8, p. 3409-3412, 2010.

MIURA, H. et al. Improvement of the transcutaneous energy transmission system utilizing ferrite cored coils for artificial hearts. **IEEE Transactions on Magnetics**, New York, v. 42, n. 10, p. 3578-3580 , Oct. 2006.

MIZANNOJEHDEHI, A.; SHAMS, M.; MUSSIVAND, T. Design and Analysis of a Class-E Frequency controlled transcutaneous energy transfer system. In: IEEE International Conference on Electronics, Circuits and Systems, 13, 2006, Nice. **Proceedings**. New York: IEEE, 2006. p. 21-24.

MOREAU, O.; POPIEL, L.; PAGES, J. L. Proximity losses computation with a 2D complex permeability modelling. **IEEE Transactions on Magnetics**, New York, v. 34, n. 5, p. 3616-3619, 1998.

OKAMOTO, E. et al. A New transcutaneous energy transmission system with hybrid energy coils for driving and implantable biventricular assist device. **Artificial Organs**, Hoboken, v. 33, n. 8, p. 622–626, 2009.

PODOLTSEV, A.; LEBEDEV, B. Analysis of effective resistance and eddy-current losses in multiturn winding of high-frequency magnetic components. **IEEE Transactions on Magnetics**, New York, v. 39, n. 1, p. 539-548, 2003.

PUERS, R.; VANDEVOORDE, G. Recent Progress on Transcutaneous Energy Transfer for Total Artificial Heart Systems. **Artificial Organs**, Hoboken, v. 25, n. 5, p. 400-405, 2001.

RASHID, M. H. **Power electronics handbook**. San Diego: Academic Press, 2001. 892 p.

SABARIEGO, R. V.; DULAR, P.; GYSELINCK, J. Time-Domain Homogenization of Windings in 3-D Finite Element Models. **IEEE Transactions on Magnetics**, New York, v. 44, n. 6, p. 1302-1305, 2008.

SCHUDER, J. C. Powering an artificial heart: birth of the inductively coupled-radio frequency system in 1960. **Artificial Organs**, Hoboken, v. 26, n. 11, p. 909-915, 2002.

SCHUDER, J. C.; GOLD, J. H.; STEPHENSON JR., H. E. An inductively coupled RF system for the transmission of 1 kw of power through the skin. **IEEE Transactions on Biomedical Engineering**, New York, v. 18, n. 4, p. 265-273, July 1971.

SHIBA, K. et al. Analysis of current density and specific absorption rate in biological tissue surrounding transcutaneous transformer for an artificial heart. **IEEE Transactions on Biomedical Engineering**, New York, v. 45, n. 1, p. 205-213, 2008.

SIBUÉ, J. R. et al. Modeling of losses and current density distribution in conductors of large air-gap transformer using homogenization and 3-D FEM. **IEEE Transactions on Magnetics**, New York, v. 48, n. 2, p. 763-766, 2012.

SIBUÉ, J. R. et al. Modeling and computation of losses in conductors and magnetic cores of a large air gap transformer dedicated to contactless energy transfer. **IEEE Transactions on Magnetics**, New York, v. 49, n. 1, p. 586-590, 2013.

SIMON, T. M. et al. Estimation of the effective permeability in magnetorheological fluids. **Mathematical and Computer Modelling**, Oxford, v. 33, n. 1/3, p. 273-284, 2001.

SOMA, M.; GALBRAITH, D. C.; WHITE, R. L. Radio-frequency coils in implantable devices: misalignment analysis and design procedure. **IEEE Transactions on Biomedical Engineering**, New York, v. 34, n. 4, p. 276-282, April 1987.

TANG, T.; ZHAO, C.; CHEN, D. Feedback analysis and design of inductive power links driven by Class-E amplifiers with variable coupling coefficients. **Journal of Zhejiang University.SCIENCE C: Computers & Electronics**, Berlin, p. 629-636, 2010.

UNIVERSITY OF OTTAWA, John A. Miller. **Transcutaneous energy transfer device**. U.S. Pat. No. 5.350.413, July 22 , 1991, Sept. 27, 1994.

VIEIRA, D. A. G. et al. Treating constraints as objectives in multiobjective optimization problems using niched pareto genetic algorithm. **IEEE Transactions on Magnetics**, New York, v. 40, n. 2, p. 1188-1191, 2004.

ZIERHOFER, C. M.; HOCHMAIR, E. S. Geometric approach of coupling enhancement of magnetically coupled coils. **IEEE Transactions on Biomedical Engineering**, New York, v. 43, n. 7, p. 708-714, July 1996.

APPENDIX A – THE MEDIUM THAT SEPARATES THE PRIMARY FROM THE SECONDARY COIL

The main part of the TET system is the magnetic transfer device (here called transformer) with the primary coil outside the body to transfer power to a secondary coil inside the body. However, the knowledge of the medium that separates the primary coil from the secondary coil, which considers the skin, is needed for better specification of this device.

Therefore, one must know where in the body the TET device can be placed. Due to the flexibility, the location next to the heart, and space, the TET secondary coil could be allocated just underneath the skin between the skin and fat near the abdomen. Thus, the medium between the coils could be a fat layer and skin, whose thickness varies from person to person.

The skin is a vital organ that covers the outside of the whole body, making a protective barrier against diseases and wounds emanating from the environment. Moreover, it helps to control the body temperature, takes sensory information from the external environment, stores water, fat and Vitamin D and participates in the immune system against diseases. It is the third most abundant tissue in the human body, whose color, thickness and texture vary throughout the body and from person to person. It consists basically of two layers separated by an extracellular matrix called basal lamina, which cover a third layer of subcutaneous fat.

These layers differ in function, thickness and strength and can be classified as:

1. Epidermis, the outermost layer of the skin. It is strong, protective and consists of multiple layers of epidermal cells at different stages of keratinocytes. The thickness varies from 0.05 mm to 1.5 mm.

2. Dermis is a fibrous connective tissue that lies beneath the basal lamina that supports and empowers the epidermis and its main cellular components are fibroblasts. It contains nerve endings, sweat glands, oil glands and follicles of hair. It is the thickest of the three layers ranging from 1.5 mm to 4 mm thick.

Figure A.1 - Skin

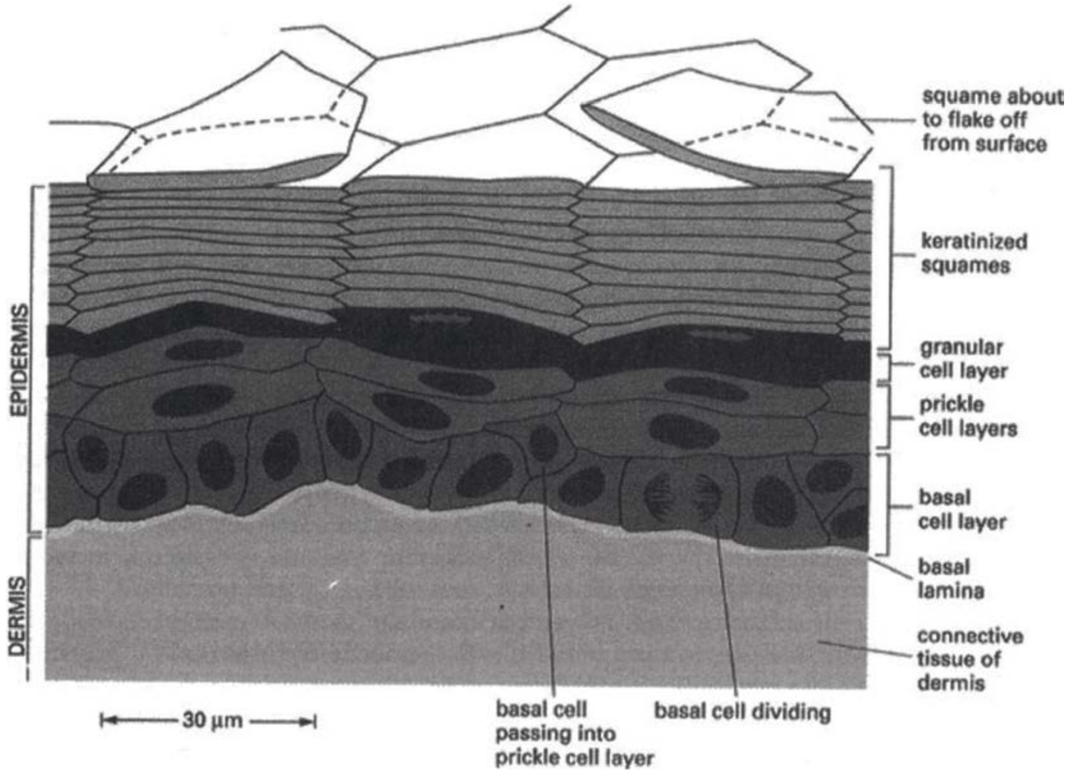

(ENDERLE; BLANCHARD; BRONZINO, 2005).

Hypodermis or subcutaneous tissue is a layer of fat and collagen cells, which provides nutrients for the other two layers of the skin and serves as a shock absorber and heat insulator for the internal organs. The thickness of this layer varies throughout the body and from person to person.

Thus, the medium which separates the primary coil (external to the body) from the secondary coil (internal to the body) is the skin that may vary in thickness from 5 mm and may contain a layer of fat with varied thickness.

Trying to get the properties of these tissues, Robert L. Macintosh and Vitas Anderson analyzed 300 references among articles and books and developed a database with six thermal properties to 43 different human tissues to improve the accuracy and consistency of the thermal modeling results:

Table A.1 – Summary of the data collected from the thermal properties of tissues.

Tissue	Specific heat Capacity, c [J/(kg.^oC)]			Thermal Conductivity, k [W/(m.^oC)]			Water, w [%]			Density, p [kg/m^3]		
	Avg.	Min.	Max.	Avg.	Min.	Max.	Avg.	Min.	Max.	Avg.	Min.	Max.
Fat	2065	1806	2324	0,21	0,18	0,23	20	20	20	909	812	961
Skin	3250			0,43	0,38	0,5	63	61	65	1114	1102	1125

(MCINTOSH; ANDERSON, 2010)

C. Gabriel and his colleagues from Brooks Air Force in the United States developed a parametric model to calculate the dielectric properties of body tissues, which was used by Institute of Applied Physics Nello Carrara in Florence, Italy in its research of protection against low frequency, radio frequency and microwave magnetic field exposure. The result of this research facilitated a website where dielectric properties of several biological tissues can be attained according to the frequency of the magnetic wave exposure (INSTITUTE FOR APPLIED PHYSICS NELLO CARRARA). Some data from this site are shown in Table A.2.

Table A.2 – Dielectric properties of the dry or humid skin and the fat.

Name of Tissue	Frequency [Hz]	Conductivity [S/m]	Relative Permissivity	Tangencial Losses	Wave length [m]	Penetration Depth [m]
Dry Skin	10000	0.000204	1133.6	0.32362	879.27	886.92
	100000	0.00045128	1119.2	0.07248	89.553	393.81
	150000	0.00071518	1111.9	0.077076	59.891	247.71
	200000	0.0010548	1104.8	0.08581	45.056	167.44
	250000	0.001463	1097.7	0.095835	36.153	120.36
	300000	0.001934	1090.5	0.10628	30.218	90.761

Name of Tissue	Frequency [Hz]	Conductivity [S/m]	Relative Permissivity	Tangencial Losses	Wave length [m]	Penetration Depth [m]
Humid Skin	10000	0.002932	29010	0.18166	175.3	309.68
	100000	0.065836	15357	0.77063	22.745	10.628
	150000	0.093995	11362	0.99141	17.088	6.6059
	200000	0.11502	8849.2	1.1682	14.146	4.8909
	250000	0.13116	7180.1	1.3135	12.292	3.9484
	300000	0.14402	6012.6	1.4352	10.992	3.3512
Fat	10000	0.02383	1085.3	39.469	202.27	33.018
	100000	0.024414	92.885	47.247	63.326	10.294
	150000	0.024513	68.11	43.131	51.548	8.3966
	200000	0.024585	56.015	39.448	44.528	7.2689
	250000	0.024642	48.837	36.281	39.737	6.5011
	300000	0.02469	44.075	33.565	36.2	5.9356

(INSTITUTE FOR APPLIED PHYSICS NELLO CARRARA)

APPENDIX B – TABLES OF THE BIOLOGIC TISSUES DIELETRIC PROPERTIES WITH RESPECT TO THE EXPOSING MAGNETIC WAVE FREQUENCY

Table B.1 – Dielectric Properties of the dry skin.

Frequency [Hz]	**Conductivity [S/m]**	**Relative Permissivity**	**Tangencial Loss**	**Wave Length [m]**	**Penetration Depth [m]**
10000	0.000204	1133.6	0.32362	879.27	886.92
24500	0.00022	1130.9	0.14298	362.94	812.13
39000	0.000247	1128.5	0.10083	228.54	723.30
53500	0.000282	1126.2	0.084273	166.83	631.26
68000	0.000327	1124	0.076793	131.41	545.48
82500	0.000379	1121.8	0.073517	108.42	470.07
97000	0.000438	1119.7	0.072502	92.304	405.78
100000	0.00045128	1119.2	0.07248	89.553	393.81
111500	0.000505	1117.5	0.072826	80.377	351.78
126000	0.000579	1115.4	0.073996	71.193	306.67
140500	0.000659	1113.3	0.075726	63.903	269.00
150000	0.00071518	1111.9	0.077076	59.891	247.71
155000	0.000746	1111.2	0.07784	57.977	237.44
169500	0.000839	1109.1	0.080225	53.065	210.88
184000	0.000938	1107.1	0.082803	48.926	188.40
198500	0.001044	1105	0.085522	45.392	169.26
200000	0.0010548	1104.8	0.08581	45.056	167.44
213000	0.001155	1102.9	0.088343	42.339	152.85
227500	0.001271	1100.9	0.091239	39.675	138.71
242000	0.001393	1098.8	0.09419	37.331	126.44
250000	0.001463	1097.7	0.095835	36.153	120.36
256500	0.001521	1096.7	0.097179	35.251	115.74
271000	0.001654	1094.7	0.1002	33.394	106.35
285500	0.001791	1092.6	0.10323	31.725	98.084
300000	0.001934	1090.5	0.10628	30.218	90.761

(INSTITUTE FOR APPLIED PHYSICS NELLO CARRARA)

Table B.2 – Dielectric Properties of the wet skin.

Frequency [Hz]	Conductivity [S/m]	Relative Permissivity	Tangencial Loss	Wave Length [m]	Penetration Depth [m]
10000	0.002932	29010	0.18166	175.3	309.68
24500	0.010626	26338	0.29602	74.603	81.941
39000	0.020909	23728	0.40616	48.942	39.878
53500	0.032091	21317	0.50581	37.272	24.871
68000	0.043247	19170	0.59635	30.61	17.681
82500	0.053908	17293	0.67923	26.295	13.609
97000	0.06387	15665	0.75557	23.264	11.042
100000	0.065836	15357	0.77063	22.745	10.628
111500	0.07307	14257	0.82625	21.011	9.2971
126000	0.081522	13038	0.89199	19.264	8.0431
140500	0.08927	11980	0.95335	17.865	7.1029
150000	0.093995	11362	0.99141	17.088	6.6059
155000	0.096377	11057	1.0108	16.715	6.3739
169500	0.10291	10249	1.0647	15.75	5.7932
184000	0.10892	9538.6	1.1155	14.927	5.3202
198500	0.11447	8910.1	1.1634	14.214	4.9277
200000	0.11502	8849.2	1.1682	14.146	4.8909
213000	0.11961	8351.8	1.2086	13.59	4.5968
227500	0.12438	7853.5	1.2514	13.037	4.3141
242000	0.12883	7407	1.292	12.543	4.0696
250000	0.13116	7180.1	1.3135	12.292	3.9484
256500	0.13299	7005	1.3305	12.099	3.8561
271000	0.13689	6641.9	1.3671	11.696	3.6679
285500	0.14056	6312.4	1.402	11.329	3.5007
300000	0.14402	6012.6	1.4352	10.992	3.3512

(INSTITUTE FOR APPLIED PHYSICS NELLO CARRARA)

Table B.3 – Dielectric Properties of the fat.

Frequency [Hz]	**Conductivity [S/m]**	**Relative Permissivity**	**Tangencial Loss**	**Wave Length [m]**	**Penetration Depth [m]**
10000	0.02383	1085.3	39.469	202.27	33.018
24500	0.024071	363.6	48.571	128.88	20.939
39000	0.024185	220.82	50.481	101.95	16.55
53500	0.024262	161.56	50.459	86.906	14.108
68000	0.02432	129.32	49.715	76.982	12.501
82500	0.024367	109.09	48.668	69.808	11.341
97000	0.024407	95.226	47.496	64.311	10.453
100000	0.024414	92.885	47.247	63.326	10.294
111500	0.02444	85.131	46.284	59.926	9.7457
126000	0.02447	77.451	45.074	56.321	9.1649
140500	0.024497	71.413	43.888	53.291	8.6769
150000	0.024513	68.11	43.131	51.548	8.3966
155000	0.024522	66.539	42.739	50.696	8.2595
169500	0.024544	62.522	41.632	48.442	7.8972
184000	0.024564	59.153	40.569	46.46	7.5789
198500	0.024583	56.287	39.551	44.7	7.2963
200000	0.024585	56.015	39.448	44.528	7.2689
213000	0.024601	53.819	38.577	43.122	7.0433
227500	0.024618	51.67	37.645	41.697	6.815
242000	0.024634	49.783	36.755	40.403	6.6077
250000	0.024642	48.837	36.281	39.737	6.5011
256500	0.024649	48.112	35.904	39.22	6.4183
271000	0.024663	46.621	35.09	38.133	6.2444
285500	0.024677	45.283	34.311	37.129	6.0841
300000	0.02469	44.075	33.565	36.2	5.9356

(INSTITUTE FOR APPLIED PHYSICS NELLO CARRARA)

APPENDIX C – SOME BASIC THEORY

C.1. PROXIMITY AND SKIN EFFECT

A time-varying current has a tendency to concentrate near the surfaces of conductors. When the frequency is very high, the current is restricted to a very thin layer near the conductor surfaces, and this effect is therefore known as the skin effect. This effect is generated by the alternating electromagnetic field action and is defined by the decrease of current density inside the conductor and simultaneously the increase of current in the crown or the most external section.

This effectively limits the cross-sectional conducting area available to carry alternating electron flow, thus increasing the resistance of that conductor above what it would normally be for direct current.

The electrical resistance of the conductor with all its cross-sectional area in use is known as the “DC resistance”. The resistance of the same conductor referring to a higher figure resulting from the skin effect is called “AC resistance”. As can be seen at high frequencies, the AC current avoids travelling through most of the conductor's cross-sectional area. For the purpose of conducting current, the wire might as well be hollow.

Furthermore, in a conductor carrying alternating current, if currents are flowing through one or more nearby conductors such as within a closely wound coil of wire, the distribution of the current within each conductor will be constrained to smaller regions depending on the intensity of the electrical field created by the currents flowing in the other conductors. The resulting current crowding is termed the proximity effect.

Summarizing, skin effect is the tendency for high-frequency currents to flow on the surface of a conductor and proximity effect is the tendency for current to flow in other undesirable patterns (loops or concentrated distributions) due to the presence of magnetic fields generated by nearby conductors. Thus, the joule loss resistances of the given TET coils may increase with the increase of frequency, depending on the thickness of the wire and they may also increase with the coil gap due to the proximity effect from one coil to the other.

C.2. THE QUALITY FACTOR

The joule loss resistance of a coil dissipates electric power into heat, causing a loss of inductive quality. Moreover, for different winding arrangements in the same volume and shape, the relation between the self-inductance *L* and the joule loss resistance *r* of a coil is constant. The higher the *Q* factor of the coil is, the closer it approaches the behavior of an ideal lossless coil. Thus, the quality factor (or *Q*) of a coil is defined by this ratio at a fixed frequency, and is a way to measure its figure of merit.

$$Q = \frac{\omega . L}{r} \tag{C.1}$$

In this equation, $\omega = 2.\pi.f$ and *f* is the frequency at which the quality factor is calculated.

Note that one way to increase the inductive quality would be increasing the frequency. Another option to increase *Q* would be the use of ferromagnetic cores, which increases the self-inductance for the same amount of turns, i.e., without increasing the joule loss resistance. However, ferromagnetic cores introduce magnetic losses that increase with frequency. For this reason, it is common to find coreless coils at higher frequencies.

That been said, the quality factor could be a good metric to evaluate the performance of the TET transformer:

$$Q_1 = \frac{\omega . L_1}{r_1} \tag{C.2}$$

$$Q_2 = \frac{\omega . L_2}{r_2 + R_L} \tag{C.3}$$

In these equations, R_L is the load resistance, and r_1, r_2 and L_1, L_2 are respectively the primary and secondary joule loss resistances and self-inductances.

C.3. THE COUPLING FACTOR

When the transformer coils have a gap, only part of the magnetic flux generated by the primary coil passes through the secondary coil and contributes to the power transmission. The more concatenated the flux is in the secondary coil, the better coupled the coils are. This relation of coupling is expressed by the coupling factor *k*, which is a value between 0 (system where primary and secondary coils are completely uncoupled of each other) and ±1 (perfect coupling, i.e. all the flux generated by the primary coil is concatenated to the secondary coil). This factor depends on the distance and the angle between the coils and their relative size and shape. If the coils are axially aligned, a displacement causes a decrease of *k*. The definition of the coupling factor is given by:

$$k = \frac{M}{\sqrt{L_1 . L_2}} \tag{C.4}$$

In this equation, M is the mutual inductance and L_1 and L_2 are respectively the primary and secondary self-inductance.

C.3.1. The effect of the coupling factor on the load power and efficiency.

According to (LI et al., 2009), for TET systems with serial resonance capacitors (SRCs) compensating the self-inductances of the coils, there is an optimal coupling factor *k* different than the maximum coupling factor, which generates the maximum load power that can be transferred by the system (note that this coupling is optimal to maximize the power and not the efficiency). This coupling factor and this maximum load power can be calculated by:

$$k_o = \frac{1}{\sqrt{Q_1.Q_2}} = \frac{1}{\sqrt{\frac{\omega.L_1}{r_1}.\frac{\omega.L_2}{r_2 + R_L}}} \tag{C.5}$$

$$P_{max} = \frac{R_L.V_1^2}{4.r_1.(r_2 + R_L)} \tag{C.6}$$

In these equations, Q_1 and Q_2 are respectively the primary and secondary quality factors, V_1 is the primary sinusoidal voltage, R_L is the load resistance, and r_1 and r_2 are respectively the primary and secondary Joule loss resistances.

Equation (C.6) is important to verify the perfect working of the system because the supplied power may not be enough at higher coupling cases even if it is enough at lower coupling cases.

APPENDIX D – DATA COLLECTION

The powers, currents and voltages of the primary and secondary coils were collected by simulations in order to compute the efficiency and regulation of the TET coils. When the TET coils were connected to SRCs, the data collected to calculate the efficiency and regulation was considering the SRCs as part of the coils:

$$\eta = \frac{P_{Load}}{P_{Source}} \tag{D.1}$$

$$\mathcal{R} = \frac{V_o - V_{Load}}{V_{Load}} \tag{D.2}$$

In these equations, P_{Load} is the power simulated in the load that models the AO with any converter electronic circuits, i.e., it is the power of the secondary coil considering the SRC if it exists; P_{Source} is the power supplied by the inverter, i.e., it is the power of the primary coil considering the SRC when it exists; V_{Load} is the simulated voltage at the secondary coil considering the existence of the SRC; and V_o is the secondary coil voltage as already mentioned, with no-load.

The SAR was computed by dividing the simulated data of power per unit of volume by the biologic tissue volumetric density. Unfortunately, the power per unit of volume can be computed in Flux-2D only inside each FE node. Thus, subroutines in Python[5]

---

[5] http://www.python.org/doc/

language were created to explore the power per unit of volume computed by Flux-2D in each FE node of the biologic tissue.

As seen in Section 2.6.3, according to ICNIRP, the average SAR should be computed in ten grams of biologic tissue. Thus, the radius of skin that makes ten grams of volume was calculated in order to define a region where the power per unit of volume should be explored.

Then, the Python subroutines calculated the barycenter and the area of each element inside the region defined by the mentioned radius in order to compute the weighted arithmetic mean of all elements of the skin inside this mentioned region. At last, the total mean was computed in the desired volume of 10 g.

Note that this procedure does not provide the SAR at precisely 10 g because some elements are only partially inside the volume of 10 g, but this technique presents a very good approximation because each element is extremely small.

APPENDIX E – COMPARISON AMONG THE METHODS

E.1. COILS WITH THICK WIRES

The set of coils of wire AWG 15 presented in Section 3.6.2 were simulated with slight coupling differences, as presented in the same section (“Uncoupled”, “No-load coupled”, “Short-circuited coupled”). Figure E.1, Figure E.2, Figure E.3, Figure E.4, Figure E.5 and Figure E.6 show the results of these simulations.

Figure E.1 – Comparison of the real and imaginary impedance (coil of 35 turns with wire AWG 15 is far from the other coil) between the data measured and calculated via Gmsh/GetDP with full model and via Gmsh/GetDP with homogenization.

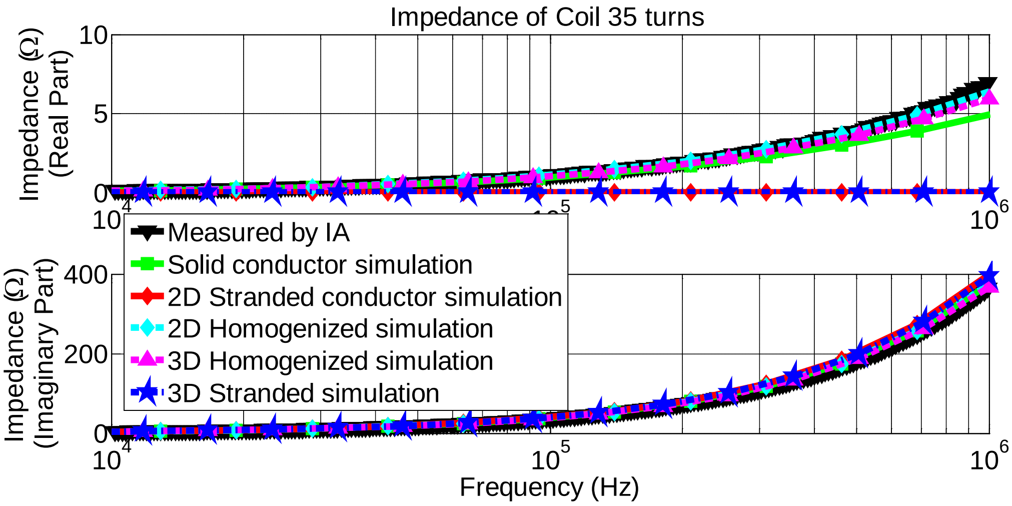

Figure E.2 – Comparison of the real and imaginary impedance (coil of 35 turns with wire AWG 15; coil gap of 5 mm; coil of 50 turns with wire AWG 15 at no-load) between the data measured and calculated via Gmsh/GetDP with full model and via Gmsh/GetDP with homogenization.

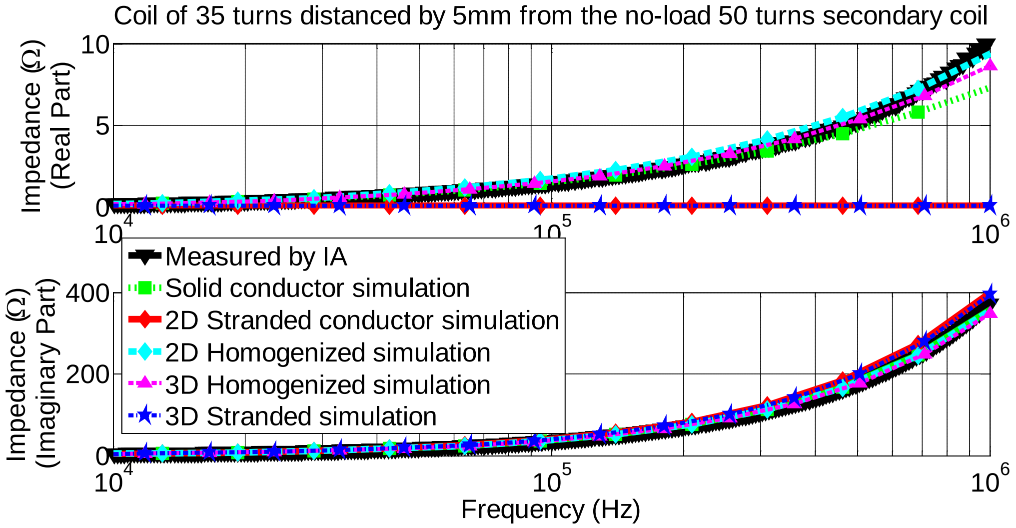

Figure E.3 – Comparison of the real and imaginary impedance (coil of 35 turns with wire AWG 15; coil gap of 5 mm; coil of 50 turns with wire AWG 15 in short-circuit) between the data measured and calculated via Gmsh/GetDP with full model and via Gmsh/GetDP with homogenization.

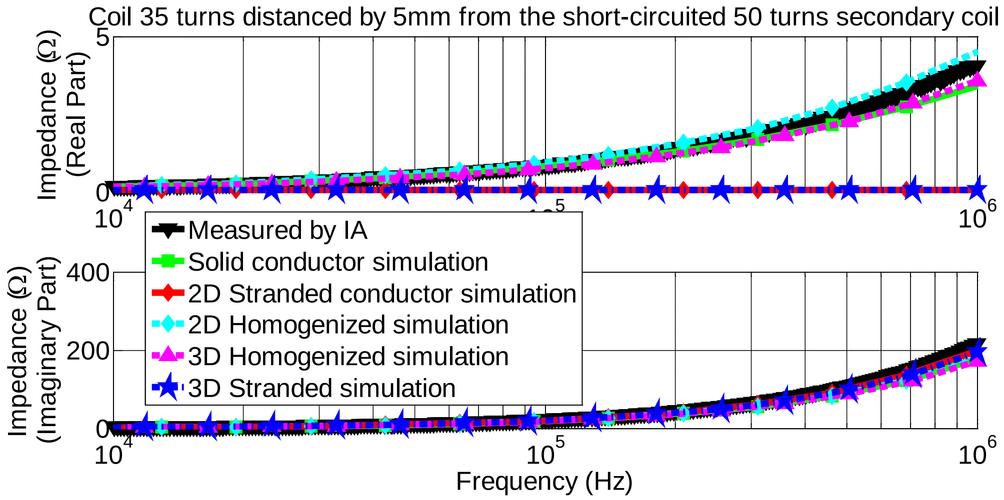

Figure E.4 – Comparison of the real and imaginary impedance (coil of 50 turns with wire AWG 15 is far from the other coil) between the data measured and calculated via Gmsh/GetDP with full model and via Gmsh/GetDP with homogenization.

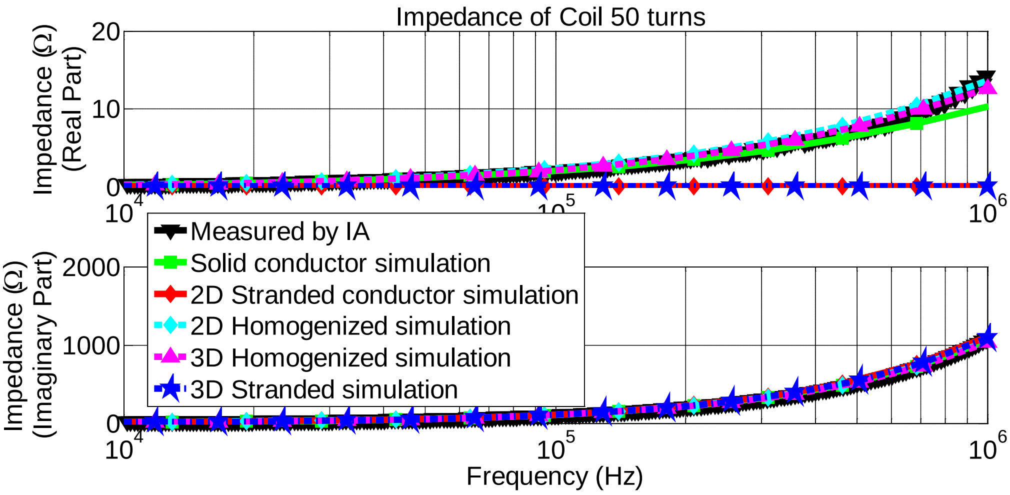

Figure E.5 – Comparison of the real and imaginary impedance (coil of 50 turns with wire AWG 15; coil gap of 5 mm; coil of 35 turns with wire AWG 15 at no-load) between the data measured and calculated via Gmsh/GetDP with full model and via Gmsh/GetDP with homogenization.

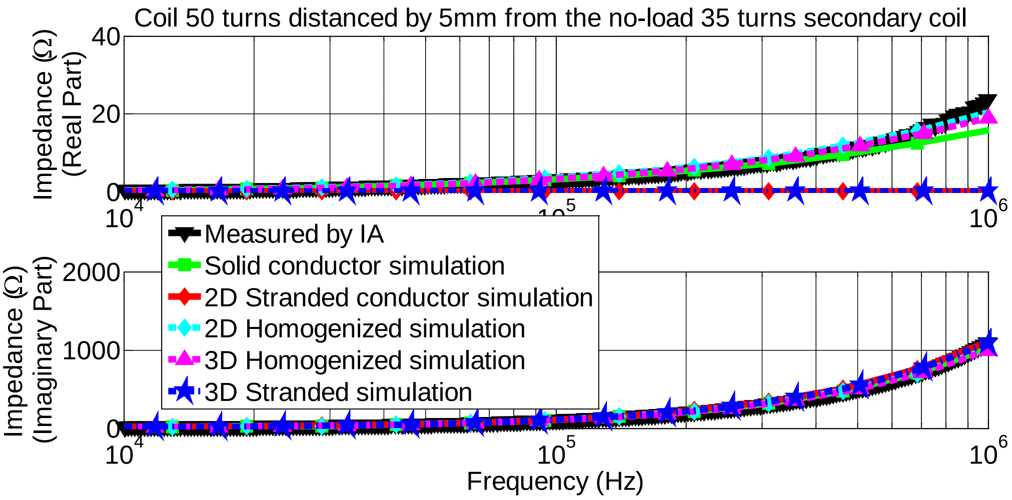

Figure E.6 – Comparison of the real and imaginary impedance (coil of 50 turns with wire AWG 15; coil gap of 5 mm; coil of 35 turns with wire AWG 15 in short-circuit) between the data measured and calculated via Gmsh/GetDP with full model and via Gmsh/GetDP with homogenization.

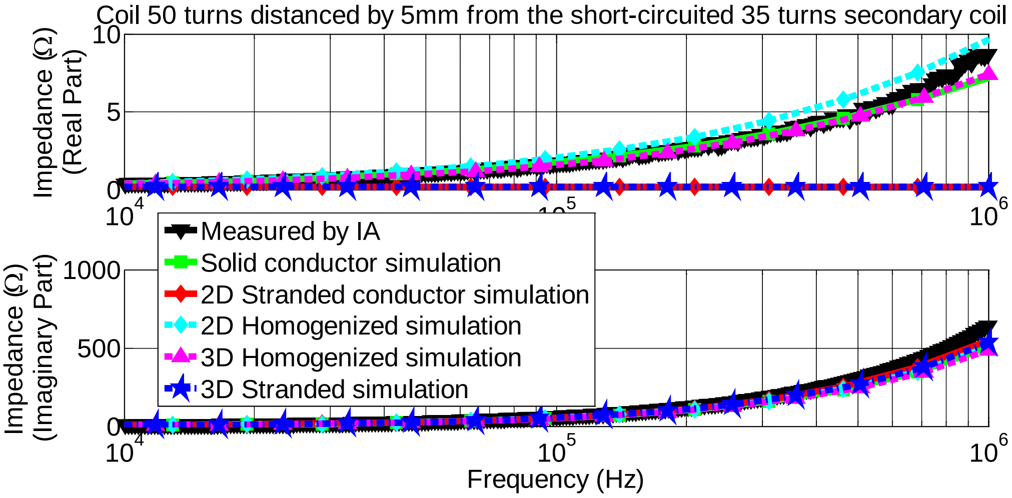

E.2. COILS WITH THIN AND THICK WIRES

Similarly to the configuration with tick wires on both coils, the set of coils with different wire cross-section (one thick and another thin) presented in Section 3.6.3 was also simulated with the slight differences mentioned in Section 3.6.2 (“Uncoupled”, “No-load coupled”, “Short-circuited coupled”). Figure E.7, Figure E.8, Figure E.9, Figure E.10, Figure E.11 and Figure E.12 show the results of these simulations.

Figure E.7 – Comparison of the real and imaginary impedance (coil of 62 turns with wire AWG 19 is far from the other coil) between the data measured and calculated via Gmsh/GetDP with full model and via Gmsh/GetDP with homogenization.

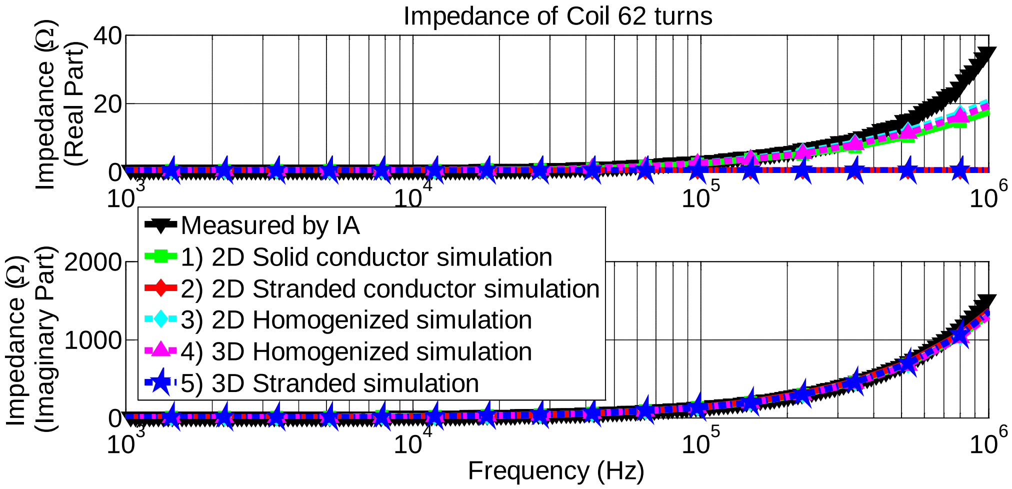

Figure E.8 – Comparison of the real and imaginary impedance (coil of 62 turns with wire AWG 19; coil gap of 5 mm; coil of 24 turns with wire AWG 26 at no-load) between the data measured and calculated via Gmsh/GetDP with full model and via Gmsh/GetDP with homogenization.

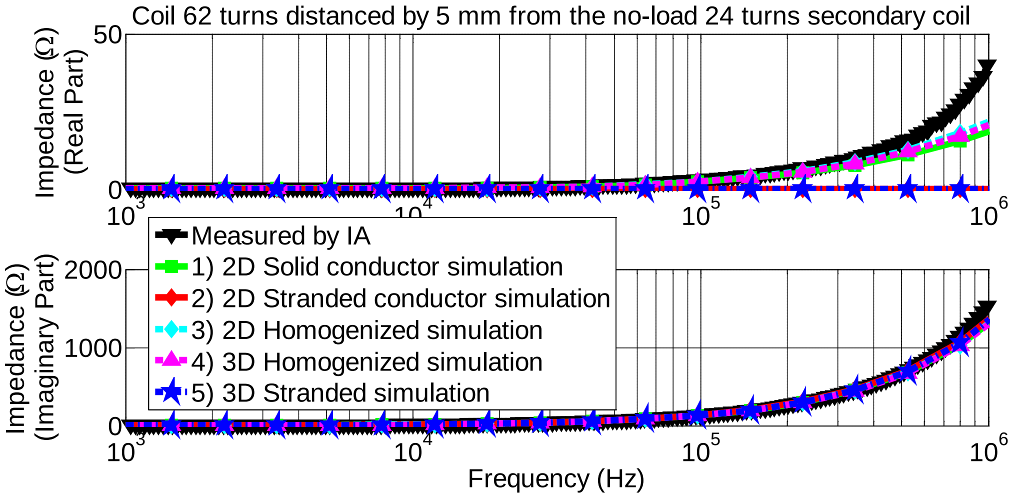

Figure E.9 – Comparison of the real and imaginary impedance (coil of 62 turns with wire AWG 19; coil gap of 5 mm; coil of 24 turns with wire AWG 26 in short-circuit) between the data measured and calculated via Gmsh/GetDP with full model and via Gmsh/GetDP with homogenization.

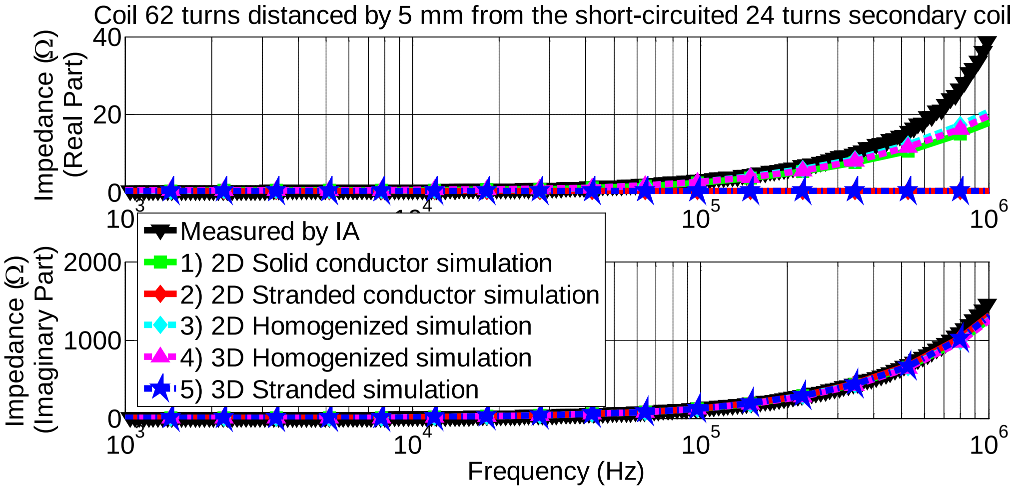

Figure E.10 – Comparison of the real and imaginary impedance (coil of 24 turns with wire AWG 26 is far from the other coil) between the data measured and calculated via Gmsh/GetDP with full model and via Gmsh/GetDP with homogenization.

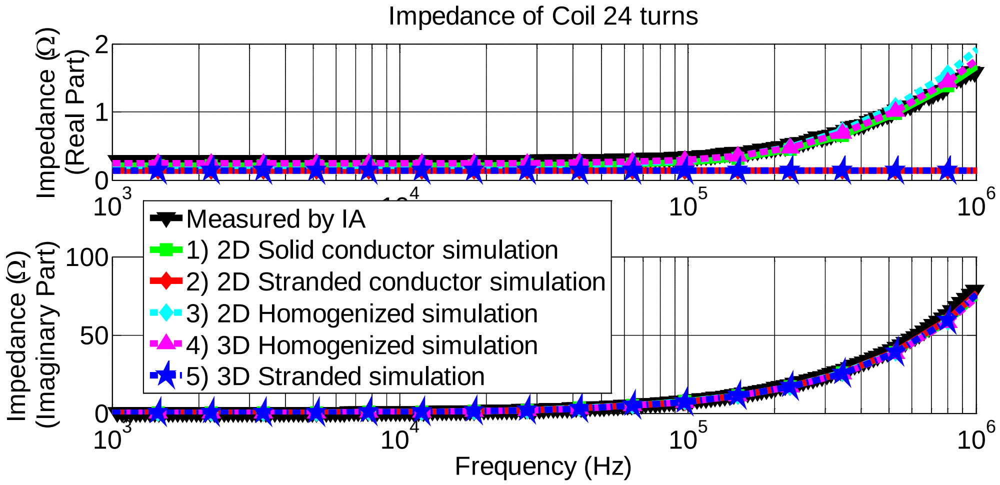

Figure E.11 – Comparison of the real and imaginary impedance (coil of 24 turns with wire AWG 26; coil gap of 5 mm; coil of 62 turns with wire AWG 19 at no-load) between the data measured and calculated via Gmsh/GetDP with full model and via Gmsh/GetDP with homogenization.

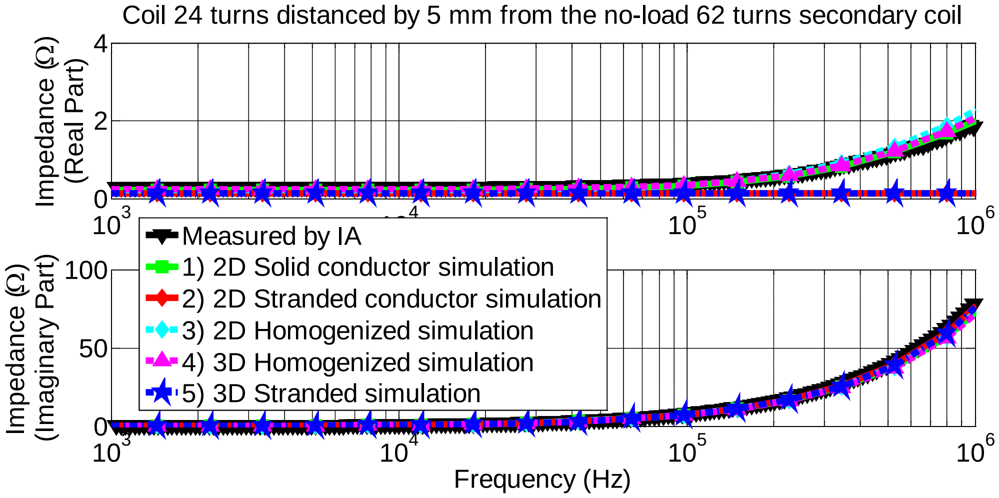

Figure E.12 – Comparison of the real and imaginary impedance (coil of 24 turns with wire AWG 26; coil gap of 5 mm; coil of 62 turns with wire AWG 19 in short-circuit) between the data measured and calculated via Gmsh/GetDP with full model and via Gmsh/GetDP with homogenization.

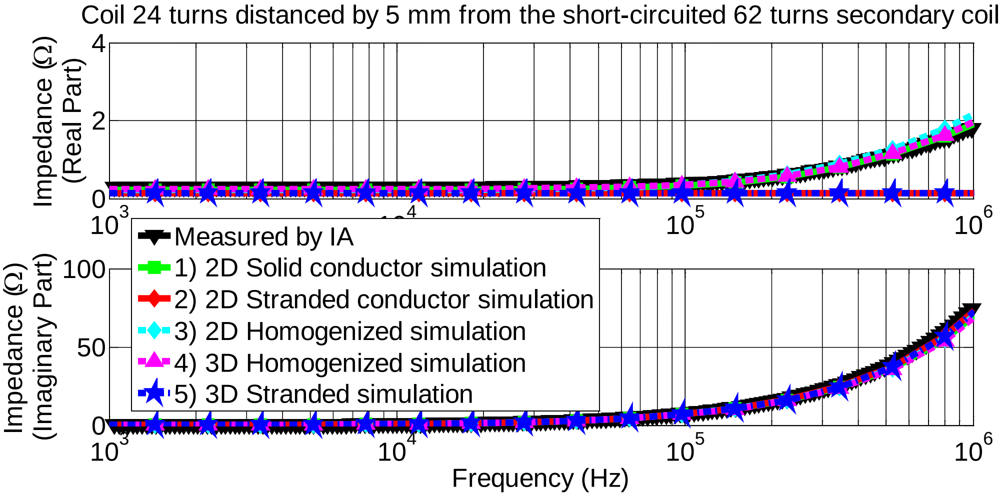

APPENDIX F – GENETIC ALGORITHM

Genetic Algorithm (GA) is an evolutionary computational technique inspired by the theory of evolution of Darwin and proposed by John Henry Holland, the author of the book "Adaption in Natural and Artificial Systems" published in 1975.

The GA has a set of points which represents a possible solution of the problem and an objective function. This set of points form an individual or chromosome that is a chain of DNA in biology serving as a template for the whole organism. One set of solutions (individuals) is called population.

The objective function, a function of which the best value is sought, is used to evaluate the suitability of each individual. Thus, the individual can have better or worse objective function, i.e., it may have more or less chance of survival.

Therefore, GA uses techniques of evolutionary biology as:

- Natural selection: the fittest individuals survive and transmit their genes to their generations. Similarly, the GA selects two individuals with better fitness function to be parents of young individuals. There are different techniques to select individuals with better objective function: roulette, Boltzman, championship, classification, steady state and other.
- Cross-over: while the reproduction occurs, there is an exchange among the genes of the parents, combining them to form a new individual. The GA uses probability to cross-over the parents and make a new generation.
- Mutation: the elements of DNA are slightly modified, for example by errors in copying the genes from parents. Following this model, the GA uses probability to change a new generation of individuals directly in the gene, or in the coding of one element. Different techniques for encoding may be used: binary permutation, etc.

- Adaptation: is measured by the survival of the organism. If the individual cannot adapt, it dies and cannot reproduce. Similarly, the genetic algorithm checks the objective function to evaluate the chance of continuing in the population to transmit their genes or simply no longer be used.

Thus, the better the population is, the more likely the reproduction will be and therefore the greater the probability of a new better generation will be.

GA can be itemized as follows:

1. Starting: Generate a random population of *n* individuals (suitable solutions for the problem).
2. Suitability: Evaluates the objective function value of each individual in the population and the chance of them to be used for reproduction.
3. Reproduction: With the fittest individuals, GA creates a new population through the different techniques of evolutionary biology (selection, cross-over and mutation) until the new population is complete.
4. Replacement: The algorithm uses the new generated population for the next round.
5. Test: If the final condition is satisfied, GA stops and supplies the best solution of the current population. Otherwise, GA return to item 2.

In this algorithm the number of individuals in a population is also important because it can slow down the algorithm and tighten the stopping criteria.